

7

# Damage Accumulation in a Gradient Stress Field in Graphite/Epoxy Laminates

by

CHRISTOPHER EDWARD WOLFE

S.B., Massachusetts Institute of Technology  
(1987)

SUBMITTED IN PARTIAL FULFILLMENT OF THE  
REQUIREMENTS FOR THE DEGREE OF

MASTER OF SCIENCE  
IN  
AERONAUTICS AND ASTRONAUTICS

May, 1989

© Massachusetts Institute of Technology, 1989

Signature of Author \_\_\_\_\_

Department of Aeronautics and Astronautics

15th, 1989

Certified by \_\_\_\_\_

Lagace

Thesis Supervisor

Accepted by \_\_\_\_\_

Professor Harold Y. Wachman  
Chairman, Departmental Graduate Committee

MASSACHUSETTS INSTITUTE  
OF TECHNOLOGY

JUN 07 1989

LIBRARIES

WITHDRAWN  
M.I.T.  
LIBRARIES

## **Damage Accumulation in a Gradient Stress Field in Graphite/Epoxy Laminates**

by

Christopher E. Wolfe

Submitted to the Department of Aeronautics and Astronautics on May 12th, 1989 in  
partial fulfillment of the requirements for the Degree of Master of Science

### **Abstract**

The progression of damage in gradient stress fields was studied both experimentally and analytically in simply-supported graphite/epoxy columns. Three layups,  $[45^\circ_4/-45^\circ_4/(0^\circ/90^\circ)_4]_{2s}$ ,  $[\pm 45^\circ/0^\circ/90^\circ_4]_{2s}$  and  $[(45^\circ_2/-45^\circ_2/0^\circ)_2/90^\circ_5]_{2s}$ , were chosen so that matrix damage would be the first type of damage to occur. Different stacking sequences and proportions of  $0^\circ$ ,  $45^\circ$  and  $90^\circ$  plies were used to cause damage to initiate in different plies in the laminates. All tests were run in displacement control, thus the occurrence of damage resulted in a drop in applied load. At each load drop, the tests were interrupted, and edge replicas and X-ray photographs were taken. From these, a damage history was pieced together for each laminate type. Damage varied both along the length and through the thickness of the specimens, but was confined almost exclusively to the tension side of the specimens. Delamination initiation always occurred at matrix cracks, and was also influenced by edge effects. The damage accumulated prior to final failure did not affect the global stiffness by more than 10%. The column was modelled using two-dimensional plane stress, eight node finite elements. The Maximum Stress failure criterion was used in conjunction with the stresses determined from the analysis to predict in-plane damage, while the Quadratic Delamination Criterion was used to predict delamination. To model damage, appropriate element stiffness properties were set to zero when in-plane damage was predicted, while the two affected elements were effectively disconnected when delamination was predicted. Predictions of specimen behavior up to the occurrence of damage were very good for all three laminate types, though it was necessary to model the material nonlinearities of the  $45^\circ$  plies. Loads at which both in-plane and delamination damage were predicted matched experimental observations very well. However, refinements in the models are necessary to improve predictions of delamination propagation, as shortcomings in this area led to significant differences between the predicted final failure modes and those observed experimentally. Even so, the center deflections at which final failures were predicted gave a useful, if conservative, indication of when the specimens would fail.

Thesis Supervisor: Paul A. Lagace

Title: Associate Professor of Aeronautics and Astronautics

## Acknowledgements

It has taken the contributions of many people to get this thesis where it is now, which is sitting on my desk, or rather one of the extra desks I have taken over in the last few weeks, waiting for all the right signatures. I would like to thank the Uropers who worked with me: Jean Kim, who started on this project at the same time as I did and persevered through those early days of total cluelessness, Charles Whetsel, whose imagination and willingness to tackle bugs in the most horribly written programs was much appreciated, Bob Cruikshank, whose stamina at the milling machine was legendary, and Michelle Perry, viewgraph creator *par excellence*. I am grateful to my fellow graduate students, John, Narendra, Tom, Ken, Kevin, Pierre, Wilson, Peter, Adam, Simon, Mike and Kiernan, for their companionship, their help and insights, and the daily, I meant occasional, hands of bridge. Kevin and Pierre were invaluable in their help in all things analytical. I would also like to thank Ping Yang, who is a visiting scientist from China, for his suggestions for the finite element models. On the experimental side of things, Don Weiner and Earle Wassmouth both deserve my gratitude for their help and advice on the design and construction of a variety of jigs, bicycle maintenance and other related topics. Al Supple, a man of infinite wisdom and patience, has made work in the lab both productive and enjoyable. TELAC would not be what it is without him. Ping Lee has been wonderful as a fountain of information on all the important matters. I would particularly thank Paul Lagace, my advisor, for his support and guidance throughout this work, and especially in these final stages. On the home front, my parents have been an unfailing source of support. Last, but certainly not least, Ellen, who has lived through every step of all this, has been the reason for my sanity (sort of...) and happiness. It's your turn next year! Once again, thank you one and all.

## **Foreword**

This work was performed in the Technology Laboratory for Advanced Composites (TELAC) of the Department of Aeronautics and Astronautics at the Massachusetts Institute of Technology. This work was sponsored by Boeing Military Aircraft under Boeing Purchase Order 644740.

**Table of Contents**

<b><u>Chapter</u></b>		<b><u>Page</u></b>
1.	INTRODUCTION	18
2.	SUMMARY OF PREVIOUS WORK	22
	2.1 Overview	22
	2.2 Buckling and Postbuckling	22
	2.3 Damage Prediction	25
	2.3.1 Initial Damage	25
	2.3.2 Modelling Damage	27
	2.3.3 Progressive Damage	28
	2.3.4 Experimental Observations	29
	2.4 Summary	30
3.	TEST DEVELOPMENT	32
	3.1 Specimen Geometry	32
	3.2 The Test Jig	33
	3.2.1 The Bearing Jig	35
	3.2.2 The Knife Edge Jig	41
4.	THE ANALYTICAL MODEL	50
	4.1 The Finite Element Model	50
	4.2 Material Nonlinearities	60
	4.3 Failure Criteria	62
	4.3.1 In-Plane Criterion	62
	4.3.2 Delamination Criterion	67
	4.4 Modelling Damage	71

## Table of Contents (continued)

<u>Chapter</u>	<u>Page</u>
4.4.1 In-Plane Damage	71
4.4.2 Delaminations	71
4.5 Model Implementation	73
5. THE EXPERIMENT	74
5.1 The Test Program	74
5.1.1 Material	74
5.1.2 Laminate Selection	74
5.1.3 Test Matrix	76
5.2 Specimen Manufacture	77
5.3 Instrumentation	85
5.4 Damage Detection	87
5.4.1 The Load Drop Technique	87
5.4.2 Edge Replication	88
5.4.3 X-Radiography	91
5.4.4 Destructive Examinations	91
5.4.5 Replica and Photograph Interpretation	93
5.5 Test Procedure	94
6. RESULTS	99
6.1 Experimental Results	99
6.1.1 Load versus Deflection	99
6.1.2 Damage Histories	102

## Table of Contents (continued)

<u>Chapter</u>	<u>Page</u>
6.1.3 Results of Destructive Examinations	116
6.2 Comparison of Model and Experimental Results	136
6.2.1 Selection of a Characteristic Specimen	136
6.2.2 Load versus Deflection Prior to Damage	136
6.2.3 Material Nonlinearities	137
6.2.4 Comparison of Damage Histories	145
7. DISCUSSION	169
7.1 Evaluation of the Experiment	169
7.1.1 The Specimen	169
7.1.2 Damage Detection Procedures	170
7.2 Characteristics of Damage Accumulation	171
7.3 Evaluation of the Model	174
7.3.1 The Finite Element Model	174
7.3.2 Material Nonlinearity	175
7.3.3 Damage Accumulation	176
8. CONCLUSIONS AND RECOMMENDATIONS	179
REFERENCES	183
Appendix A	188
Appendix B	212

## List of Figures

<u>Figure</u>	<u>Page</u>
3.1 Test specimen characteristics.	34
3.2 Characteristics of the Bearing Jig	36
3.3 Side view of Bearing Jig with alignment plate.	37
3.4 Load versus center deflection for an aluminum specimen tested in the Bearing Jig.	38
3.5 Comparison of deflection along the length of the specimen with cosine and sine waves, before and after deflection shape change, respectively.	39
3.6 Initial configuration of the Knife Edge Jig.	43
3.7 Load versus center deflection for an aluminum	44
3.8 Load versus center deflection for an aluminum specimen tested in the Knife Edge Jig with eccentric load application.	47
3.9 Comparison of deflection along the length with a sine wave for an aluminum specimen.	48
3.10 Final configuration of the Knife Edge Jig.	49
3.11 Load versus center deflection for a $[\pm 45^\circ/0^\circ]_{10s}$ graphite/epoxy specimen tested in the completed Knife Edge Jig.	50
4.1 Characteristics of the basic eight-node element.	52
4.2 The finite element model of the $[45^\circ_4/-45^\circ_4/(0^\circ/90^\circ)_4]_{2s}$ specimen type.	54
4.3 The finite element model of the $[\pm 45^\circ/0^\circ/90^\circ_4]_{4s}$ specimen type.	55
4.4 The finite element model of the $[(45^\circ_2/-45^\circ_2/0^\circ)_2/90^\circ_5]_{2s}$ specimen type.	56

## List of Figures (Continued)

<u>Figure</u>	<u>Page</u>
4.5 Flow chart outlining use made of ADINA results.	61
4.6 Stiffness versus strain used for 45° plies in models.	63
4.7 Poisson's ratio versus strain used for 45° plies in model.	64
4.8 Flow chart outlining the ADINA runs made.	65
4.9 Sketch showing how load versus deflection data from several ADINA runs is spliced together to model nonlinear stiffness.	66
4.10 Refined mesh around the stress concentration at	69
4.11 Refined mesh at a delamination tip.	72
5.1 Schematics of Cure Setup	81
5.2 Schematic of cure cycle	82
5.3 Locations of measurements	83
5.4 Strain gage locations.	86
5.5 Illustration of load increase obscuring a load drop.	89
5.6 Illustration of a specimen cut for destructive examination.	92
5.7 Photograph of the edge replica of a $[\pm 45^\circ/0^\circ/90^\circ]_4$ specimen, with the corresponding transcription.	95
6.1 Typical Southwell Plot.	100
6.2 Load versus center deflection for uninterrupted test of $[45^\circ_4/-45^\circ_4/(0^\circ/90^\circ)_4]_{2S}$ specimen.	106
6.3 Load versus center deflection for uninterrupted test of $[\pm 45^\circ/0^\circ/90^\circ]_4$ specimen.	107
6.4 Load versus center deflection for uninterrupted test of $[(45^\circ_2/-45^\circ_2/0^\circ)_2/90^\circ_5]_{2S}$ specimen.	108

### List of Figures (Continued)

<u>Figure</u>		<u>Page</u>
6.5	Load versus center deflection for a $[45^\circ_4/-45^\circ_4/(0^\circ/90^\circ)_4]_{2S}$ specimen at each characteristic damage state.	109
6.6	Load versus center deflection for a $[\pm 45^\circ/0^\circ/90^\circ_4]_{4S}$ specimen at each characteristic damage state.	110
6.7	Load versus center deflection for a $[(45^\circ_2/-45^\circ_2/0^\circ)_2/90^\circ_5]_{2S}$ specimen at each characteristic damage state.	111
6.8	X-ray photographs of a $[45^\circ_4/-45^\circ_4/(0^\circ/90^\circ)_4]_{2S}$ specimen at (a) the first and (b) the second characteristic damage states.	117
6.9	Illustrations of the four characteristic damage states of the $[45^\circ_4/-45^\circ_4/(0^\circ/90^\circ)_4]_{2S}$ layup.	118
6.10	Photograph of a $[45^\circ_4/-45^\circ_4/(0^\circ/90^\circ)_4]_{2S}$ specimen after failure.	119
6.11	X-ray photographs of an $[\pm 45^\circ/0^\circ/90^\circ_4]_{4S}$ specimen at (a) the first and (b) the second damage states.	120
6.12	Illustrations of the four characteristic damage states of the $[\pm 45^\circ/0^\circ/90^\circ_4]_{4S}$ layup.	121
6.13	Photograph of a $[\pm 45^\circ/0^\circ/90^\circ_4]_{4S}$ specimen after failure.	122
6.14	X-ray photographs of an $[(45^\circ_2/-45^\circ_2/0^\circ)_2/90^\circ_5]_{2S}$ specimen at (a) the first and (b) the second damage state.	123
6.15	X-ray photograph of an $[(45^\circ_2/-45^\circ_2/0^\circ)_2/90^\circ_5]_{2S}$ specimen at the third characteristic damage state.	124
6.16	Illustrations of the four characteristic damage states of the $[(45^\circ_2/-45^\circ_2/0^\circ)_2/90^\circ_5]_{2S}$ layup.	125
6.17	Photograph of a $[(45^\circ_2/-45^\circ_2/0^\circ)_2/90^\circ_5]_{2S}$ specimen after failure.	126

## List of Figures (Continued)

<u>Figure</u>	<u>Page</u>
6.18 Comparison of damage across width at the first characteristic damage state of the $[45^{\circ}_4/-45^{\circ}_4/(0^{\circ}/90^{\circ})_4]_{2s}$ layup.	129
6.19 Comparison of damage across width at the second characteristic damage state of the $[45^{\circ}_4/-45^{\circ}_4/(0^{\circ}/90^{\circ})_4]_{2s}$ layup.	130
6.20 Comparison of damage across width at the fourth characteristic damage state of the $[45^{\circ}_4/-45^{\circ}_4/(0^{\circ}/90^{\circ})_4]_{2s}$ layup.	131
6.21 Comparison of damage across width at the third characteristic damage state of the $[\pm 45^{\circ}/0^{\circ}/90^{\circ}]_{4s}$ layup.	132
6.22 Comparison of damage across width at the fourth characteristic damage state of the $[\pm 45^{\circ}/0^{\circ}/90^{\circ}]_{4s}$ layup.	133
6.23 Comparison of damage across width at the third characteristic damage state of the $[(45^{\circ}_2/-45^{\circ}_2/0^{\circ})_2/90^{\circ}]_{5} ]_{2s}$ layup.	134
6.24 Comparison of damage across width at the fourth characteristic damage state of the $[(45^{\circ}_2/-45^{\circ}_2/0^{\circ})_2/90^{\circ}]_{5} ]_{2s}$ layup.	135
6.25 Experimental and predicted load versus center deflection for the $[45^{\circ}_4/-45^{\circ}_4/(0^{\circ}/90^{\circ})_4]_{2s}$ layup prior to damage.	139
6.26 Experimental and predicted load versus centerline strain on the compression side for the $[45^{\circ}_4/-45^{\circ}_4/(0^{\circ}/90^{\circ})_4]_{2s}$ layup prior to damage.	140
6.27 Experimental and predicted load versus center deflection for the $[\pm 45^{\circ}/0^{\circ}/90^{\circ}]_{4s}$ layup prior to damage.	141

### List of Figures (Continued)

<u>Figure</u>		<u>Page</u>
6.28	Experimental and predicted load versus centerline strain on the compression side for the $[\pm 45^\circ/0^\circ/90^\circ]_4$ layup prior to damage.	142
6.29	Experimental and predicted load versus center deflection for the $[(45^\circ_2/-45^\circ_2/0^\circ)_2/90^\circ_5]_{2S}$ layup prior to damage.	143
6.30	Experimental and predicted load versus centerline strain on the compression side for the $[(45^\circ_2/-45^\circ_2/0^\circ)_2/90^\circ_5]_{2S}$ layup prior to damage.	144
6.31	Comparison of damage between model and experiment for the $[45^\circ_4/-45^\circ_4/(0^\circ/90^\circ)_4]_{2S}$ layup at (a) experimental and (b) predicted damage initiation loads.	150
6.32	Comparison of damage between model and experiment for the $[45^\circ_4/-45^\circ_4/(0^\circ/90^\circ)_4]_{2S}$ layup at the (a) first and (b) second characteristic damage states.	151
6.33	Comparison of damage between model and experiment for the $[45^\circ_4/-45^\circ_4/(0^\circ/90^\circ)_4]_{2S}$ layup at the (a) third and (b) fourth characteristic damage states.	152
6.34	Predicted damage accumulation in the $[45^\circ_4/-45^\circ_4/(0^\circ/90^\circ)_4]_{2S}$ layup beyond the fourth characteristic damage state.	153
6.35	Experimental and predicted load versus center deflection for the $[45^\circ_4/-45^\circ_4/(0^\circ/90^\circ)_4]_{2S}$ layup.	154
6.36	Predicted and experimental damage levels for the $[\pm 45^\circ/0^\circ/90^\circ]_4$ layup at the (a) predicted damage initiation load and (b) experimental in-plane damage initiation load.	155
6.37	Predicted and experimental damage levels for the $[\pm 45^\circ/0^\circ/90^\circ]_4$ layup at the experimental delamination initiation load.	156

### List of Figures (Continued)

<u>Figure</u>	<u>Page</u>
6.38 Predicted and experimental damage levels for the $[\pm 45^\circ/0^\circ/90^\circ_4]_{4s}$ layup at (a) predicted damage initiation and (b) the first characteristic damage state.	157
6.39 Predicted and experimental damage levels for the $[\pm 45^\circ/0^\circ/90^\circ_4]_{4s}$ layup at (a) the second characteristic damage state and (b) between the second and third damage states.	158
6.40 Predicted and experimental damage levels for the $[\pm 45^\circ/0^\circ/90^\circ_4]_{4s}$ layup (a) between the second and third damage states and (b) at the third damage state.	159
6.41 Predicted and experimental damage levels for the $[\pm 45^\circ/0^\circ/90^\circ_4]_{4s}$ layup (a) between the third and fourth damage states and (b) at the fourth damage state.	160
6.42 Experimental and predicted load versus center deflection for $[\pm 45^\circ/0^\circ/90^\circ_4]_{4s}$ layup.	161
6.43 Predicted and experimental damage levels for the $[(45^\circ_2/-45^\circ_2/0^\circ)_2/90^\circ_5]_{2s}$ layup at the (a) predicted damage initiation load and (b) experimental in-plane damage initiation load.	162
6.44 Predicted and experimental damage levels for the $[(45^\circ_2/-45^\circ_2/0^\circ)_2/90^\circ_5]_{2s}$ layup at the experimental delamination initiation load.	163
6.45 Comparison of damage between model and experiment for the $[(45^\circ_2/-45^\circ_2/0^\circ)_2/90^\circ_5]_{2s}$ layup at the (a) first and (b) second characteristic damage states.	164
6.46 Predicted and experimental damage levels for the $[(45^\circ_2/-45^\circ_2/0^\circ)_2/90^\circ_5]_{2s}$ layup at (a) predicted damage initiation and (b) the third characteristic damage state.	165

## List of Figures (Continued)

<u>Figure</u>	<u>Page</u>
6.47 Predicted and experimental damage accumulation in the $[(45^\circ_2/-45^\circ_2/0^\circ)_2/90^\circ_5]_{2S}$ layup (a) at the fourth damage state and (b) beyond.	166
6.48 Predicted damage accumulation in the $[(45^\circ_2/-45^\circ_2/0^\circ)_2/90^\circ_5]_{2S}$ layup beyond the fourth damage state.	167
6.49 Experimental and predicted load versus deflection for $[(45^\circ_2/-45^\circ_2/0^\circ)_2/90^\circ_5]_{2S}$ layup.	168
B.1 Comparison of damage across width at the first characteristic damage state of the $[45^\circ_4/-45^\circ_4/(0^\circ/90^\circ)_4]_{2S}$ layup.	213
B.2 Comparison of damage across width at the second characteristic damage state of the $[45^\circ_4/-45^\circ_4/(0^\circ/90^\circ)_4]_{2S}$ layup.	214
B.3 Comparison of damage across width at the third characteristic damage state of the $[45^\circ_4/-45^\circ_4/(0^\circ/90^\circ)_4]_{2S}$ layup.	215
B.4 Comparison of damage across width at the fourth characteristic damage state of the $[45^\circ_4/-45^\circ_4/(0^\circ/90^\circ)_4]_{2S}$ layup.	216
B.5 Comparison of damage across width at the first characteristic damage state of the $[\pm 45^\circ/0^\circ/90^\circ_4]_{4S}$ layup.	217
B.6 Comparison of damage across width at the second characteristic damage state of the $[\pm 45^\circ/0^\circ/90^\circ_4]_{4S}$ layup.	218
B.7 Comparison of damage across width at the third characteristic damage state of the $[\pm 45^\circ/0^\circ/90^\circ_4]_{4S}$ layup.	219

### List of Figures (Continued)

<i>Figure</i>	<i>Page</i>
B.8 Comparison of damage across width at the fourth characteristic damage state of the $[\pm 45^\circ/0^\circ/90^\circ]_4$ layup.	220
B.9 Comparison of damage across width at the first characteristic damage state of the $[(45^\circ_2/-45^\circ_2/0^\circ)_2/90^\circ_5]_{2s}$ layup.	221
B.10 Comparison of damage across width at the second characteristic damage state of the $[(45^\circ_2/-45^\circ_2/0^\circ)_2/90^\circ_5]_{2s}$ layup.	222
B.11 Comparison of damage across width at the third characteristic damage state of the $[(45^\circ_2/-45^\circ_2/0^\circ)_2/90^\circ_5]_{2s}$ layup.	223
B.12 Comparison of damage across width at the fourth characteristic damage state of the $[(45^\circ_2/-45^\circ_2/0^\circ)_2/90^\circ_5]_{2s}$ layup.	224

## List of Tables

<u>Table</u>	<u>Page</u>
5.1 AS4/3501-6 Material Properties [36]	75
5.2 Test Matrix	78
5.3 Specimen Measurements.	84
6.1 Experimental Southwell buckling loads and maximum loads for the $[45^\circ_4/-45^\circ_4/(0^\circ/90^\circ)_4]_{2S}$ specimens.	103
6.2 Experimental Southwell buckling loads and maximum loads for the $[\pm 45^\circ/0^\circ/90^\circ_4]_{4S}$ specimens.	104
6.3 Experimental Southwell buckling loads and maximum loads for the $[(45^\circ_2/-45^\circ_2/0^\circ)_2/90^\circ_5]_{2S}$ specimens.	105
6.4 Experimental Southwell buckling loads and center deflection at each characteristic damage state for a typical specimen of each layup.	112
6.5 Euler buckling loads, and experimental and predicted Southwell buckling loads, maximum loads and damage initiation loads.	138

## Nomenclature

$b$	Element width
$E$	Young's modulus
$E_{ijkl}^{\theta}$	Stiffness tensor in ply axes
$F_{bc}^a$	Nodal forces: the superscript "a" refers to the element; the subscript "b" refers to the node number; and the subscript "c" refers to the direction of the force
$I$	Area moment of inertia
$l$	Element length
$L$	Specimen length
$P_{cr}$	Euler bifurcation load
$S$	Maximum shear stress
$X^T$	Maximum longitudinal tensile stress
$X^C$	Maximum longitudinal compressive stress
$Y^T$	Maximum transverse tensile stress
$Y^C$	Maximum transverse compressive stress
$\epsilon_{ij}^L$	Strain tensor in laminate axes
$\epsilon_{ij}^{\theta}$	Strain tensor in ply axes
$\nu_{ij}^L$	Poisson's ratio
$\sigma_{ij}$ or $\sigma_{ij}^L$	Stress tensor in laminate axes
$\sigma_{ij}^{\theta}$	Stress tensor in ply axes
$\bar{\sigma}_{ij}$	Stress tensor in laminate axes averaged over specified distance.

*Chapter 1***INTRODUCTION**

As early as the late 1950's, advanced composite materials promised to revolutionize structural design in the aerospace industry as they allow substantial weight savings, as well as more exotic advantages, over conventional isotropic materials. In the last decade, much progress has been made in the understanding of the behavior of composite materials, and their use is becoming more widespread.

The first aircraft in which extensive use of advanced composites was made were German sailplanes. Today's high performance sailplanes are made almost exclusively of composites; fiberglass is the most common material, but graphite and kevlar are also used. Materials like graphite/epoxy are used in the secondary structure of commercial transport aircraft, such as the Boeing 757 and 767, to save weight in the structure. These savings can result in an increase in payload which, over the lifetime of the aircraft, yields a substantial economic gain. The use of graphite and kevlar on helicopters and high performance fighters leads to more efficient structures, allowing higher payloads, longer ranges and better performance. Composite materials are also being used in a new generation of fuel efficient all-composite business class aircraft, such as the Beech Starship I.

As well as their advantages over conventional isotropic materials in specific strength and specific stiffness, composites have strongly orthotropic strength and stiffness properties. However, because their behavior is poorly understood, composites tend to be used in nearly quasi-isotropic layups. This makes the least efficient use of their properties.

Taking advantage of the orthotropic stiffness properties of composites makes aeroelastic tailoring possible. This was used in the development of the forward-swept wing X-29. Much work has also been done to use these advantages on helicopter rotor blades. The thermal properties of composites are also orthotropic and the coefficient of thermal expansion can be negative in one direction. This is important in the design of space-based satellite dishes, as the shape of a dish must be preserved accurately over a wide range of temperatures.

Structural components used for aerospace applications are often subjected to compressive loads. As a result, the phenomenon of buckling must be understood. The buckling and postbuckling behavior of composite plates and panels has been studied extensively. Predictions of incipient buckling loads and of postbuckling behavior are complicated by boundary conditions, material couplings, and damage. Models of buckling behavior work relatively well up to the occurrence of damage. However, once damage occurs, the symmetry of the specimen is usually destroyed. As a result, predictions become difficult to make.

The failure characteristics of composite materials are inherently more complex than those of isotropic materials and, though much work has been done in that area, these characteristics are not fully understood. For maximum efficiency, some structures, wing panels on gliders for example, can be designed to buckle before reaching their limit load, and others, like fuselage panels, can be designed to buckle before the ultimate load is reached. Because of the lack of a complete understanding of their buckling performance, especially when coupled with their failure characteristics, and the effects of damage on a structure's performance,

composite materials are generally not yet designed to be used in the postbuckled regime.

The occurrence of buckling in a structure results in stresses which vary in magnitude along the length as well as through the thickness of the structure. The objective of this work is to understand and model damage accumulation in such a gradient stress field. This work is the first step in developing a design tool which will give an engineer insight into the behavior of composite structures operating in the postbuckled regime. Such a tool should be capable of modelling many laminate types in gradient stress fields. This would enable one to use composite materials with confidence in parts designed to buckle. The physics of the problem of damage accumulation must first be understood. To this end, a simply-supported, buckled column is used as a specimen; this is chosen to provide an easily analyzed stress state. Damage initiates at the specimen center, and is not affected by the boundary conditions at the ends. Furthermore, in a narrow column, stresses can be assumed not to vary significantly through the width, effectively reducing the problem to two dimensions. A test program is developed to provide a damage accumulation history for three different layups. The finite element method is used to model the stress and displacement state of the specimen; in-plane and out-of-plane failure criteria are applied on an element by element basis, with stiffness properties degraded as appropriate when damage is predicted in a given element.

The second chapter contains a brief summary of previous work done on buckling, failure prediction, progressive failure and damage modelling, along with a short discussion. In the third chapter, the development of the specimen and the test set-up is presented. The finite element model and the

failure criteria used are described in the fourth chapter. The test program, along with manufacturing, instrumentation and testing procedures, is presented in the fifth chapter. The experimental results, including damage histories, are presented in the sixth chapter. These damage histories are compared to the model results for damage prediction and effects of damage. The seventh chapter is a discussion of these results and the conclusions and recommendations made from this work are presented in the last chapter.

*Chapter 2***SUMMARY OF PREVIOUS WORK****2.1 Overview**

Elastic stability has been the subject of study for centuries, starting in the eighteenth century with Leonhard Euler [1]. For isotropic plates and symmetric, balanced composite laminates, the problem is well understood. Postbuckling behavior for such plates has also been studied. While many problems require numerical solutions, exact solutions exist for certain laminate types and boundary conditions. However, solutions for the buckling and postbuckling behavior of unsymmetric or unbalanced laminates, of stiffened panels or of laminates with notches, ply drop-offs or damage invariably require numerical solutions. The fact that damage can reduce a "well-behaved" symmetric laminate to a generally anisotropic one becomes a serious issue, complicated further by the fact that the occurrence of damage itself is not a completely understood phenomenon. As composite plates can carry significant loads after buckling, it is important to understand how these plates behave after the occurrence of damage.

**2.2 Buckling and Postbuckling**

In 1985, Leissa [2] compiled a review of over 400 works, which summarizes the current state of the art in buckling and postbuckling behavior in composite plates. He deals primarily with balanced, symmetric laminates, looking at a large variety of boundary conditions, shear

deformation, hygrothermal effects and the effects of holes. Exact solutions for critical buckling loads and postbuckling behavior can be found for a limited number of cases, depending on boundary conditions as well as layup. Good approximate solutions are possible for symmetric laminates. He concludes that composite plates exhibit reduced buckling loads due to material couplings, yet have significant load-bearing capabilities after buckling. Anisotropic and generally unsymmetric laminates introduce elastic couplings which greatly complicate their behavior.

Most of the work done on anisotropic plates focuses on specially orthotropic, midplane symmetric, antisymmetric or crossply laminates. Reissner and Stavsky [3] were the first to undertake a theoretical investigation of stretching-bending coupling in a plate. Kicher and Mandell [4] carried out an experimental study of the buckling behavior of plates made up of a variety of materials, including unbalanced and unsymmetric laminates. In plates where significant bending-stretching coupling existed, classical buckling analysis, with reduced flexural stiffness, gave very non-conservative critical load predictions. Ashton and Love [5] studied the buckling behavior of symmetric and antisymmetric laminates. Southwell [6] plots of their data compared well with analytic predictions, except for the antisymmetric laminates, where the critical load was overestimated by a factor of approximately two.

Minguet, Dugundji and Lagace [7] developed a model for the postbuckling behavior of rectangular flat laminated plates or sandwich panels which included material coupling terms, the effects of transverse shear, nonlinear strains and initial out-of-plane imperfections. They used a Reissner-Mindlin plate model with the Rayleigh-Ritz method to represent plate deformations. An efficient solution technique based on a direct

minimization of the potential energy was used to solve the nonlinear problem. Model results correlate well with corresponding experimental data.

Jensen and Lagace [8] carried out an experimental and analytical investigation of buckling and postbuckling behavior of generally anisotropic plates in uniaxial compression under a variety of boundary conditions. They used both a linear Rayleigh-Ritz solution and a linear hybrid stress finite element model to find solutions for the first bifurcation load, which corresponded closely to Southwell plot results. In addition, the finite element solutions correlated reasonably well with a second bifurcation load, if such existed, in most plates. They found that material couplings greatly complicated a plate's behavior and reduced buckling loads. When bending-extension coupling was present, lateral displacements started as soon as load was applied; as a result classical bifurcation loads did not truly exist. Thus, a nonlinear analysis was appropriate from the start. They used the method presented in [7] and obtained very good results.

Ply drop-offs, notches and stiffeners all complicate the behavior of a plate. Ply drop-offs make plate behavior difficult to describe with simple deflection modes. DiNardo and Lagace [9] used a hybrid stress finite element model and a superelement model based on a Rayleigh-Ritz solution, both of which correlated well with test results for the first bifurcation load and mode shape.

Starnes *et al* [10,11] used a nonlinear general shell finite element code to model buckling and postbuckling behavior in notched plates and stiffened panels; some of the latter were subjected to impact damage. Model and experimental results correlated well up to failure. Both plate types exhibited significant postbuckling strength, with failure loads exceeding

buckling loads by factors of five for notched plates and three for stiffened panels. The extent of strength degradation due to the notches and impact damage were found to depend on the initial buckling strain of the unnotched specimen and on the location of the damage.

Exact solutions or simple approximate solutions exist for some buckling problems. However solutions for the behavior of specimens, such as stiffened or notched panels, which more closely resemble real structural components, require sophisticated numerical methods for the accurate modelling of buckling and postbuckling behavior. Furthermore, little work has been done on the effects of damage on buckling behavior.

## **2.3 Damage Prediction**

### **2.3.1 Initial Damage**

Nahas [12] has compiled some 30 failure theories which have been described in the literature for composites. These are all semi-empirical in that they involve curve fits to experimental data. Furthermore, these failure theories can be divided into Interactive Failure Theories and Limit Failure Theories. The former trace their origins to the von Mises Yield Criterion obtained for ductile isotropic materials; the Hill [13] and Tsai-Wu [14] criteria are well-known examples of this. Limit Failure Theories are based on maximum stress and strain values obtained from unidirectional test data, whereas Interactive Theories involve all stresses which contribute to distortion energy, normalized by appropriate maximum allowable values. Both are generally applied on a ply by ply basis. These theories ignore any effects neighboring plies may have on the ply in question, and often also out-of-plane stresses; such stresses can arise from damage in neighboring

plies or edge effects, and can lead to delamination as well as in-plane damage. Nahas also describes a number of direct laminate failure theories, applied to a laminate as a whole. These essentially treat each layup as a new material.

Micromechanics and fracture mechanics have also been used to predict damage by more closely modelling observed phenomena. Dvorak and Laws [15] assume that cracks initiate at fiber/matrix debonds. These microcracks propagate in a stable manner until a critical strain is reached, and then behave like Griffith cracks.

The study of delaminations is often restricted to those caused by stress concentrations which arise due to edge effects rather than matrix cracks. Brewer and Lagace [16] developed the Quadratic Delamination Criterion to predict delamination due to edge effects. They calculated the three dimensional stress state at the edge of a plate, using the Force Balance Method [17] and applied the criterion over an averaging distance from the edge. The criterion is based on both the out-of-plane normal and shear stresses. The averaging distance was found to be a material property.

Much work has been done on delamination initiation prediction using the energy release rate approach [18-20]. A delamination is modelled as an interlaminar crack, assumed to initiate at a pre-existing flaw. This justifies a fracture mechanics approach to the problem. The crack is assumed to grow when the strain energy released as the crack grows is sufficient to provide the energy needed to generate a new surface. The energy available per unit area of delamination is calculated as a function of far-field stress or strain. Wang and Crossman [19] found that the available energy rises, dips and then rises again with increasing delamination size. When this is compared to the energy needed for delamination, one can see

that delaminations grow in a stable manner up to a critical value of stress. At that point, corresponding to the dip in the available energy curve, an instantaneous but limited growth occurs. Thereafter, growth is unstable and results in failure.

### **2.3.2 Modelling Damage**

Most approaches to modelling damage are limited to matrix damage; this can be justified by the observation that fiber damage usually coincides with the ultimate failure of the specimen. These approaches can be divided into three types: a single crack is modelled in detail [21-23]; damage is assumed to occur uniformly everywhere in the laminate in the form of a uniform crack density, and stiffness property degradation is proportional to the extent of the damage [21,24,25]; and a discretized model is made and appropriate element stiffness properties are set to zero when damage is predicted in a particular element [26,27]. In a discretized model, crack separation at crack saturation should be taken into account when the elements' dimensions are chosen. Sun and Jen [22] used a two dimensional finite element model to predict crack saturation density. With a very fine mesh they found the stress state and concentrations which resulted from a matrix crack, and found good agreement with experimental results for crack separation.

While detailed crack models provide insight into the specimen's behavior in the region of a crack, they can be ungainly when extrapolated to an entire part. Stiffness degradation models for uniform cracking are applicable to progressive failure models, but are limited to uniform stress fields where first ply failure consists of matrix cracks. They also rarely take

out-of-plane effects into account. If the location of damage can be predicted, a discretized model allows a relatively straightforward approach; failure criteria can be designed to predict out-of-plane as well as in-plane phenomena. Within an element, damage can be modelled by degrading properties progressively as loading increases, or simply by degrading properties completely. Total degradation of the stiffness properties can give very good results if the element dimensions are such as to include only a small number of cracks.

### **2.3.3 Progressive Damage**

With the exception of notched specimens, most of the work on progressive failure reported in the literature is in non-gradient stress fields. When predicting damage in such a stress field, the first problem is that the location of the damage within a particular ply is impossible to predict. One approach is to degrade the stiffness properties of the entire ply where the damage occurs. Hahn and Tsai [24] do this as a function of stress above a critical value. Swanson and Christoforou [25] degrade stiffness as a function of strain, using an empirical softening factor. Dvorak and Laws [28] find a relationship between strain and crack density, and another between crack density and ply stiffness.

Ochoa and Engblom [26] and Chang and Chang [27] use finite elements to model composite plates, with failure criteria which differentiate between different damage types. Stiffness properties are then degraded accordingly. In a purely analytical study, Ochoa and Engblom model a three-dimensional plate under uniform loading with a single element per ply over the entire plate. This ignores the possibility that

damage might be localized. Chang and Chang use a two-dimensional model to predict progressive failure in a plate with a hole, using one element per ply through the thickness and a mesh which is refined in the vicinity of around the hole in the plane of the plate. The model treats each ply separately in the same manner that Classical Laminated Plate Theory does. No attempt is made to take out-of-plane effects into account; nevertheless model predictions match experimental results well.

### 2.3.4 Experimental Observations

A number of studies give experimental observations on the occurrence of damage which are relevant to the current work. However these are not understood well enough to make quantitative predictions.

Flaggs and Kural [29] found that a relationship exists between ply thickness and the *in situ* ply strength for transverse cracks in  $[0^\circ_2/90^\circ_n]_s$  laminates. For a value of  $n$  equal to one, failure stresses could exceed the nominal maximum transverse strength of the  $90^\circ$  plies by a factor of 2.5. They also found that the neighboring ply constraints were important. The orientation of the plies sandwiching the  $90^\circ$  plies affect the *in situ* ply strength. They were unable, however, to offer a quantitative explanation for these phenomena. Dvorak and Laws [15] found that cracks can propagate in two directions, on planes which are parallel to the fiber axis and on planes which are perpendicular to the midplane of the ply. They suggest that thinner plies are stronger because microcracks are prevented from propagating along the plane perpendicular to the midplane of the ply in thin plies because of the dimensions of the ply.

Maximum compressive stress values are more difficult to determine accurately than maximum tensile stress values because of the interaction of local and global effects. Lagace and Vizzini [30] developed a compressive test specimen to determine these values, noting that global Euler buckling alters stress-strain behavior, whereas supporting jigs designed to suppress this prevent the legitimate local failure of ply buckling [31]. Furthermore, it has been observed that curvature can prevent ply buckling or delamination failure [32]. As a result, compressive fiber failure in a curved specimen is difficult to predict accurately; compressive ultimate strength values obtained from flat specimens, where failure involves buckling, can underestimate the compressive ultimate strength of a curved specimen.

## **2.4 Summary**

Though much work has been done on the subject, damage is still difficult to predict in many circumstances. Models based on observed phenomena are insightful, but are difficult to apply, while Interactive and Limit Theories can lead to misleading predictions when the effects of neighboring plies or specimen geometry are not properly taken into account. When these uncertainties are coupled with the complex postbuckling behavior of most of the structures described above, it becomes very difficult to predict the behavior of a part to ultimate failure with confidence without experimental verification.

Accurate micromechanical methods and discrete models exist to model the stress state around a crack, and sophisticated methods exist to predict stiffness degradation due to uniform damage in non-gradient stress fields, based on applied load. In a discretized model it is possible to degrade

stiffness properties in a very simple manner, namely by setting properties to zero when damage is predicted, and still use the model effectively in a gradient stress field.

While damage in uniform stress fields has been studied extensively, little work has been done on the failure mechanisms in gradient stress fields. The need for a reliable design tool for structures to be used in the post-buckled regime becomes clear when one considers the difficulties associated with the modelling of buckling behavior, given the uncertainties in damage prediction.

*Chapter 3***TEST DEVELOPMENT****3.1 Specimen Geometry**

The requirements for the test specimen are threefold. First, the stress state must be relatively straightforward to calculate so that the study of the failure mechanisms should not be obstructed by a complex stress state. Second, damage must initiate away from load introduction points. The importance of this requirement lies in the observation that the failure of plates constrained on all boundaries generally initiates at some point on a boundary [8]. Accurately calculating the stress state at such a point would be very difficult. Third, the progression of damage must be observable. It is important that damage initiation not coincide with final failure, and there should ideally be several stages in the accumulation of damage prior to final failure.

A simply-supported column was chosen. In such a configuration, the stress state varies sinusoidally along the length, providing a simple, gradient stress field in which the maximum stresses are away from the ends, where load is introduced. These maximum stresses occur in the middle of the specimen, so the place where damage should initiate is known. The column was made as narrow as possible so that variations through the width could be ignored, reducing the problem to two dimensions. The specimen could not be so narrow, however, that the edge effects from the two edges interact. The width was chosen to be 37.5 mm. In the selection of the length and thickness of the column, the following factors were considered. The specimen should be thick enough so as to be relatively

insensitive to manufacturing irregularities. To this end, thicknesses of fifty-six, sixty and sixty-four plies, with a ply thickness of 0.134 mm, were chosen. The specimen should have a bending stiffness high enough to give a reasonable buckling load on the order of 1000 pounds; the test machine used is rated to 100,000 pounds, and its smallest range setting is 10,000 pounds. The specimen could not be so short that it failed in compression before buckling. The buckling load was found for a variety of dimensions using the Euler buckling equation shown below:

$$P_{cr} = \frac{\pi^2 EI}{L^2} \quad (3.1)$$

The laminate longitudinal stiffness was used as a value for the stiffness  $E$ ;  $I$  represents the area moment of inertia of the specimen's cross-section, and  $L$  represents the length of the specimen. A length of 200 mm was thus chosen. The specimen geometry is illustrated in Figure 3.1. It should be noted that if this specimen were to be used for other laminates which were thinner than those tested in this work, it may be necessary to decrease the specimen length as per the equation above.

### **3.2 The Test Jig**

A test jig was needed with which to load the column with simply-supported boundary conditions. In the course of the jig design process, it became evident that the coefficient of end fixity was very sensitive to friction in the mechanism which provided the pinned conditions. With any friction in the mechanism, the initial buckling of the column occurred with the buckling load and mode of a clamped column. After a small lateral deflection was achieved, the column would snap to the simply-supported

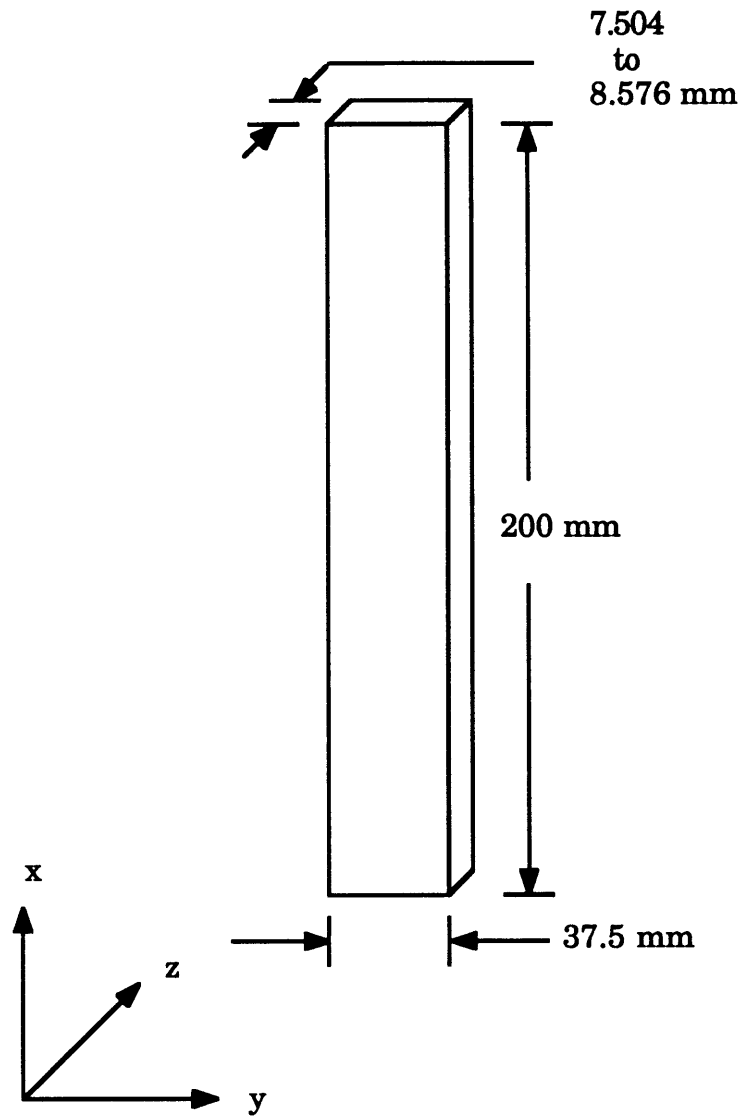


Figure 3.1 Test specimen characteristics.

deflection mode, and the load would drop. The resulting load spike was considered unacceptable.

The initial design involved a bearing system. It was not possible to overcome the friction problem with this system, so a knife edge design was adopted. Friction problems with this jig were overcome by making the load introduction points eccentric.

### **3.2.1 The Bearing Jig**

In this jig, the specimen ends fit into shaft sections, which rotate within bearings. These bearings fit into steel supports, which are clamped into the test machine. This jig is shown in Figure 3.2. The specimen ends fit into slotted shaft sections with brass shims to ensure a tight fit. These sections fit into oil-impregnated bronze bushings; the bushings had a section removed to make room for the specimen. The bushings fit into steel supports which are clamped into the testing machine's hydraulic grips. This design was chosen because it was thought that the bearings would provide the desired boundary conditions. Furthermore, the specimen would be contained at all times, as it would not be possible for the specimen to break away from the jig. The alignment of the top and bottom support was considered critical. The shaft sections had to be parallel to each other for the specimen to be simply-supported. Correct alignment was assured by bolting the two supports onto either end of a flat steel plate. The bolt holes were placed such that when the plate was bolted on, the shaft sections would be aligned. Two bolts were used at each end to prevent the plate from rotating about a bolt. After the supports were placed in the test machine's

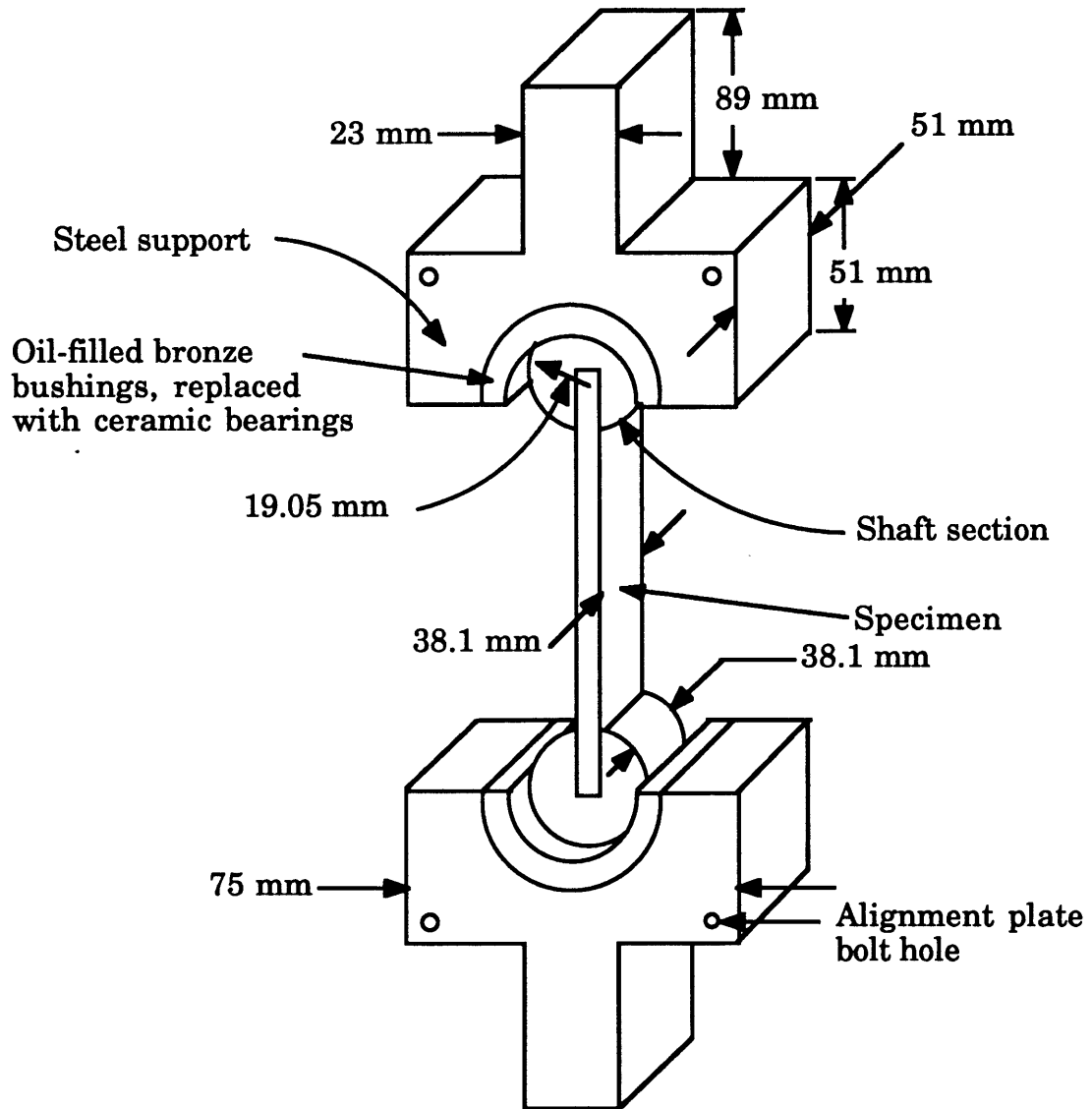


Figure 3.2 Characteristics of the Bearing Jig

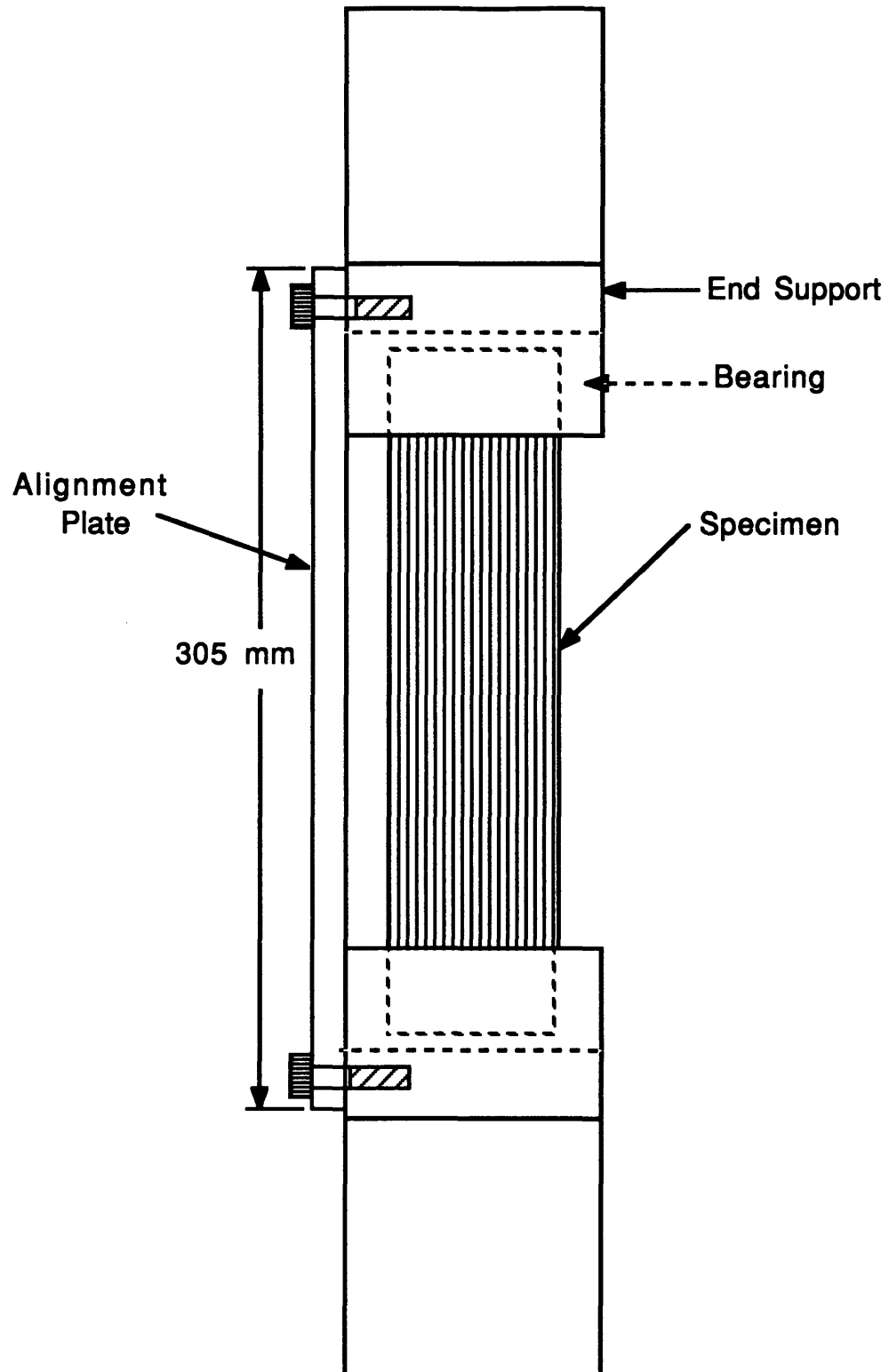


Figure 3.3 Side view of Bearing Jig with alignment plate.

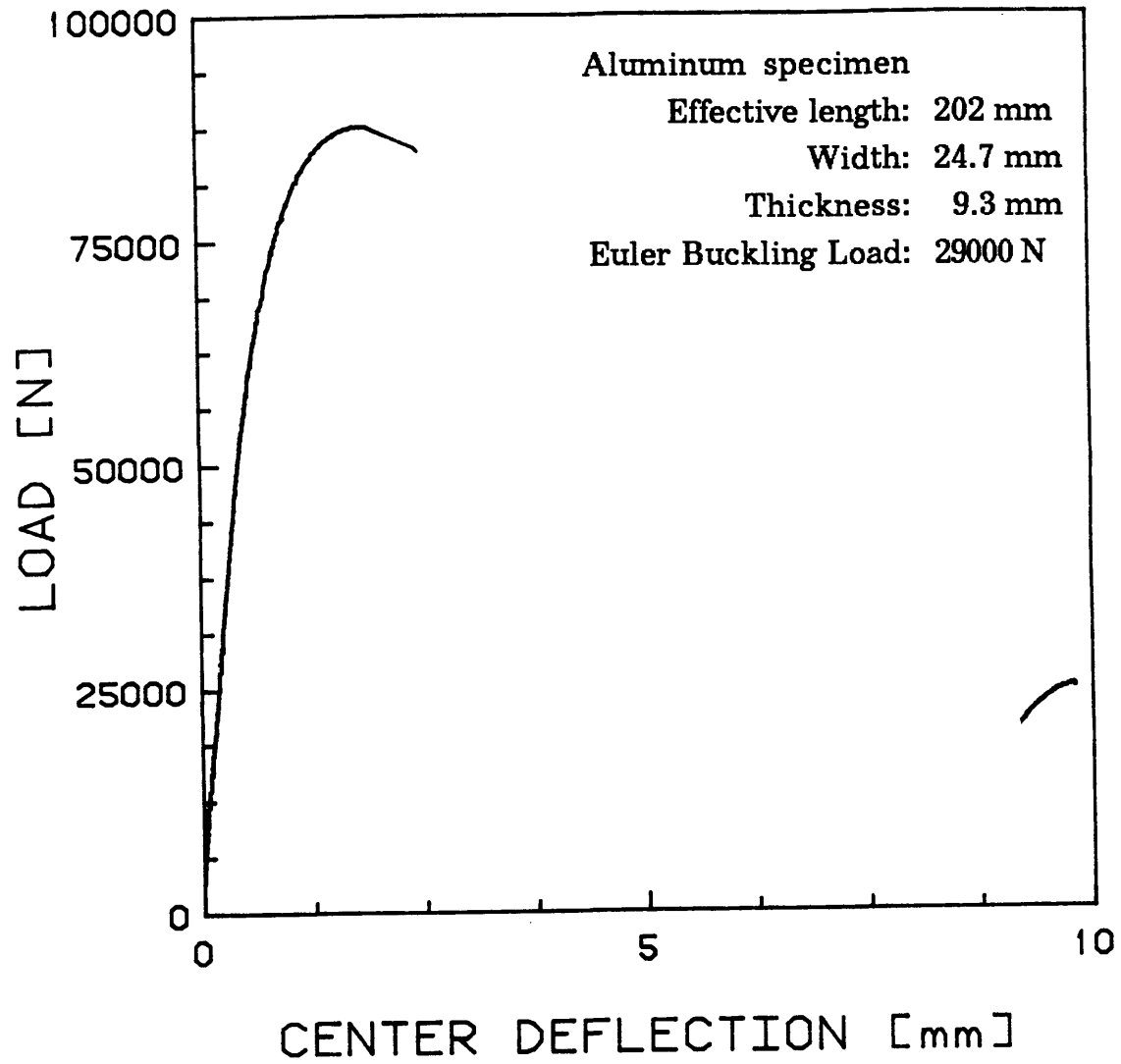


Figure 3.4 Load versus center deflection for an aluminum specimen tested in the Bearing Jig.

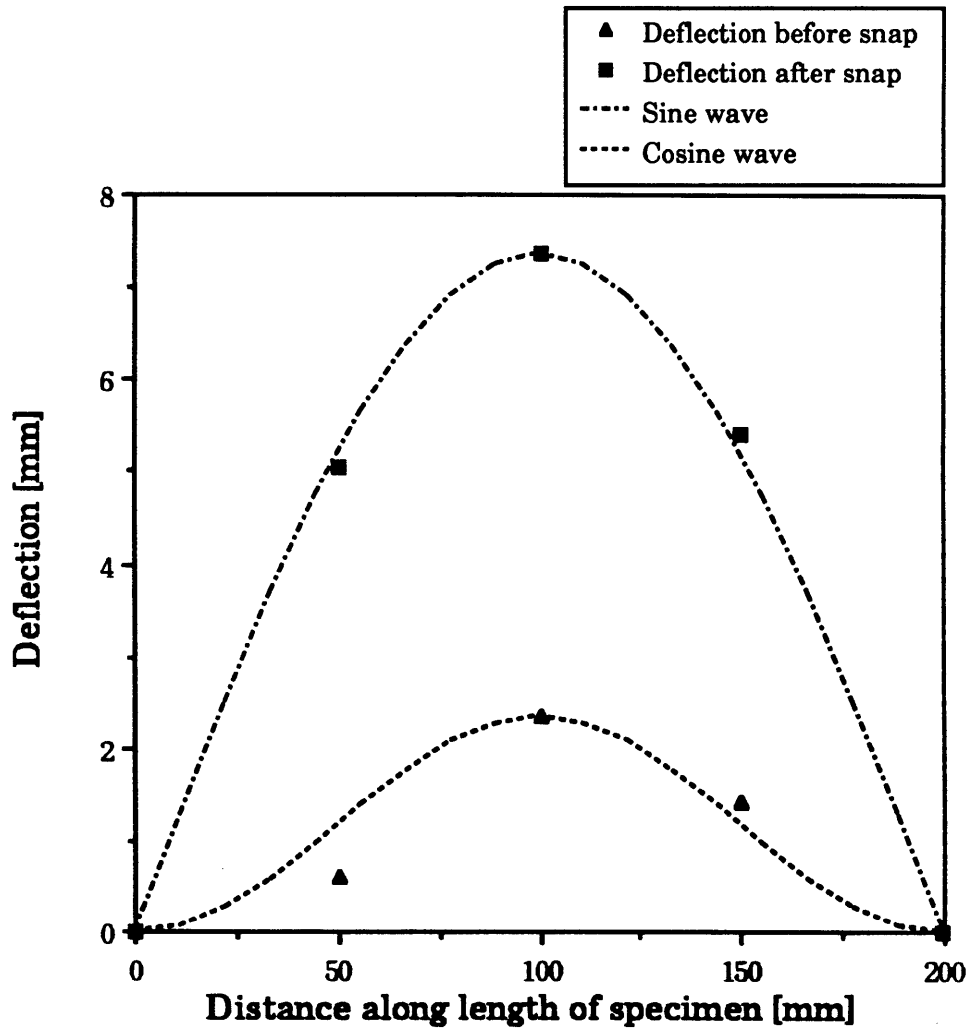


Figure 3.5 Comparison of deflection along the length of the specimen with cosine and sine waves, before and after deflection shape change, respectively.

grips and the grips were closed, the plate was removed. A side view of the jig is shown in Figure 3.3 with the plate in place.

Test jig performance was tested with aluminum specimens sized to have buckling loads similar to those of the graphite/epoxy specimens. The length of the aluminum specimens varied from 210 mm to 235 mm. The thickness varied from 6.5 mm to 10 mm, and the width varied from 12.7 mm to 42 mm. The Euler bifurcation load for these specimen varied from 11,000 N to 36,000 N.

The test procedure used is described in detail in section 5.3. In brief, an MTS 810 material testing machine was used. The specimen was loaded monotonically in compression in displacement (stroke) control. Load and stroke data was collected by a computer from the test machine's load cell. Data from three transducers, which were placed at the center and at the quarter points of the specimen, was also collected by the computer. A typical load versus center deflection plot for an aluminum specimen tested in this jig is shown in Figure 3.4. The specimen's effective length in the jig was 202 mm, its width 24.7 mm and its thickness 9.3 mm. The initial deflection mode was like that of a clamped column: the tips of the transducers and the end points of the specimen fit a cosine wave reasonably well, as shown in Figure 3.5. The buckling load of the column was larger than the Euler Bifurcation load for a pinned column of 29000N by a factor of approximately 3. After the initial spike, the specimen snapped to a sinusoidal deflection shape, as shown in Figure 3.5. The difference in center deflection in the two mode shapes leads to the discontinuity in the plot in Figure 3.4.

The bushings were replaced with ceramic linear/rotary bearings with very low coefficients of friction. They are rated to 5000 psi and have coefficients of friction of 0.04 both as rotary bearings and as linear bearings. The pressure the bearings were subjected to was on the order of 3000 psi. This however was enough to generate too much friction, resulting in a moment at the specimen's ends large enough for initial buckling to be as a clamped column with the characteristic load spike.

### **3.2.2 The Knife Edge Jig**

When it was judged that the bearing jig could not be further improved, it was abandoned, and a knife edge type jig was built. In this jig, the specimen ends fit into end pieces which rest on rounded knife edges, through which the load is introduced. The jig is shown in Figure 3.6. The specimen ends are fitted into slotted steel blocks; again a tight fit is ensured with brass and steel shims. The slots are made 25 mm deep, so the test section of the specimen between the end pieces is 37.5 mm by 150 mm. The total length of the column including the end pieces is 224 mm. These end pieces have a groove on the opposite surface into which the knife edge fit. The knife edges consist of blocks of 4041 steel, hardened to 36 Rockwell, with one end machined down to a wedge with a rounded edge. A radius of 1.59 mm was chosen for the knife edge and the grooves in the end pieces. The blocks were then placed in the grips of the test machine. Alignment was carried out in the same manner as for the bearing jig. As before, two bolt holes were used on the upper end support to prevent the plate from rotating.

The performance of this jig was also tested with an aluminum specimen. This specimen's effective length was 260 mm, its width 19.2 mm

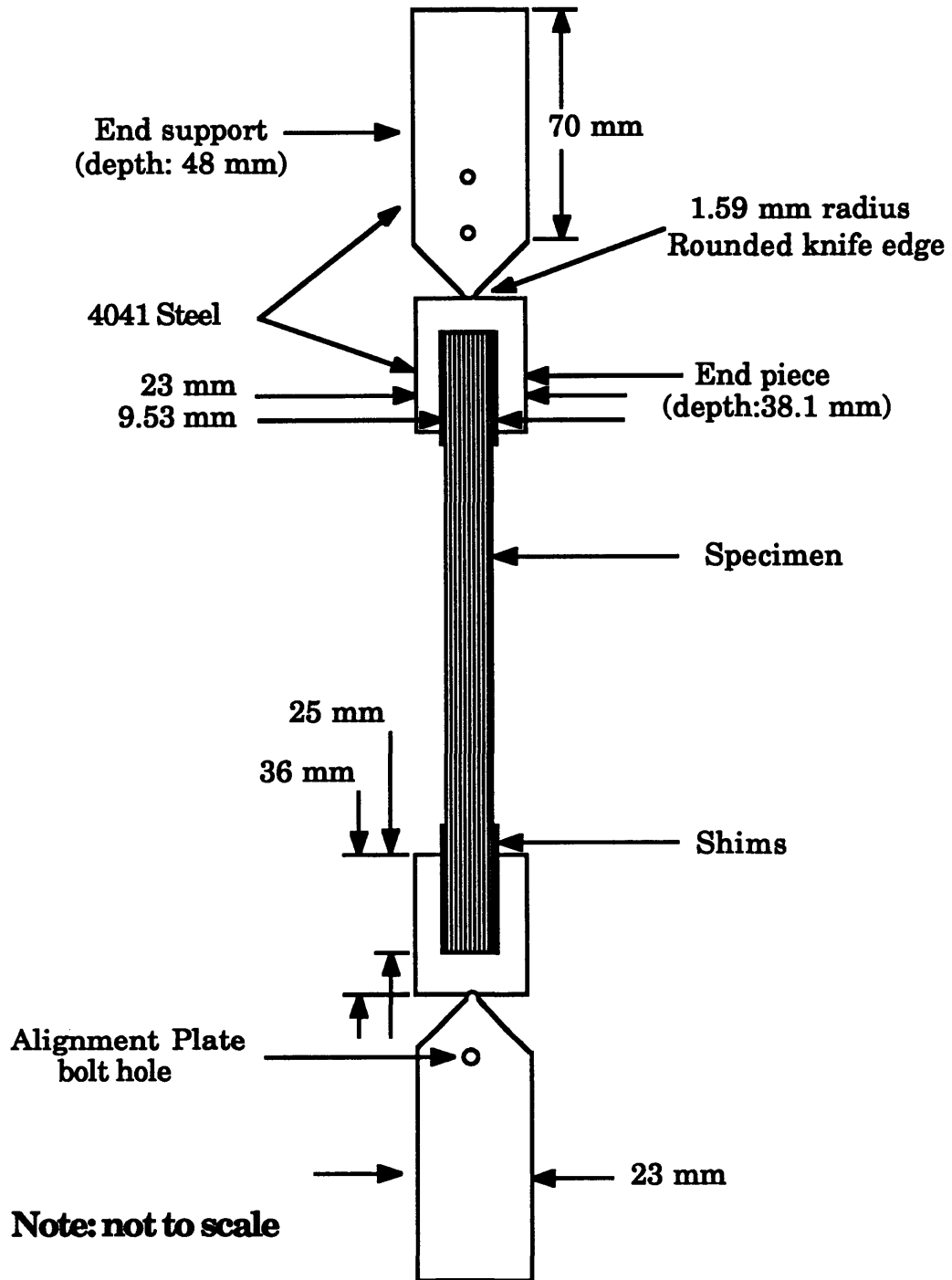


Figure 3.6 Initial configuration of the Knife Edge Jig.

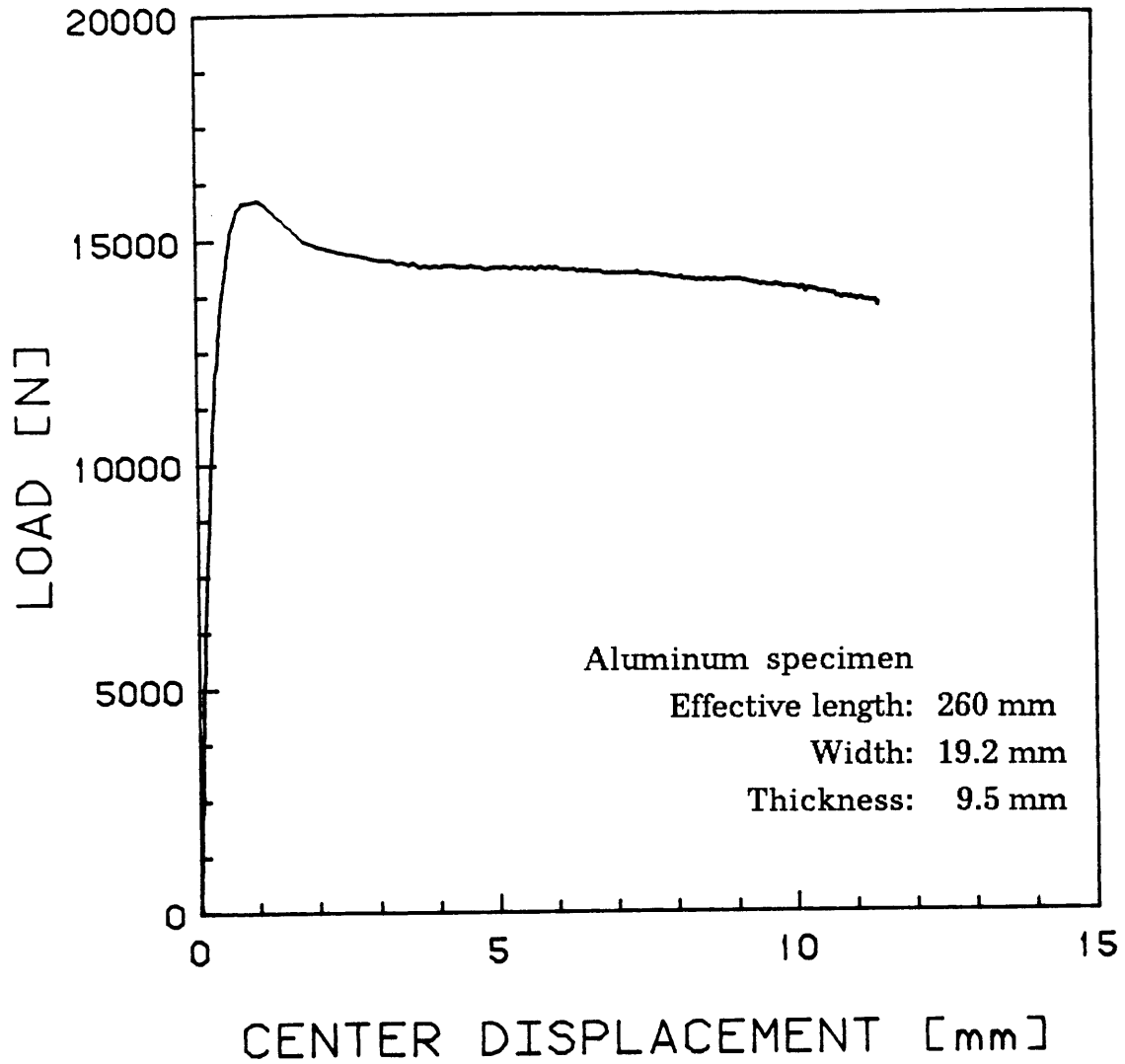


Figure 3.7 Load versus center deflection for an aluminum specimen tested in the Knife Edge Jig.

and its thickness 9.5 mm. The resulting load versus deflection plot is shown in Figure 3.7 with a coefficient of end fixity of 1.1. The initial deflection mode still resembled that of a clamped column. Although this was a significant improvement over previous results, it was decided that a load spike was undesirable.

The load spike was eliminated by moving the groove on the endpieces into which the knife edge fit over by 2.54 mm (0.1 inch). The load introduction was thus made eccentric. Eccentricity in the load introduction results in a moment at the specimen's ends. If this moment is large enough, friction at the knife edge is overcome, and the specimen deforms as a simply-supported column. An eccentricity of 2.54 mm was chosen, as that would be larger than any eccentricity from slight manufacturing defects in the specimens. Variations in eccentricity from specimen to specimen would therefore be negligible, simplifying the modelling.

Tests with an aluminum specimen, which was 235 mm long, 19.2 mm wide and 9.5 mm thick, gave no load spike, as can be seen in Figure 3.8. Again, the deflection shape resembled a sine wave, as can be seen in Figure 3.9. The Euler buckling load was never reached. This is probably due to stresses in the specimen exceeding the yield stress for aluminum. However, tests with graphite/epoxy specimens showed that damage initiated at the specimens' ends in the form of delaminations. It was observed that the endpieces tended to rotate slightly more than the ends of the specimens. Contact between the endpiece and the specimen was then reduced to the edge of the end surface of the specimen only. This resulted in a shear stress concentration which caused premature failure. This problem was remedied by placing neoprene rubber strips in the bottom of the slots in the endpieces. These strips ensured that the load distribution

was more even. The fact that soft rubber blocks were put in the endpieces meant that end displacement data as recorded by the test machine's load cell was meaningless.

The last modification was to add a lip to the end pieces on the compression side of the knife edge. This lip was supposed to prevent the specimens from flying out of the test jig upon ultimate failure. Apart from the dangers involved in having specimens flying across the room, it was considered undesirable to have the specimen leave the jig because the damage levels seen in these specimens were more severe than the damage levels in the specimens which had been successfully contained. This modification proved to be only a partial success, as ballistic behavior in the specimens was curbed, but not completely suppressed.

The test jig development was now complete, and the final configuration is shown in Figure 3.10. A plot of load versus center deflection for a  $[\pm 45^\circ/0^\circ]_{10s}$  graphite/epoxy specimen tested in this completed jig is shown in Figure 3.11. The test jig now provides the desired stress state in the specimen. This configuration was thus used for the remainder of this work.

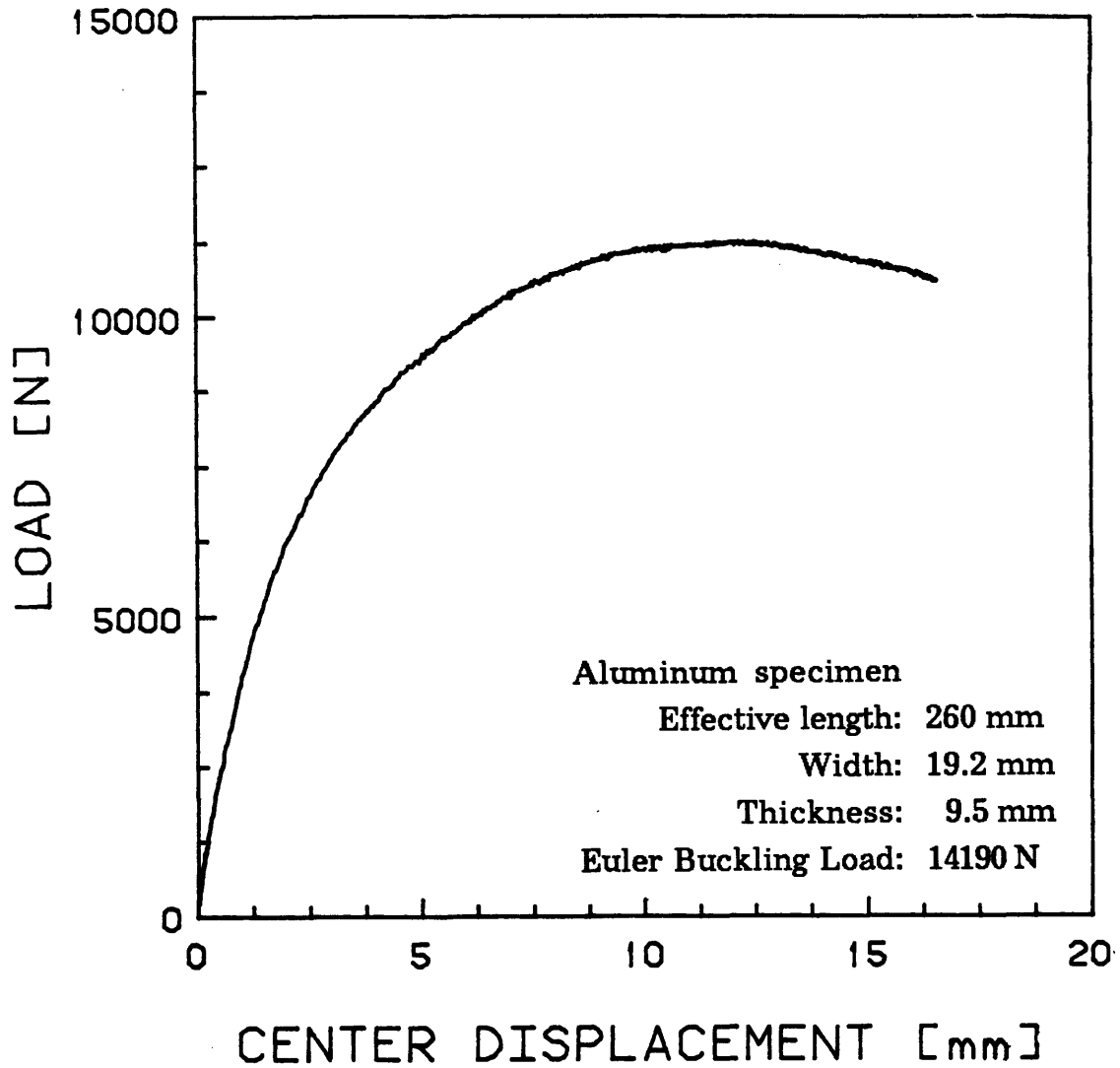
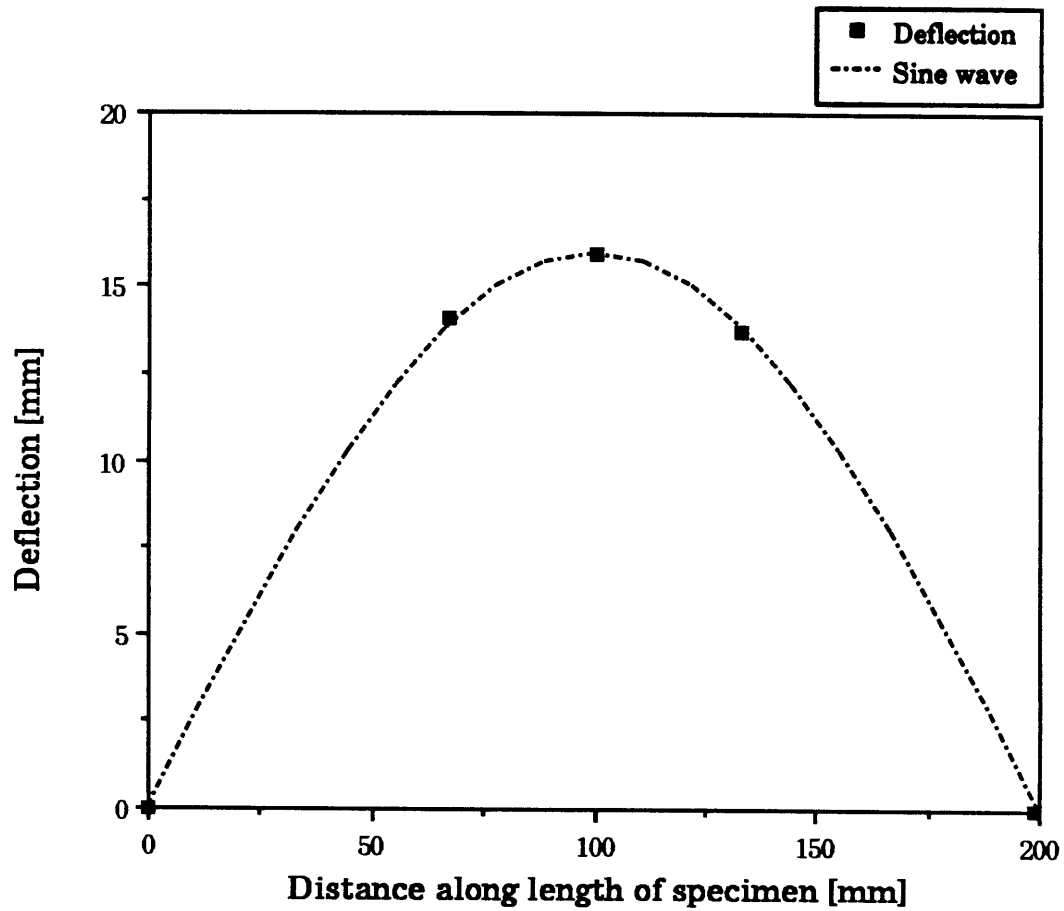


Figure 3.8 Load versus center deflection for an aluminum specimen tested in the Knife Edge Jig with eccentric load application.



**Figure 3.9 Comparison of deflection along the length with a sine wave for an aluminum specimen.**

**Note: first and third transducers were moved to 32 mm either side of the center.**

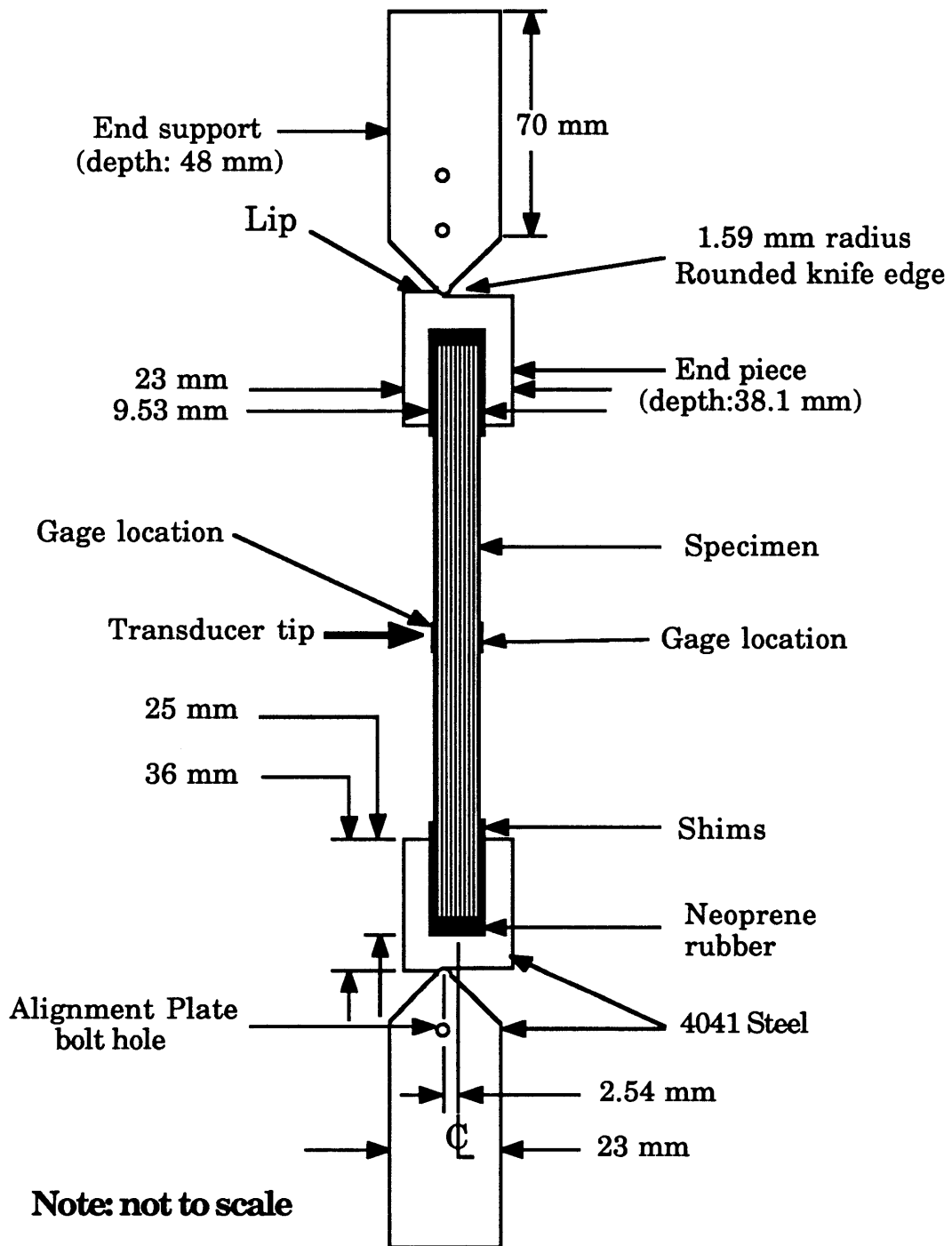


Figure 3.10 Final configuration of the Knife Edge Jig.

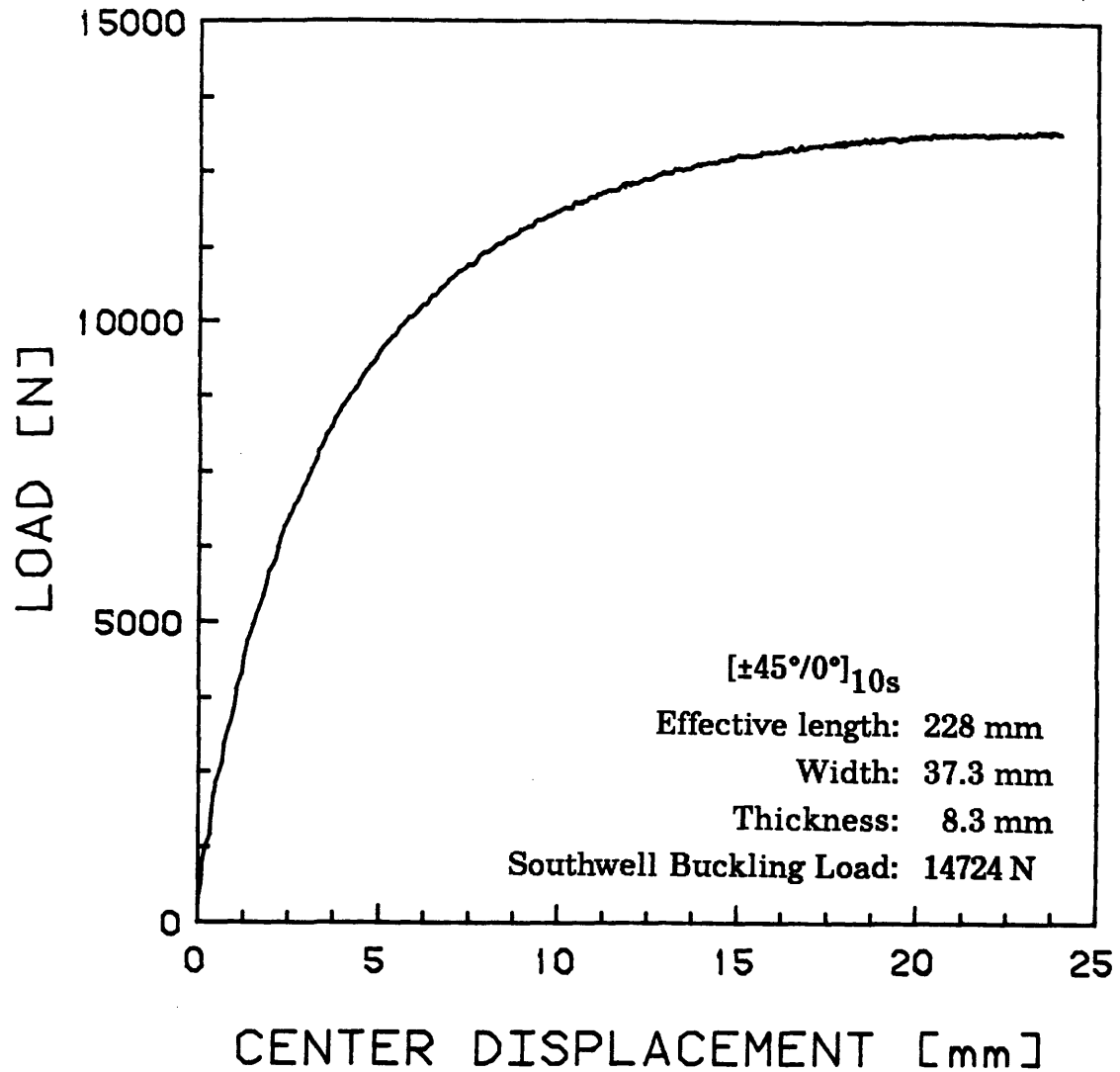


Figure 3.11 Load versus center deflection for a  $[\pm 45^\circ/0^\circ]_{10s}$  graphite/epoxy specimen tested in the completed Knife Edge Jig.

## *Chapter 4*

### **THE ANALYTICAL MODEL**

As the specimens were subjected to a gradient stress field, the level of damage varied along the length of the specimens. For this reason, a spacial discretization was used in the models. The finite element method was used to model the stress state of the specimens in two dimensions. The material nonlinearities which had to be predicted and modelled included the nonlinear elastic properties of the 45° plies, in-plane damage, and delamination. The behavior of the 45° plies depended on local strain, while damage predictions were made with a number of stress-based failure criteria.

#### **4.1 The Finite Element Model**

The specimen was modelled in two dimensions in the x-z plane with a displacement-based finite element code, ADINA [33], on a DEC MicroVAX. Eight node plane stress elements were used. As stated in Chapter 3, the width of the specimens was small enough for variations through the width to be ignored, justifying the use of a two-dimensional model. Bending-twisting and extension-twisting material couplings which might arise from damage were ignored. Such couplings would have little effect on a beam, and, furthermore, it is assumed that damage will be fairly uniform across the width of the specimen. The assumption of plane stress implies that stresses in the x-y plane are zero. This is not strictly true in that  $\sigma_{22}$  and  $\sigma_{12}$  are generally not zero in any given ply. However the sum of

these stresses through the thickness must be zero, as there is no transverse loading applied; this makes the assumption valid. This does, however, lead to inconsistencies when calculating stresses in the x-y plane, as will be shown later. Eight node elements were chosen for their ability to model displacements due to bending and transverse shear stresses. The degrees of freedom consist of vertical and horizontal displacements at each node. The basic element is shown in Figure 4.1. To take advantage of the symmetry of the problem, only half the specimen along the length was modelled.

Two factors influenced the choice of the length of the elements. First, the minimum crack separation, which was observed experimentally to be about 2 mm, represented the minimum size for the element. The length of the ply along which stress transfer takes place from one damaged ply to its neighbors through shear lag would thus be contained in an element of this length. Second, in order to contain a matrix crack in a 45° ply with a two-dimensional element, the element should be at least as long as the specimen is wide. It would be desirable to contain such a crack because the stiffness of the ply is affected by the crack over the entire section where the crack exists. As a compromise between these two requirements, and also in order to keep the model as simple as possible, ten elements were used along the length of the model, making each element 11.2 mm long. One element was used through the thickness for each group of plies with the same fiber orientation, except on the model of the  $[45^\circ_4/-45^\circ_4/(0^\circ/90^\circ)_4]_{2s}$ , where two elements were used for each group of four 45° or -45° plies. This was done because strain could change by as much as 20% through the thickness of the group of plies due to bending. As the stiffness was dependent on strain, this variation was considered to be excessive.

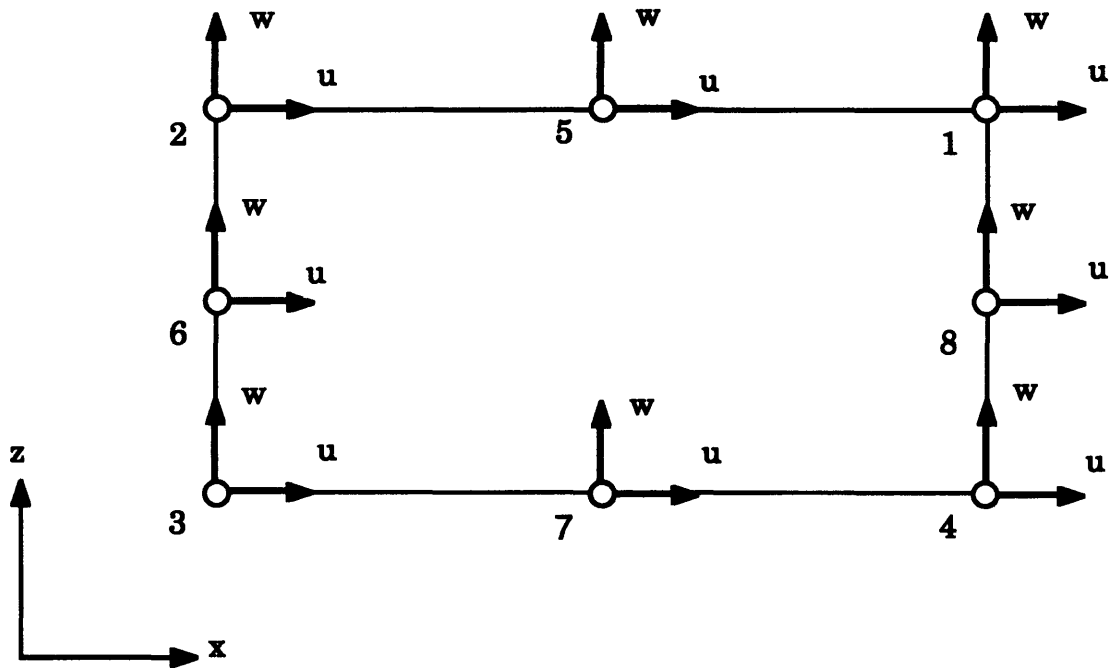


Figure 4.1 Characteristics of the basic eight-node element.

Each of the three ply orientations were treated by ADINA as a different material. The material properties needed by ADINA were  $E_1$ ,  $E_3$ ,  $G_{13}$  and  $\nu_{13}$ . The basic unidirectional values used are shown in Table 5.1.

The boundary conditions of the specimen were modelled as follows. All the nodes along one end of the model were constrained to be able to move in the z direction only; this line modelled the centerline of the specimen parallel to the z axis. A single node at the other end was constrained to be able to move in the x direction only; this was the node through which load was applied, and its selection corresponded to the eccentricity of the load application. A schematic of the model for each of the three laminates in this investigation is shown in Figures 4.2 through 4.4 with the boundary conditions. As can be seen in Figure 4.4, the nominal eccentricity for the  $[(45^\circ_2/-45^\circ_2/0^\circ)_2/90^\circ_5]_{2s}$  specimen type was 2.66 mm, rather than the 2.54 mm of the other two specimen types. This comes about because of the asymmetric use of shims in the test jig end pieces.

At the start of a modelling run, the node to be moved incrementally was specified; this was always the single node through which load was introduced, and the choice of this node corresponded to the eccentricity of the load application. The size of the first increment in end displacement was specified, as was the number of increments. The first increment in end displacement was 0.015 mm, and the number of increments was 35. This choice for increment size provided a suitable interval between increments, and the choice of 35 increments resulted in a final center deflection slightly larger than that observed experimentally. After the first increment, the increment size was determined by the program based on convergence requirements. To calculate the increment size, a constant arc length constraint on the load versus end displacement curve was used far from

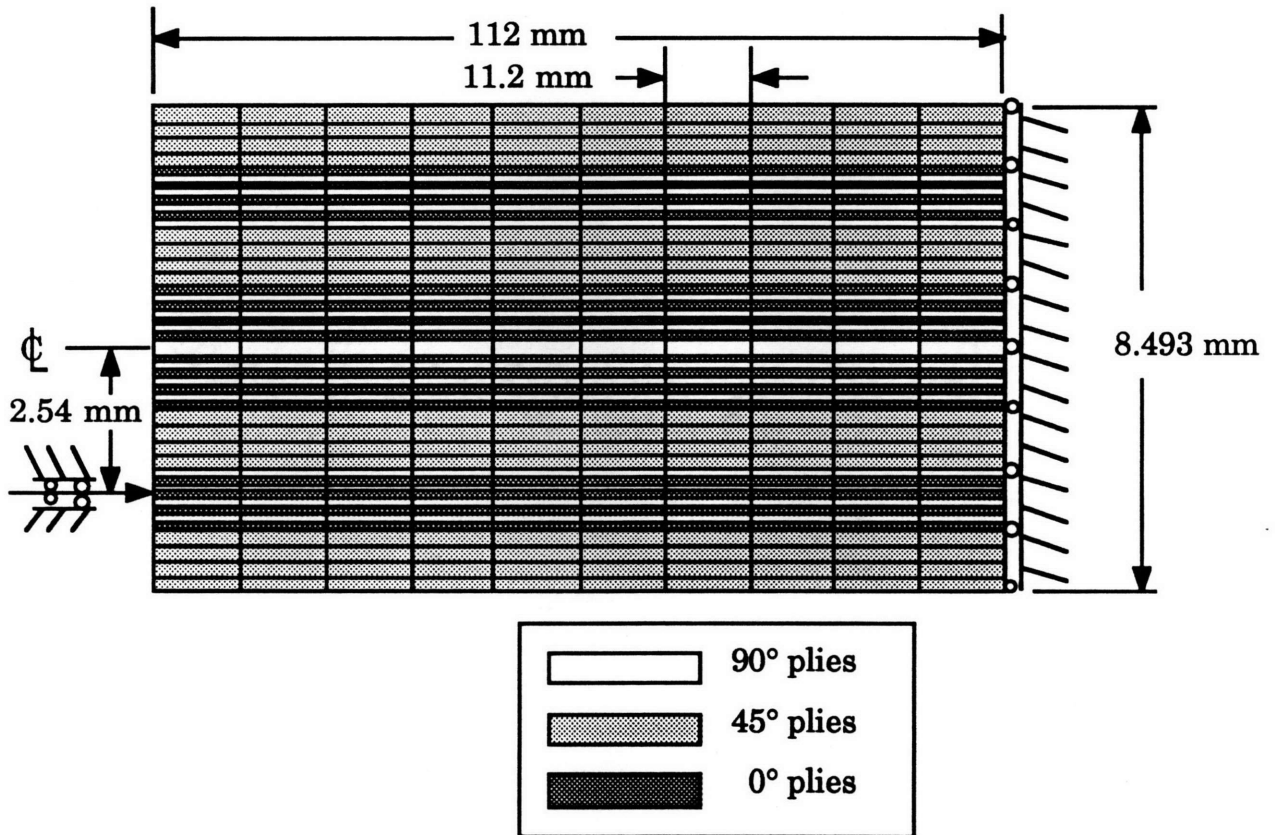


Figure 4.2 The finite element model of the  $[45^\circ_4/-45^\circ_4/(0^\circ/90^\circ)_4]_{2s}$  specimen type.

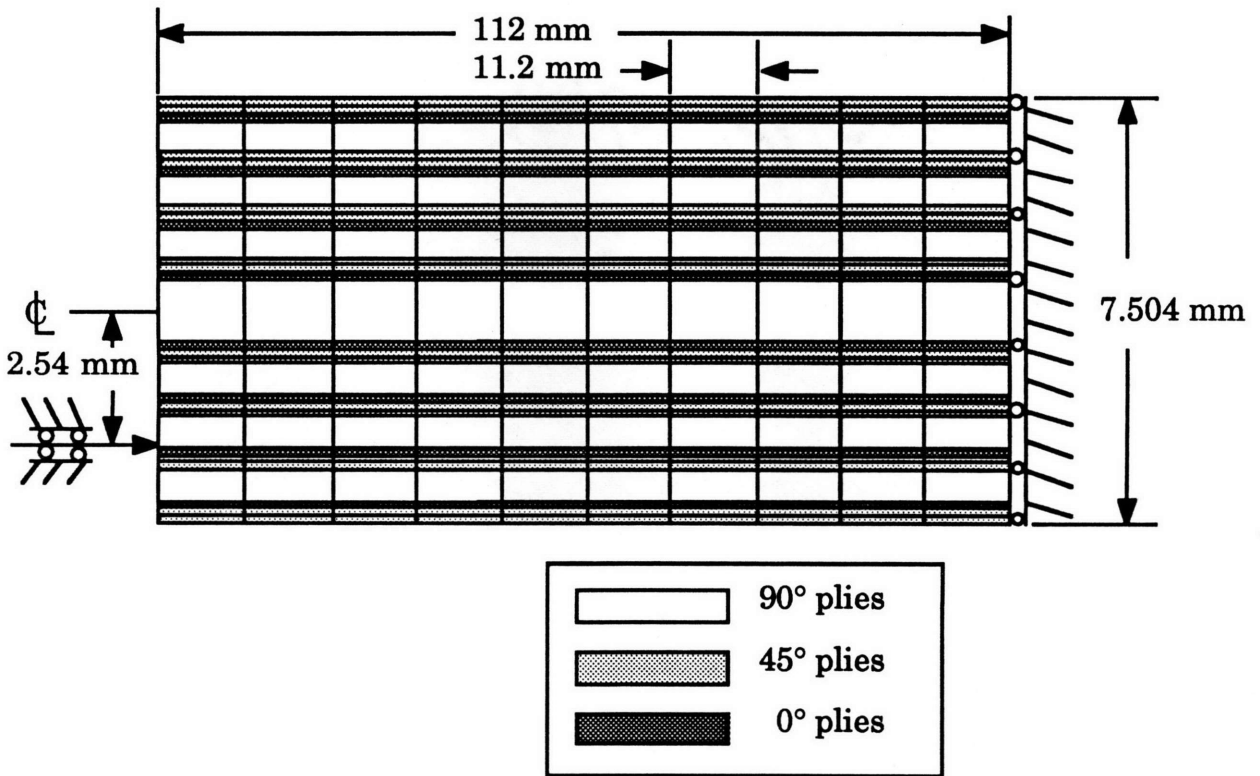


Figure 4.3 The finite element model of the  $[\pm 45^\circ/0^\circ/90^\circ]_4$  specimen type.

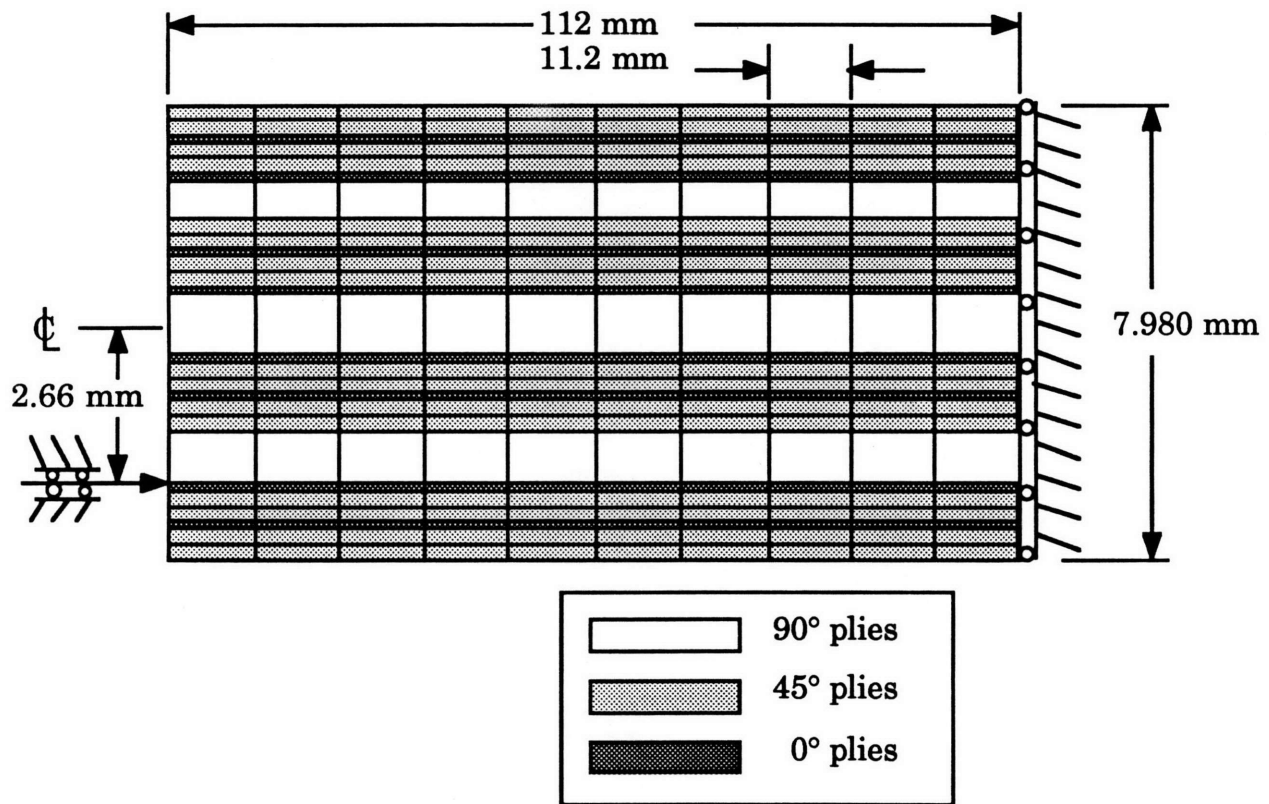


Figure 4.4 The finite element model of the  $[(45^\circ_2/-45^\circ_2/0^\circ)_2/90^\circ_5]_{2s}$  specimen type.

critical points, for instance buckling, and a scheme of constant increments in external work was used near the critical points. The possible results printed out after a run included nodal displacements for specified nodes, stresses at Gaussian integration points or node locations, including the center of the element, for specified elements, and nodal forces for specified elements.

The results actually printed out were the following: the displacements of the single constrained node and of the node in the lower right hand corner of the model, giving the end displacement and the center deflection of the model, respectively. The value of  $\sigma_{11}$  at the center of the element was the only one printed out, and it was used as an average value for the whole element. Average values of  $\sigma_{13}$  and  $\sigma_{33}$  for a given element were determined from the nodal forces using the following expressions. For the shear stress along the top edge:

$$\sigma_{13} = [0.5(F_{1x}^c + F_{2x}^r) + F_{5x}^c + 0.5(F_{2x}^c + F_{x1}^l)]/bl \quad (4.1)$$

Where b and l represent the element width and length, respectively. For the shear stress along the bottom edge:

$$\sigma_{13} = [0.5(F_{4x}^c + F_{3x}^r) + F_{7x}^c + 0.5(F_{3x}^c + F_{4x}^l)]/bl \quad (4.2)$$

In the first and third terms, taking the average of the nodal forces from the element for which the stresses are being calculated and its neighbors removes the component due to  $\sigma_{11}$ . For the normal stress along the right edge:

$$\sigma_{33} = [0.5(F_{4z}^a - F_{1z}^c) + F_{8z}^c + 0.5(F_{4z}^c - F_{1z}^b)]/bl \quad (4.3)$$

For the normal stress along the left edge:

$$\sigma_{33} = [0.5(F_{3z}^a - F_{2z}^c) + F_{6z}^c + 0.5(F_{3z}^c - F_{2z}^b)]/bl \quad (4.4)$$

In the first and third terms, taking the average of the nodal forces from the element for which the stresses are being calculated and its neighbors removes the component due to  $\sigma_{13}$ . The number in the subscript refers to the node number, as illustrated in Figure 4.1, and the letter in the subscript refers to the direction of the nodal force. The superscript refers to the element from which the nodal force is used: "c" refers to the element for which the stresses are being calculated; "l" and "r" refer to the elements to the left and right in the mesh of the element for which the stresses are being calculated; "a" and "b" refer to the elements above and below the element for which the stresses are being calculated. In equations 4.1 and 4.2, the first and third terms average out the  $\sigma_{11}$  components from the nodal forces. In equations 4.3 and 4.4, the first and third terms average out the  $\sigma_{13}$  components from the nodal forces. It was necessary to use the nodal forces to obtain reasonably accurate values, as these stresses were generally two orders of magnitude smaller than  $\sigma_{11}$ .

The stresses in the x-y plane were obtained as follows. The longitudinal strain in an element was calculated directly from the  $\sigma_{11}$  value given by ADINA and the ply longitudinal stiffness,  $E_1$ , using the expression below,  $\sigma_{33}$  and  $\sigma_{13}$  being small enough to be neglected:

$$\varepsilon_{11}^L = \sigma_{11}/E_1 \quad (4.5)$$

The Poisson's ratio of the laminate was used to find the element transverse strain in laminate axes.

$$\varepsilon_{22}^L = \varepsilon_{11}^L \cdot \nu_{12}^L \quad (4.6)$$

It was assumed that the laminate shear strain is zero since the laminate is balanced while undamaged, and it is assumed to remain approximately balanced when damaged. The laminate strains obtained in this manner were rotated to ply strains in the ply axes of that ply:

$$\varepsilon_{11}^{\theta} = 0.5.(\varepsilon_{11}^L + \varepsilon_{22}^L) + 0.5.(\varepsilon_{11}^L - \varepsilon_{22}^L)\cos 2\theta + \varepsilon_{12}^L\sin 2\theta \quad (4.7)$$

$$\varepsilon_{22}^{\theta} = 0.5.(\varepsilon_{11}^L + \varepsilon_{22}^L) - 0.5.(\varepsilon_{11}^L - \varepsilon_{22}^L)\cos 2\theta - \varepsilon_{12}^L\sin 2\theta \quad (4.8)$$

$$\varepsilon_{12}^{\theta} = -0.5.(\varepsilon_{11}^L - \varepsilon_{22}^L)\sin 2\theta + \varepsilon_{12}^L\cos 2\theta \quad (4.9)$$

The ply strains were used to calculate ply stresses with the uniply elastic properties:

$$\begin{Bmatrix} \sigma_{11}^{\theta} \\ \sigma_{22}^{\theta} \\ \sigma_{12}^{\theta} \end{Bmatrix} = \begin{bmatrix} E_{1111}^{\theta} & E_{1122}^{\theta} & 0 \\ E_{1122}^{\theta} & E_{2222}^{\theta} & 0 \\ 0 & 0 & E_{1212}^{\theta} \end{bmatrix} \begin{Bmatrix} \varepsilon_{11}^{\theta} \\ \varepsilon_{22}^{\theta} \\ \varepsilon_{12}^{\theta} \end{Bmatrix} \quad (4.10)$$

The ply stresses are used for the failure analysis. Because of the assumption of plane stress, these ply stress values rotated back to laminate axes gave a value for  $\sigma_{11}$  which differs from that originally given by ADINA, especially for the 45° plies. It is assumed in the model that  $\sigma_{22}$  and  $\sigma_{12}$  are zero, nevertheless, nonzero values for these stresses exist in the specimen, and are recovered from the model's results. The assumption of plane stress also implies that variations in the y directions are zero. However, nonzero strains in the y direction are allowed. Because of these strains, stresses in the y direction in each ply through the thickness sum to zero, but, because of Poisson's ratios mismatches, nonzero stresses generally exist in each ply. In the 0° and 90° plies, these inconsistencies have relatively little effect because these plies have a small Poisson's ratio.

plies, so the difference in  $\sigma_{11}$  is significant. A flow chart is depicted in Figure 4.5, showing how ADINA results are used.

## **4.2 Material Nonlinearities**

The nonlinear elastic behavior of 45° plies is well documented in the literature [34] as these plies begin to soften with increasing strain as soon as load is applied. Nonlinear ply properties were obtained from TELAC data on  $[\pm 45^\circ]_{2s}$  coupons and  $[(\pm 45^\circ)_2/\text{honeycomb}]_s$  sandwich columns; the former provided tensile data and the latter compressive data. For modelling purposes,  $E_1$  and  $\nu_{12}$  in laminate axes are assumed to be constant from -4500  $\mu\text{strain}$  to 4500  $\mu\text{strain}$ . The secant modulus, which uses only the values of stress and strain at a particular point on a stress-strain plot and not the slope of the curve, and the secant Poisson's ratio at 5000  $\mu\text{strain}$  are used for strains from 4500  $\mu\text{strain}$  to 5500  $\mu\text{strain}$ . In a similar manner, the material properties are updated every 1000  $\mu\text{strain}$ , both in tension and in compression. The stiffness versus strain and Poisson's ratio versus strain used for modelling purposes are shown in Figures 4.6 and 4.7 for tensile and compressive strains, respectively.

Nonlinear orthotropic elastic properties are not allowed by ADINA; these therefore had to be updated on an element by element basis at every step. The first run for a model type gave results for 35 increments in end displacement, resulting in a final center deflection larger than that observed experimentally. After this run, the results were examined and the increment at which strains in some of the 45° ply elements exceeded the range treated as linear, which is 4500  $\mu\text{strain}$  to -4500  $\mu\text{strain}$ , was identified. For each increment after that point, two single-point run were

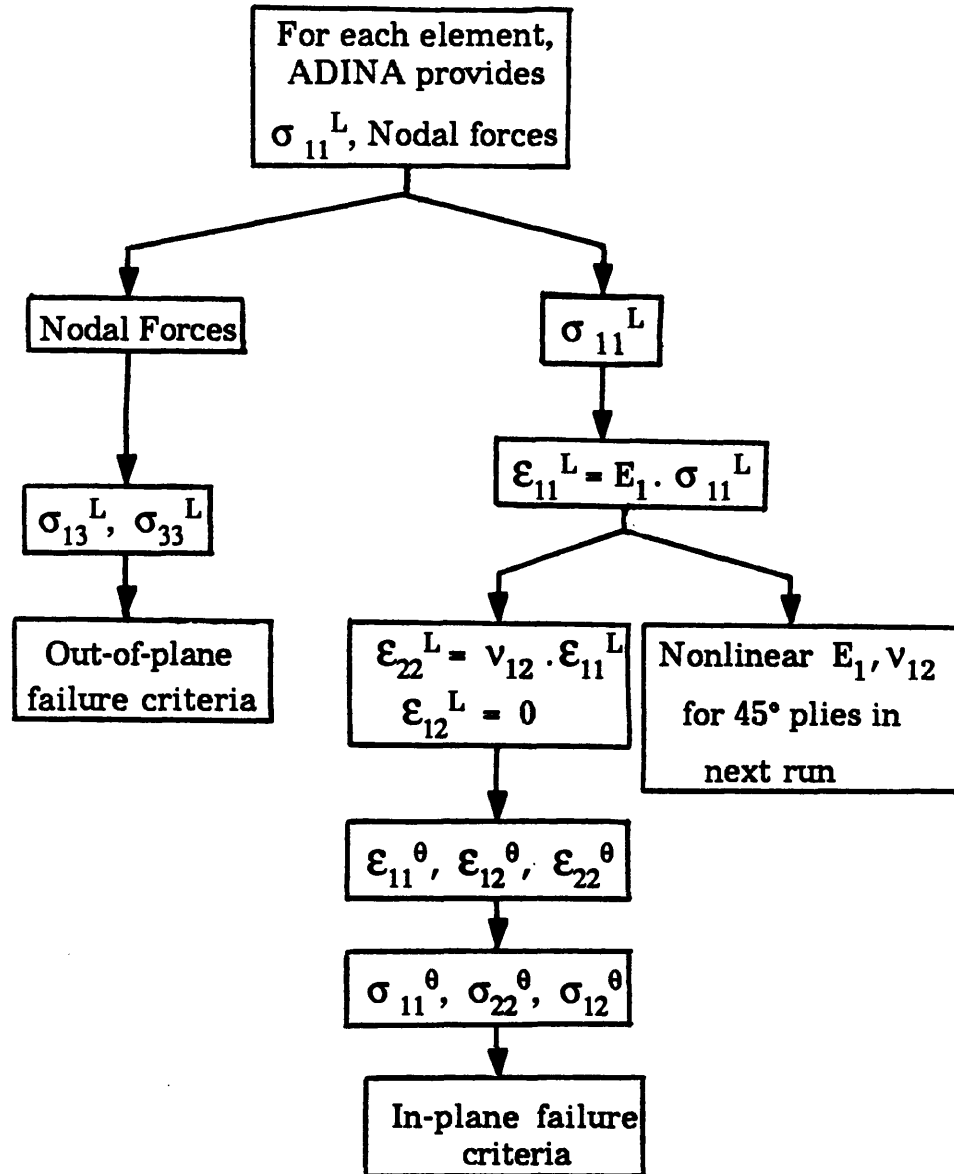


Figure 4.5 Flow chart outlining use made of ADINA results.

carried out at the same end displacement as at that increment. In the second of these runs, the stiffness of each 45° ply element was adjusted to match the strain levels reached in that element, as found in the first single-point run. A flow chart which shows these steps can be seen in Figure 4.8, and the manner in which the results from these runs were put together to model the nonlinear material behavior is illustrated in Figure 4.9.

### 4.3 Failure Criteria

#### 4.3.1 In-Plane Criterion

In order to be able to ascertain the damage modes present, in-plane damage was predicted using a maximum stress failure criterion [35]. Five maximum allowable stresses were used so as to differentiate between matrix and fiber damage in tension and compression. Damage was said to have occurred if the limits shown below are exceeded:

$$\text{For fiber breakage: } X^C < \sigma_{11} < X^T \quad (4.11)$$

$$\text{For matrix damage: } Y^C < \sigma_{22} < Y^T \quad (4.12)$$

$$\text{or: } |\sigma_{12}| < S \quad (4.13)$$

where  $X^C$  and  $X^T$  represent the maximum allowable compressive and tensile longitudinal stresses, respectively;  $Y^C$  and  $Y^T$  represent the maximum allowable compressive and tensile transverse stresses; and  $S$  represents the maximum allowable shear stress with the effect of shear stress being independent of sign. The values for the maximum allowable stresses are listed in Table 5.1 [36]. When predicted stresses exceeded these maximum values, the element was considered damaged, with the damage

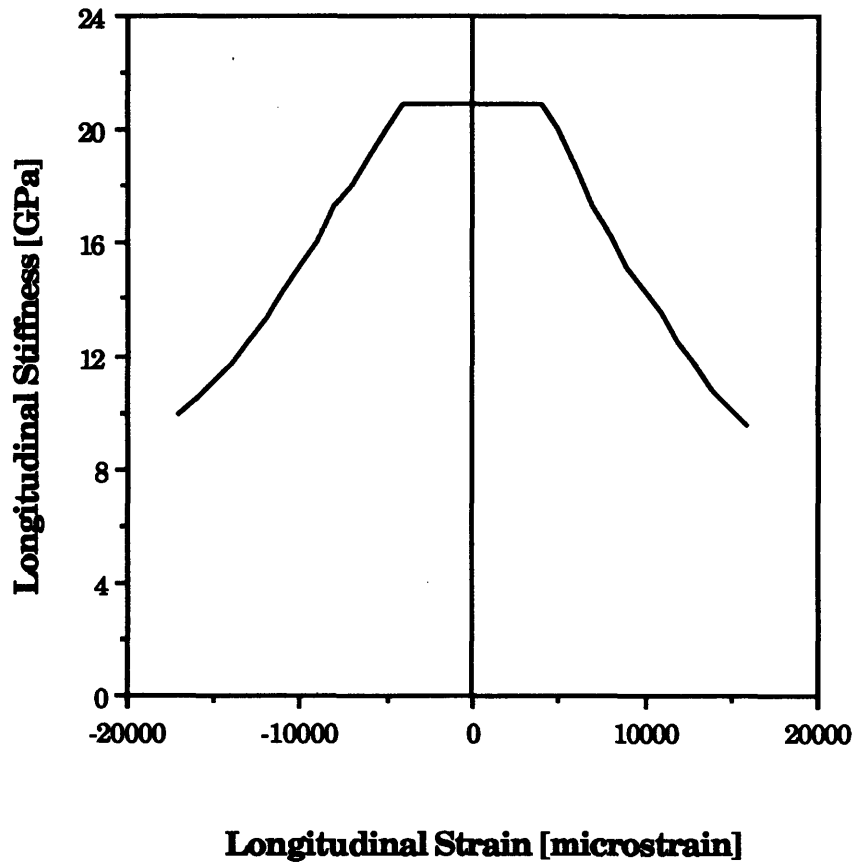


Figure 4.6 Stiffness versus strain used for 45° plies in models.

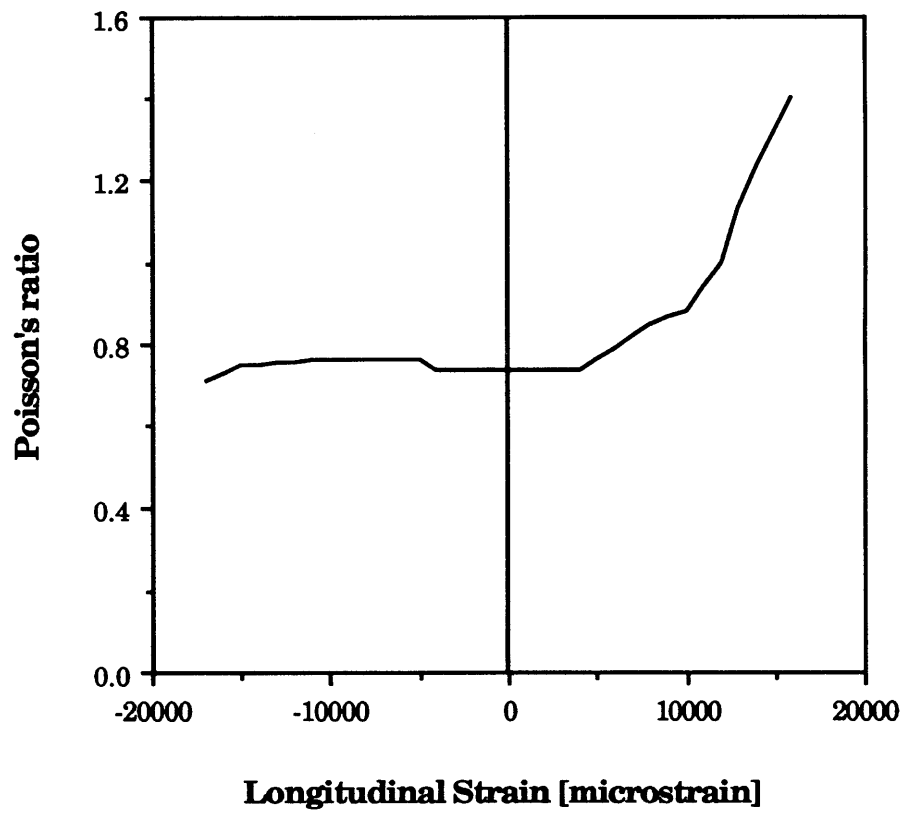


Figure 4.7 Poisson's ratio versus strain used for 45° plies in model.

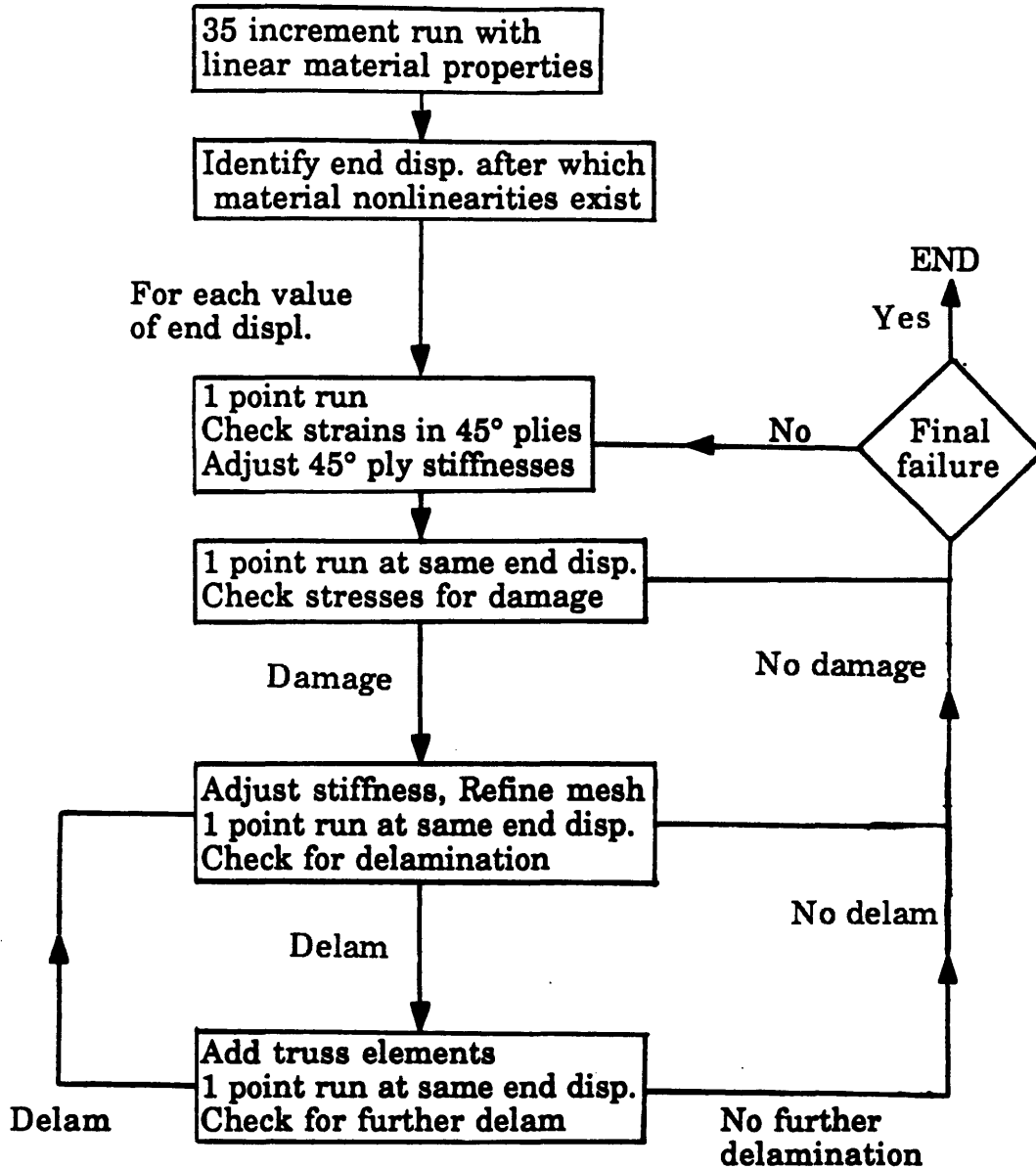


Figure 4.8 Flow chart outlining the ADINA runs made.

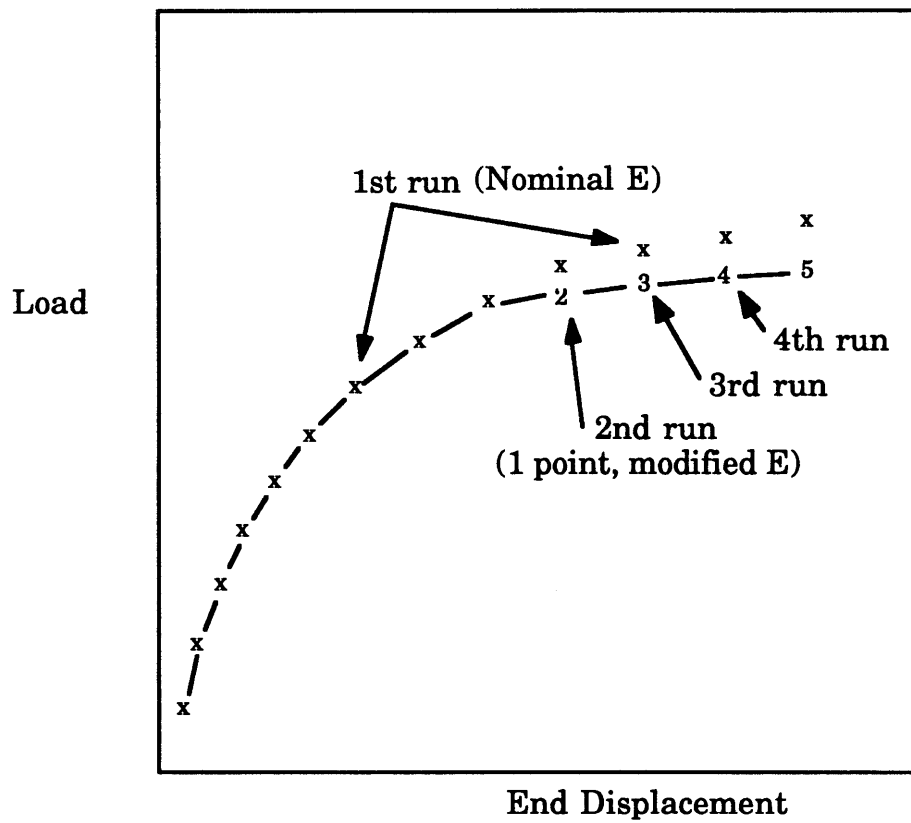


Figure 4.9 Sketch showing how load versus deflection data from several ADINA runs is spliced together to model nonlinear stiffness.

type depending on the value exceeded.

The effects of ply thickness discussed by Flaggs and Kural [29] were accounted for in a qualitative manner in that tensile matrix failure predictions in single plies, the neighbors of which had different fiber orientations, were ignored as long as the stress levels did not exceed the maximum allowable  $Y^T$  by a factor greater than 2.5. This factor of 2.5 is utilized since Flaggs and Kural found that matrix failure stresses in the 90° plies in  $[0^\circ_2/90^\circ]_S$  laminates exceeded the nominal maximum allowable stress by this factor. In the current investigation, matrix cracks were never observed experimentally prior to final failure in single plies with neighboring plies of different fiber orientations.

In some cases, compressive longitudinal stresses which exceeded the maximum allowable stress were predicted. Compressive fiber failures were not observed experimentally. As discussed in reference [32], the curvature in the specimens may have prevented sublaminates buckling, thereby effectively increasing the maximum allowable stress. This possible effect was taken into account by ignoring compressive fiber failure predictions. Such predictions were made in the  $[(45^\circ_2/-45^\circ_2/0^\circ)_2/90^\circ_5]_{2S}$  and  $[45^\circ_4/-45^\circ_4/(0^\circ/90^\circ)_4]_{2S}$  specimen types, with the predicted longitudinal stress exceeding the maximum allowable by 60% in the case of the latter.

### 4.3.2 Delamination Criterion

Delamination was predicted using the Quadratic Delamination Criterion described in reference [16]. Only out-of-plane stresses are considered. This criterion is applied at a ply interface, with stresses averaged over a specified distance. This averaging dimension is a material

constant. The effect of shear stress is considered to be independent of sign, and compressive  $\sigma_{33}$  stresses are assumed not to affect delamination initiation. The maximum allowables used were the same as the maximum in-plane shear stress and the maximum in-plane transverse tensile stress shown in Table 5.1. The effective criterion is shown below:

$$(\bar{\sigma}_{13}/S)^2 + (\bar{\sigma}_{33}/Y^T)^2 = 1 \quad (4.14)$$

The overbars signify that average stresses were used in the criterion.

Simple calculations show that transverse shear stresses in the undamaged columns amount to only a small fraction of the maximum allowable shear stress for center deflections up to 25 mm. This implies that delamination initiation requires a stress concentration. Experimental observations showed that delaminations occurred only in the presence of matrix cracks. The stress concentration occurred because of shear lag due to load transfer from the damaged ply onto its neighbors, and was located along the side where damaged element and undamaged element touch. The mesh was therefore refined in the vicinity of an element with matrix damage. The refined mesh is shown in Figure 4.10. As can be seen in the figure, the refined region is centered about the top edge of the damaged element. Shear stress concentrations existed both above and below the damaged ply, but, because gradient stresses through the thickness are due to bending, the more important stress concentration was that on the upper surface of the ply. Extra elements were inserted in the mesh at the stress concentration. These were the elements along the edge of which Quadratic Delamination Criterion was applied. The  $\sigma_{13}$  and  $\sigma_{33}$  stresses were

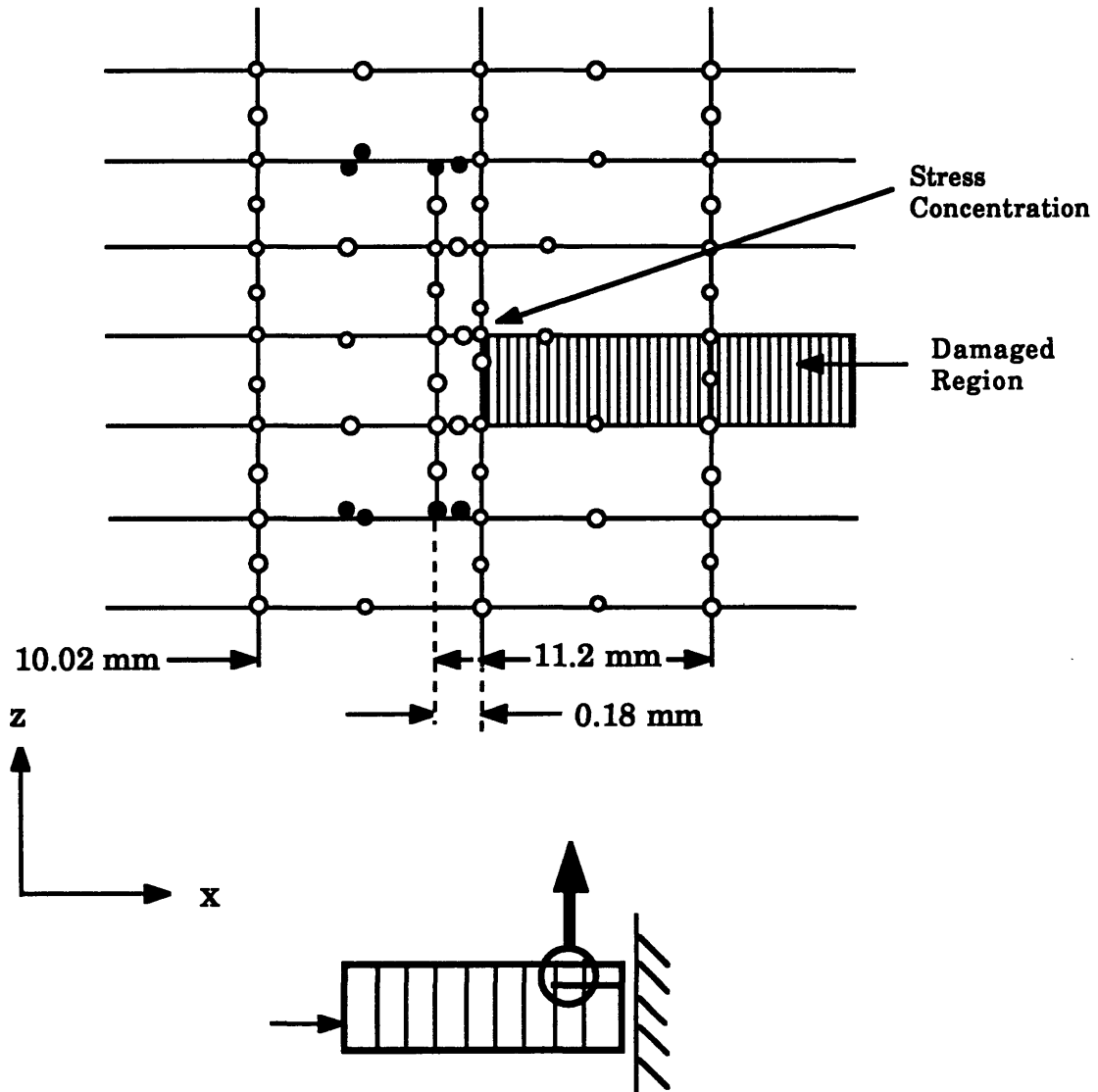


Figure 4.10 Refined mesh around the stress concentration at an element modelling matrix damage.

averaged over the length of these elements, which was set at 0.18 mm. This is the averaging distance which Brewer and Lagace [16] determined should be used for this material. As the extra elements were not inserted throughout the thickness of the model, the mesh became inconsistent at the edges of the refined area, in that some nodes did not belong to all the elements with which they came into contact. These nodes are filled in in the drawing of the refined mesh in Figure 4.10. The refined area was large enough so that these inconsistencies had no significant effect on the stresses at the stress concentration. Similarly, the inconsistencies were also insignificant at the global level.

Eight node elements with nodes at the corners and halfway along each edge model stress singularities poorly. The plane elements used in ADINA are isoparametric elements. Placing the edge nodes exactly one quarter of the way along the edge would cause a  $1/\sqrt{x}$  singularity in the interpolation functions. However, such a singularity would cause a 'divide by zero' error to occur in the computer program. Therefore, the edge nodes of the two edges nearest the stress concentration are positioned between one third and one quarter of the way along the edge from the corner nearest the concentration. This makes the element capable of modelling the stress singularity around a crack. Within this range, the predicted results are insensitive to the exact location of the edge nodes. Such elements are commonly used in linear fracture mechanics models.

## **4.4 Modelling Damage**

### **4.4.1 In-Plane Damage**

Matrix damage was modelled by effectively setting the values for  $E_2$ ,  $G_{12}$  and  $\nu_{12}$  in ply coordinates to zero in the damaged element. Nonzero values are required by ADINA for elastic properties, so the values used were actually 0.01 GPa for the stiffnesses and 0.001 for the Poisson's ratio. Fiber damage was modelled by setting all the elastic properties of the element to zero. Again, a value of 0.01 GPa was used for the stiffnesses and 0.001 for the Poisson's ratio. Experimental observations indicate that fiber breakage is usually accompanied by substantial matrix damage.

### **4.4.2 Delaminations**

Modelling the delaminations involved effectively disconnecting the two plies on opposite sides of the delamination from each other. It was important that the two plies be able to pull apart. However, if the plies are in contact, one must be able to push against the other, yet not be able to penetrate the other. This was accomplished by placing truss elements with nonlinear elastic properties between the two plies. These trusses are very stiff in compression, but very soft in tension. The trusses therefore did not have much effect when the plies pulled away from each other, but prevented the plies from penetrating each other. They also introduced no shear stiffness. Compressive stiffness was set at 100 GPa, while tensile stiffness was set at 0.01 GPa. The length was set at 0.01 mm, which was less than 10% of a ply thickness. A mesh with a delamination in it is shown in Figure 4.11. The mesh is refined at the delamination tip as it is around

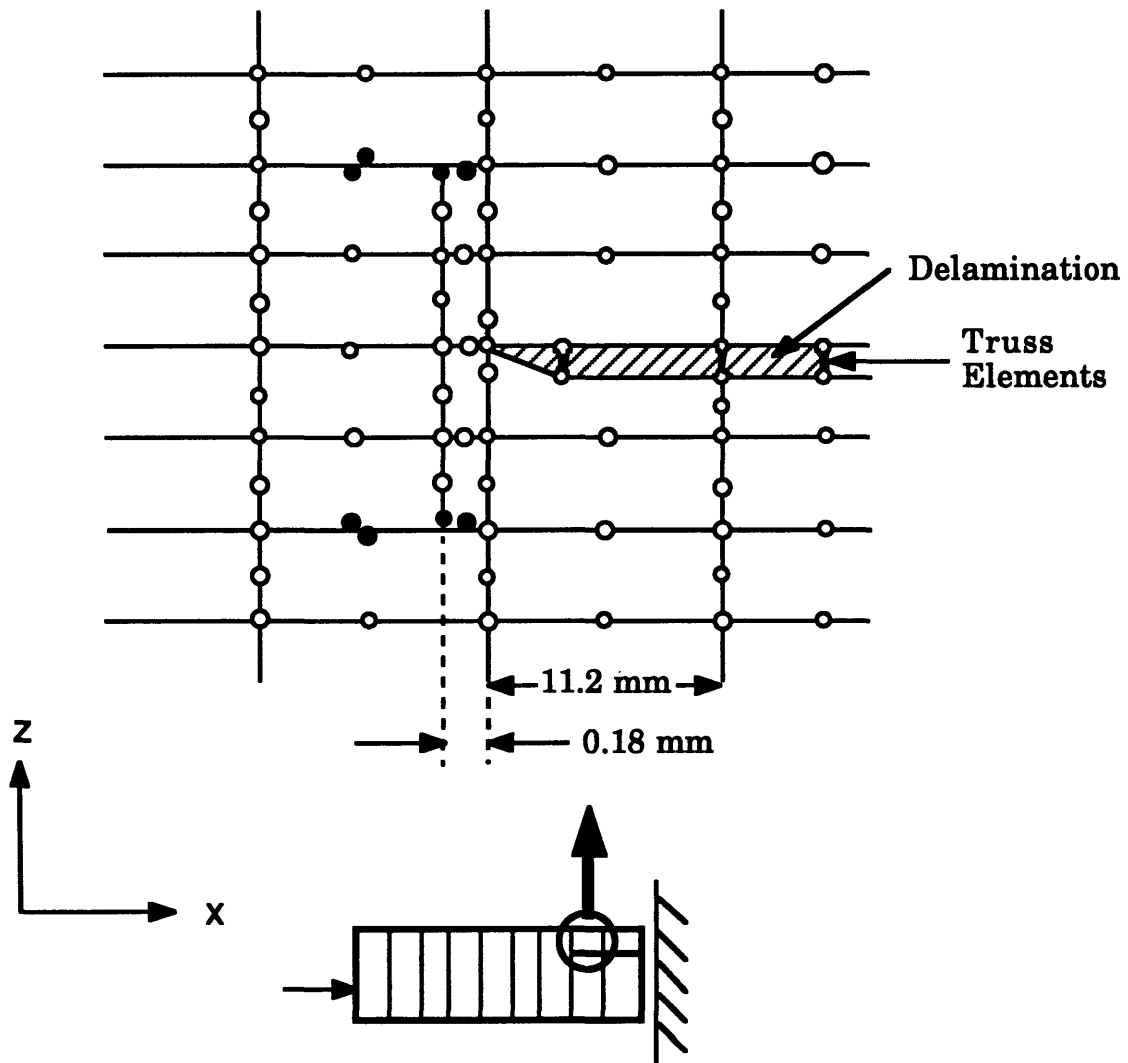


Figure 4.11 Refined mesh at a delamination tip.

an element with matrix damage. The Quadratic Delamination Criterion is applied at the delamination tip in the same manner.

#### **4.5 Model Implementation**

The finite element program was run on a Digital Equipment Corporation MicroVax. The cost in terms of CPU time for a single-point run of the model of an undamaged specimen was between seven and fifteen minutes, depending on the layup. The time needed for a run of the model of a damaged specimen could take as much as twenty minutes. These variations depend on the number of degrees of freedom and on the number of element groups, each of which has a new set of material properties, in the model. The initial thirty-five point runs took between two and three and a half hours of CPU time, again depending on the layup. In the thirty-five point runs, the stiffness matrix was not calculated at each step. Copies of the ADINA inputs for the three models are included in Appendix A. These inputs are for the thirty-five point runs and do not include damage or elements with nonlinear material properties.

*Chapter 5***THE EXPERIMENT****5.1 The Test Program****5.1.1 Material**

The material used for all the composite specimens was Hercules AS4/3501-6. This consists of unidirectional AS4 graphite fibers in a thermoset 3501-6 matrix system. It is supplied in a semi-cured state as preimpregnated tape, nominally 305 mm wide, and must therefore be stored at  $-18^{\circ}\text{C}$  or colder before being cured. The nominal elastic and strength properties of a unidirectional ply are shown in Table 5.1.

**5.1.2 Laminate Selection**

Initial tests were conducted on  $[\pm 45^{\circ}/0^{\circ}]_{10\text{S}}$  specimens. The  $[\pm 45^{\circ}/0^{\circ}]$  type lay-ups continue to be used extensively in a great variety of studies, and hence their general behavior is well understood. Furthermore, laminates consisting of  $\pm 45^{\circ}$ ,  $0^{\circ}$  and  $90^{\circ}$  plies are very commonly used in industry. In these tests, however, the initial damage, which occurred in the outermost  $0^{\circ}$  ply on the tension side, coincided with ultimate failure. Thus, there was no observable progression of damage.

The next tests were conducted on  $[\pm 45^{\circ}/0^{\circ}/90^{\circ}]_{8\text{S}}$  specimens. Classical Laminated Plate Theory used in conjunction with the Maximum Stress

Table 5.1 AS4/3501-6 Material Properties [36]

Stiffness Properties			Strength Properties		
$E_1$	142	GPa	$X^T$	2356	MPa
$E_2$	9.81	GPa	$X^C$	1468	MPa
$E_3$	9.81	GPa	$Y^T$	49.4	MPa
$G_{12}$	6.0	GPa	$Y^C$	186	MPa
$G_{13}$	6.0	GPa	S	105	MPa
$G_{23}$	4.8	GPa			
$\nu_{12}$	0.3				
$\nu_{13}$	0.3				
$\nu_{23}$	0.34				

failure criterion predicted that damage would initiate in the outermost 90° ply on the tension side. The effect of ply thickness on failure stress [29] was neglected however, and once again, damage initiated in the outermost 0° ply on the tension side, providing no observable damage progression.

Three layups were then chosen so as to ensure that initial damage was in the form of matrix cracks, making the accumulation of damage observable. The plies in which damage was expected to initiate were groups of at least four plies with the same fiber orientation. Such groups of plies always behave as a single ply, in that a matrix crack will propagate through the entire thickness of the ply [16]. For this reason, such a group of plies is considered as a single "effective ply". When the effective ply is at least four plies thick, the experimentally observed transverse tensile strength approaches the nominal value [29]. Using Classical Laminated Plate Theory and the Maximum Stress failure criterion, two laminates were chosen such that initial damage would occur in 90° plies and one such that damage would initially occur in the 45° plies, all on the tension side. The first two lay-ups are  $[\pm 45^\circ/0^\circ/90^\circ_4]_{4s}$  and  $[(45^\circ_2/-45^\circ_2/0^\circ)_2/90^\circ_5]_{2s}$ . The last lay-up is  $[45^\circ_4/-45^\circ_4/(0^\circ/90^\circ)_4]_{2s}$ .

### 5.1.3 Test Matrix

A test program was designed to determine the damage accumulation history of the three layups. The tests of the first two specimens of a particular layup were uninterrupted to failure. These tests showed the general behavior of the layup, including maximum loads and deflections reached. The remainder of the specimens were used to obtain the damage accumulation history for the layup. They were tested using the Load Drop

Technique: the specimens were loaded in displacement control, and the detection of a drop in load was interpreted as the occurrence of damage. On the first five specimens, an edge replica was taken of both edges at each load drop; on the next five, X-ray pictures were taken at every load drop. From these edge replicas and X-ray pictures, the damage accumulation history was pieced together.

From the X-ray photos, it was clear that there was some variation in damage across the width of the specimens. In order to find the extent of this variation, destructive examinations were carried out on specimens of each layup at different damage levels. These examinations were carried out on one specimen at each of four levels of damage for each layup. The test program is shown in its entirety in Table 5.2.

## **5.2 Specimen Manufacture**

Eighteen specimens of each layup were manufactured for this study. The procedures used were developed in TELAC [37], and are described briefly below.

On being taken out of the freezer, the composite was left sealed in its bag at room temperature for thirty minutes. Letting it warm up while sealed helps prevent condensation from forming on the material. Aluminum templates covered in teflon-coated glass fabric and razor blades were used to cut the tape accurately into the shapes required for each of the different ply orientations. The 45° plies were cut into trapezoidal shapes which were then placed together to form a 305 mm by 350 mm rectangle. These trapezoids were designed such that there were no fiber breaks in any ply. The edges of the trapezoids which butted together were parallel to the

Table 5.2 Test Matrix

Layup	Number of Specimens	Type of Test
[45° <sub>4</sub> /-45° <sub>4</sub> /(0°/90°) <sub>4</sub> ] <sub>2s</sub>	2	Uninterrupted to failure
	5	Tested to failure Edge replicas at load drops
	5	Tested to failure X-ray photos at load drops
	4	Destructive examinations
[±45°/0°/90° <sub>4</sub> ] <sub>4s</sub>	2	Uninterrupted to failure
	5	Tested to failure Edge replicas at load drops
	5	Tested to failure X-ray photos at load drops
	4	Destructive examinations
[(45° <sub>2</sub> /-45° <sub>2</sub> /0°) <sub>2</sub> /90° <sub>5</sub> ] <sub>2s</sub>	2	Uninterrupted to failure
	5	Tested to failure Edge replicas at load drops
	5	Tested to failure X-ray photos at load drops
	4	Destructive examinations

fiber direction. The only joints within a ply were "matrix joints", and these became indistinguishable during curing. The tape was cut into squares and rectangles to get the 0° and 90° plies.

The cut prepreg was layered into uncured sublaminates of approximately twenty plies. These were compacted by being placed in a vacuum for two hours. This closes gaps left between plies during layup and results in a lower void content after curing. After compaction, the sublaminates were joined together to form the laminate.

A variety of materials was used to ensure the proper curing of the laminate, as can be seen in Figure 5.1. The surface of the laminate was protected throughout the cure by peel-ply; this is a nylon-like fabric which is porous to the epoxy. The laminate was placed on the aluminum caul plate, which was covered with Mold Wiz<sup>®</sup> mold release, manufactured by Axel Plastics Research Laboratories, and nonporous teflon-coated glass fabric (TCGF). A sheet of porous teflon-coated glass fabric was placed on top of the laminate, and a number of sheets of bleeder material were placed on top of that. This bleeder material absorbs excess epoxy as it flows out of the laminate during the cure. The number of sheets was half the number of plies in the laminate. Aluminum top plates 305 mm by 350 mm in size wrapped in nonporous teflon-coated glass fabric were then placed on top of the bleeder material. Dams made out of a corprene rubber material (cork) were built up all around the laminate and top plate to ensure that neither shifted during the cure.

Depending on the caul plate used, either three or six laminates could be cured at once. Sheets of porous teflon-coated glass fabric were placed over all the top plates, and a heavy fiberglass cloth was placed over the teflon-

coated glass fabric. The fiberglass served as an air breather, and allowed air and other gases to escape into the vacuum system. The entire assembly was vacuum bagged with a high-temperature nylon bagging material and vacuum tape. The manner in which six laminates are arranged on a caul plate is shown in Figure 5.1.

The curing of the composite takes place in two stages; the first is a one hour flow stage at 117°C during which the epoxy is at its lowest viscosity. This allows excess epoxy to flow away, and makes for proper bonding of the plies. The second stage is a two hour set stage at 177°C. This is where most of the chemical cross-linking of the polymer chains in the epoxy occurs. Both stages are carried out in a vacuum of at least 740 mm Hg (29" Hg) and under a pressure of 0.59 MPa (85 psig). Heating and cooling rates were kept within 1°C to 3°C per minute to avoid thermally shocking the laminates. The last step was a postcure of eight hours at 177°C in an unpressurized oven. The cure cycle is illustrated in Figure 5.2.

After the cure, each laminate was machined into six 200 mm by 37.5 mm specimens using a water-cooled diamond grit cutting wheel mounted on a milling machine. Due to the thickness of the specimen, a table speed of 28 mm per minute was used. The specimen widths were measured at three points and thickness at nine points. The locations of these points are shown in Figure 5.3, and the average values for widths and thicknesses for each laminate are reported in Table 5.3. Both specimen thickness and width tend to vary by less than 1% for a given laminate. The average ply thickness for all laminates was 0.133 mm, compared to a nominal value of 0.134 mm, with a coefficient of variation of 0.9%. It was noticed that laminates were generally thicker in the middle than at the edges. Variation in thickness from laminate to laminate are more

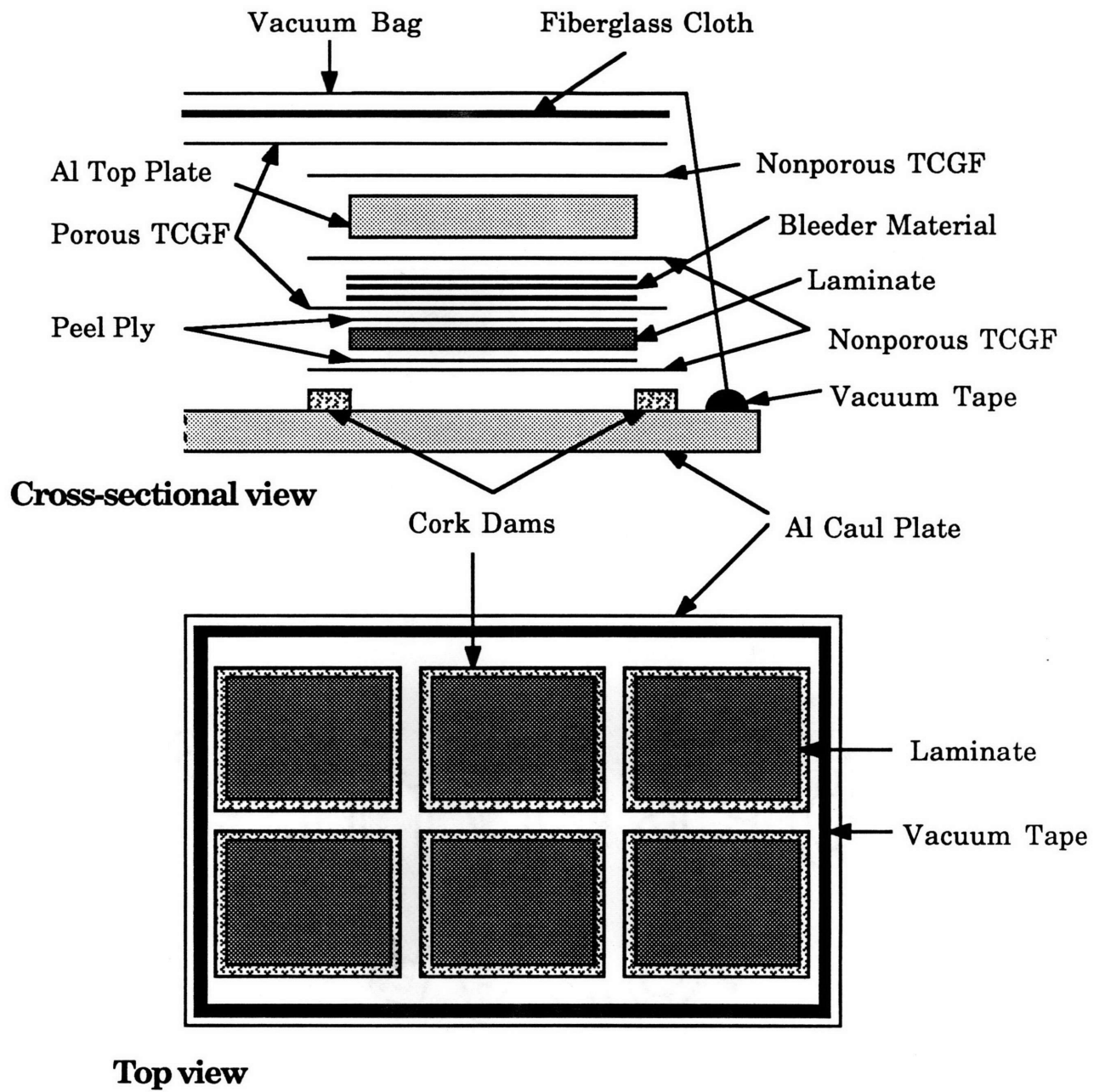


Figure 5.1 Schematics of Cure Setup

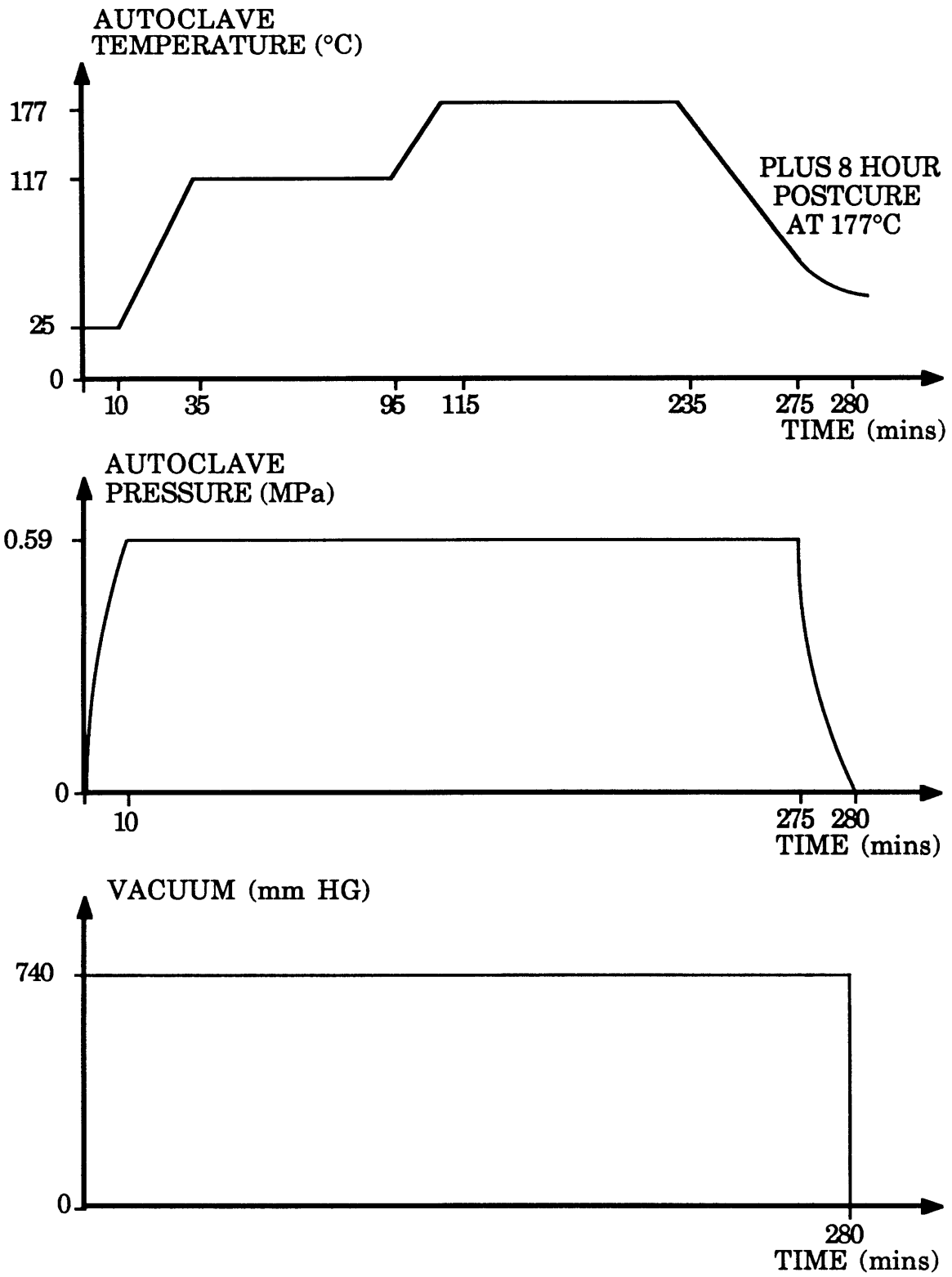


Figure 5.2 Schematic of cure cycle

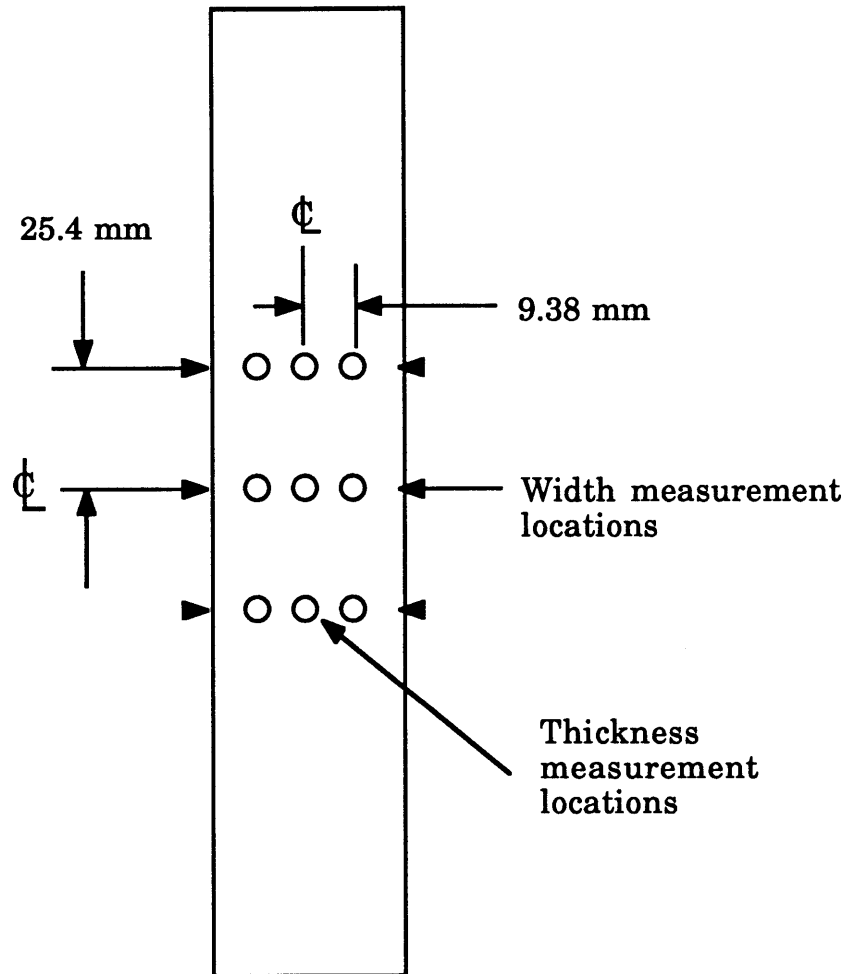


Figure 5.3 Locations of measurements

Table 5.3 Specimen Measurements.

All measurements in mm.

Layup	Panel No.	Average Thickness	Coefficient of Variation	Average Width	Coefficient of Variation
[45° <sub>4</sub> /-45° <sub>4</sub> /(0°/90°) <sub>4</sub> ]2 <sub>s</sub>	1	8.443	0.6%	38.05	0.2%
	2	8.842	0.9%	38.00	0.6%
	3	8.482	0.8%	38.51	0.1%
	Nominal	8.576	–	37.5	–
[±45°/0°/90° <sub>4</sub> ]4 <sub>s</sub>	1	7.185	0.5%	38.03	0.6%
	2	7.660	0.6%	38.44	0.2%
	3	7.472	0.6%	38.67	1.4%
	Nominal	7.504	–	37.5	–
[(45° <sub>2</sub> /-45° <sub>2</sub> /0°) <sub>2</sub> /90° <sub>5</sub> ]2 <sub>s</sub>	1	7.670	0.5%	37.78	0.8%
	2	7.998	1.2%	38.47	0.2%
	3	7.965	0.5%	38.43	0.1%
	Nominal	8.040	–	37.5	–

pronounced, without being consistently thicker or thinner than nominal values. The measured dimensions for width and thickness, rather than nominal values, were used in establishing the finite element models.

### **5.3 Instrumentation**

Two strain gages were attached to each specimen to record longitudinal strain during tests. One gage was mounted on each face of the specimen to one side of the center point, as shown in Figure 5.4. Having two gages back to back makes it possible to obtain bending strains as well as extensional strains. The latter is the average of the two gage readings; the strain due to curvature is obtained by subtracting the extensional strain from each gage reading. The gages used were Micro Measurements EA-06-125AD-120 with a 3.175 mm square constantin wire element on a 0.025 mm thick polyimide backing. The gages were aligned with the longitudinal axis and the centerline of the specimen using lines which were lightly scribed into the thin epoxy layer of the laminate surface. M-Bond 200 adhesive was used to bond the gages onto the specimen surfaces. The gage resistance was  $120 \Omega \pm 0.15\%$ , and the gage factor was  $2.055 \pm 0.5\%$ .

A transducer was used to record deflection at the center of the specimen. The transducer used was a Trans-Tek DC-DC model 355 gaging transducer, or Linear Variable Differential Transformer, with a range of  $\pm 51$  mm and an accuracy of  $\pm 0.5\%$  linearity. The transducer was placed in a jig which was attached to the testing machine's vertical supports. This jig allowed both vertical and horizontal transducer movement for adjustment purposes prior to testing.

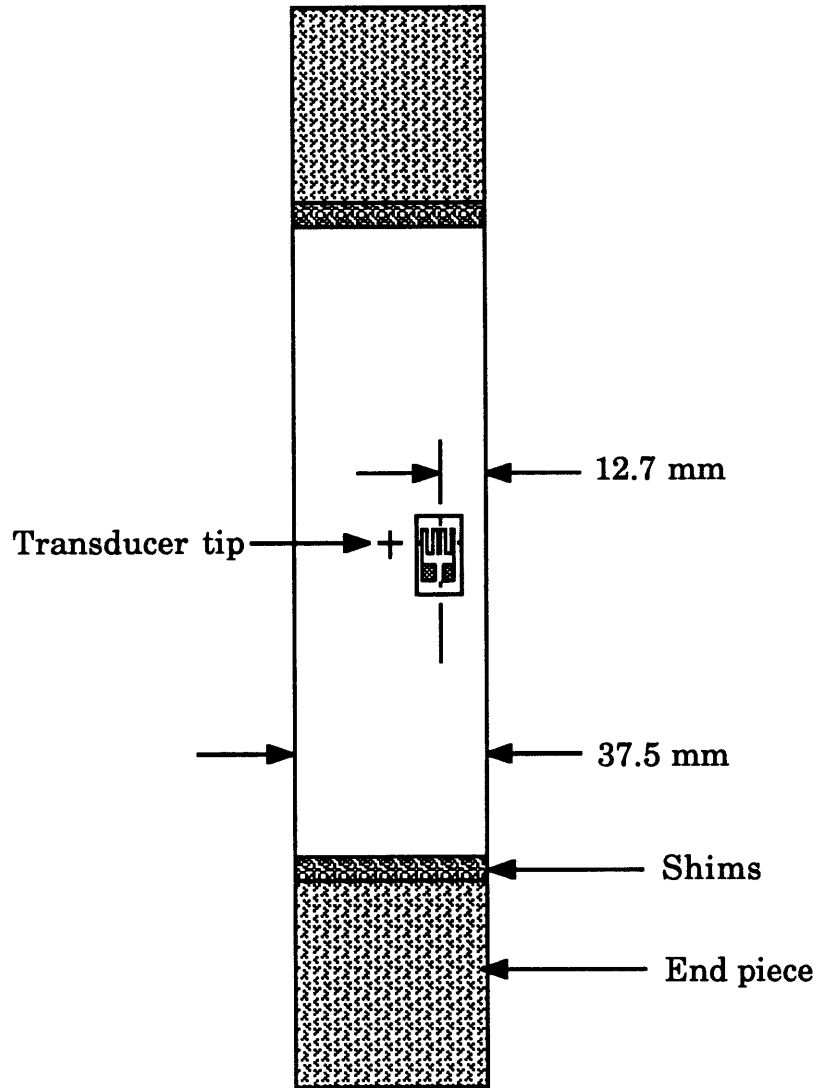


Figure 5.4 Strain gage locations.

## **5.4 Damage Detection**

The possible occurrence of damage was detected using the Load Drop Technique. The nature and extent of the damage was found using two non-destructive evaluation techniques: edge replicas and X-radiography. It is considered impossible to successfully use both NDE techniques on the same specimen because the tape used in the replication process may block some of the paths of the dye penetrant used for the X-ray photos. Destructive examinations were also carried out on some of the specimen to determine whether damage varied through the width of the specimen.

### **5.4.1 The Load Drop Technique**

The Load Drop Technique in its present form was developed by Brewer [36] in TELAC. The occurrence of damage will result in a drop in the modulus of the specimen. This change in modulus is normally difficult to detect for slight damage, and is particularly difficult to detect in a buckled column. However, as the column is loaded in displacement (stroke) control, a change in modulus will manifest itself in the form of an instantaneous drop in load. Hence, a drop in load in a quasistatically loaded specimen may indicate the occurrence of damage. As long as the load drop is not obscured by the increase in load due to normal loading of the specimen, damage initiation can be detected in this manner.

A program, which allowed the termination of the test when a load drop was detected, was written to control tests. The program's ability to detect load drops depends on the magnitude of the load drop, the loading rate and the time interval chosen between data points. The load data is

obtained by the computer from the testing machine through analog-to-digital converters, which digitize the analog voltage data, representing the applied load with discrete computer units. The load equivalent to a computer unit depends on the load range selected. The program compares each new load datum with the previous one, and if the new point's value is lower, the test is halted.

It is necessary that the load drop be larger than the normal increase in load in the time interval between data points by at least one computer unit, otherwise the drop will be obscured, as illustrated in Figure 5.5. If the time interval is too short, however, the noise in the system can be larger than the normal rise in load, resulting in erroneous stops. Trial and error were used to find a time interval which was short enough to provide the necessary sensitivity, but long enough to avoid problems with noise. The interval chosen tended to err on the side of being too short; this resulted in the first few load drops for a specimen being erroneous, but ensured that the first sign of damage was detected. The time interval used was 1.0 seconds.

#### **5.4.2 Edge Replication**

Edge replicas were taken to monitor the accumulation of damage during a series of tests on a specimen. For a specimen designated for edge replication, replicas were taken at every interruption in a test due to a load drop. Edge replication involves the use of a strip of acetate film to make an impression of the edge of a specimen. The specimen's edge were carefully polished before testing with felt bobs mounted in a drill press. These bobs were dipped into a colloidal solution of a fine abrasive, Kaopolite-SF, with

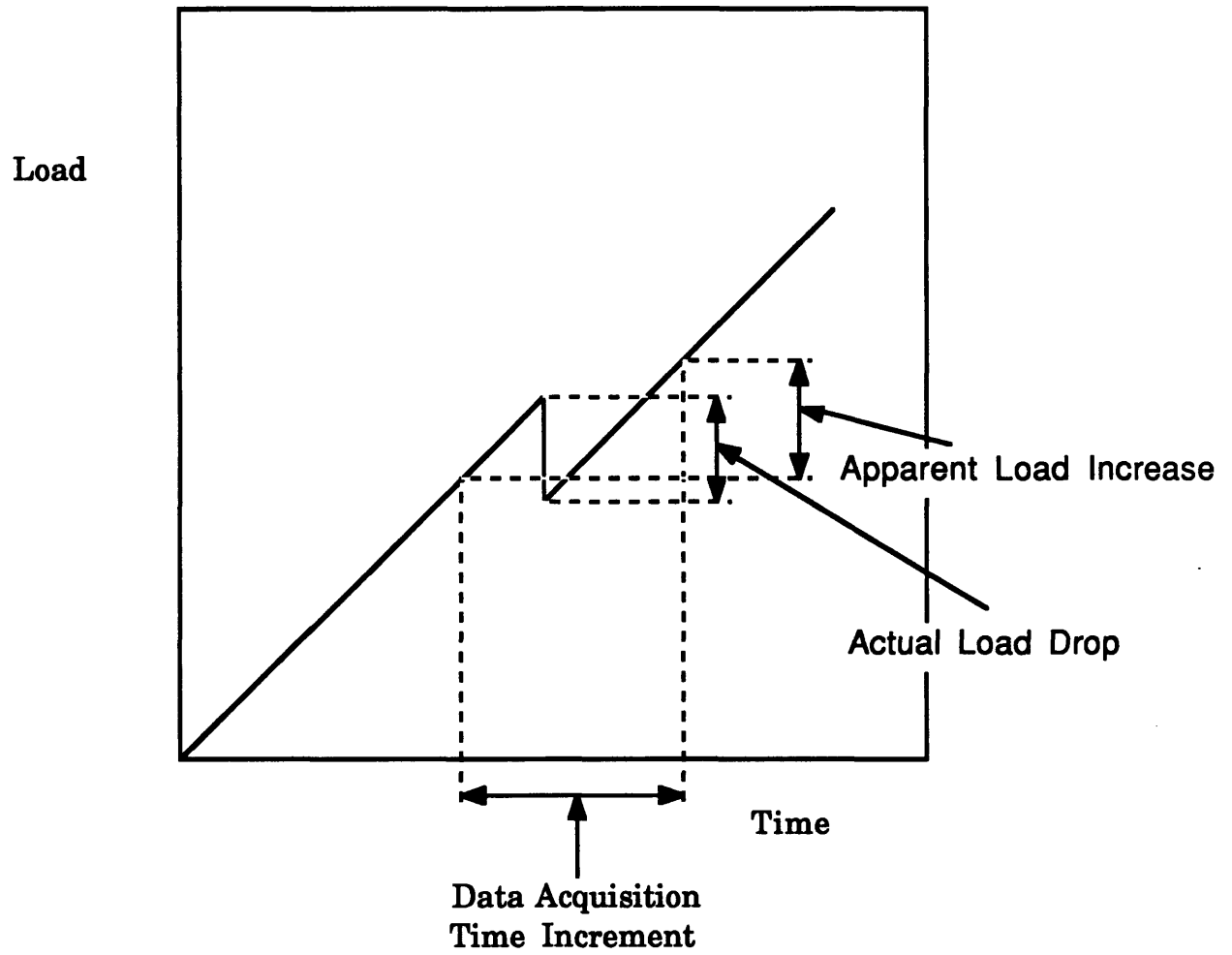


Figure 5.5 Illustration of load increase obscuring a load drop.

an average particle size of 0.7  $\mu\text{m}$ . The solution was hand-mixed and contained approximately two parts tap water for each part of abrasive. After polishing, the specimen was quickly rinsed to prevent the solution from drying on the edge. This gave the specimen's edge a glossy finish.

A line was scribed across the specimen's edges at the center of the specimen. This line was used as a reference on replicas, and can be seen in the photo in Figure 5.7.

The replicas were made while the specimen was under load. The load holds cracks and delamination open, thus making them more easily visible. To make a replica, a strip of replicating tape was cut to a length of approximately 125 mm. This was the length of the section of specimen easily accessible between the end pieces. One end of the tape was held onto the lower end of the specimen's edge while acetone was sprayed along the rest of the edge; the acetone softens the tape for replication. The tape was then smoothed onto the edge with a finger. The tape was allowed to dry for approximately half a minute, during which time it was labelled with a felt tip pen.

Once dry, the replica was removed and inspected for smudges. If insufficient or uneven pressure had been applied, smudges were made which could be seen with the naked eye. When this happened, the smudged replica was discarded, and the specimen rereplicated. If the replica was acceptable, it was placed between two sheets of glass to prevent the replica from curling.

### **5.4.3 X-Radiography**

Specimens designated for X-ray photography were photographed at every interruption in a test due to a load drop. While the specimen was still under load, diiodobutane (DIB) dye penetrant was wiped onto the edges. DIB is opaque to X-ray wavelengths, and so makes cracks and delaminations visible. As cracks would tend to be held open while the specimen was under load, wiping the dye penetrant on at that point made it easier for the dye to penetrate as far as possible into the cracks. The specimen was then unloaded and photographed.

### **5.4.4 Destructive Examinations**

The X-ray photographs clearly indicated that damage was not always uniform across the width of the specimens, as was assumed for modelling purposes. Damage generally initiated at the specimen edge and propagated inwards. To find the extent of the variation of damage across the width at different load levels, destructive evaluations were carried out. Specimens were loaded so as to be damaged but not failed. They were then cut in two along the specimens' centerline parallel to the longitudinal axis, as illustrated in Figure 5.6. Replicas were taken of the inner edges and compared to replicas of the outer edges. This represents the two extremes in terms of damage state variation across the width of the specimen.

From the results of replica and X-ray photo data, four characteristic damage states were identified for each of the layups. Reifsnider and Masters [37] found that in some laminate types, final failure was always preceded by the same characteristic damage state. These characteristic damage states are stages in the damage accumulation process through

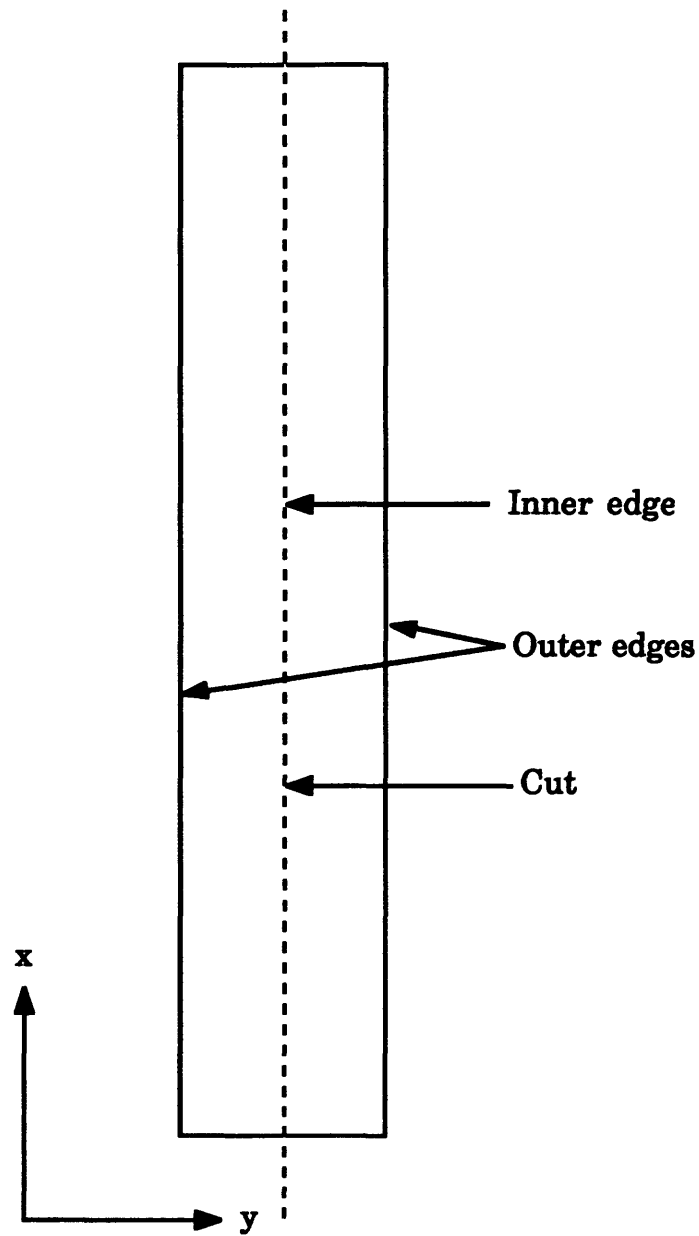


Figure 5.6 Illustration of a specimen cut for destructive examination.

which each specimen passes, and are independent of the load history. The characteristic damage states for the three layups are described in Chapter 6. The destructive examinations were carried out at each of these characteristic damage states. One specimen was loaded to the center deflection at which each damage state exists for all three layups. These specimens' edges were replicated at every load drop up to and including the last halt.

#### **5.4.5 Replica and Photograph Interpretation**

When properly done, replicas can show features as small as individual fibers. Differences in plies, interlaminar resin layers and an occasional void can easily be seen. During replication, the softened tape seeps into cracks and delaminations, especially when they are susceptible to being opened under load. The difference in surface texture in the replicas of these features makes them very easy to detect when examined under a microscope, especially when backlighted. These features are difficult to detect when examining the specimen directly because they all appear as dark details on a dark background.

After the tests, the replicas were examined while backlighted under a microscope at a magnification of fifteen. The damage observed was transcribed onto schematics of the specimen. These schematics are drawn to scale along the length of the specimen and expanded by a factor of about seven through the thickness. The effective plies are all drawn in. Damage in the form of cracks and delaminations are drawn on the schematic in the appropriate plies essentially as seen. Crack density was found by counting the number of cracks over a given length of specimen. Replicas could be

made reliably only of the central 100 to 120 mm of the specimen because of the presence of the end pieces and shims. A typical schematic with a photo of the matching section of a replica are shown in Figure 5.7.

X-ray photographs were examined with the naked eye. Crack density could be obtained by counting the number of cracks in each 1 cm section, as was done with the replicas. Finding the crack density was done more effectively with the replicas, as cracks showed up more clearly there, especially when there was damage in more than one ply. Furthermore, the location in the specimen of the plies in which damage had occurred could not be determined from an X-ray photo. As the photo covered almost the entire test section, variations in crack density along the length were better determined from the X-ray photos. They also showed how damage varied across the width. In general, delaminations did not show up clearly on the X-ray photos. Delaminations above and below cracks in 45° plies showed up the most clearly.

## **5.5 Test Procedure**

All tests were carried out on an MTS 810 Material Testing System in TELAC. They were conducted under quasistatic monotonic compressive loading in stroke control. The stroke rate was set at 0.0254 mm per second (0.001" per second). This stroke rate combined with the time interval chosen between data points made the Load Drop Technique very effective. The load range used was  $\pm 44.5$  kN (10,000 pounds), and the stroke range used was  $\pm 25.4$  mm (1").

As mentioned in the description of the test jig design, correct knife edge alignment was considered important in achieving simply-supported

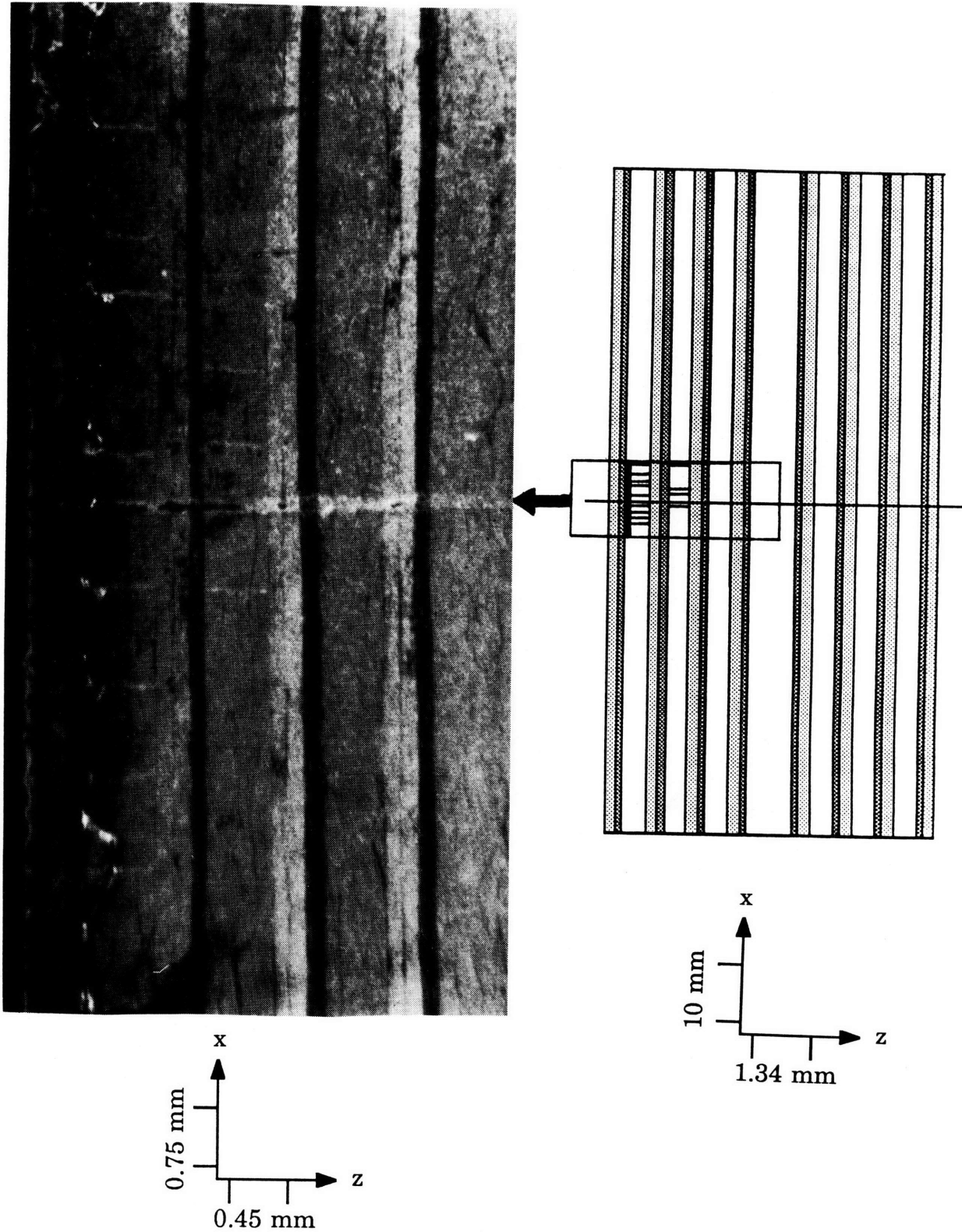


Figure 5.7 Photograph of the edge replica of a  $[\pm 45^\circ/0^\circ/90^\circ]_4$  specimen, with the corresponding transcription.

end conditions. The top knife edge end fixture was aligned in the machine's upper grip with a machinist's square. The alignment plate was then bolted to it, and the lower end fixture was bolted onto the plate. After the lower grip was closed, the plate was removed. The lower grip could be moved up and down to get the correct distance between the knife edges. When this distance was correct, the specimen could be slipped in between the knife edges. The specimen would stay in place under no load. This was the 'zero position' in which the strain gages were calibrated.

The strain gages were monitored by the computer using Vishay strain gage conditioners. These conditioners amplify and filter the signal from the gages. The computer stored data received from the conditioners, the transducer or the testing machine's load cell through analog-to-digital converters, which divided the full range of the channel into  $\pm 2048$  digital units. The value of a computer unit for load data was therefore 21.7 N, and for stroke data, 0.0062 mm. For strain data, the value of a computer unit could be adjusted using the gain control on the strain gage conditioner. The Wheatstone Bridge circuit, of which the gage was a part, was first balanced so that zero strain was registered. A calibration resistance was then connected in parallel with the gage in order to calibrate the system. The circuit was calibrated so that each computer unit represented 12.5  $\mu$ strain.

With the specimen in place, the transducer tip was aligned with the center point of the specimen. A water level was used to ensure that the transducer was horizontal. The transducer was calibrated by placing a 1.000" block between the transducer tip and the specimen surface; the difference in readings with and without the block gave the number of computer units per inch.

The specimens for which the tests were to be uninterrupted, were tested monotonically to failure. Final failure was considered to have occurred when the load had dropped to less than half the maximum value reached, or when more than half the number of plies was damaged. During the test, it was possible to include 'marks' in the data file at specified data points. This was done when acoustic emissions were heard, or when visible damage occurred.

For the interrupted tests, the testing machine was run under the computer's control such that data acquisition and load application were started simultaneously. A test normally ended when the load recorded at one data point was lower than that at the previous point; this load drop was interpreted as the possible occurrence of damage. The maximum load and stroke values recorded by the test machine were noted. The stroke was reduced by a factor of two because the testing machine had a tendency to slightly increase the load when held at a given point, resulting in the possible occurrence of damage while no data was being recorded. The specimen was then ready for edge replication or X-ray photography. As stated above, it was preferable to make the edge replicas or wipe the edges with dye penetrant while the specimen was under load.

Once the replica or photo had been taken, the specimen was unloaded and then retested. The computer was instructed to ignore any load drops which occurred at load levels previously encountered. This procedure was repeated until the final failure of the specimen, with a new data file being created for each test.

The specimens designated for destructive examination were tested in the same manner with the Load Drop Technique until the desired damage level was reached. Edge replicas were made as for the normal edge replica

specimens. The center deflection data was shown on a voltmeter during the test for comparison with previous test results. When the center deflection at a load drop was similar to that seen in previous tests at a characteristic damage state, the replicas were examined to find the extent of damage. These replicas were compared to transcriptions of replicas of specimens at the characteristic damage state. If the damage levels in the transcriptions and the replicas of the specimen being tested appeared to match, the specimen was put aside for destructive examination. Otherwise, the specimen was tested again.

## *Chapter 6*

# **RESULTS**

The results of the test program described in Chapter 5 are shown and compared with the predictions of the model described in Chapter 4. In the first section, the load-deflection behavior and damage histories are presented. In the second section, the experimental results are compared with model predictions.

### **6.1 Experimental Results**

#### **6.1.1 Load versus Deflection**

The uninterrupted tests showed the general behavior of the layups, in terms of maximum loads and deflections reached, and in terms of failure modes. Southwell [6] buckling loads were used as a way of characterizing the load versus center deflection plots. Southwell plots were made from the data of these tests. Center deflection divided by load was plotted against center deflection, and a line was fitted to the straight section of the graph, the slope of which gives the buckling load. These loads were used for the comparison of experimental test results with one another and with model predictions. A typical Southwell plot is shown in Figure 6.1.

The maximum loads reached in these tests were 70 to 80% of the indicated Southwell buckling loads. It would be expected that this buckling load would be higher than the maximum experimental load, as the

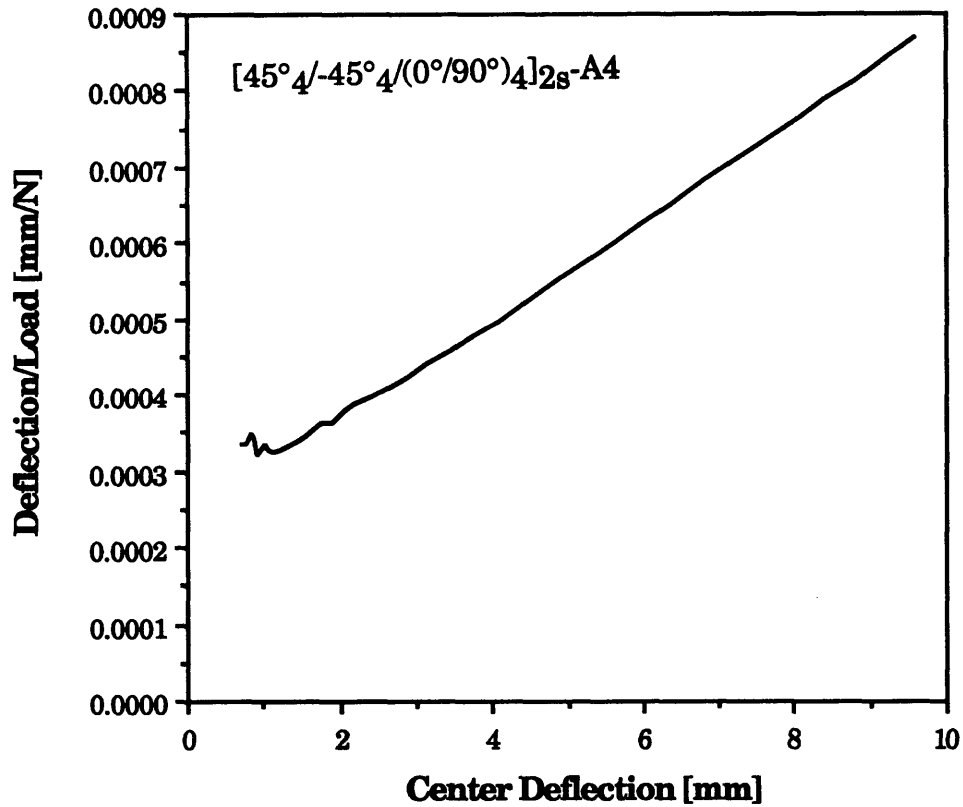


Figure 6.1 Typical Southwell Plot of specimen  $[45^\circ_4/-45^\circ_4/(0^\circ/90^\circ)_4]_{2s}\text{-A4}$

nonlinear stiffness properties of the 45° plies and the occurrence of damage would decrease the flexural stiffness of the specimens at large deflections, thereby reducing the applied load. The experimental Southwell Buckling load for each specimen is shown in Tables 6.1 through 6.3, along, where possible, with the average maximum load reached. Specimens from one laminate from each layup were used for destructive examinations; these specimens were not loaded to failure. Buckling and maximum loads were all reasonably consistent within each layup, with coefficients of variation below 10%.

Typical load versus center deflection plots for the uninterrupted tests are shown in Figures 6.2 to 6.4. In the test of the  $[45^{\circ}_4/-45^{\circ}_4/(0^{\circ}/90^{\circ})_4]_{2S}$  specimens, the occurrences of damage resulted in clear load drops, as can be seen in Figure 6.2. This damage consisted of matrix cracks in the 45° plies on the tension side of the specimen. The tension side is the face of the specimen where the bending strain is tensile. The formation of a crack was audible. These cracks were followed by very obvious delaminations, where sections of the outermost 45° occasionally were broken off the specimens. In the  $[\pm 45^{\circ}/0^{\circ}/90^{\circ}]_4]_{4S}$  specimens, damage consisted of the accumulation of matrix cracks in the 90° plies on the tension side. On the graph in Figure 6.3, this occurred during the relatively flat part of the plot where the center deflection goes from approximately 6 mm to 10 mm. Initial damage on the  $[(45^{\circ}_2/-45^{\circ}_2/0^{\circ})_2/90^{\circ}_5]_{2S}$  specimens also consisted of matrix cracks in the 90° ply on the tension side. Again, this resulted in a relatively flat section in the load versus center deflection graph in Figure 6.4 for between 12 mm and 18 mm of deflection. The large load drop occurred when a delamination appeared on both sides of the central 90° effective ply, essentially splitting

the specimen in two through the thickness. The damage accumulation histories for each layup are described in detail below.

The results of the interrupted tests show that, prior to final failure, the effects of damage on the flexural stiffness of the specimen were slight in general. In these tests, the specimens were loaded until a load drop was detected by the computer. At that point, the specimens were unloaded, edge replicas or X-ray photographs were taken, and then the specimens were retested. Typical plots of load versus center deflection for the three specimen types are shown in Figures 6.5 through 6.7. In each plot, the data from the test up to each characteristic damage state is shown, as well as that from the test while the specimen was undamaged and that from the final test. The buckling load calculated via the Southwell method for these three specimens are given at each characteristic damage state in Table 6.4. The corresponding center deflection are included. For all three, the experimental buckling load is reduced by less than 10% at the fourth characteristic damage state, compared to the undamaged specimen. Matrix damage, as encountered in these layups, thus does not seriously affect the specimen bending stiffness in this loading configuration. This would not necessarily be true in a part under more complex loading.

### **6.1.2 Damage Histories**

For all laminate types, damage initiated in the central region of the specimen, in the plies where it was expected to. In general, damage accumulated in the form of matrix cracks and delaminations, resulting in ultimate failure when at least half of the plies were damaged, and the applied load had dropped to less than half of the maximum load reached.

Table 6.1 Experimental Southwell buckling loads and maximum loads for the  $[45^{\circ}_4/-45^{\circ}_4/(0^{\circ}/90^{\circ})_4]_{2s}$  specimens.

All loads in Newtons

Specimen	Buckling Load	Max. Load
A1	13776	10278
A2	14261	11080
A3	a	a
A4	15449	11298
A5	14328	11734
A6	16022	11494
B1	13425	b
B2	14003	b
B3	15773	b
B4	14728	b
B5	a	a
B6	14394	b
C1	16538	10320
C2	16365	10974
C3	16650	12144
C4	15204	12343
C5	17388	12059
C6	16022	11365
Average for Layup	15270 (7.5%) <sup>c</sup>	11225 (5.7%)

a Data not available for this specimen

b This specimen used for destructive examinations

c Coefficient of variation

Table 6.2 Experimental Southwell buckling loads and maximum loads for the  $[\pm 45^\circ/0^\circ/90^\circ]_4$  specimens.

All loads in Newtons

Specimen	Buckling Load	Max. Load
A1	7758	6170
A2	8394	6539
A3	8741	6712
A4	7691	6606
A5	8879	6841
A6	9332	6757
B1	9323	b
B2	9439	b
B3	9403	b
B4	8127	b
B5	a	a
B6	8968	b
C1	9003	7540
C2	9510	7584
C3	8634	7624
C4	9279	7540
C5	8874	7517
C6	8581	7584
Average for Layup	8820 (6.2%) <sup>c</sup>	7085 (7.1%)

a Data not available for this specimen

b This specimen used for destructive examinations

c Coefficient of variation

**Table 6.3 Experimental Southwell buckling loads and maximum loads for the  $[(45^\circ_2/-45^\circ_2/0^\circ)_2/90^\circ_5]_{2s}$  specimens.**

All loads in Newtons

Specimen	Buckling Load	Max. Load
A1	8976	7455
A2	9684	7646
A3	11040	8139
A4	10008	7976
A5	10275	7976
A6	9928	8105
B1	9835	8412
B2	11040	8954
B3	11499	9497
B4	11748	9475
B5	11187	9234
B6	10329	b
C1	10306	8300
C2	11067	b
C3	11032	b
C4	11209	b
C5	a	a
C6	a	a
Average for Layup	10573 (7.0%) <sup>c</sup>	8442 (8.2%)

a Data not available for this specimen

b This specimen used for destructive examinations

c Coefficient of variation

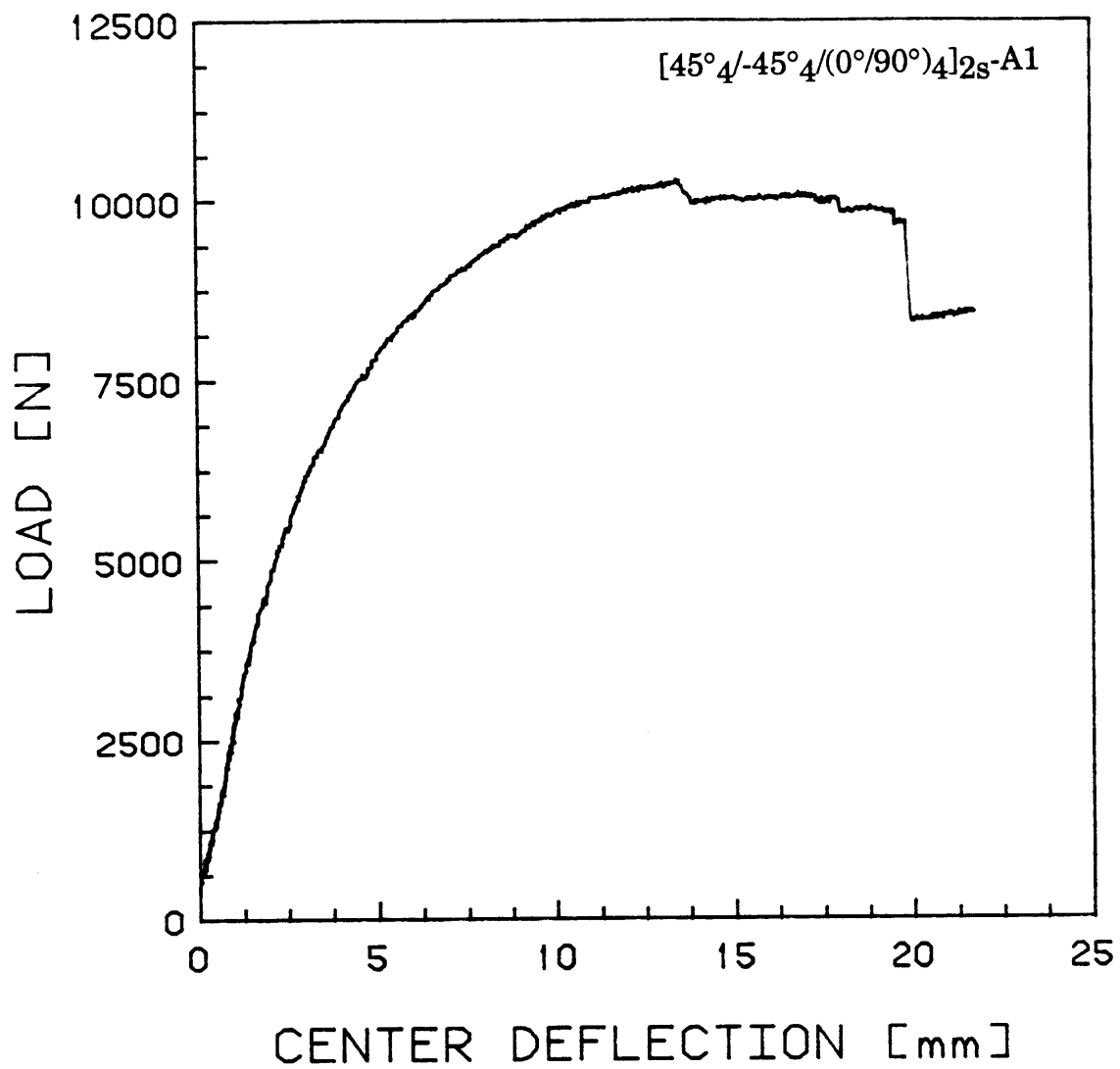


Figure 6.2 Load versus center deflection for uninterrupted test of  $[45^{\circ}_4/-45^{\circ}_4/(0^{\circ}/90^{\circ})_4]_{2s}$  specimen.

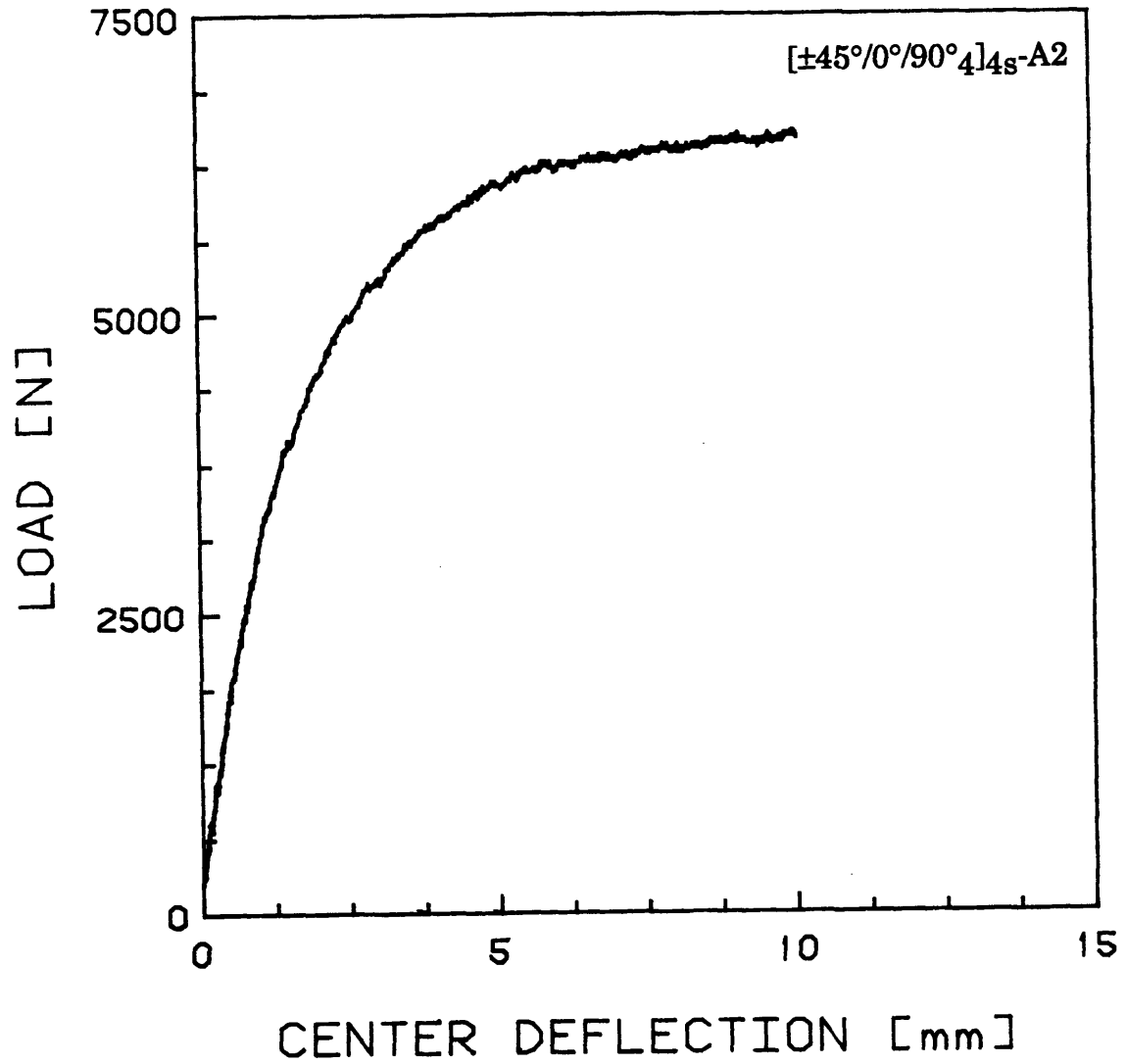


Figure 6.3 Load versus center deflection for uninterrupted test of  $[\pm 45^\circ/0^\circ/90^\circ]_{4s}$  specimen.

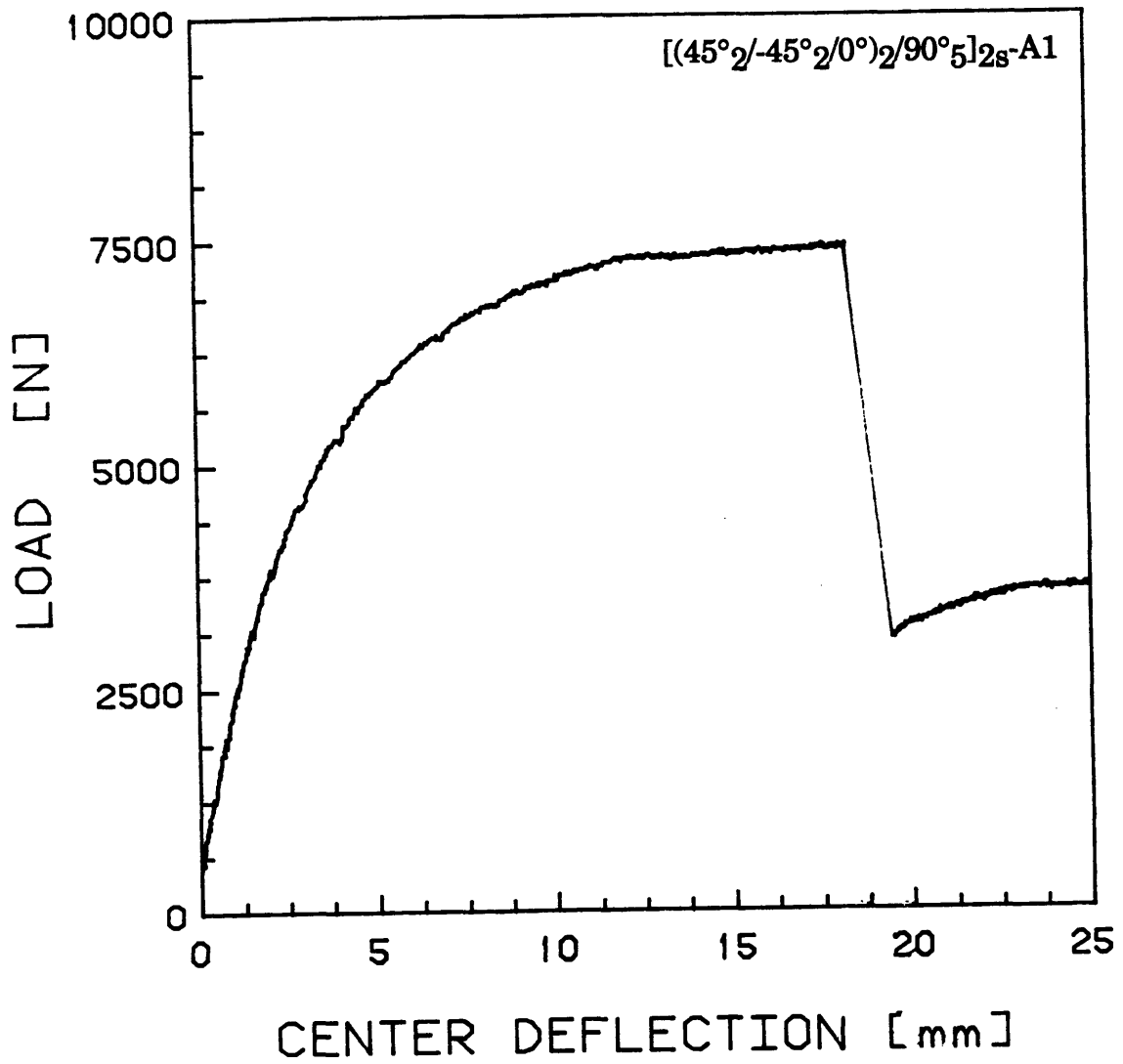


Figure 6.4 Load versus center deflection for uninterrupted test of [(45°₂/-45°₂/0°)₂/90°₅]₂ₛ specimen.

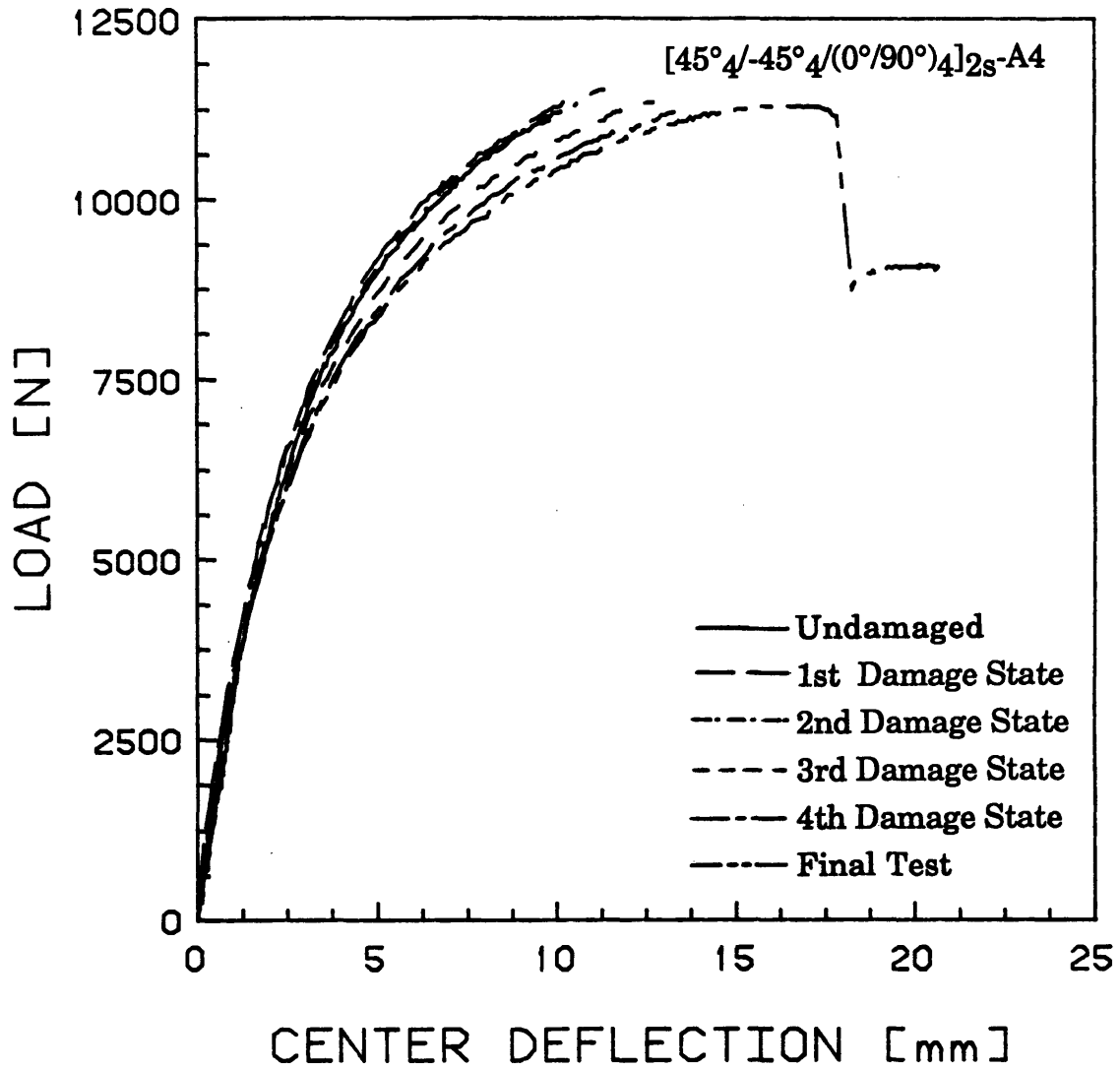


Figure 6.5 Load versus center deflection for a  $[45^\circ_4/-45^\circ_4/(0^\circ/90^\circ)_4]_{2s}$  specimen at each characteristic damage state.

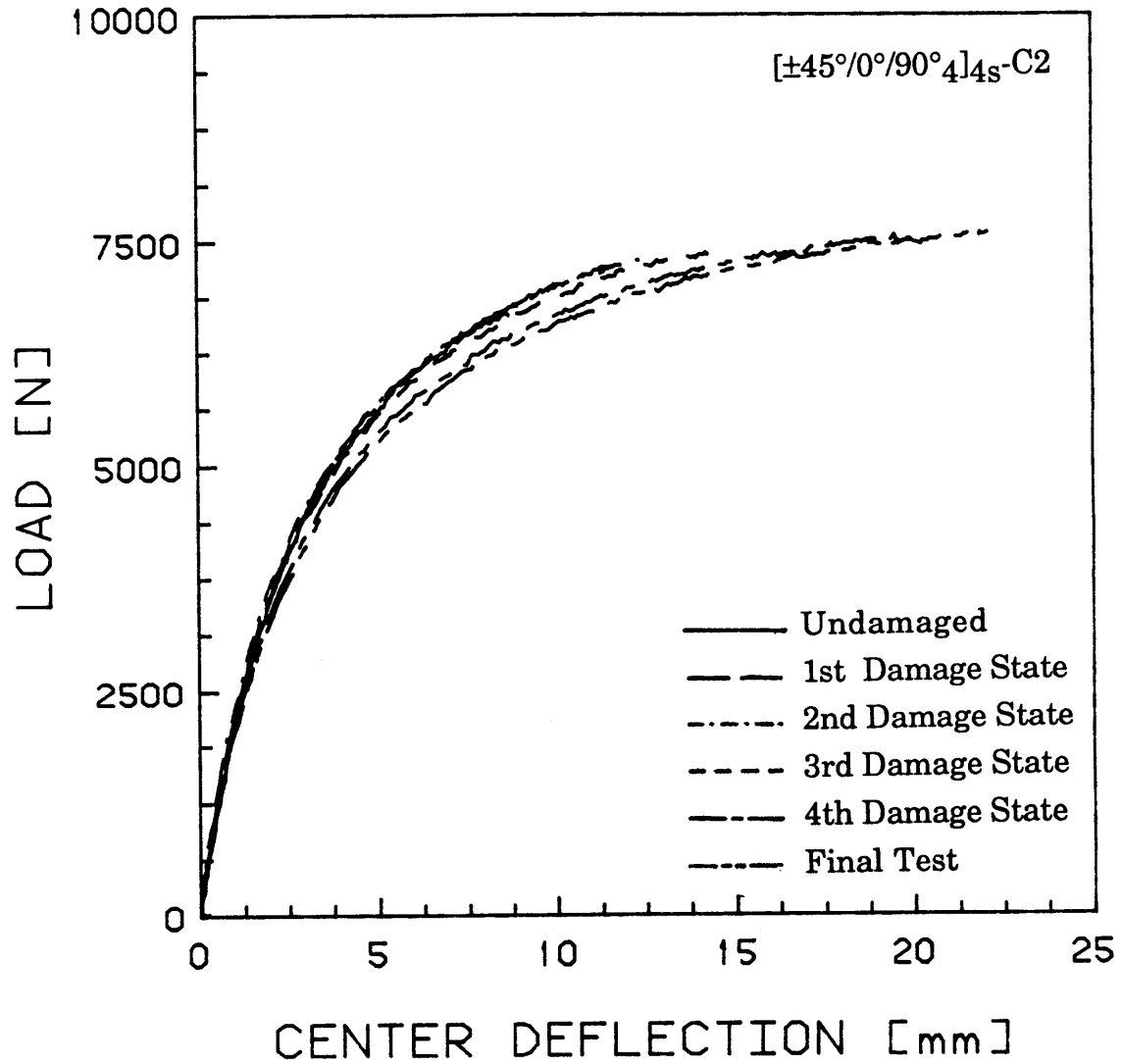


Figure 6.6 Load versus center deflection for a  $[\pm 45^\circ/0^\circ/90^\circ]_4s$  specimen at each characteristic damage state.

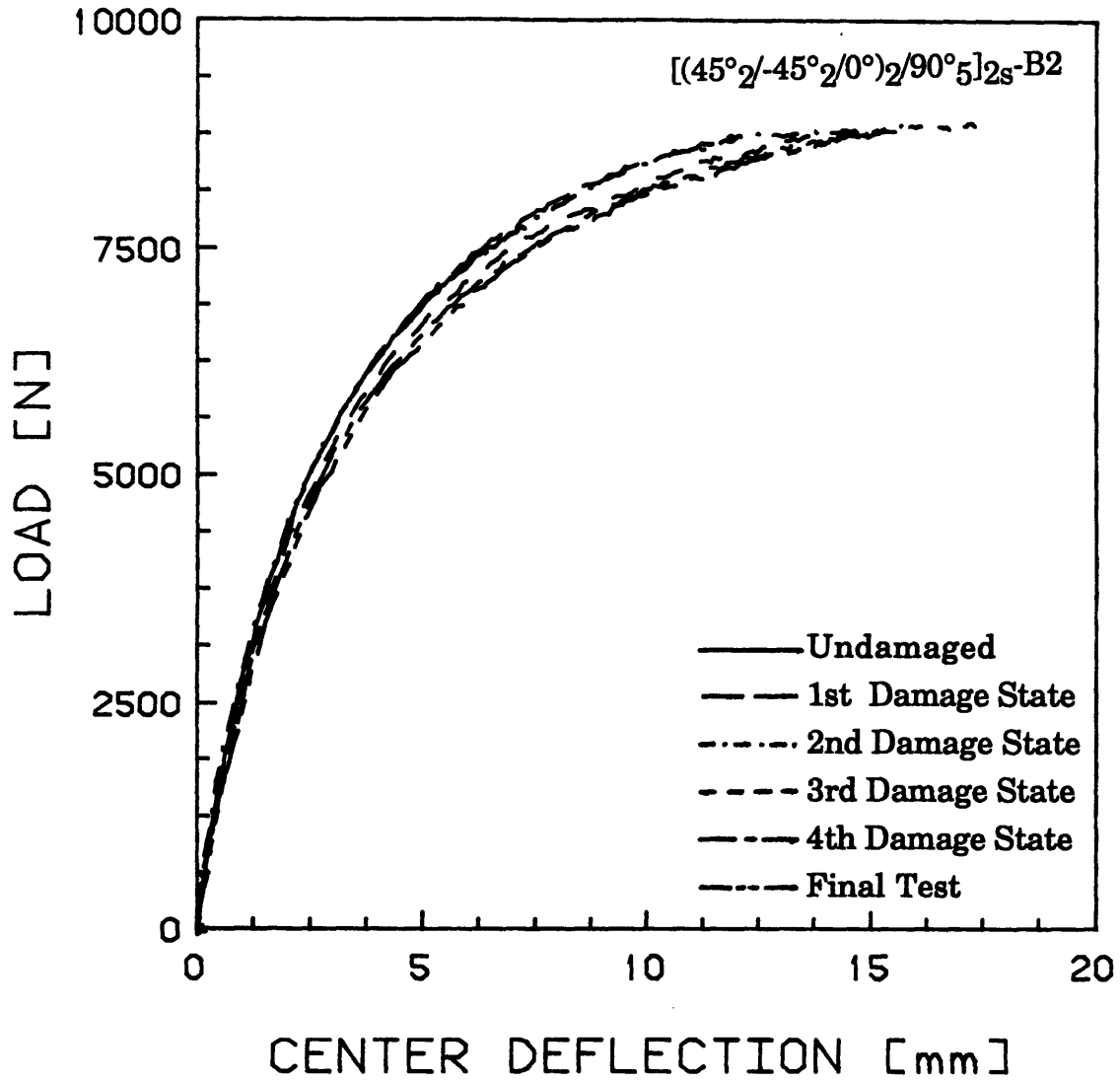


Figure 6.7 Load versus center deflection for a  $[(45^\circ_2/-45^\circ_2/0^\circ)_2/90^\circ_5]_{2s}$  specimen at each characteristic damage state.

**Table 6.4 Experimental Southwell buckling loads and center deflection at each characteristic damage state for a typical specimen of each layup.**

Layup	Damage State	Buckling Load [N]	Center Deflection [mm]
[45° <sub>4</sub> /-45° <sub>4</sub> /(0°/90°) <sub>4</sub> ] <sub>2s</sub>	Undamaged	15449	9.8
	1	14933	10.2
	2	14848	11.3
	3	14216	12.7
	4	14185	13.3
[±45°/0°/90° <sub>4</sub> ] <sub>4s</sub>	Undamaged	9510	8.7
	1	9141	11.5
	2	8957	12.7
	3	8985	14.3
	4	8754	19.6
[(45° <sub>2</sub> /-45° <sub>2</sub> /0°) <sub>2</sub> /90° <sub>5</sub> ] <sub>2s</sub>	Undamaged	11040	7.3
	1	10925	12.0
	2	10689	13.8
	3	10747	14.9
	4	10671	15.7

In many cases, the specimen flew out of the test jig at ultimate failure, making it particularly clear that the test was over, and lending a certain amount of excitement to the test procedure.

Detailed, ply-by-ply damage histories were pieced together from the edge replicas. These histories are described below for the three specimen types. Typical transcriptions of the edge replicas at each damage state are shown with some of the corresponding X-ray photographs and pictures of failed specimens in Figures 6.8 through 6.17. The transcriptions cover only half the length of the test section up to the centerline parallel to the z axis. They are drawn to scale along their length, but are magnified by a factor of approximately eight through the thickness. In all cases, damage occurred only on the tension side of the specimen. The center deflection at which each characteristic damage state was reached is shown on the figures depicting the replicas, as is the crack separation at crack density saturation. The X-ray photographs showed how damage tended to progress across the width of the specimen, and also how damage varied along the length. The replicas from the specimen on which destructive examinations had been carried out provided detailed data on the damage variation across the width.

In the  $[45^{\circ}_4/-45^{\circ}_4/(0^{\circ}/90^{\circ})_4]_{2s}$  specimen type, damage initiated in the form of matrix cracks in the outermost  $45^{\circ}$  effective ply on the tension side. The first characteristic damage state consisted of sporadic cracks in the outermost  $45^{\circ}$  and  $-45^{\circ}$  effective plies, covering the central 80 mm of the specimen. As can be seen in the X-ray photographs shown in Figures 6.8 (a) and 6.8 (b), the cracks started at the edges and propagated across the specimen. As is shown in the replica transcription in Figure 6.9 (1), these

cracks link up with discontinuous delaminations. In the second damage state, these discontinuous delaminations between the  $45^\circ$  and  $-45^\circ$  plies spread, as can be seen in Figure 6.9 (2). The third damage state was characterized by the  $45^\circ$  ply separating from the specimen in the central 50 mm of the specimen, as shown in Figure 6.9 (3). This was the first sign of damage which was visible to the naked eye. The crack density in the  $-45^\circ$  ply reached saturation in the fourth damage state, as can be seen in Figure 6.9 (4). Final failure occurred when the  $0^\circ$  plies on the tension side failed. A photograph of a failed specimen is shown in Figure 6.10. The half of the specimen through the thickness on the tension side is completely destroyed, while the half on the compression side is intact. Each of these characteristic damage states can be matched to one of the load versus center deflection plot in Figure 6.5. The damage states were reached at the end of the corresponding graphs.

First ply failure occurred in the outermost  $90^\circ$  effective ply on the tension side in the  $[\pm 45^\circ/0^\circ/90^\circ_4]_{4s}$  specimen type. The first damage state consisted of sporadic matrix cracks in the outermost  $90^\circ$  effective ply in the central 50 mm of the specimen, as can be seen in the X-ray photograph in Figure 6.11 (a). and the replica transcription in Figure 6.12 (1). The second state was reached when discontinuous delaminations appeared between the  $90^\circ$  and  $0^\circ$  plies. This can be seen in Figure 6.12 (2). At that time, the crack density in the  $90^\circ$  ply had reached 50 to 75% of saturation in the central 75 mm of the specimen, and 25 to 50% of saturation in the rest of the test section. This can be seen in the X-ray photograph in Figure 6.11 (b). In the third state, sporadic cracks appeared in the second  $90^\circ$  effective ply on the tension side, and crack density had reached saturation in the central 75 mm in the first  $90^\circ$  ply. This is shown in Figure 6.12 (3). The

delamination between the first 90° effective ply and the neighboring 0° ply became continuous in the fourth damage state, and crack density in the second 90° ply reached 25% of saturation, as can be seen in Figure 6.12 (4). In some specimens, discontinuous delaminations appeared between the second 90° and 0° plies, and cracks appeared in the third 90° effective ply prior to final failure, which occurred when the 0° plies on the tension side failed. As can be seen in the photograph of a failed specimen in Figure 6.13, the specimen is intact from the compression surface to the fourth 0° ply on the compression side. Thereafter, the specimen is completely destroyed. Each of these characteristic damage states can be matched to one of the load versus center deflection plot in Figure 6.6. The damage states were reached at the end of the corresponding graphs.

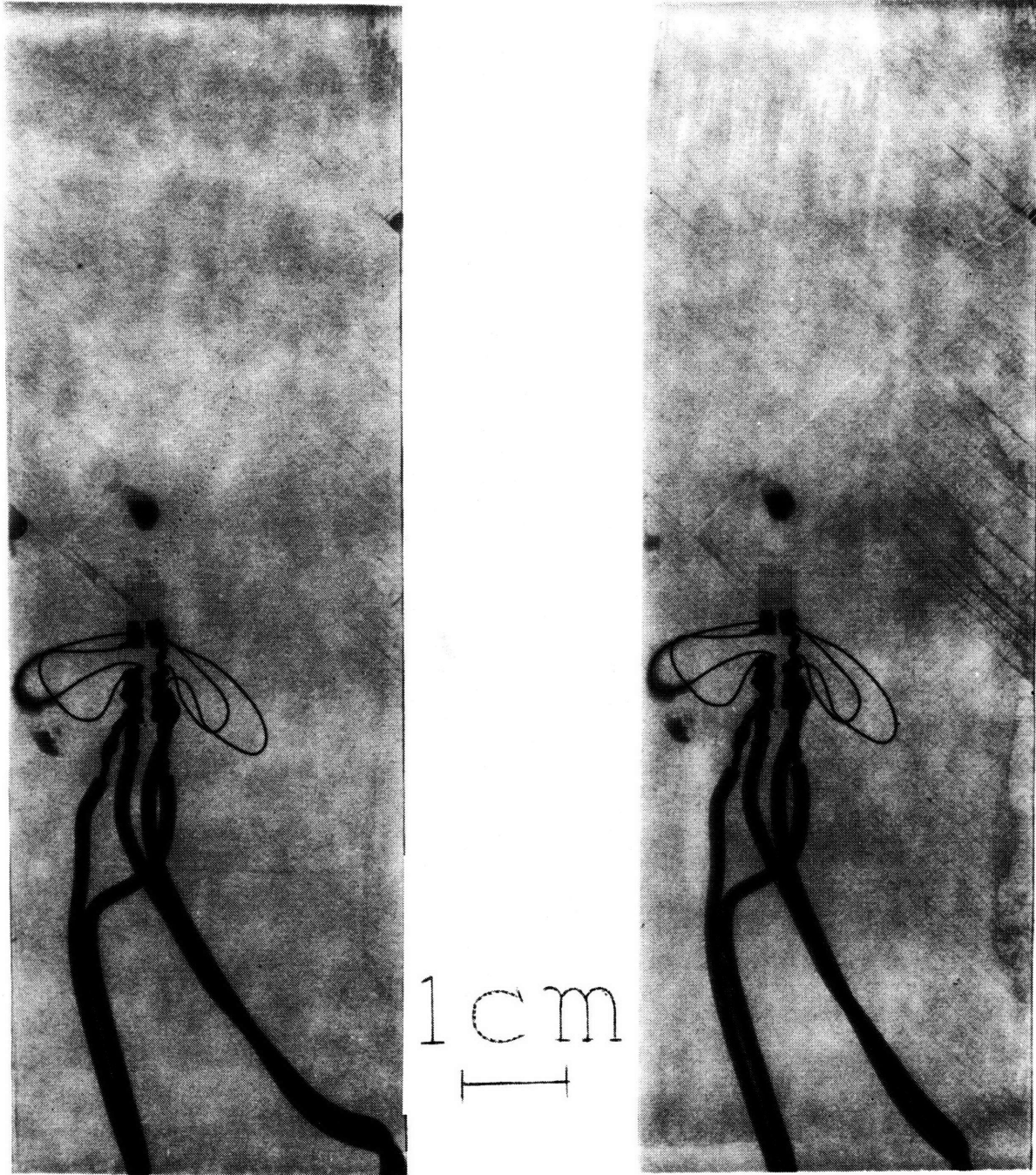
In the  $[(45^\circ_2/-45^\circ_2/0^\circ)_2/90^\circ_5]_{2s}$  laminates, first ply failure again occurred in the 90° effective ply on the tension side. The first characteristic damage state consisted of a crack density up to 25% of saturation in the central 50 mm of the specimen, as can be seen in the X-ray photograph in Figure 6.14 (a) and in the transcription in Figure 6.16 (1). The second state was reached when the crack density reached 75% of saturation in the central 75 mm of the specimen and 25 to 50% of saturation in the rest of the test section. This can be seen in the X-ray photograph in Figure 6.14 (b). Discontinuous delaminations appeared between the 90° effective ply and the 0° ply outside it, as can be seen in the transcription in Figure 6.16 (2). This delamination became continuous in the third damage state. Also, as is shown in the X-ray photograph in Figure 6.15 and the transcription in Figure 6.16 (3), the crack density reached saturation all along the test section. In the fourth state, discontinuous delaminations appeared between the 90° ply and the neighboring 45° ply. This is shown in Figure 6.16 (4).

Final failure occurred when the specimen split in half at the central 90° ply. It is presumed that a matrix crack appeared in the 90° ply, which caused a delamination, which in turn propagated to the ends of the specimen. A failed specimen is shown in Figure 6.17. The damage shown in the photograph consists of delaminations on both sides of the central 90° effective ply and on both sides of the 90° effective ply on the tension side, and matrix cracks in the same two 90° plies. Each of the characteristic damage states can be matched to one of the load versus center deflection plot in Figure 6.7. The damage states were reached at the end of the corresponding graphs.

### **6.1.3 Results of Destructive Examinations**

A narrow column specimen was chosen so that the problem could be reduced to two dimensions. It is important, therefore, that damage not vary significantly across the width. The greatest possible variation across the width is seen by comparing the damage at the edges of a specimen with that along its centerline. To find the extent of that variation, four specimens from each layup were loaded such that the damage matched the four characteristic damage states. After being tested, these specimens were cut in two along their length, and inner and outer edges were replicated. The comparison of inner and outer edge replicas are discussed below.

In general, crack density varied little across the width, except in the first characteristic damage state of the  $[45^{\circ}_4/-45^{\circ}_4/(0^{\circ}/90^{\circ})_4]_{2s}$  specimen type, where there were slightly more cracks at the edges than in the middle of the 45° ply, and in the third and fourth damage states of the  $[45^{\circ}_4/-45^{\circ}_4/(0^{\circ}/90^{\circ})_4]_{2s}$  and  $[\pm 45^{\circ}/0^{\circ}/90^{\circ}_4]_{4s}$  specimen types, where there



(a)

(b)

Figure 6.8 X-ray photographs of a  $[45^{\circ}_4/-45^{\circ}_4/(0^{\circ}/90^{\circ})_4]_{2s}$  specimen at (a) the first and (b) the second characteristic damage states.

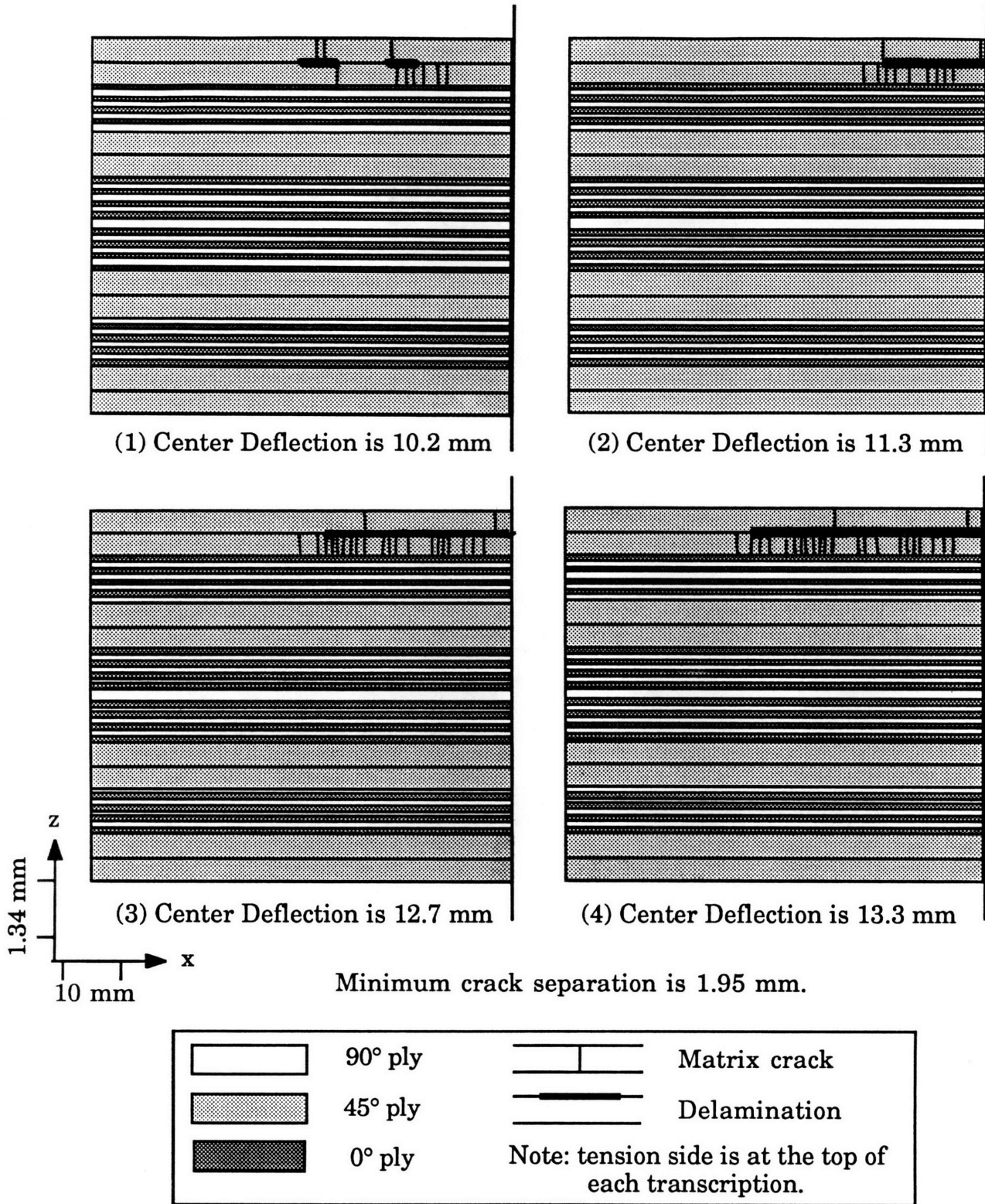


Figure 6.9 Illustrations of the four characteristic damage states of the  $[45^{\circ}_4/45^{\circ}_4/(0^{\circ}/90^{\circ})_4]_{2S}$  layup.

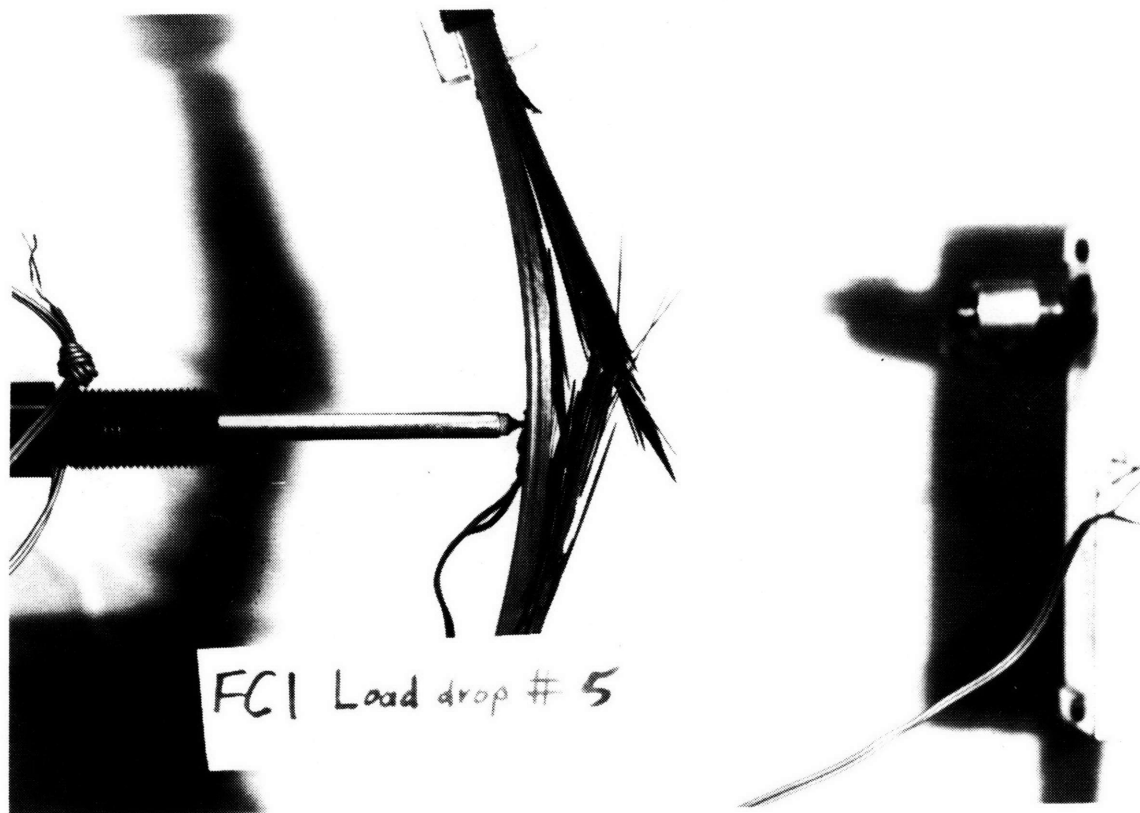


Figure 6.10 Photograph of a  $[45^{\circ}_4/-45^{\circ}_4/(0^{\circ}/90^{\circ})_4]_{2s}$  specimen after failure.

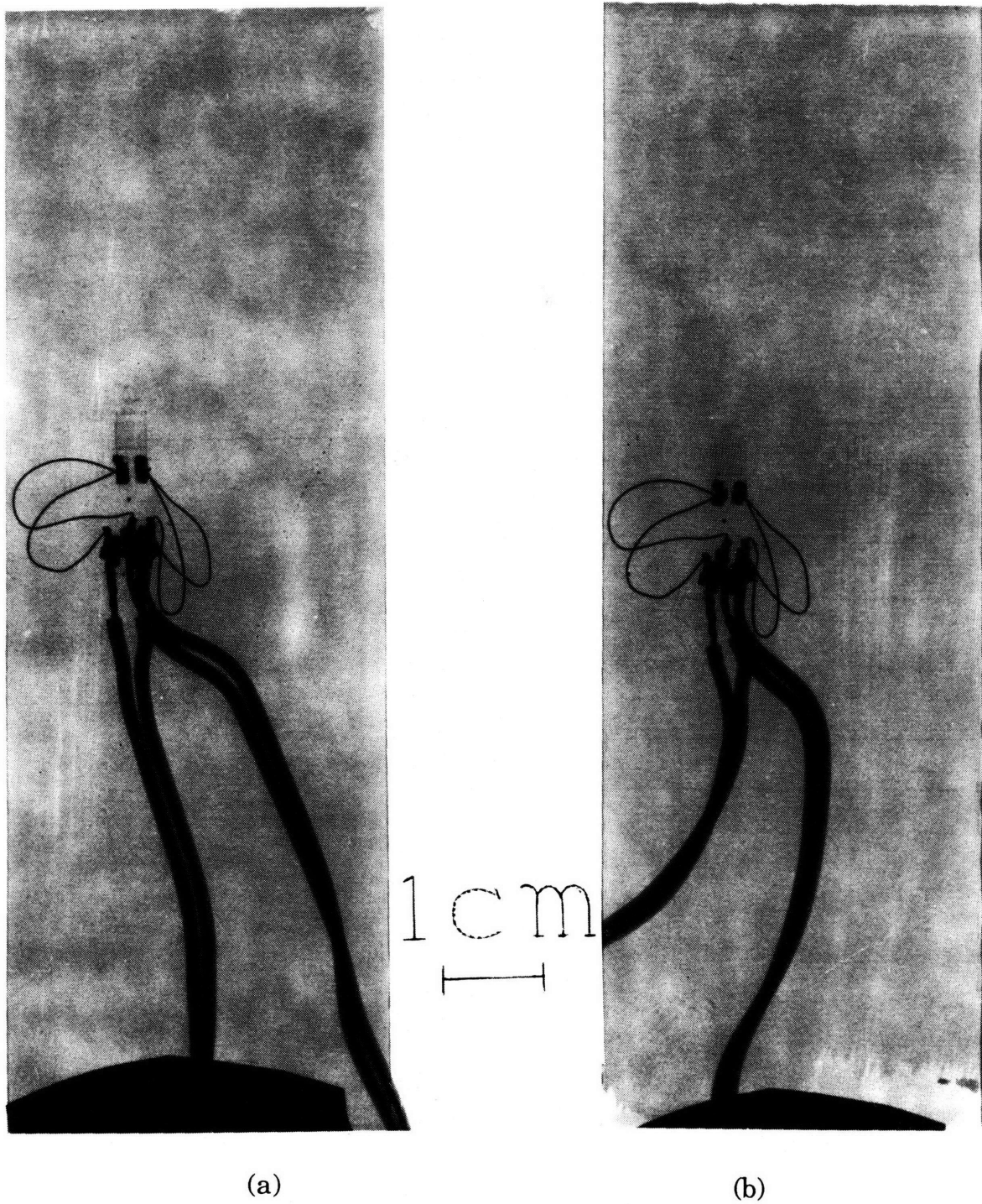


Figure 6.11 X-ray photographs of an  $[\pm 45^\circ/0^\circ/90^\circ_4]_{4s}$  specimen at (a) the first and (b) the second damage states.

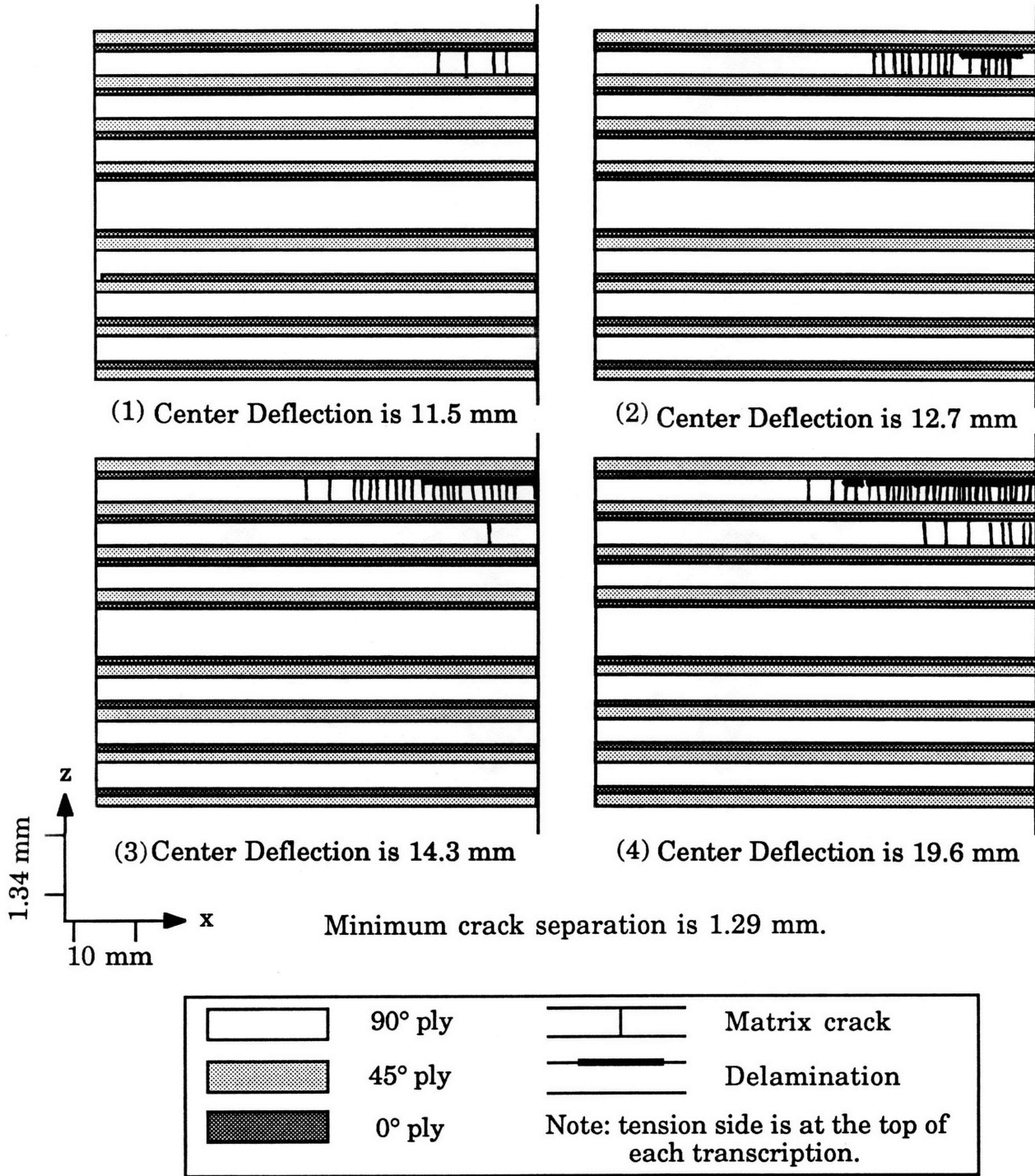


Figure 6.12 Illustrations of the four characteristic damage states of the  $[\pm 45^\circ/0^\circ/90^\circ_4]_{4s}$  layup.

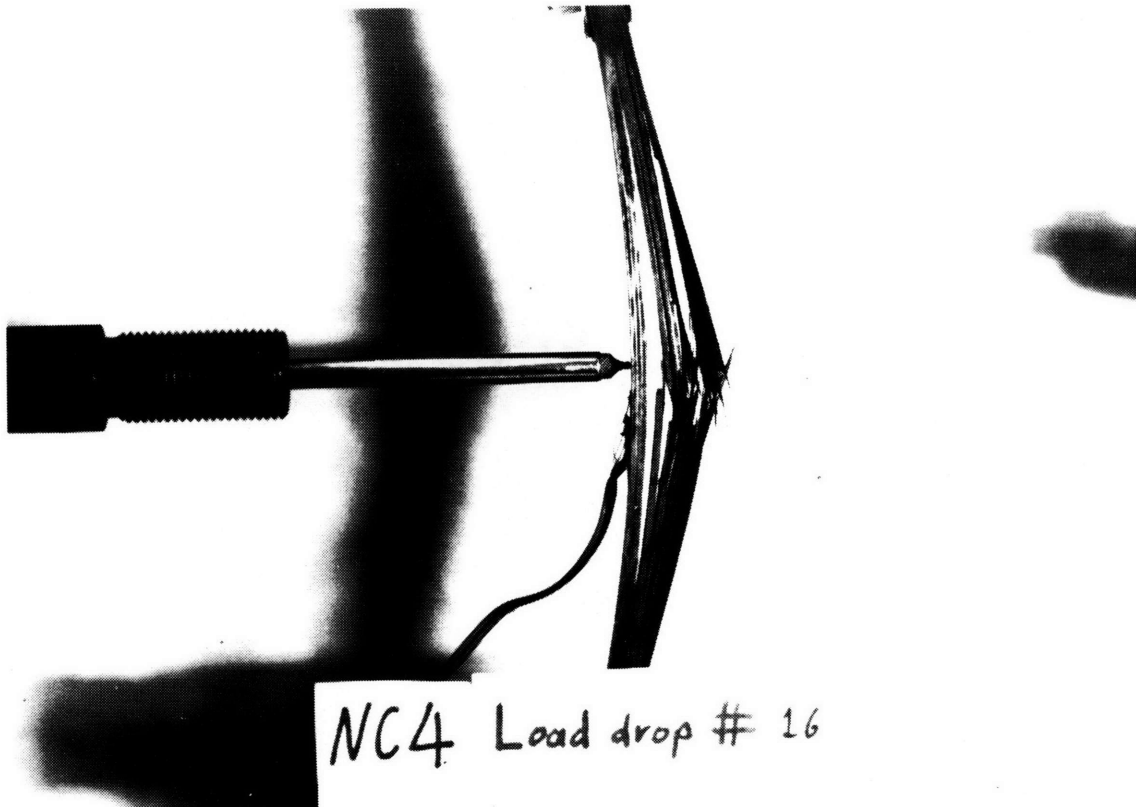


Figure 6.13 Photograph of a  $[\pm 45^\circ/0^\circ/90^\circ]_4$  specimen after failure.

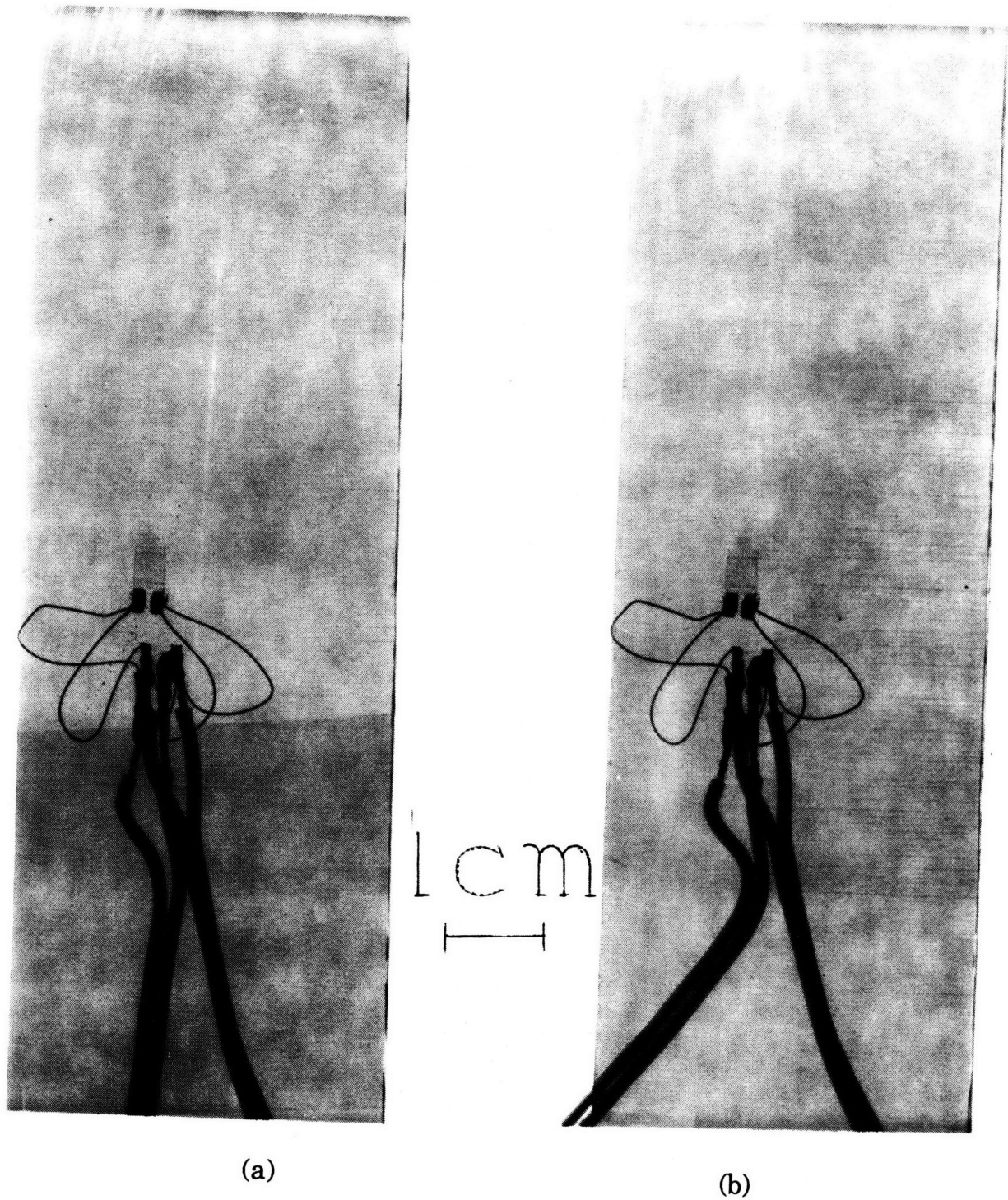


Figure 6.14 X-ray photographs of an  $[(45^\circ_2/-45^\circ_2/0^\circ)_2/90^\circ_5]_{2s}$  specimen at (a) the first and (b) the second damage state.

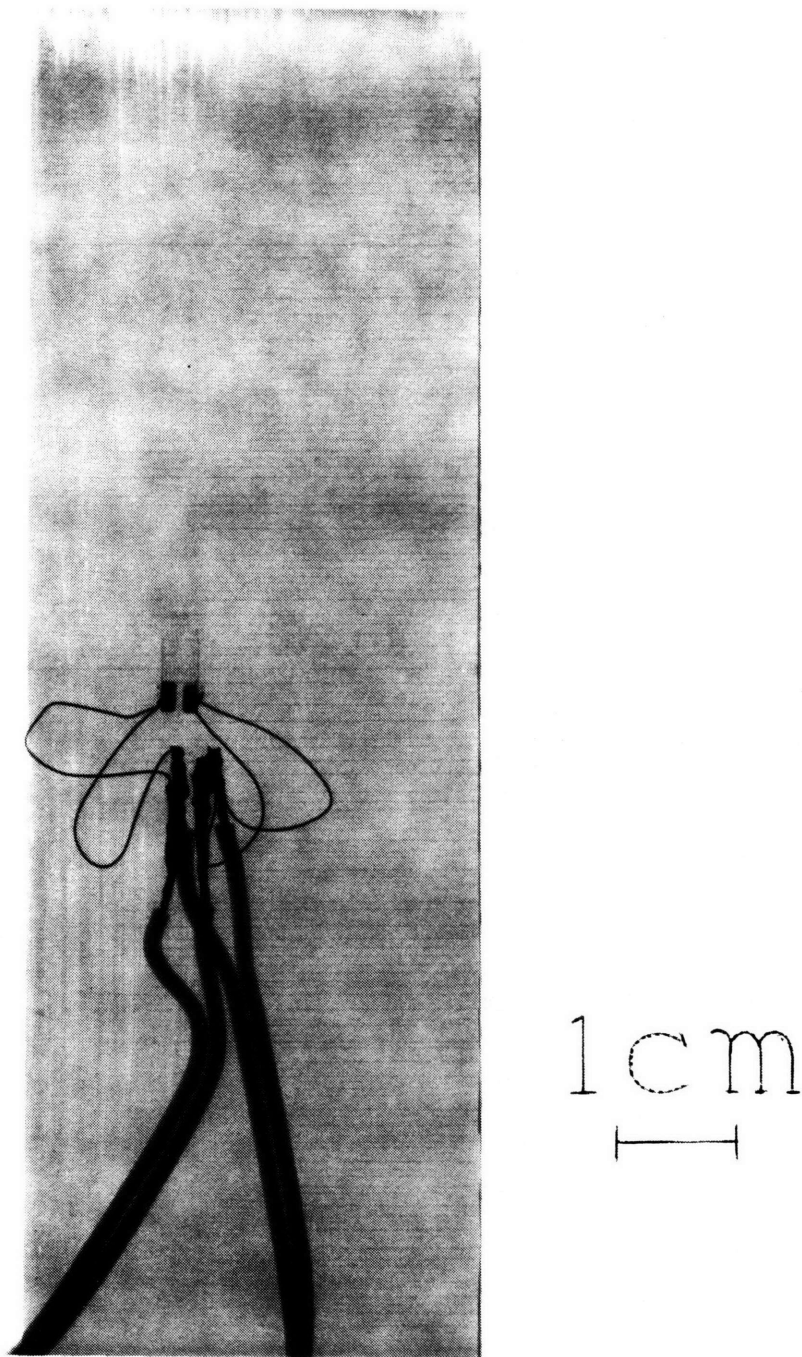


Figure 6.15 X-ray photograph of an  $[(45^\circ_2/-45^\circ_2/0^\circ)_2/90^\circ_5]_{2s}$  specimen at the third characteristic damage state.

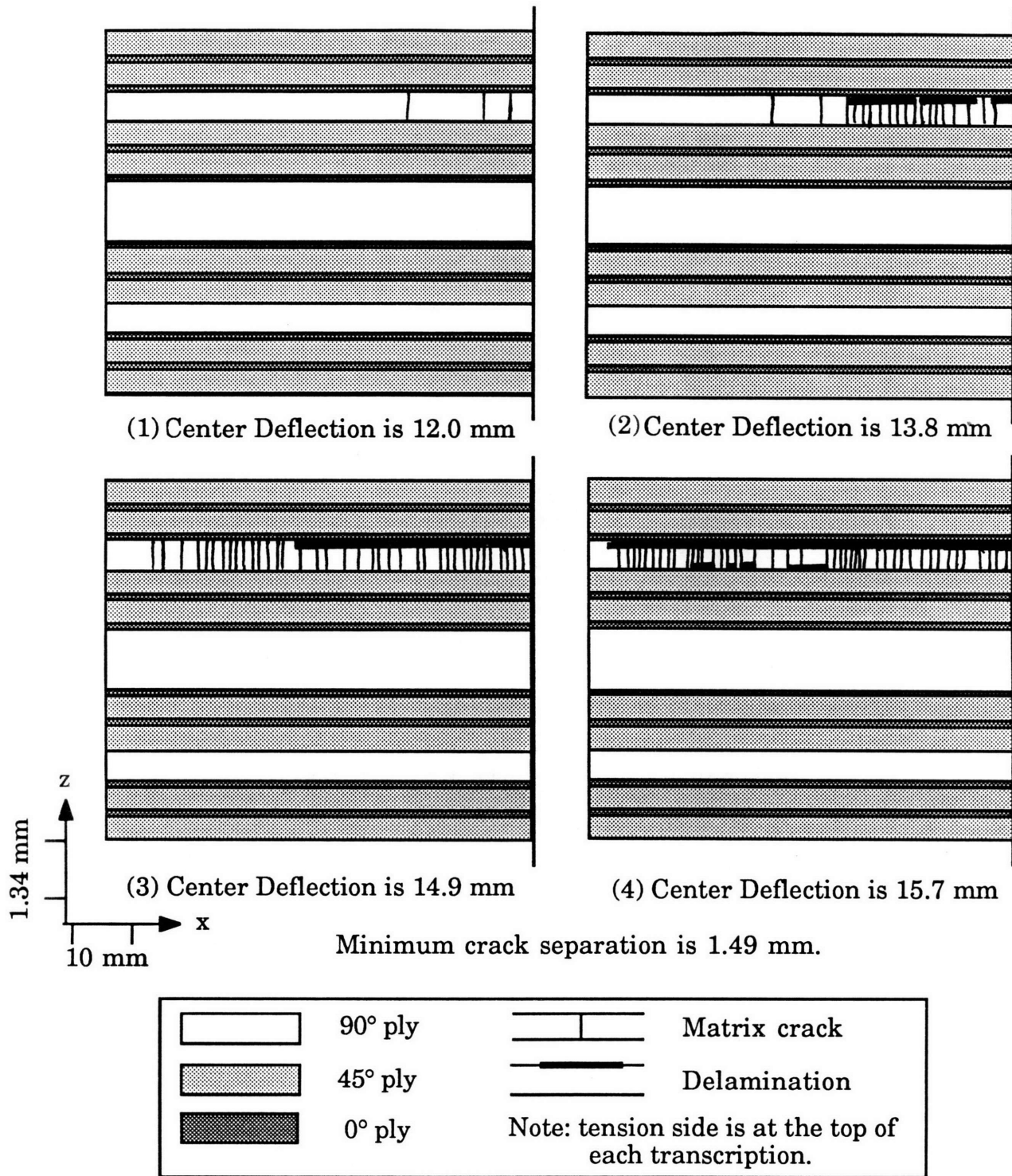


Figure 6.16 Illustrations of the four characteristic damage states of the  $[(45^\circ_2/-45^\circ_2/0^\circ)_2/90^\circ_5]_{2s}$  layup.



Figure 6.17 Photograph of a  $[(45^\circ_2/-45^\circ_2/0^\circ)_2/90^\circ_5]_{2s}$  specimen after failure.

were more cracks in the middle than at the edges in the second set of  $\pm 45^\circ$  plies and  $90^\circ$  plies, respectively. There was, in general, less delamination in the middle of the specimens than at the edges. Transcriptions of the edge replicas from these tests are shown in Figures 6.18 through 6.24. These figures represent the greatest variation seen across the width in all three layups. A complete set of figures comparing edge replicas of inner and outer edges for all four characteristic damage states for the three layups is included in Appendix B. In each figure, the transcriptions of the left, center and right edges are shown. As before, the transcriptions cover only half the length of the test section up to the centerline parallel to the z axis. They are drawn to scale along their length, but are magnified by a factor of approximately eight through the thickness. In all cases, damage occurred only on the tension side of the specimen.

The first damage state of the  $[45^\circ_4/-45^\circ_4/(0^\circ/90^\circ)_4]_{2s}$  specimen type is shown in Figure 6.18. As stated above, there is slightly more cracking at the edges than in the center, particularly in the  $-45^\circ$  effective ply. This may be due to the fact that a crack in a  $45^\circ$  ply covers a significant length of the specimen, over which the stress state can vary significantly. As a result, the cracks do not immediately propagate from edge to edge. By the second damage state, the damage has become uniform across the width, as can be seen in Figure 6.19. The fourth damage state is shown in Figure 6.20; damage in the outermost  $\pm 45^\circ$  effective plies is fairly uniform, given the extent of the damage. However, the second  $45^\circ$  effective ply contains significantly more cracks at the inner edge than at the outer edges, and the second  $-45^\circ$  effective ply has damage only at the inner edge. The reason for this is not clear.

In the  $[\pm 45^\circ/0^\circ/90^\circ_4]_{4s}$  specimen type, some differences in damage across the width appear in the last two damage states. The third damage state is shown in Figure 6.21. There is slightly less delamination between the first  $90^\circ$  effective ply and the first  $0^\circ$  ply, and there are slightly more cracks in the second  $90^\circ$  effective ply at the center of the specimen than at the edge. In the fourth damage state, which is shown in Figure 6.22, the crack density is fairly uniform across the width in the two outermost  $90^\circ$  effective plies, but there is significantly more delamination at the edges than in the center. The extent of the delaminations at the edges can probably be attributed to the three-dimensional state of stress which exists at the edge of the specimen. This stress state exists because the stress-free boundary results in a discontinuity in transverse stresses, and is important only in a boundary layer a few millimeters wide.

In the  $[(45^\circ_2/-45^\circ_2/0^\circ)_2/90^\circ_5]_{2s}$  specimens, crack density is uniform across the width throughout the tests, but again there is less delamination in the center than at the edges in the later damage states. In Figure 6.23, the third damage state is shown. There is slightly less delamination between the outer  $90^\circ$  effective ply and the neighboring  $0^\circ$  ply in the center. In the fourth damage state, shown in Figure 6.24, this difference is more marked, and discontinuous delaminations between the outer  $90^\circ$  effective ply and the  $45^\circ$  effective ply exist only at one of the edges. Again, these differences are probably due to edge effects.

There is some variation in damage across the width in all three layups, particularly in the form of delamination damage in the specimens where matrix cracks occur in  $90^\circ$  plies. However, these variations are minor and, for modelling purposes, can probably be ignored.

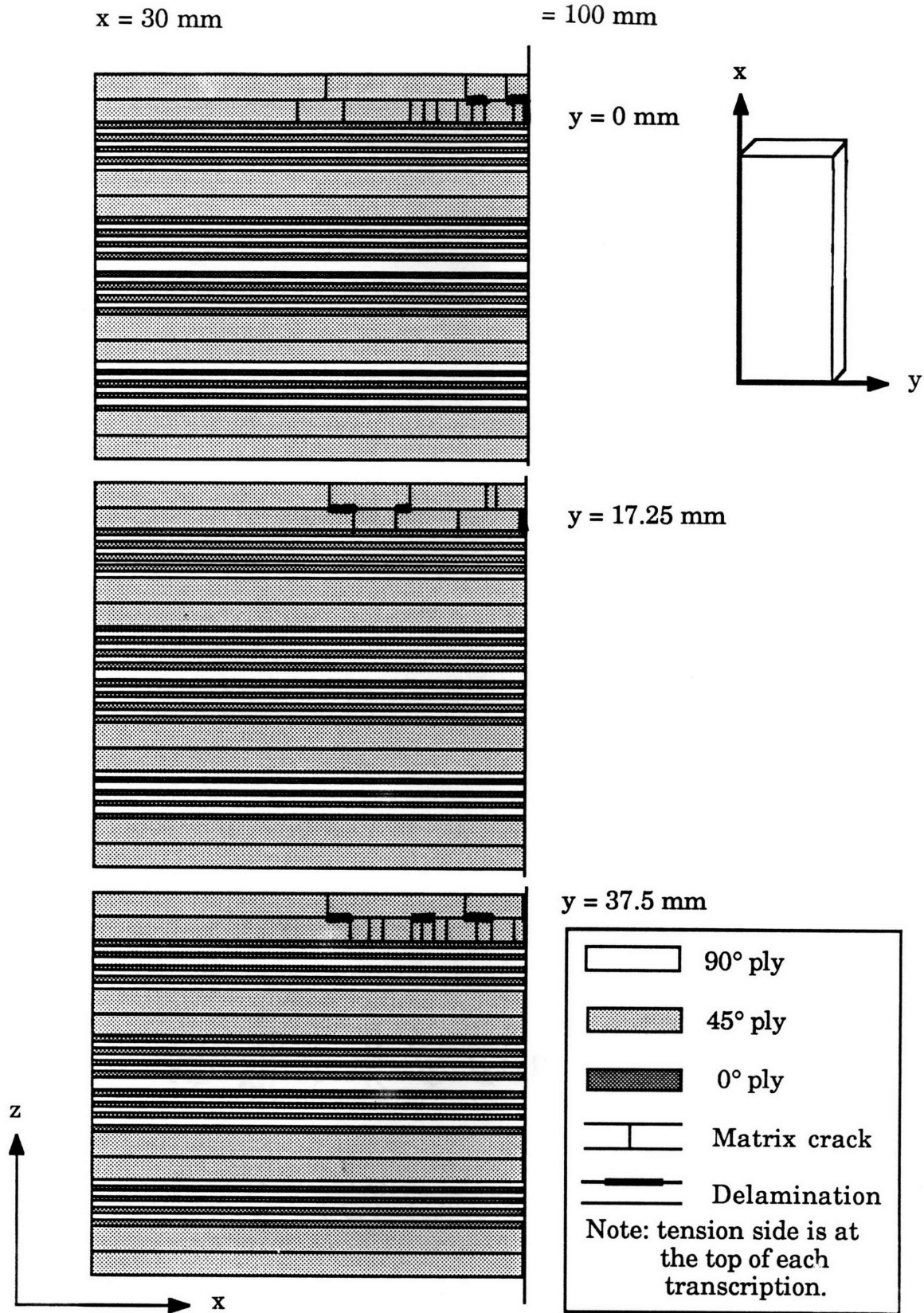


Figure 6.18 Comparison of damage across width at the first characteristic damage state of the  $[45^\circ_4/-45^\circ_4/(0^\circ/90^\circ)_4]_{2s}$  layup.

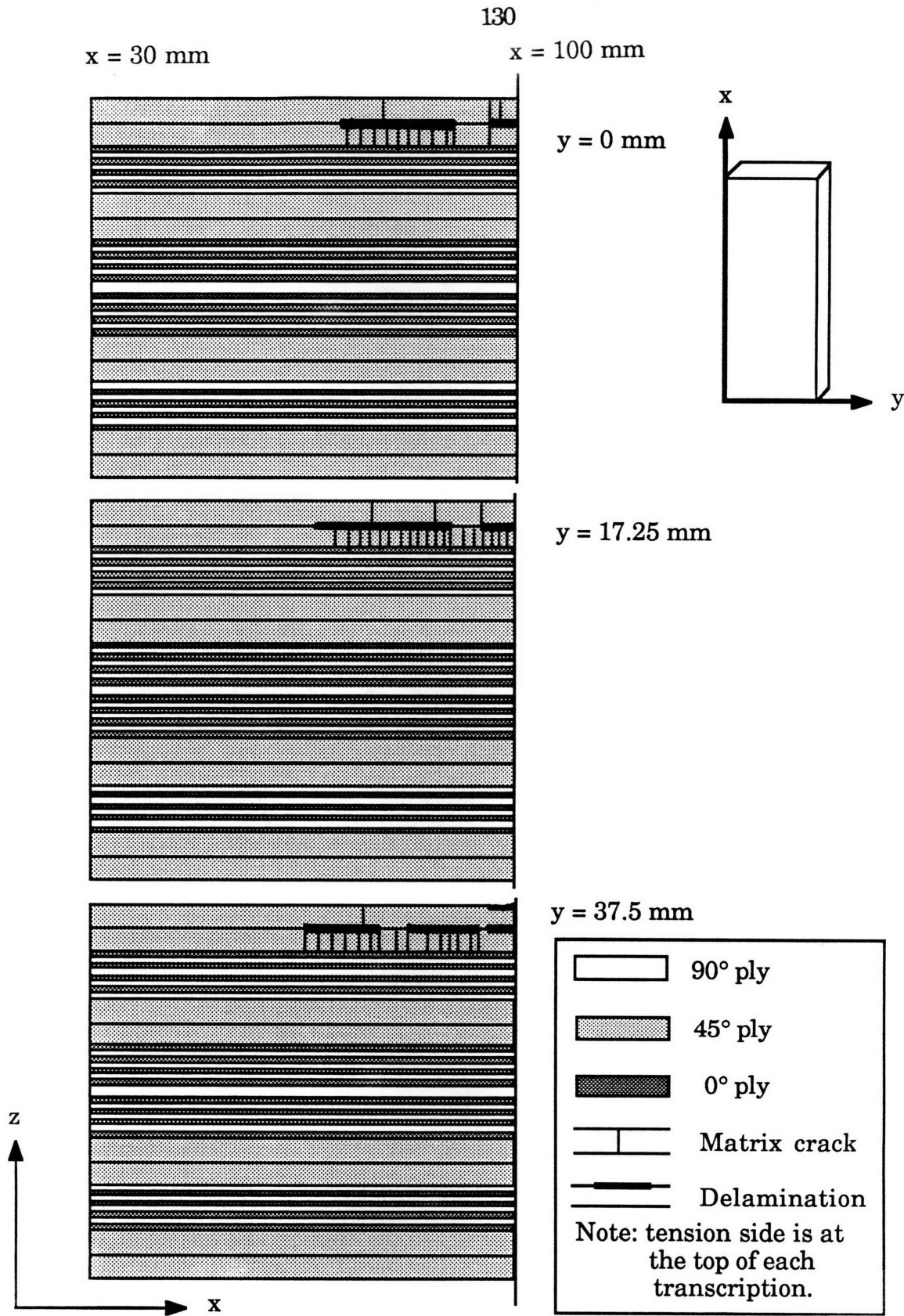


Figure 6.19 Comparison of damage across width at the second characteristic damage state of the  $[45^\circ_4/-45^\circ_4/(0^\circ/90^\circ)_4]_{2s}$  layup.

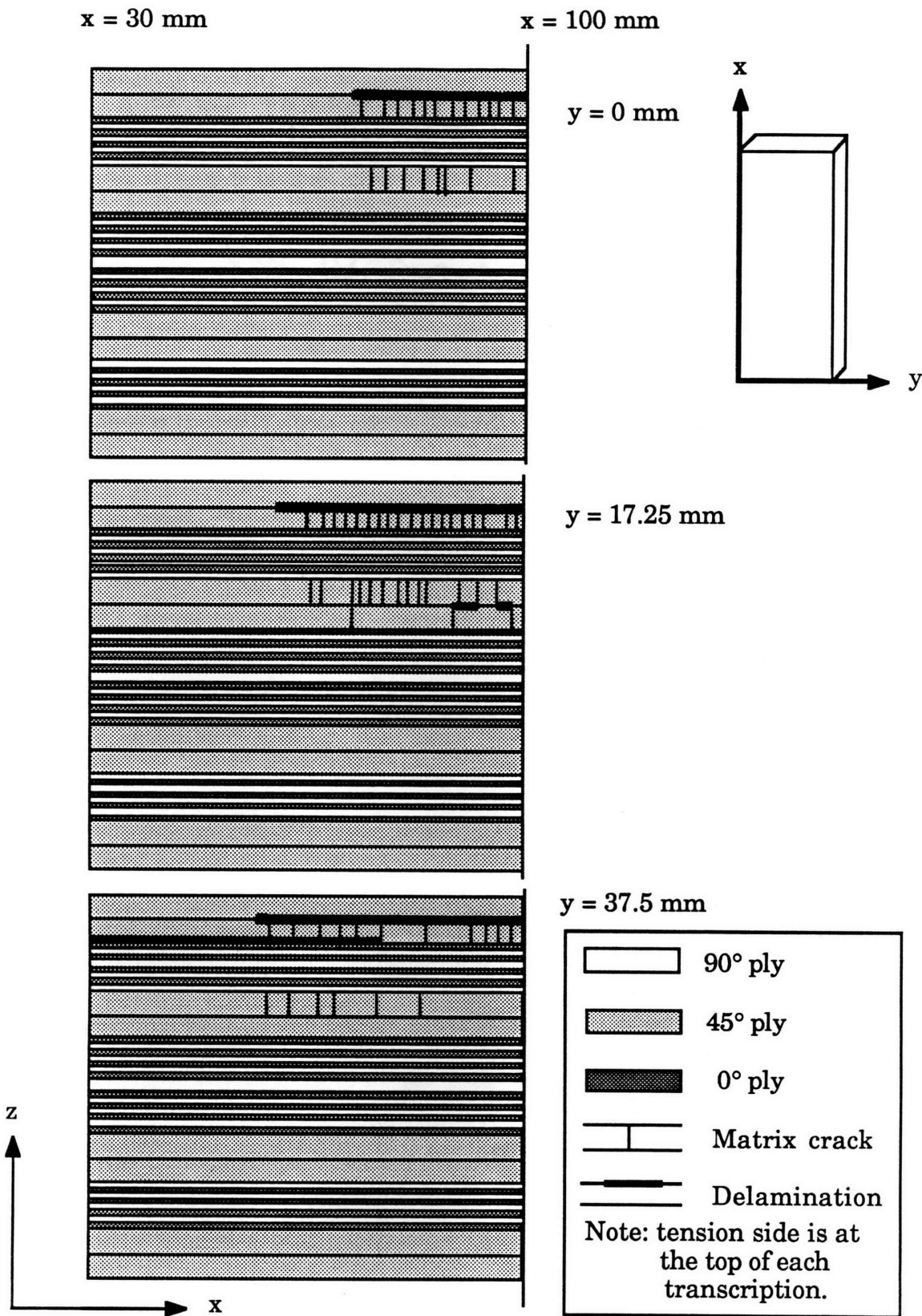


Figure 6.20 Comparison of damage across width at the fourth characteristic damage state of the  $[45^\circ_4/-45^\circ_4/(0^\circ/90^\circ)_4]_{2s}$  layup.

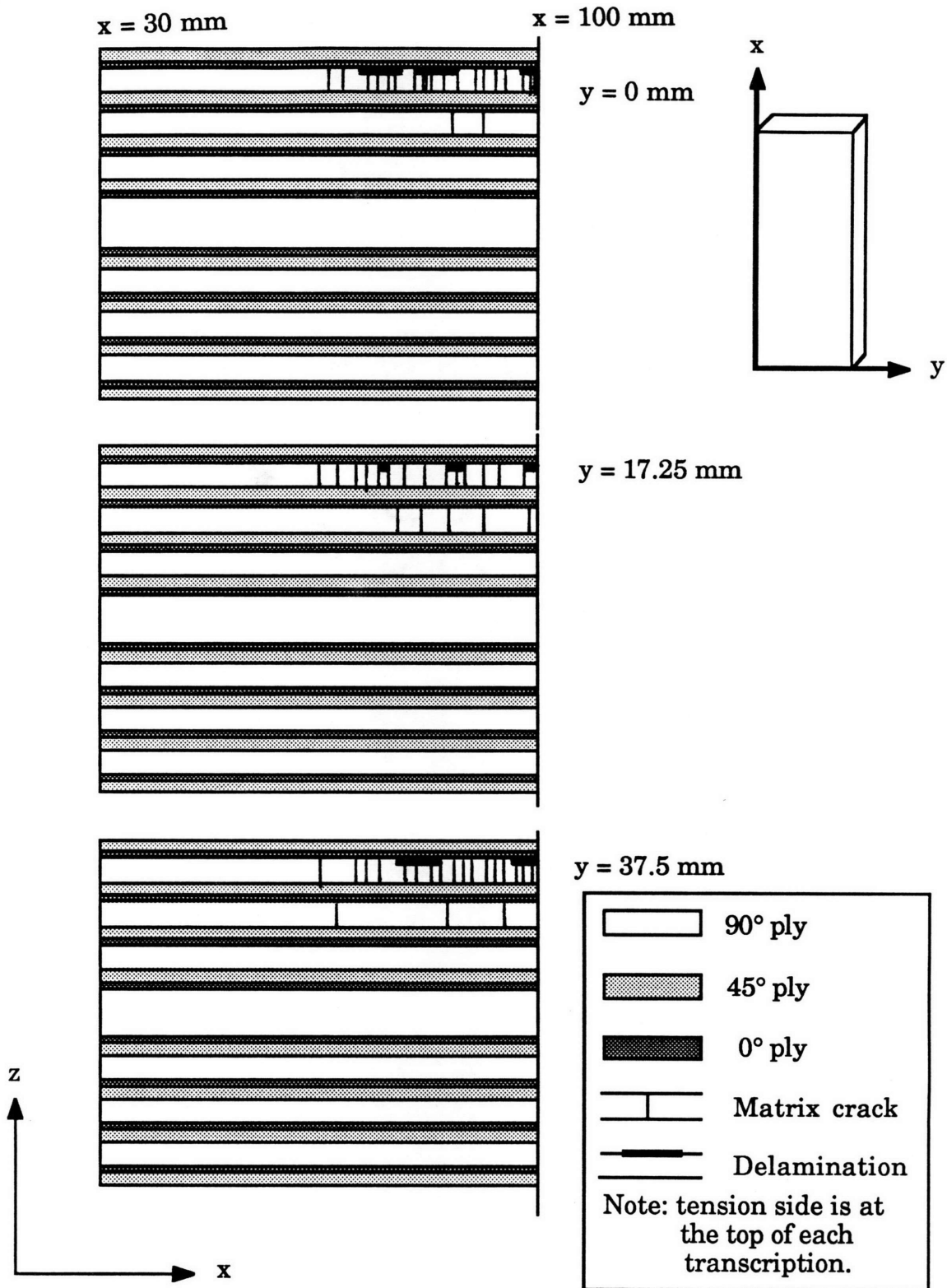


Figure 6.21 Comparison of damage across width at the third characteristic damage state of the  $[\pm 45^\circ/0^\circ/90^\circ]_4s$  layup.

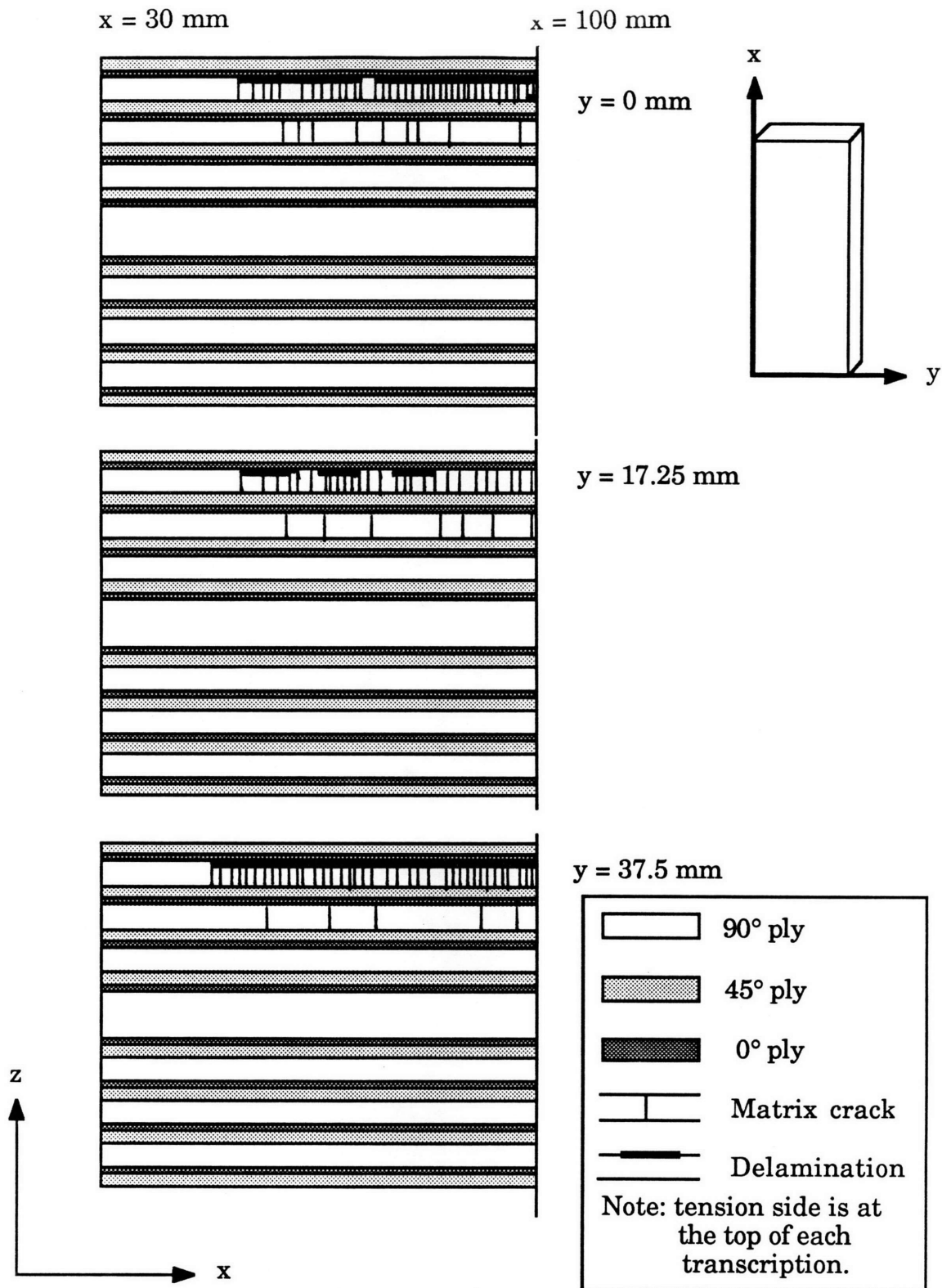


Figure 6.22 Comparison of damage across width at the fourth characteristic damage state of the  $[\pm 45^\circ/0^\circ/90^\circ_4]_{4s}$  layup.

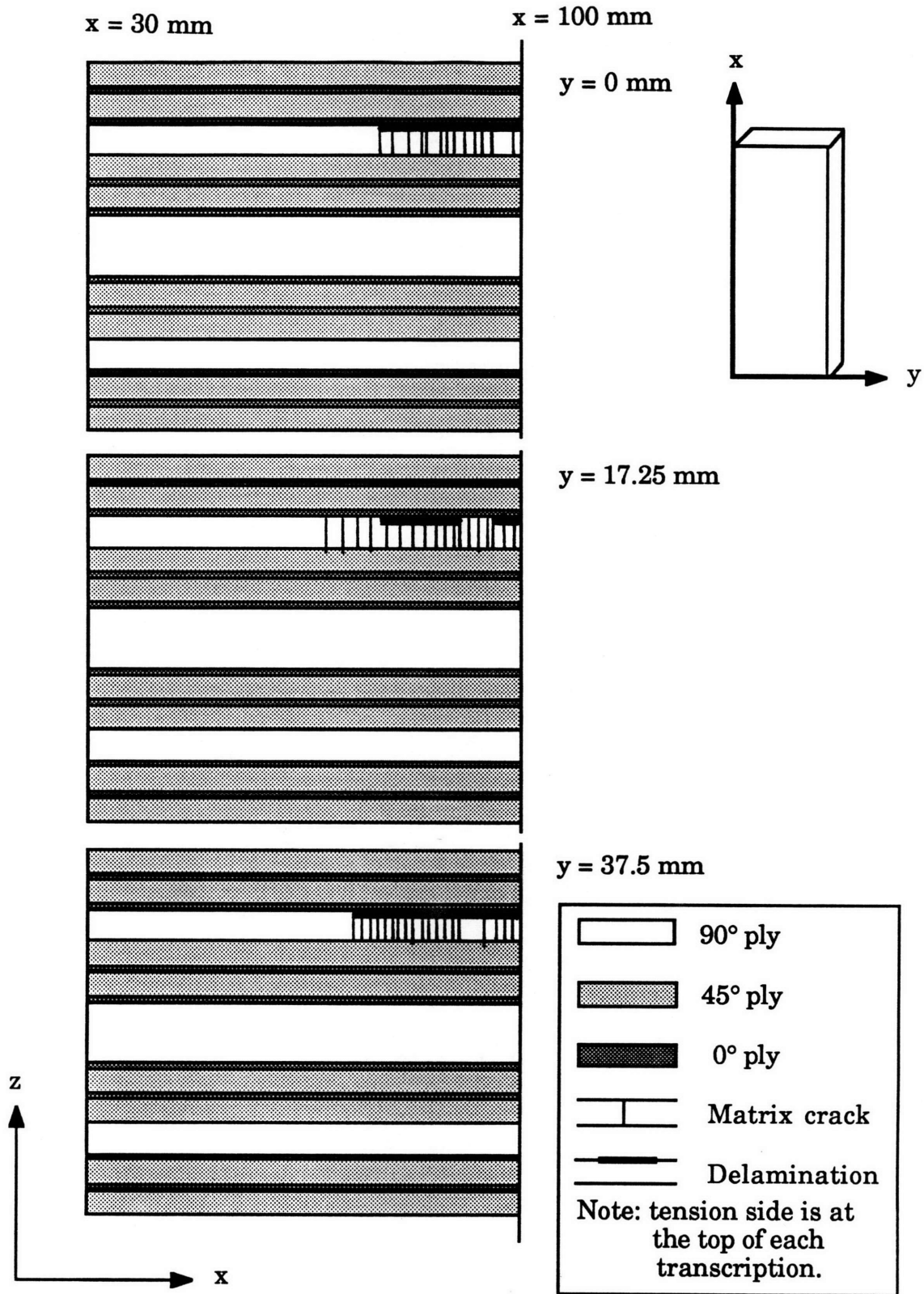


Figure 6.23 Comparison of damage across width at the third characteristic damage state of the  $[(45^\circ_2/-45^\circ_2/0^\circ)_2/90^\circ_5]_{2s}$  layup.

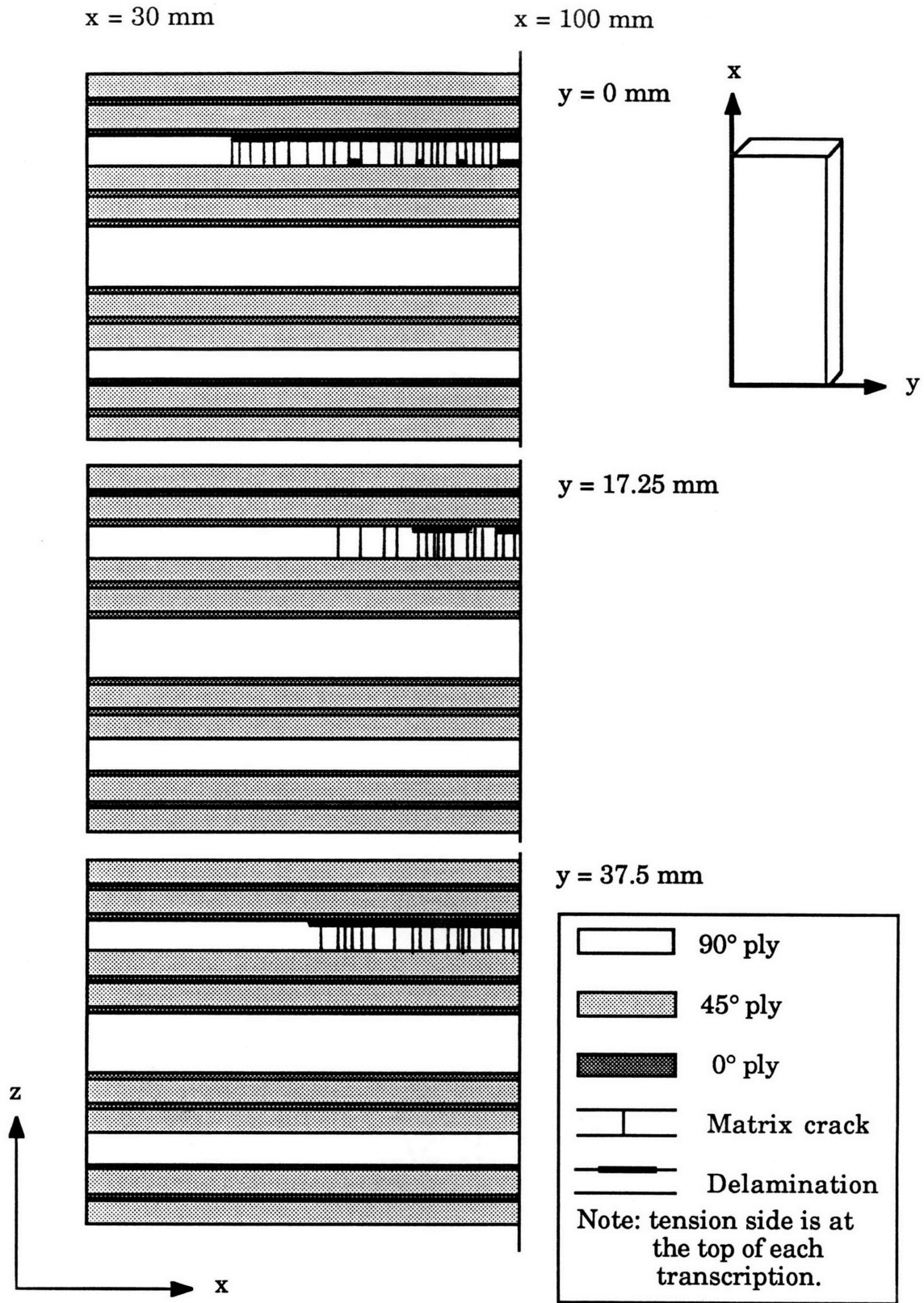


Figure 6.24 Comparison of damage across width at the fourth characteristic damage state of the  $[(45^\circ_2/-45^\circ_2/0^\circ)_2/90^\circ_5]_{2s}$  layup.

## **6.2 Comparison of Model and Experimental Results**

### **6.2.1 Selection of a Characteristic Specimen**

For each of the three specimen types, the thickness of one specific specimen was used in the corresponding model. Model results were compared only with the data from those specimens. This was done because, though trends in damage accumulation for a given specimen type are easily discerned, variations exist from specimen to specimen. Quantitatively averaging damage states in a meaningful manner would be difficult.

For each specimen type, a characteristic specimen was chosen with this reasons in mind. All four characteristic damage states were clearly defined. In addition, the chosen specimen had a thickness which was near the middle of the range of thicknesses for the specimen type, and exhibited a bending stiffness which was also near the middle of the range.

### **6.2.2 Load versus Deflection Prior to Damage**

Load versus center deflection and load versus compressive strain plots are shown in Figures 6.25 to 6.30. In each figure, two versions of model results are shown up to the initiation of damage along with the experimental results . The first version takes the nonlinearity of the 45° ply stiffness properties into account, as described in section 4.2, while the second does not. These plots show the performance of the models in predicting the behavior of the undamaged specimens. As can be seen in the plots, agreement is excellent for all three layups in the region where 45° ply

stiffness is treated as linear. In the region where the nonlinear behavior becomes important, the agreement is less good.

The experimental Southwell buckling loads for a typical specimen from the three layups are compared to the results of the model which took material nonlinearities into account in Table 6.5. The Southwell Buckling Loads of the models are all 5 to 10% lower than the corresponding experimental values. This is due to the fact that, at strain levels where material nonlinearities are important, the model exhibits a lower bending stiffness. This is discussed in more detail in the next section. The Euler buckling load was also calculated for each of the three layups using the reduced bending stiffness. The Southwell buckling loads are 82% to 88% of the Euler buckling loads, which are also shown in Table 6.5.

### **6.2.3 Material Nonlinearities**

In the region where the nonlinear stiffness properties of the 45° plies are important, the models which take material nonlinearities into account tend to exhibit a slightly lower flexural stiffness than was observed experimentally, as can be seen in Figures 6.25 to 6.30. This is also reflected in a comparison of the Southwell Buckling Loads. While disagreement between the two models of the  $[\pm 45^\circ/0^\circ/90^\circ_4]_{4s}$  layup and the experimental results are insignificant, the differences in the two models for the  $[45^\circ_4/-45^\circ_4/(0^\circ/90^\circ)_4]_{2s}$  and  $[(45^\circ_2/-45^\circ_2/0^\circ)_2/90^\circ_5]_{2s}$  layups and their corresponding experimental results are more important. The model which takes material nonlinearities into account is significantly less stiff than the specimen just prior to the onset of damage, while the other model is much stiffer than the specimen. This can be attributed to the proportion of 45°

**Table 6.5 Euler buckling loads, and experimental and predicted Southwell buckling loads, maximum loads and damage initiation loads.**

All loads in Newtons

Specimen	Euler Buckling Load	Southwell Buckling Load	Max. Load	In-Plane Damage Initiation	Delam. Damage Initiation
$[45^{\circ}_4/-45^{\circ}_4/(0^{\circ}/90^{\circ})_4]_{2s}$ -A4	17519	15449	11298	11370	11370
Model Results		13923	11419	11419	11419
$[\pm 45^{\circ}/0^{\circ}/90^{\circ}]_4]_{4s}$ -C2	10953	9510	7584	7215	7322
Model Results		9008	7006	6943	6843
$[(45^{\circ}_2/-45^{\circ}_2/0^{\circ})_2/90^{\circ}_5]_{2s}$ -B2	13476	11040	8954	8759	8821
Model Results		10609	8498	8491	8491

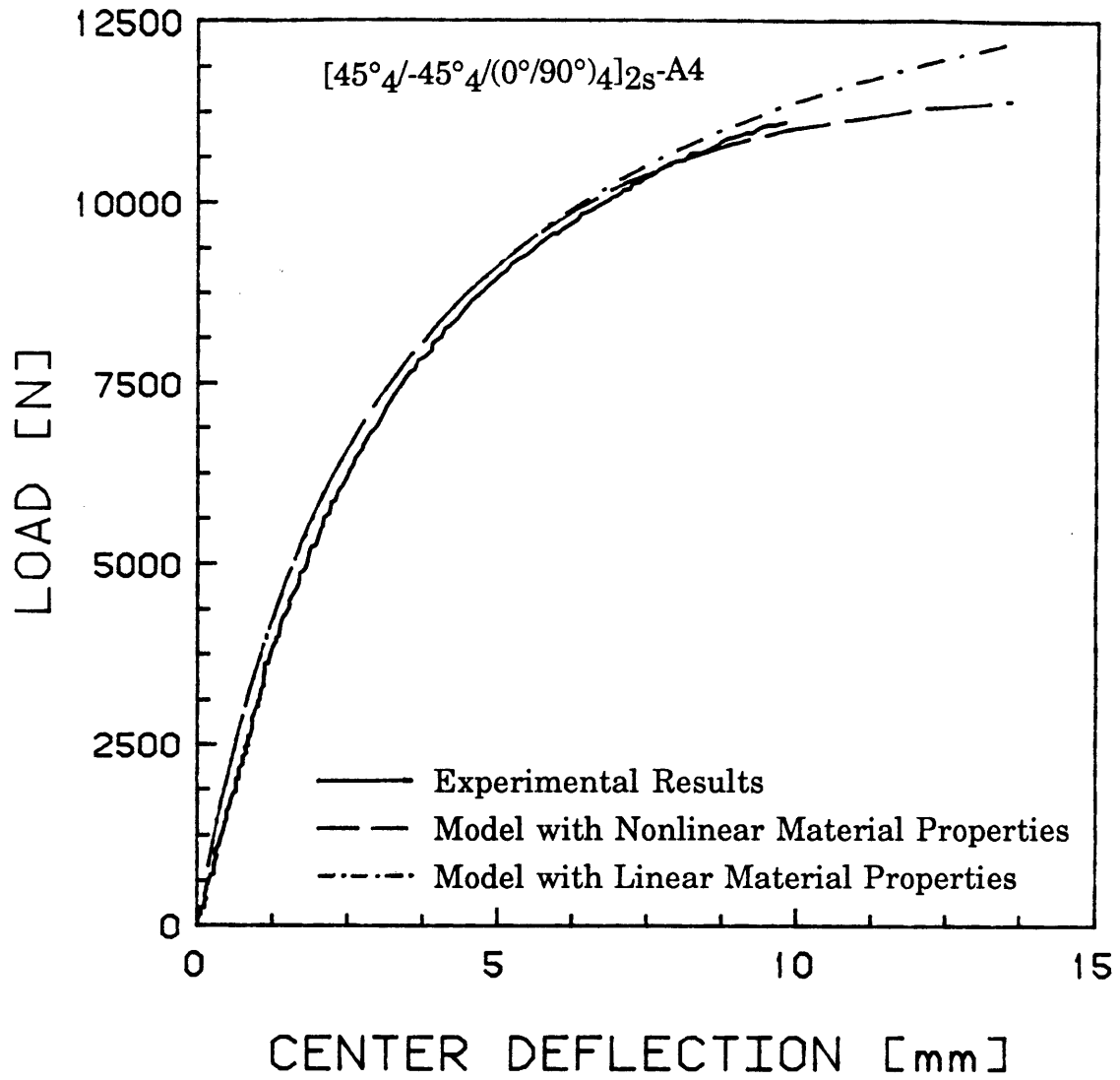


Figure 6.25 Experimental and predicted load versus center deflection for the  $[45^{\circ}_4/-45^{\circ}_4/(0^{\circ}/90^{\circ})_4]_{2s}$  layup prior to damage.

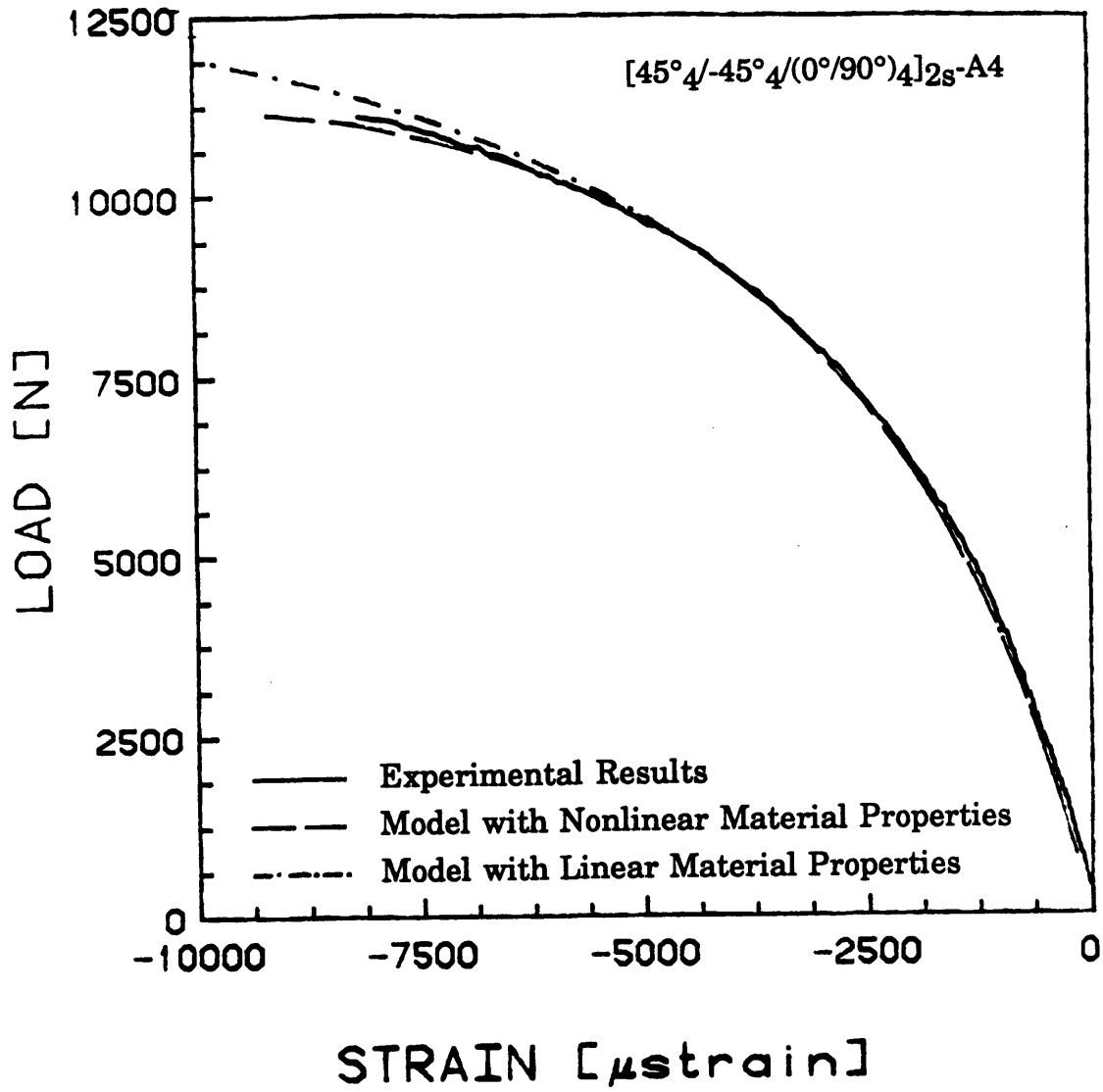


Figure 6.26 Experimental and predicted load versus centerline strain on the compression side for the [45°<sub>4</sub>/-45°<sub>4</sub>/(0°/90°)<sub>4</sub>]<sub>2s</sub> layup prior to damage.

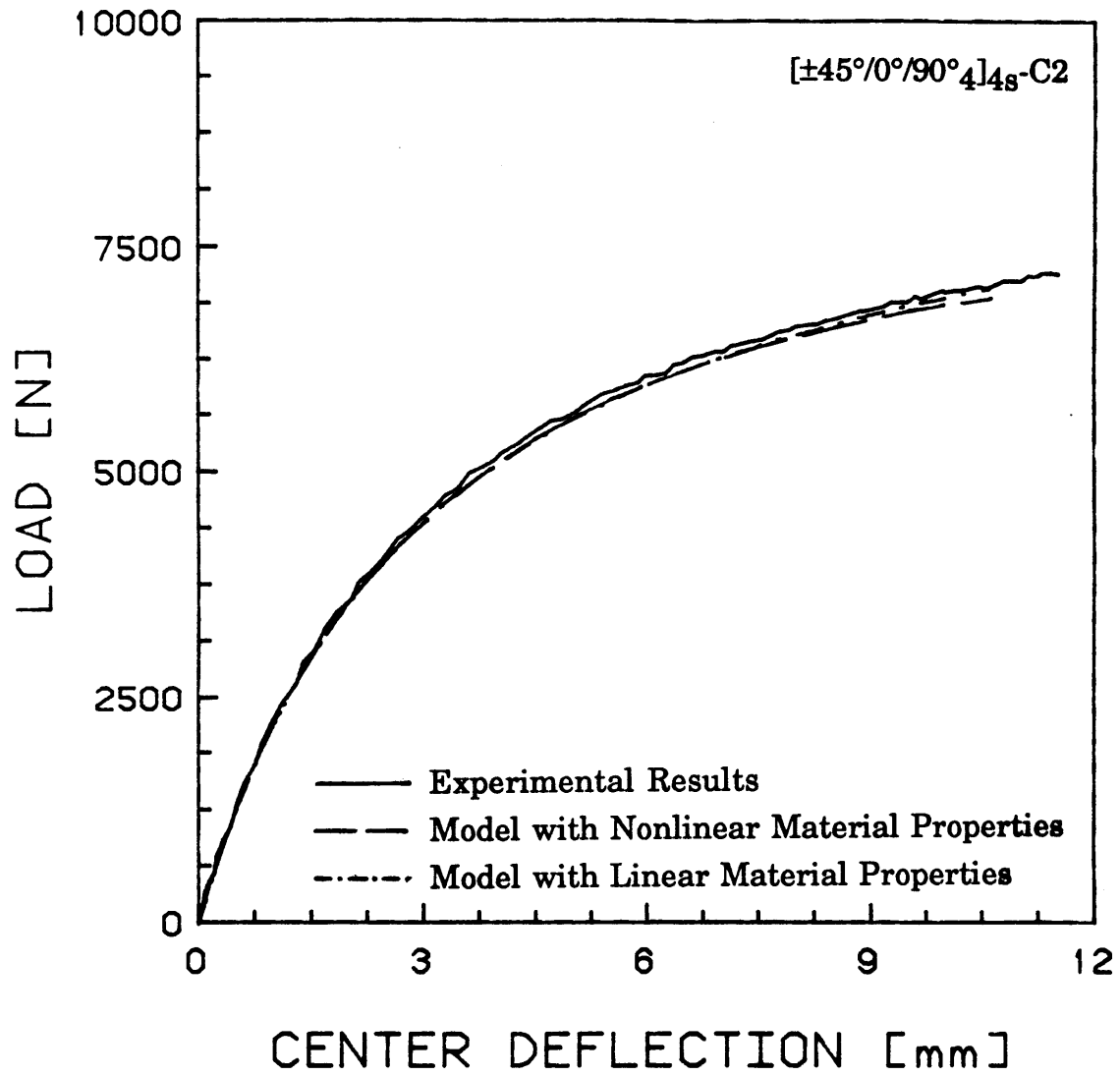


Figure 6.27 Experimental and predicted load versus center deflection for the  $[\pm 45^\circ/0^\circ/90^\circ_4]_{4s}$  layup prior to damage.

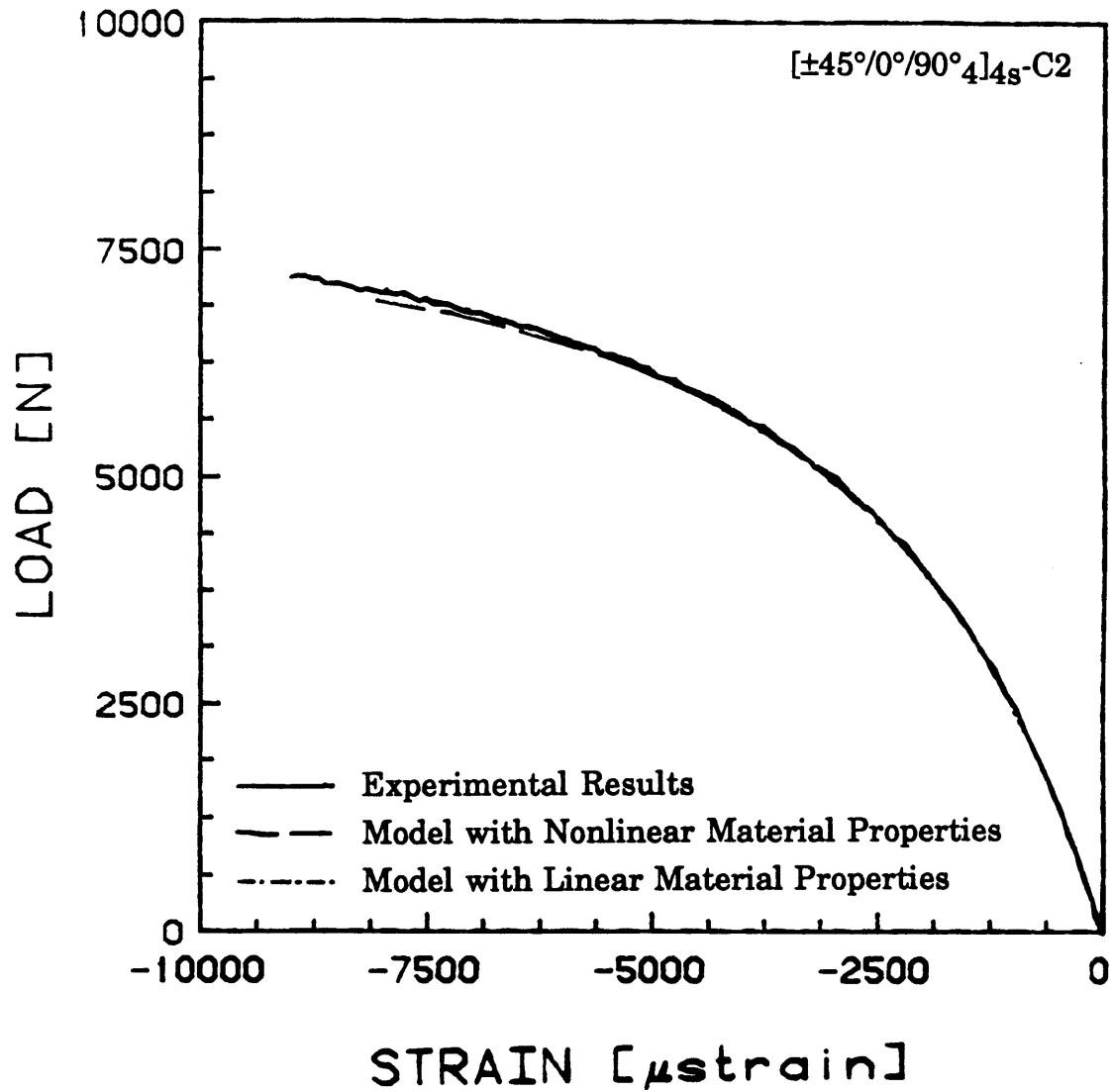


Figure 6.28 Experimental and predicted load versus centerline strain on the compression side for the  $[\pm 45^\circ/0^\circ/90^\circ_4]_{4s}$  layup prior to damage.

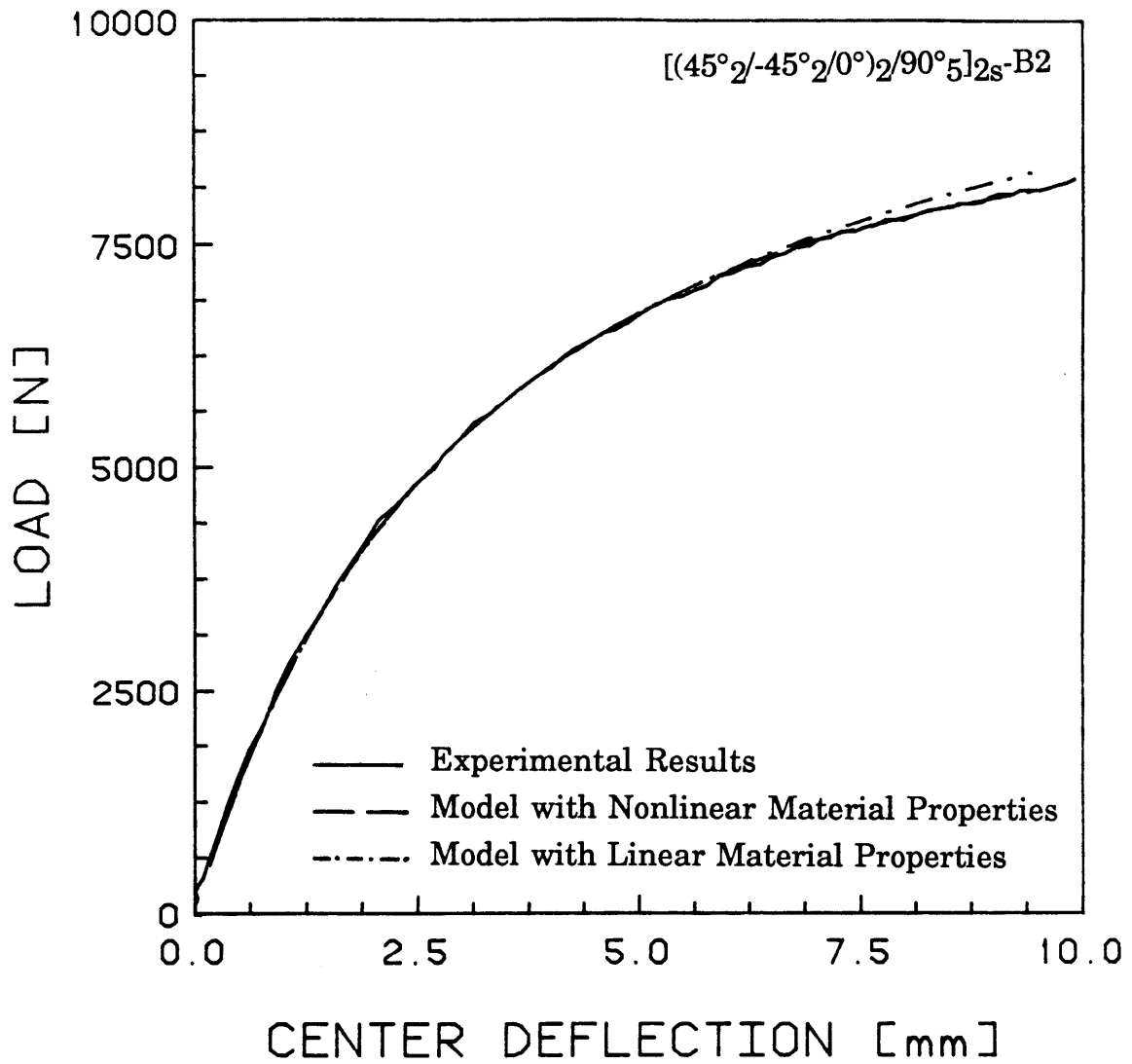


Figure 6.29 Experimental and predicted load versus center deflection for the  $[(45^\circ_2/-45^\circ_2/0^\circ)_2/90^\circ_5]_{2s}$  layup prior to damage.

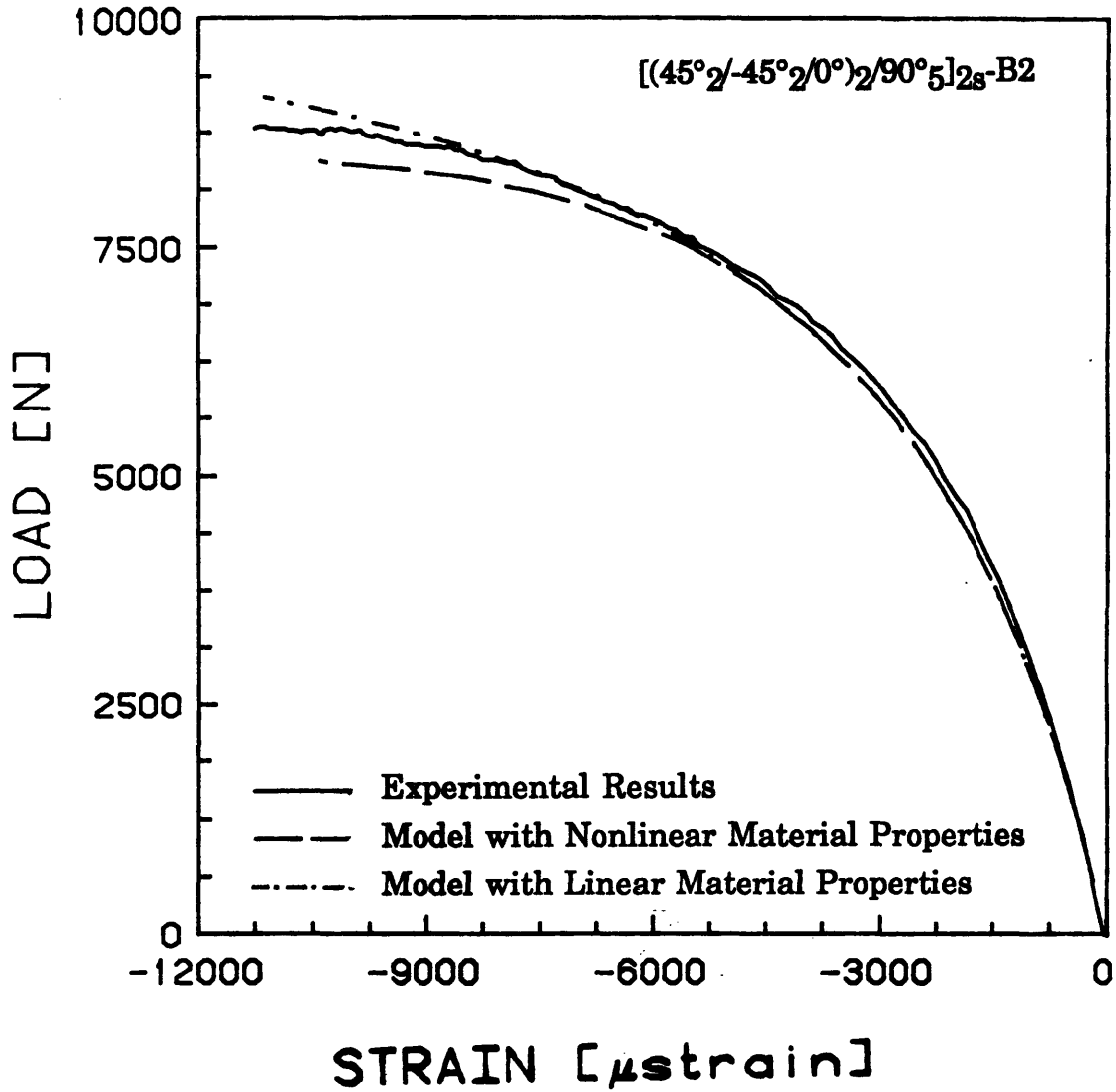


Figure 6.30 Experimental and predicted load versus centerline strain on the compression side for the [(45°<sub>2</sub>/-45°<sub>2</sub>/0°)<sub>2</sub>/90°<sub>5</sub>]<sub>2s</sub> layup prior to damage.

plies in each layup; the first is made up of 29% 45° plies, while the last two are made up of 50% and 53%, respectively.

The data used to obtain the nonlinear stress-strain behavior of the 45° plies came from  $[\pm 45^\circ]_{2s}$  specimens subjected to a uniaxial stress state. Because of the mismatch in Poisson's ratios between plies, the 45° plies in the laminates studied in this investigation were subjected to a biaxial stress state. This affects the nonlinear longitudinal stiffness of the 45° plies, accounting for the discrepancies seen between model and experiment. This comparison does show that these nonlinearities cannot be ignored in laminates with a high proportion of 45° plies at the strain levels encountered in this work. The nonlinearities become noticeable in the layups studied in this investigation at strains exceeding 6000  $\mu$ strain, and become important, in that the applied loads in models with and without the material nonlinearities differ by more than 5%, at strains exceeding 8000  $\mu$ strain.

#### **6.2.4 Comparison of Damage Histories**

The loads at which initial damage was predicted, both for in-plane and out-of-plane damage, match experimental results very well, as can be seen in Table 6.5, in which damage initiation loads are listed. In terms of center deflection, damage is predicted in the  $[\pm 45^\circ/0^\circ/90^\circ]_4$  model before it occurs in the experiment, but in the cases of the other two models, damage was predicted at a center deflection greater than was observed experimentally. Comparing center deflections at which damage occurs, as well as the corresponding loads, is important because the place on the load versus deflection graph where damage initiates is relatively flat: the load changes little for significant changes in deflection. Even though the load

may not change much, increasing the center deflection increases the stresses in the specimen.

After damage initiation, model and experiment differ markedly. Delaminations in the model tend to propagate much earlier and to a greater extent than was observed experimentally. This results in entire plies being removed from the model. Final failure modes were therefore usually incorrectly predicted. In Figures 6.31 to 6.34, 6.36 to 6.41 and 6.43 to 6.48, the stages in damage progression for the models of the three specimen types are shown with the characteristic damage states observed experimentally. The corresponding center deflection are included. The corresponding load versus center deflection plots of both models and experiments are shown in Figures 6.35, 6.42 and 6.49. In these figures, the experimental results are shown as a composite plot. The first plot, at the end of which the specimen is undamaged, is shown in its entirety. Data from the next test are shown only for center deflections larger than those of the first plot. In a similar manner, the remaining experimental plots have been snipped so as to show only a single line at a given value of displacement.

In the  $[45^{\circ}_4/-45^{\circ}_4/(0^{\circ}/90^{\circ})_4]_{2s}$  laminate, the model predicted damage initiation at a load slightly larger than that observed experimentally, as is shown in Table 6.5. In both the experiment and the model, delamination and in-plane damage appear to have occurred simultaneously. In Figure 6.31, the loads at which damage initiated (11370 N) and at which damage was predicted (11419 N) are shown with the corresponding damage states. The model's damage prediction came at a center deflection larger than that where damage was first observed experimentally by 4 mm. In terms of center deflection, all four damage states occurred before damage was predicted in the model, as can be seen in Figures 6.32 through 6.34. In these

figures, damage accumulation is shown with increasing center deflection, starting with the experimental first characteristic damage state. The corresponding load versus center deflection plot is shown in Figure 6.35. As can be seen in Figure 6.34 (a) and (b), when damage initiated in the model in the form of matrix cracks in the outermost  $\pm 45^\circ$  plies, delaminations formed immediately, and these propagated to the ends of the specimen. Such behavior was not observed in the experiments. In both model and experiment, final failure occurred when the  $0^\circ$  plies on the tension side failed.

Damage initiated at very similar loads and center deflections in the  $[\pm 45^\circ/0^\circ/90^\circ]_4$  model and experiment, though the extent of the damage was greater in the model. In-plane and delamination damage were predicted to initiate simultaneously in the model at 6943 N, while matrix cracks were observed experimentally to occur first at 7215 N, followed by delamination damage at 7322 N. Damage initiation loads are shown in Figure 6.36 and 6.37 with the corresponding damage states. The experimental and predicted progressions of damage can be seen in Figures 6.38 through 6.41 with the corresponding center deflection, starting with the predicted damage initiation. Initial predictions of damage match experimental observations well. However, the delamination in the model present in Figure 6.39 (b) propagates to the end of the specimen in Figure 6.40 (a), effectively removing the top three plies from the model. This did not happen in the experiment. In a similar manner, the second delamination shown in Figure 6.40 (b) propagates to the end of the specimen in Figure 6.41 (a), removing a further seven plies. These two delamination propagations result in large load drops in the model which are not seen in the experimental load versus center deflection results as shown in Figure 6.42. While final failure in the

experiment was due to fiber breakage, in the model, the load dropped to less than half the maximum value when a third delamination propagated to the end of the specimen and removed the next seven plies.

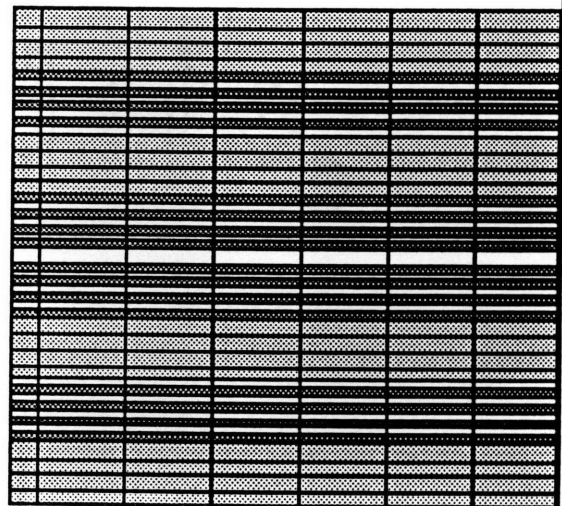
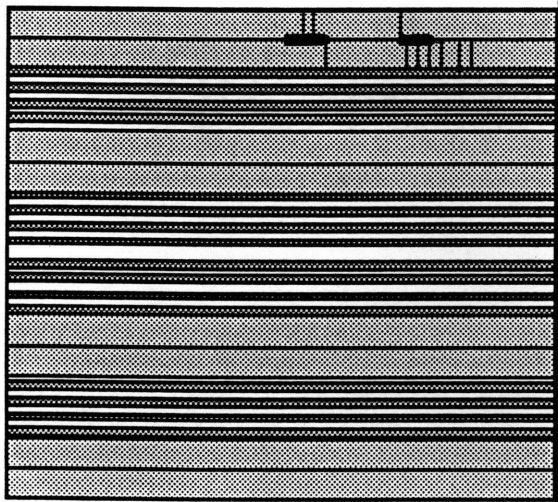
Damage initiated at a slightly larger center deflection and a slightly lower load in the  $[(45^\circ_2/-45^\circ_2/0^\circ)_2/90^\circ_5]_{2s}$  model than was observed experimentally. Once again, in-plane and delamination damage were predicted to occur simultaneously at 8491 N. Matrix cracks were first observed at 8759 N, while delaminations were first observed at 8821 N. Predicted and experimental damage initiation loads and the corresponding damage states are illustrated in Figures 6.43 and 6.44. The damage progression is shown in Figures 6.45 through 6.48 with the corresponding center deflections, starting with the experimental first characteristic damage state. Damage levels are lower in the model, as can be seen in Figures 6.45 and 6.46, up to the point where the delamination shown in Figure 6.47 (a) propagates to the end of the specimen, effectively removing the top ten plies from the model. Neither this phenomenon nor the resulting load drop shown in Figure 6.49 were observed experimentally. In both model and experiment, final failure occurred when matrix cracks appeared in the central  $90^\circ$  effective ply and delaminations between it and its neighbors propagated to the ends of the specimen. This can be seen for the model in Figure 6.48. This is not shown for the specimen because specimen edges proved impossible to successfully replicate after final failure.

For all three specimen types, model predictions of initial damage were fairly accurate in terms of when that damage occurred, which plies it occurred in and the extent of the damage. However, in all three models, delaminations were predicted to propagate to the end of the specimen in a manner which was not observed experimentally. In the models of the

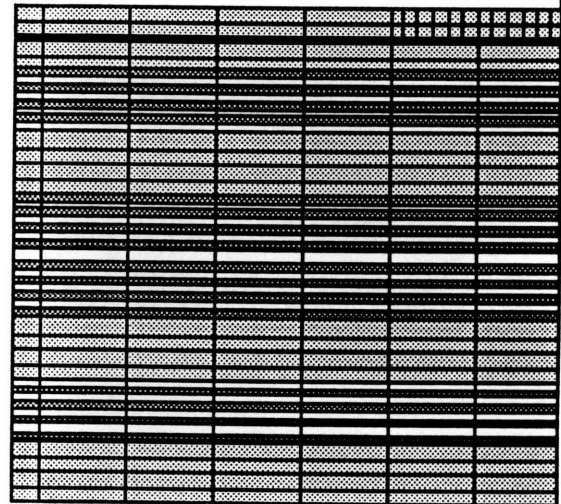
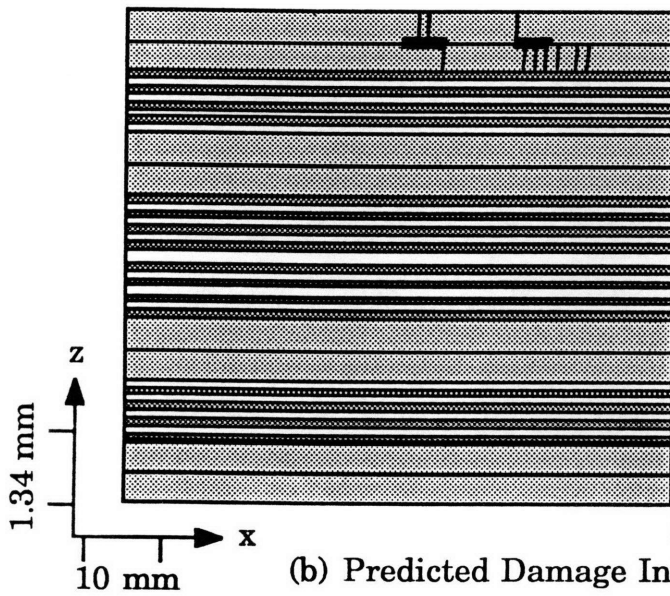
$[\pm 45^\circ/0^\circ/90^\circ_4]_{4s}$  and  $[(45^\circ_2/-45^\circ_2/0^\circ)_2/90^\circ_5]_{2s}$  specimens, these delaminations seriously affected the overall behavior of the model to the point where the predictions would not be useful after the occurrence of these delaminations.

**Experimental**

**Predicted**



(a) Experimental Damage Initiation Load is 11370 N



(b) Predicted Damage Initiation Load is 11419 N

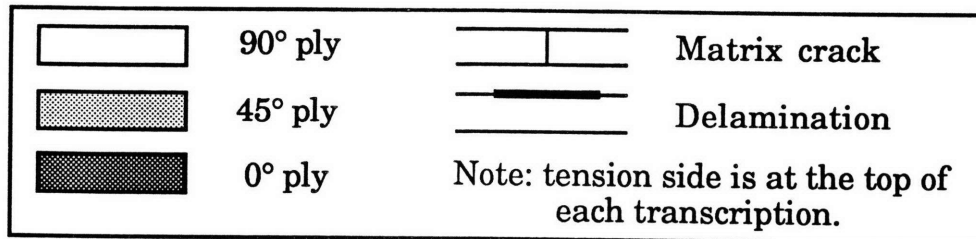
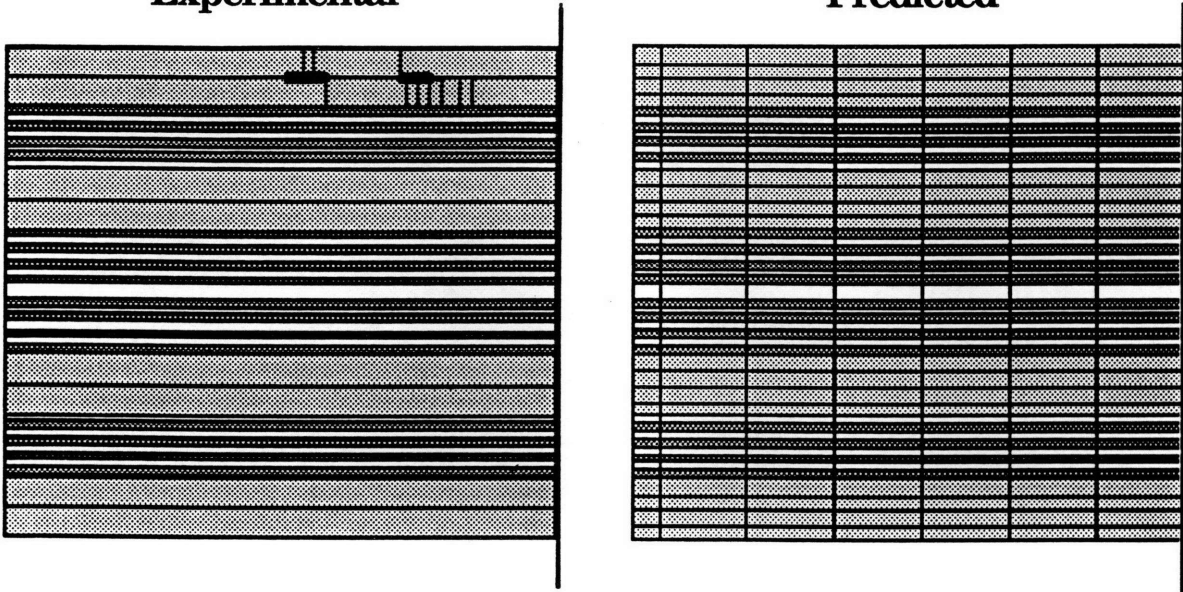


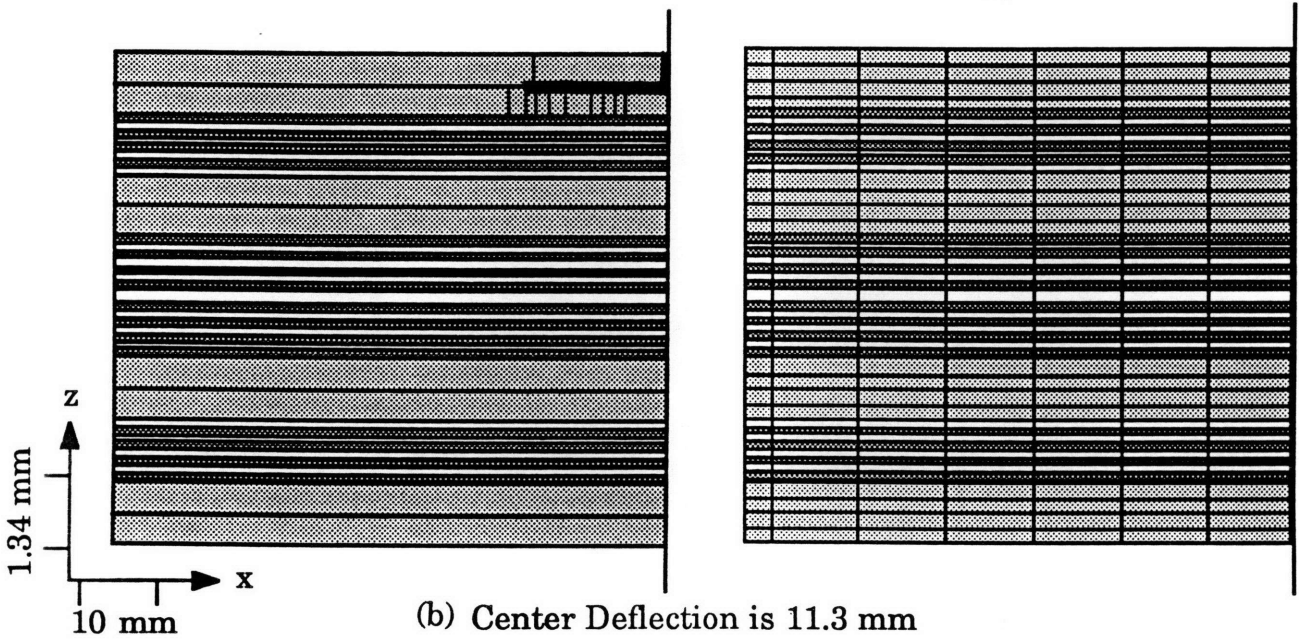
Figure 6.31 Comparison of damage between model and experiment for the  $[45^{\circ}_4/45^{\circ}_4/(0^{\circ}/90^{\circ})_4]_{2S}$  layup at (a) experimental and (b) predicted damage initiation loads.

**Experimental**

**Predicted**



(a) Center Deflection is 10.2 mm



(b) Center Deflection is 11.3 mm

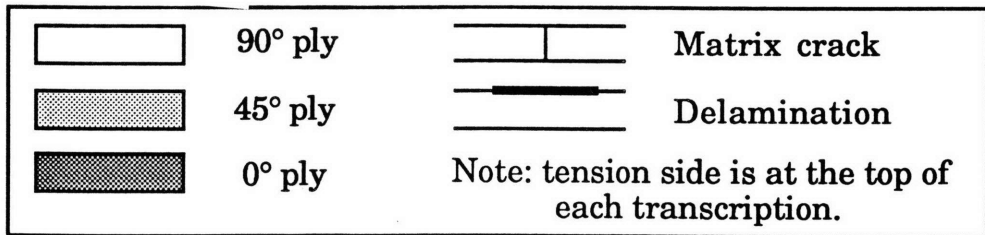
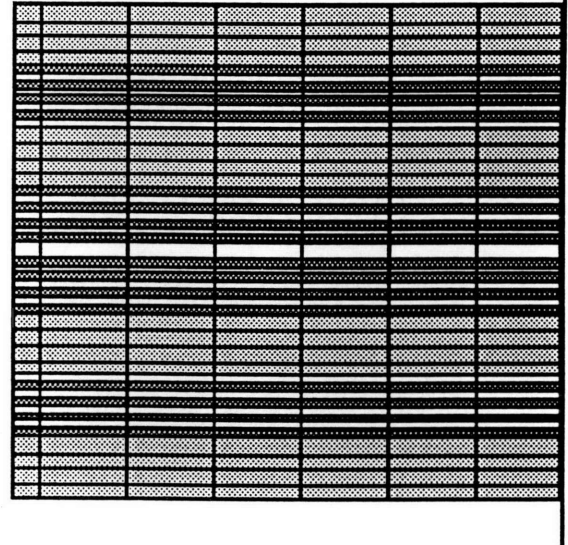
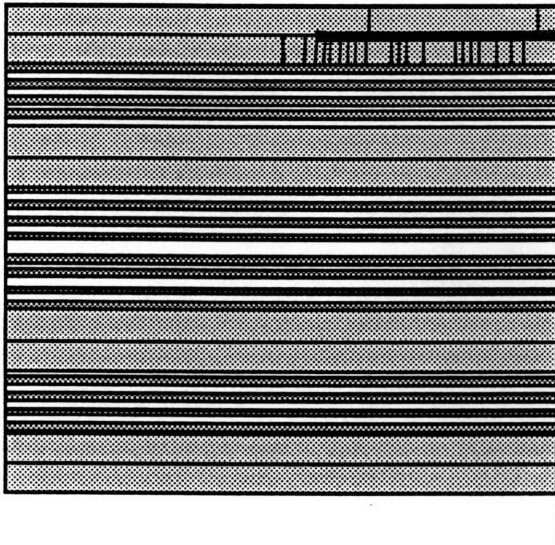


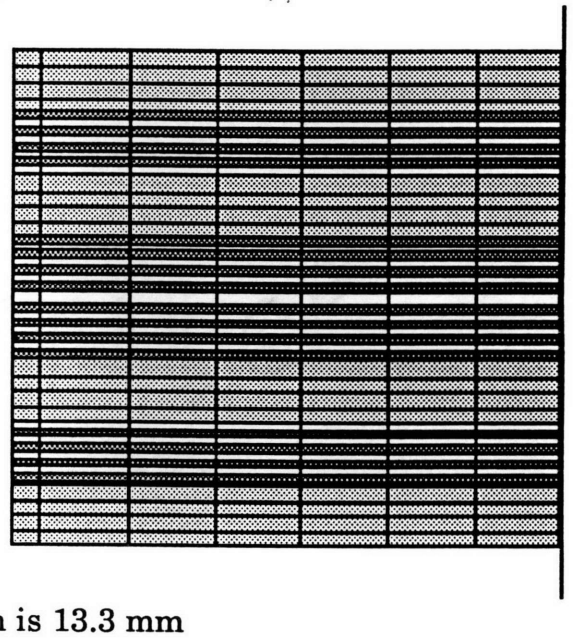
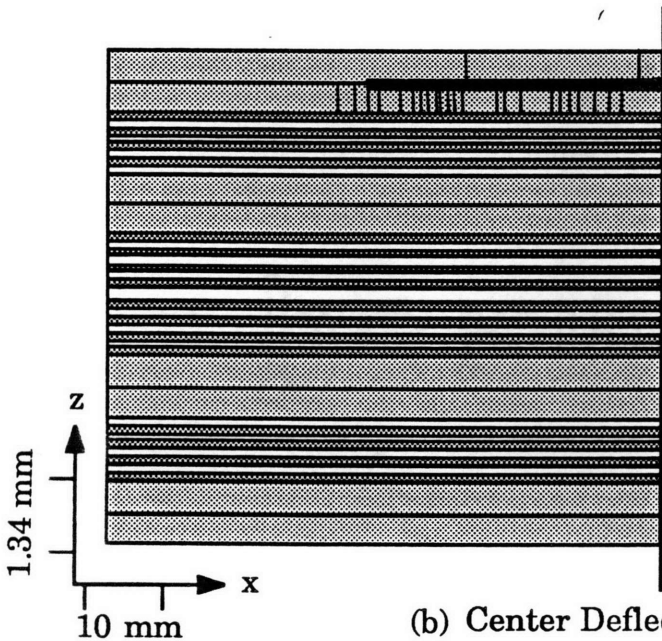
Figure 6.32 Comparison of damage between model and experiment for the  $[45^\circ_4/45^\circ_4/(0^\circ/90^\circ)_4]_{2S}$  layup at the (a) first and (b) second characteristic damage states.

**Experimental**

**Predicted**



(a) Center Deflection is 12.7 mm



(b) Center Deflection is 13.3 mm

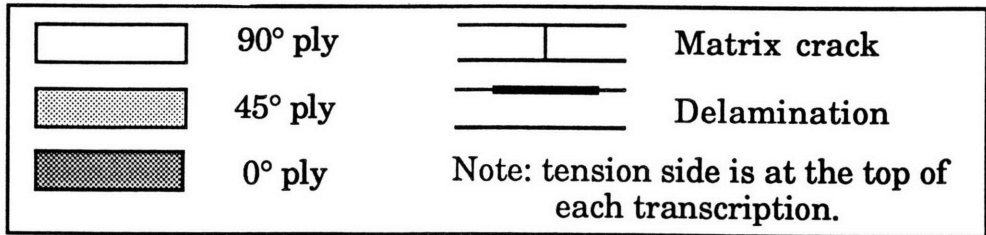


Figure 6.33 Comparison of damage between model and experiment for the  $[45^{\circ}_4/-45^{\circ}_4/(0^{\circ}/90^{\circ})_4]_{2S}$  layup at the (a) third and (b) fourth characteristic damage states.

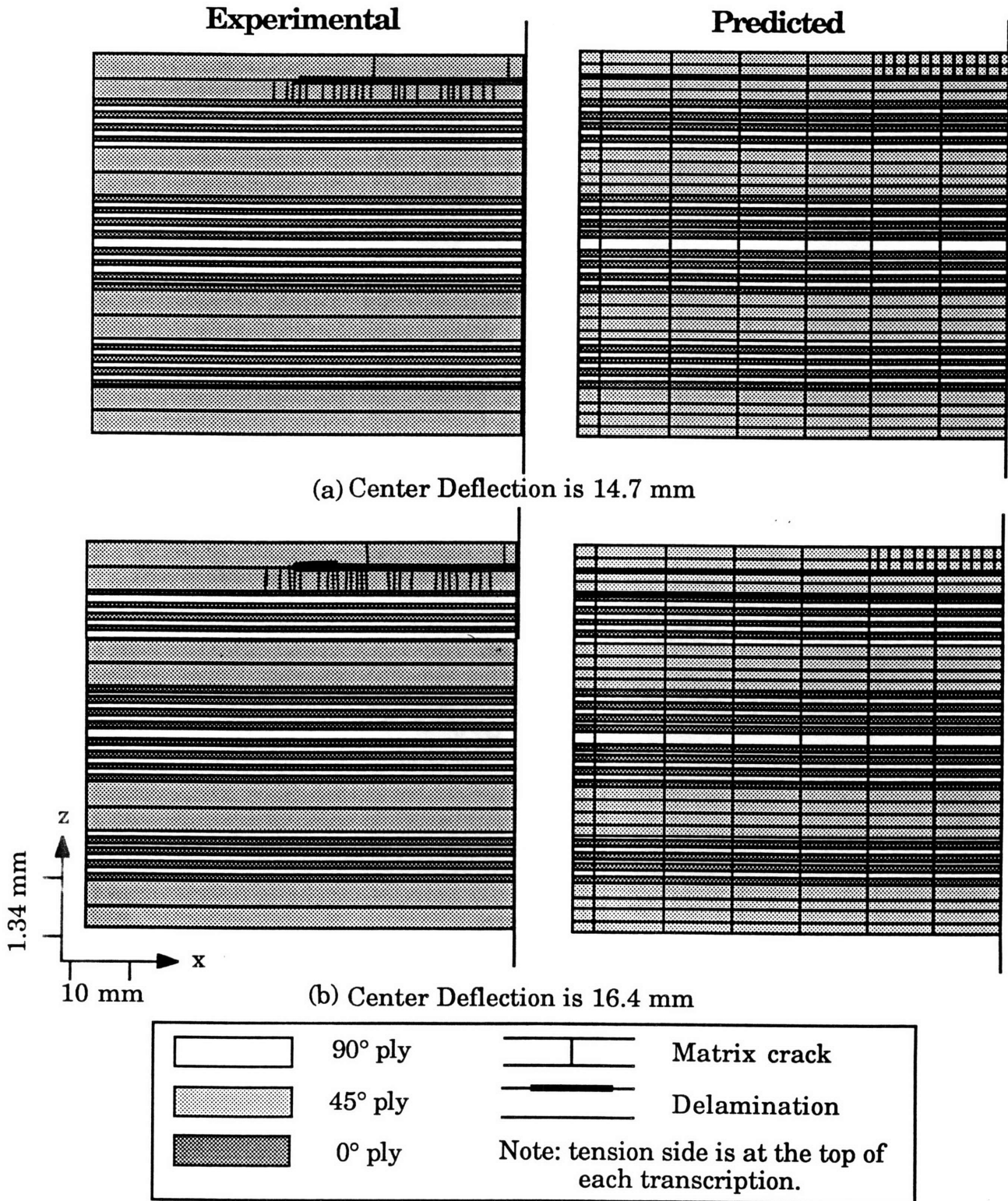


Figure 6.34 Predicted damage accumulation in the  $[45^{\circ}_4/45^{\circ}_4/(0^{\circ}/90^{\circ})_4]_{2s}$  layup beyond the fourth characteristic damage state.

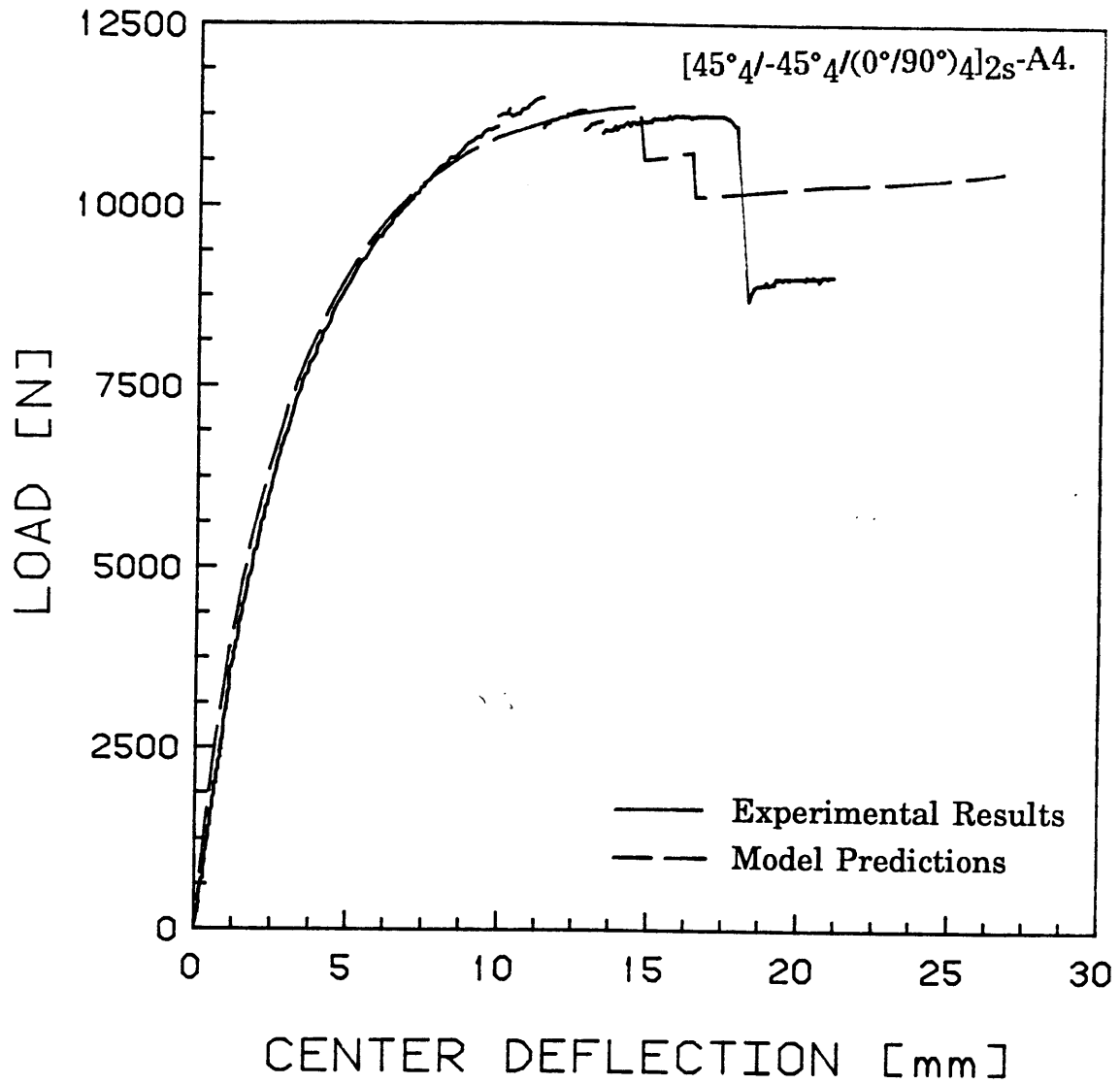


Figure 6.35 Experimental and predicted load versus center deflection for the  $[45^{\circ}_4/-45^{\circ}_4/(0^{\circ}/90^{\circ})_4]_{2s}$  layup.

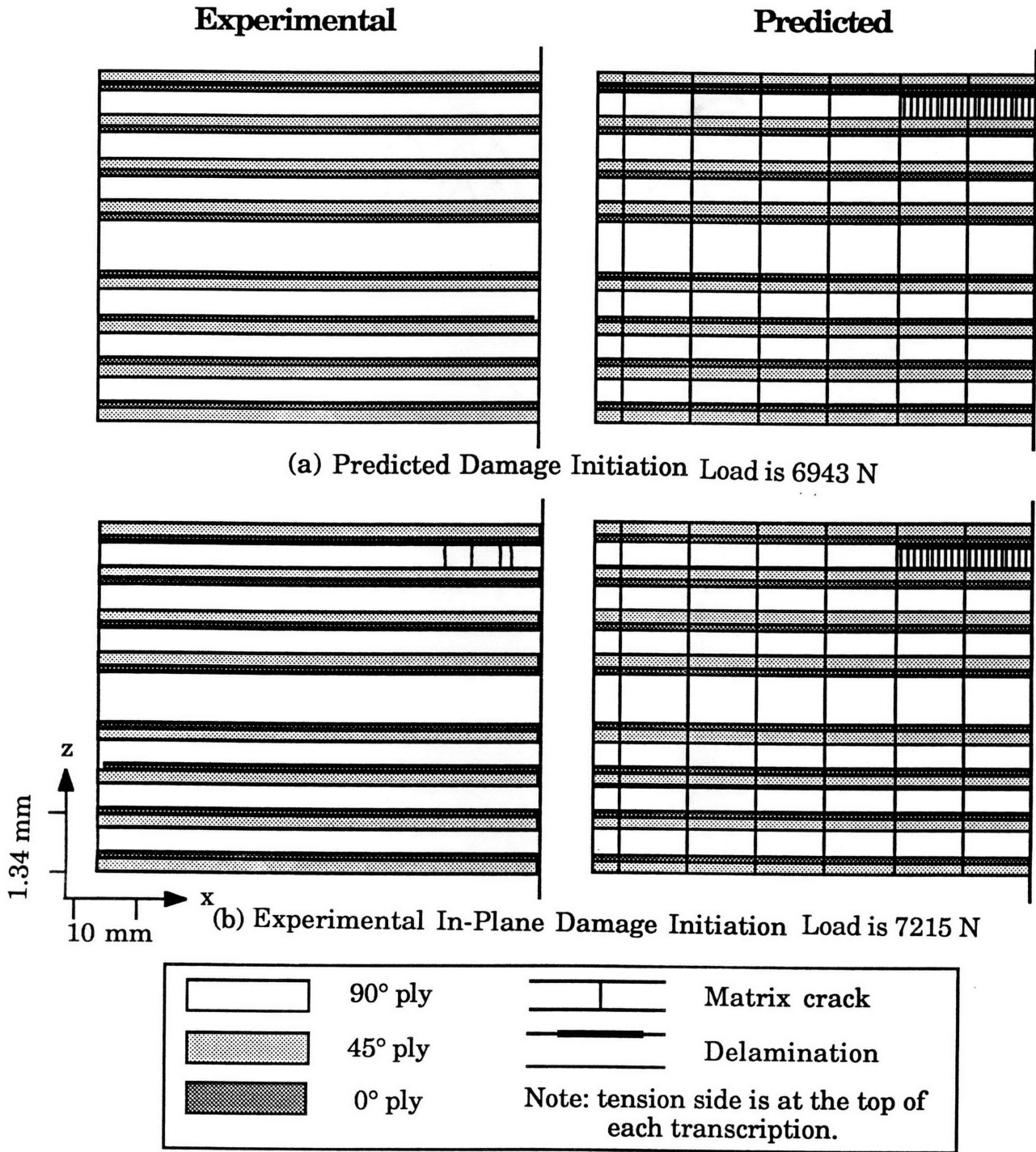


Figure 6.36 Predicted and experimental damage levels for the  $[\pm 45^\circ/0^\circ/90^\circ]_4s$  layup at the (a) predicted damage initiation load and (b) experimental in-plane damage initiation load.

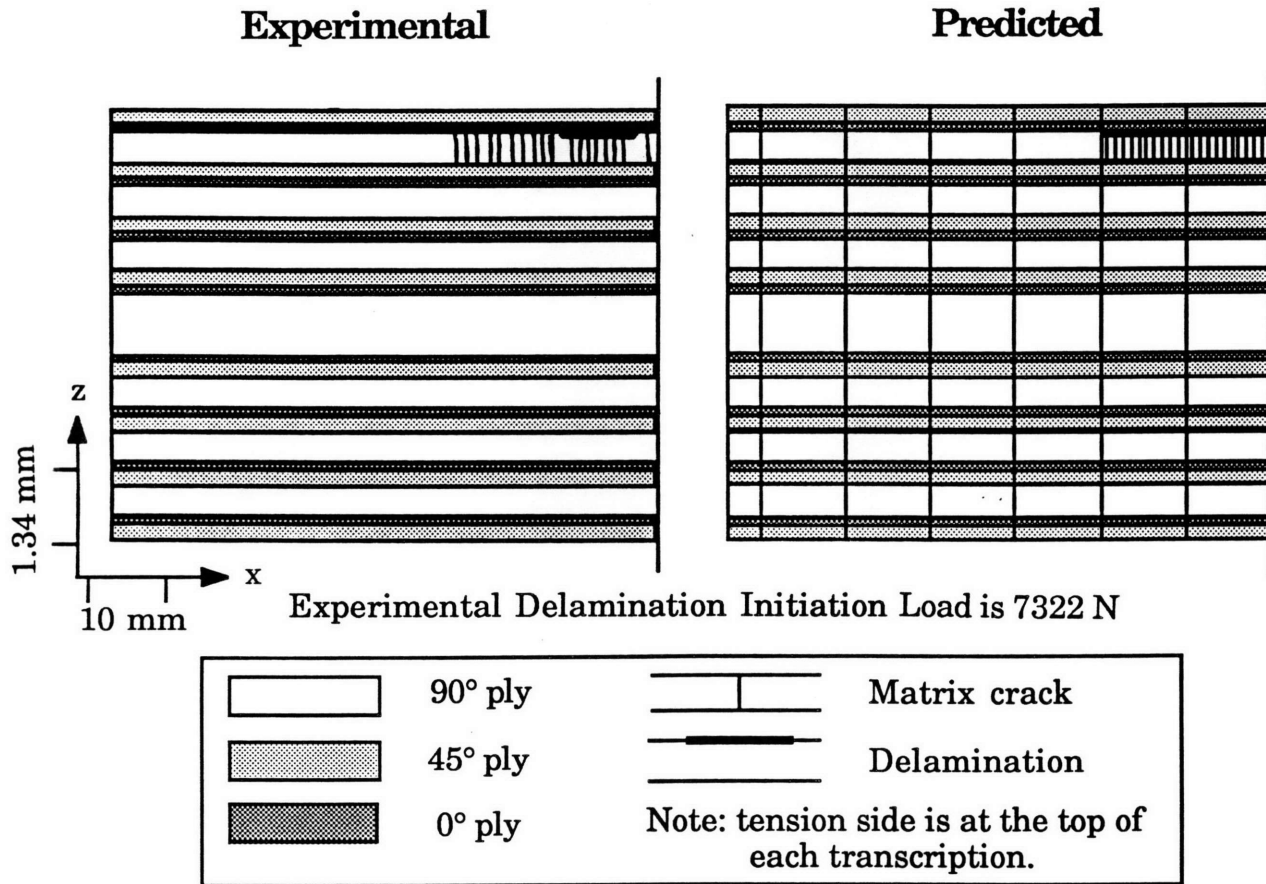


Figure 6.37 Predicted and experimental damage levels for the  $[\pm 45^\circ/0^\circ/90^\circ_4]_{4s}$  layup at the experimental delamination initiation load.

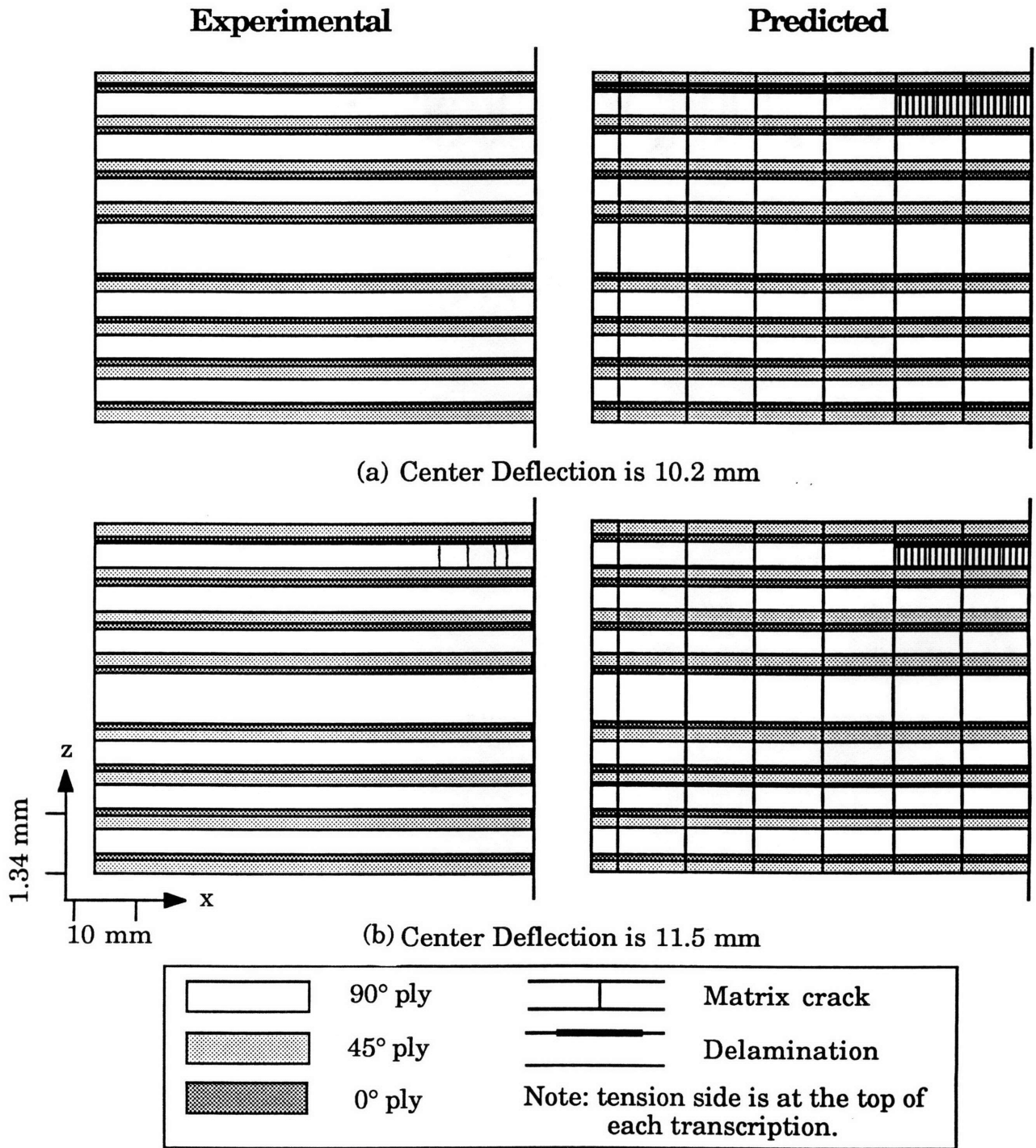


Figure 6.38 Predicted and experimental damage levels for the  $[\pm 45^\circ/0^\circ/90^\circ]_4s$  layup at (a) predicted damage initiation and (b) the first characteristic damage state.

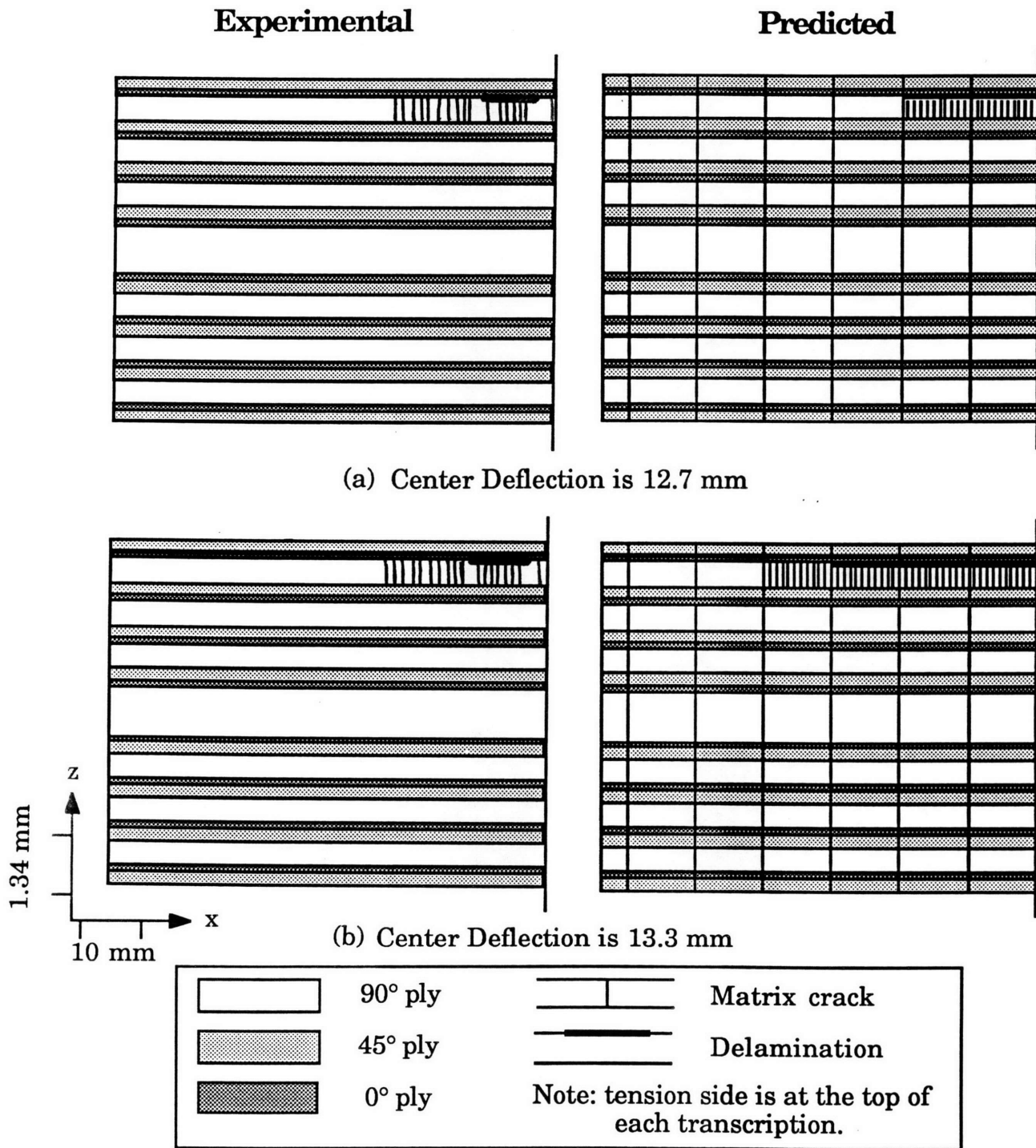
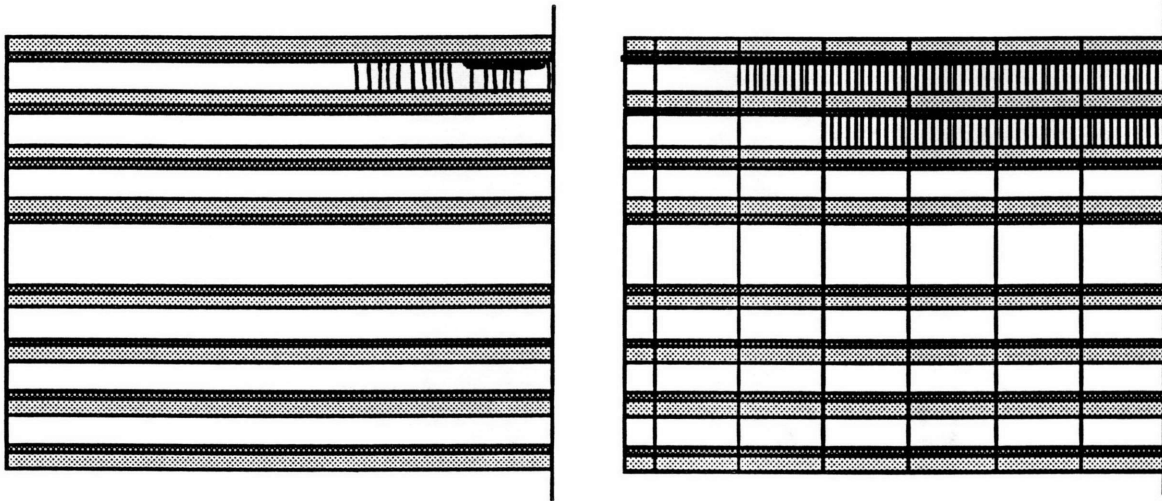


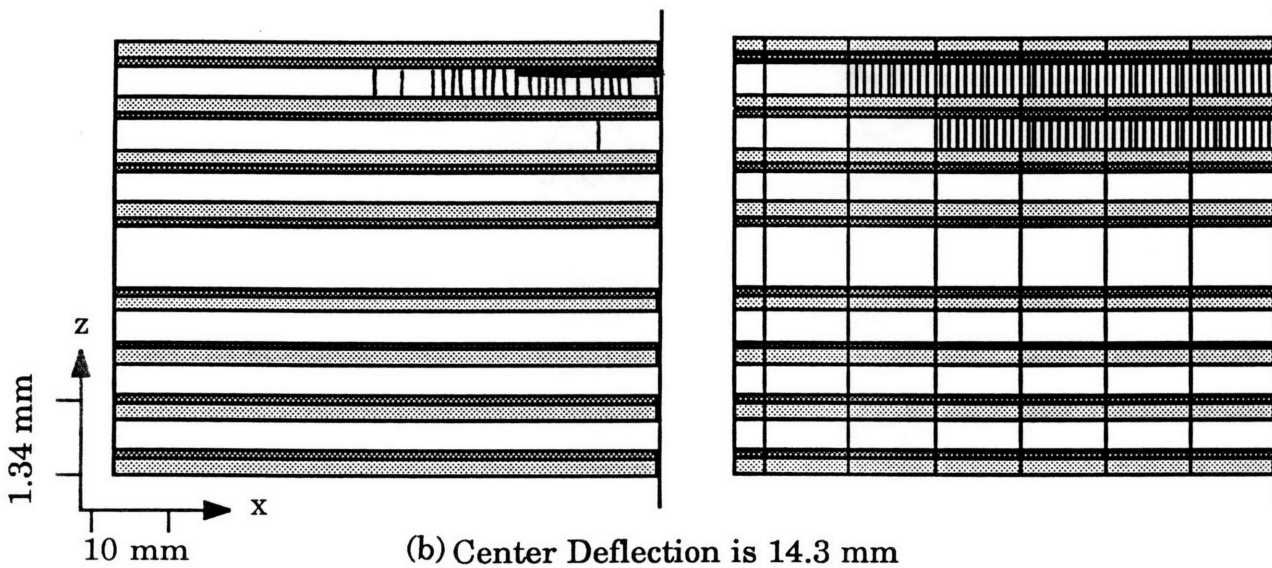
Figure 6.39 Predicted and experimental damage levels for the  $[\pm 45^\circ/0^\circ/90^\circ_4]_{4s}$  layup at (a) the second characteristic damage state and (b) between the second and third damage states.

**Experimental**

**Predicted**



(a) Center Deflection is 14.0 mm



(b) Center Deflection is 14.3 mm

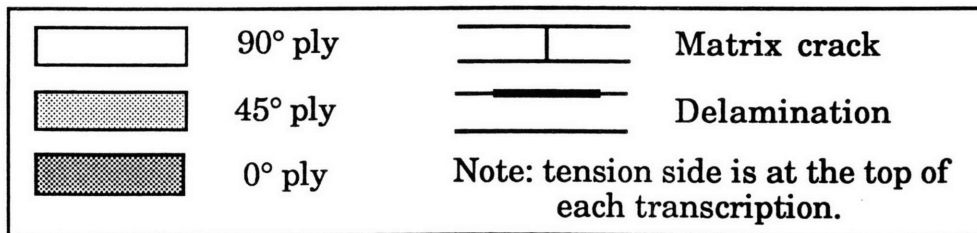
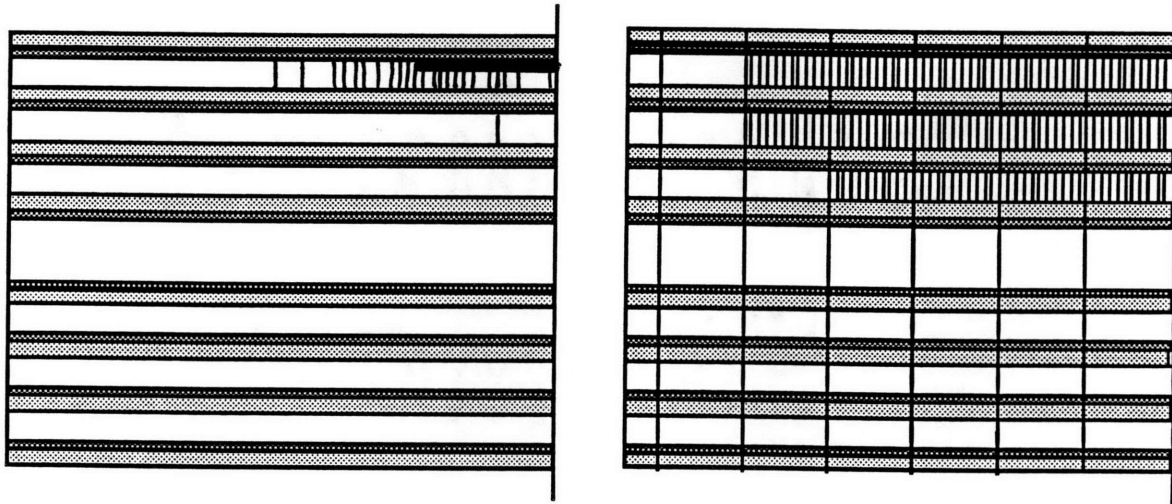


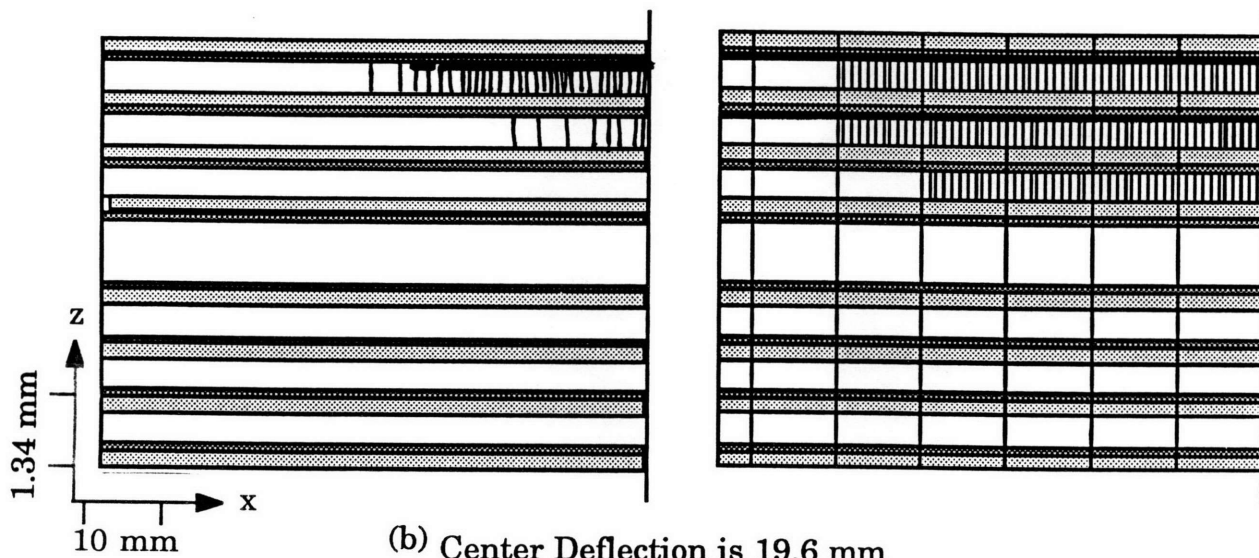
Figure 6.40 Predicted and experimental damage levels for the  $[\pm 45^\circ/0^\circ/90^\circ]_4s$  layup (a) between the second and third damage states and (b) at the third damage state.

Experimental

Predicted



(a) Center Deflection is 16.8 mm



(b) Center Deflection is 19.6 mm

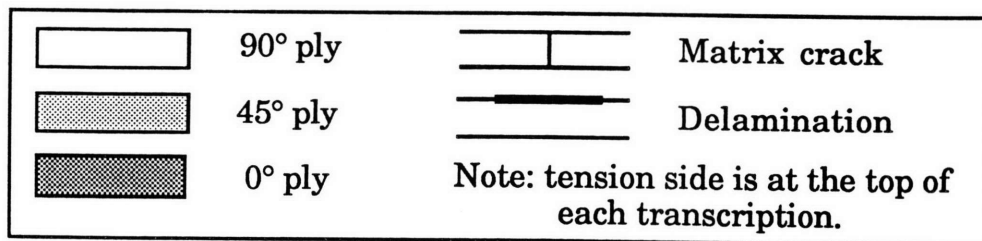


Figure 6.41 Predicted and experimental damage levels for the  $[\pm 45^\circ/0^\circ/90^\circ_4]_{4s}$  layup (a) between the third and fourth damage states and (b) at the fourth damage state.

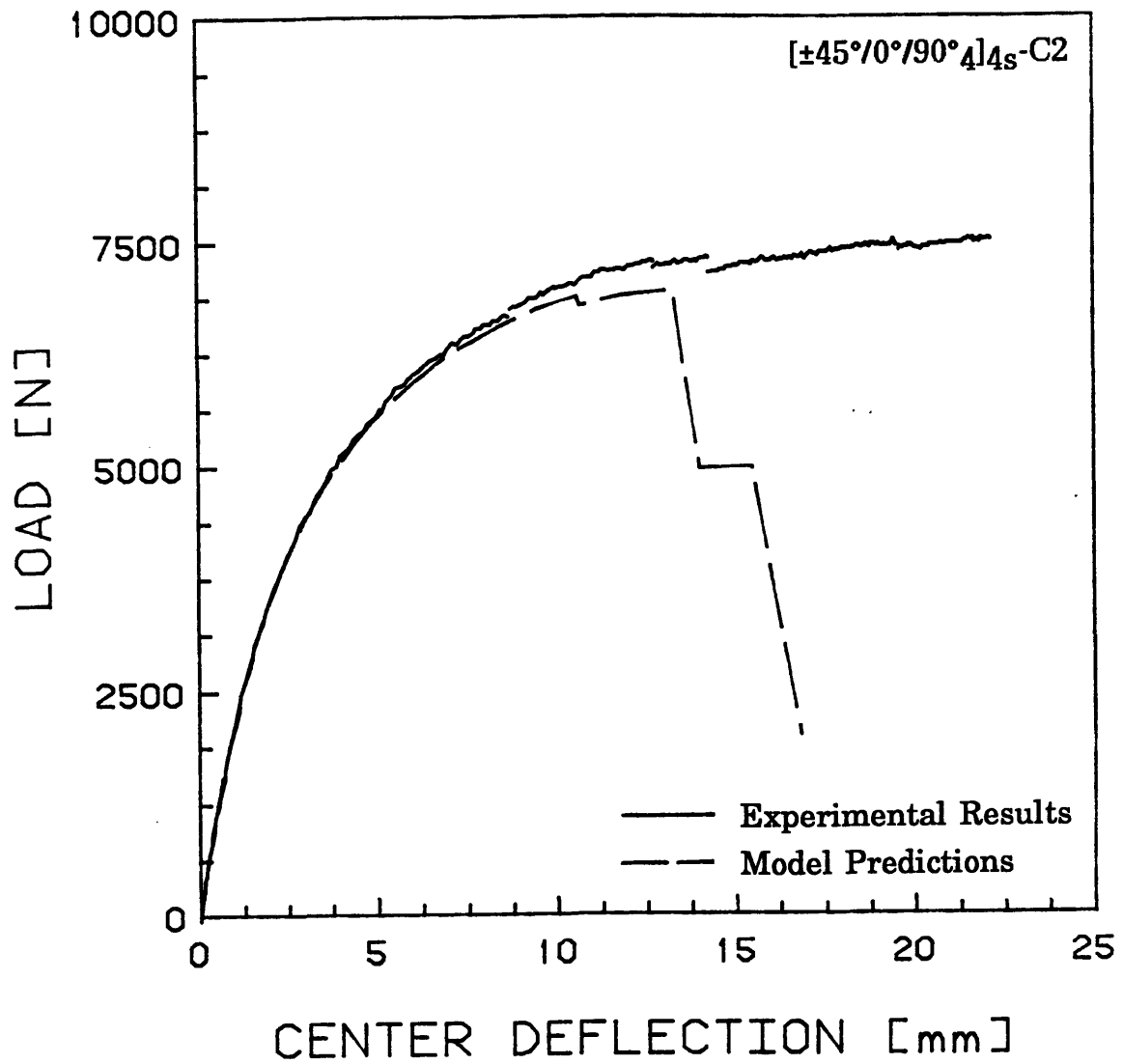


Figure 6.42 Experimental and predicted load versus center deflection for  $[\pm 45^\circ/0^\circ/90^\circ]_4s$  layup.

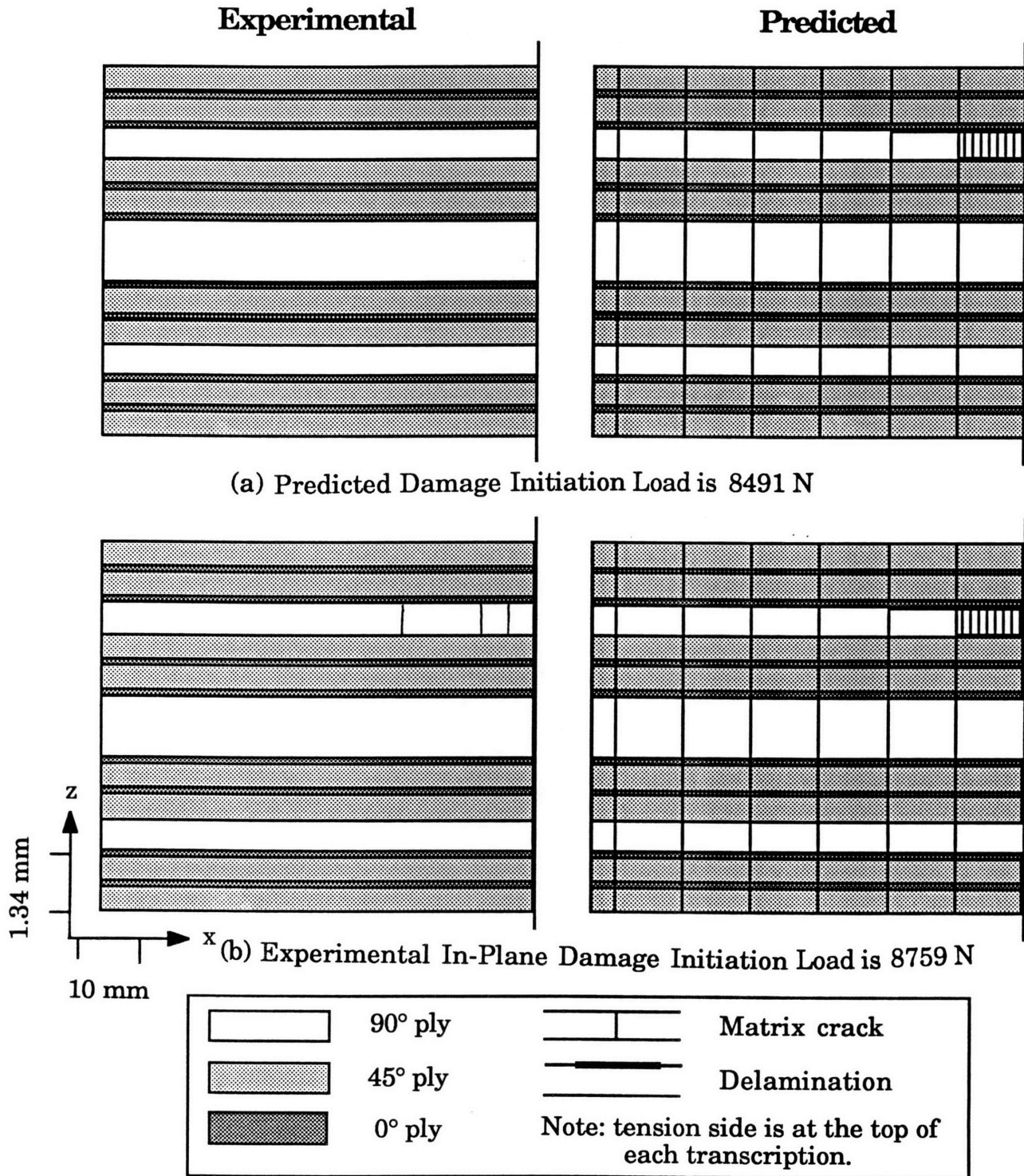


Figure 6.43 Predicted and experimental damage levels for the  $[(45^\circ_2/-45^\circ_2/0^\circ)_2/90^\circ_5]_{2s}$  layup at the (a) predicted damage initiation load and (b) experimental in-plane damage initiation load.

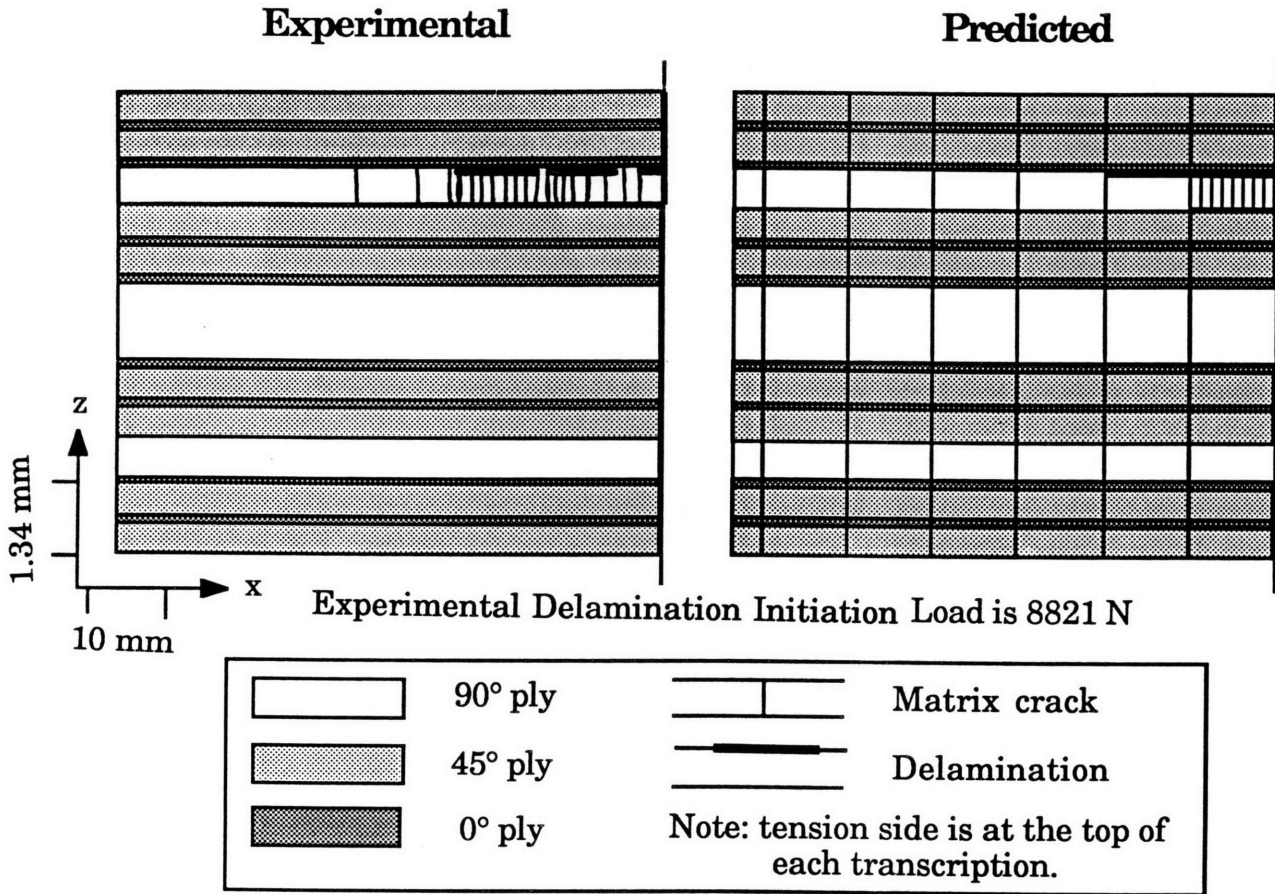
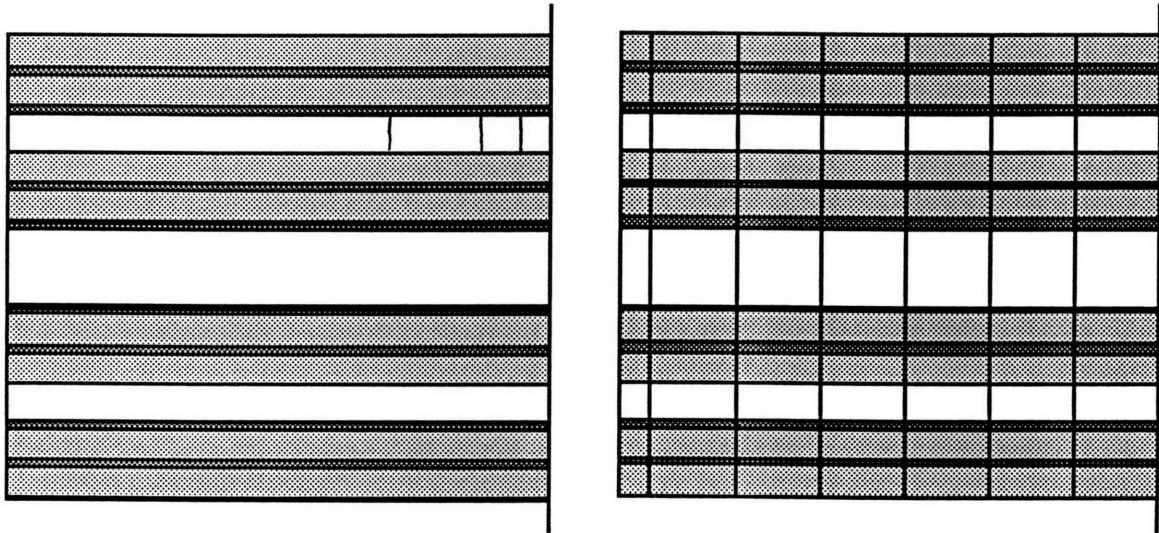


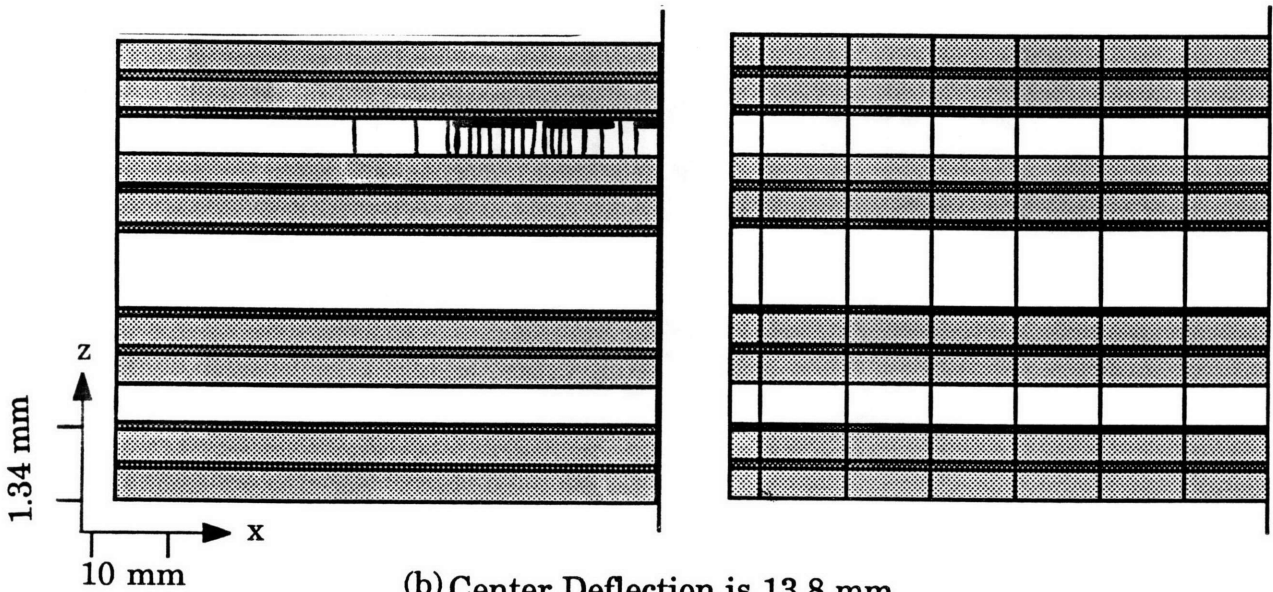
Figure 6.44 Predicted and experimental damage levels for the  $[(45^\circ_2/-45^\circ_2/0^\circ)_2/90^\circ_5]_{2s}$  layup at the experimental delamination initiation load.

**Experimental**

**Predicted**



(a) Center Deflection is 12.0 mm



(b) Center Deflection is 13.8 mm

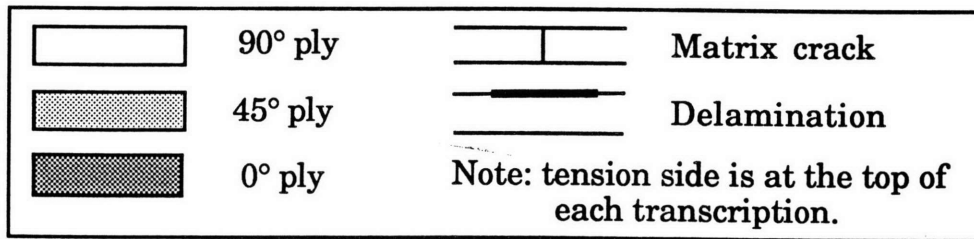
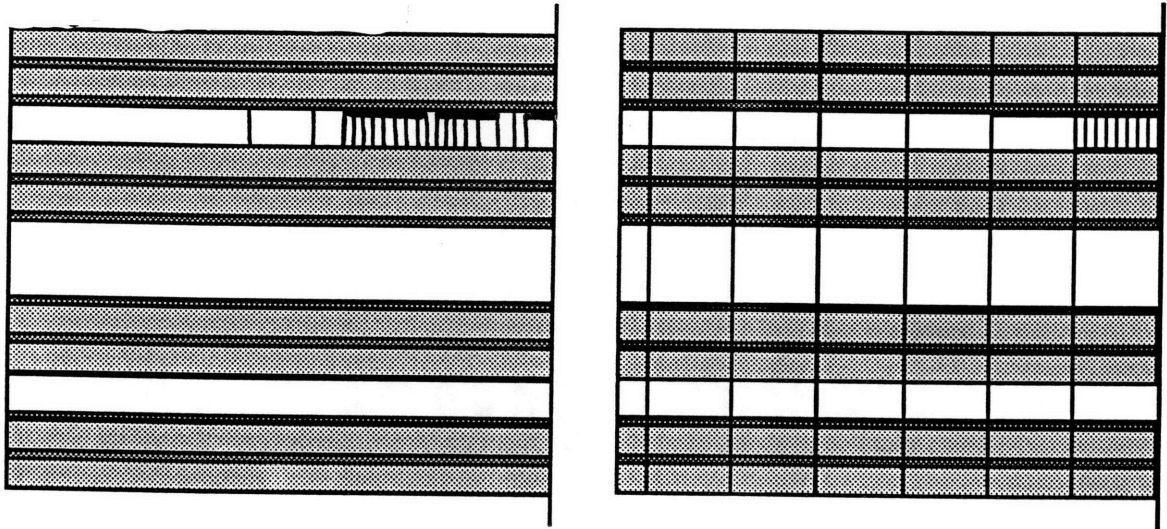


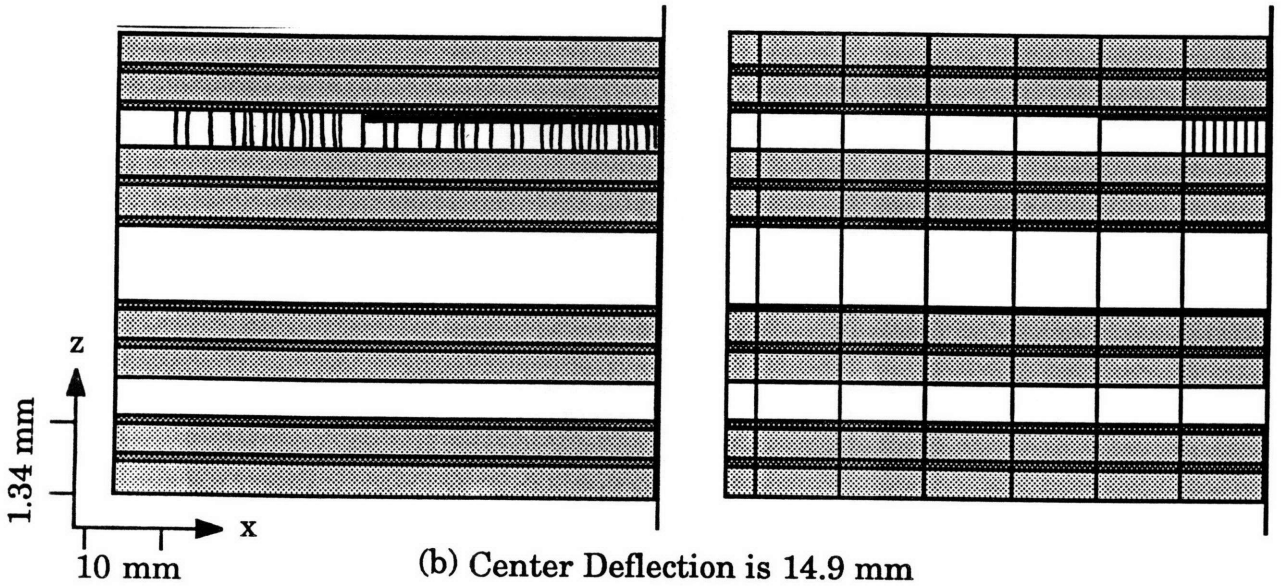
Figure 6.45 Comparison of damage between model and experiment for the  $[(45^\circ_2/-45^\circ_2/0^\circ)_2/90^\circ_5]_{2s}$  layup at the (a) first and (b) second characteristic damage states.

**Experimental**

**Predicted**



(a) Center Deflection is 14.8 mm



(b) Center Deflection is 14.9 mm

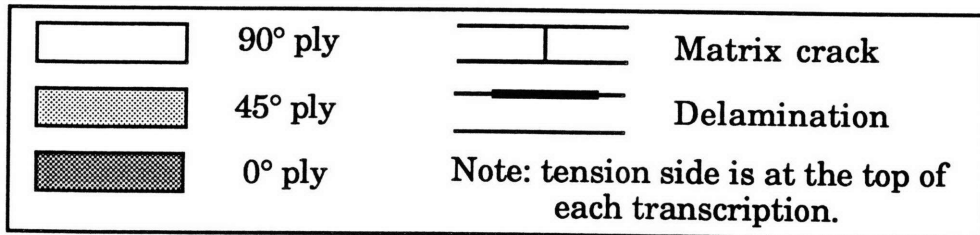


Figure 6.46 Predicted and experimental damage levels for the  $[(45^\circ_2/-45^\circ_2/0^\circ)_2/90^\circ_5]_{2s}$  layup at (a) predicted damage initiation and (b) the third characteristic damage state.

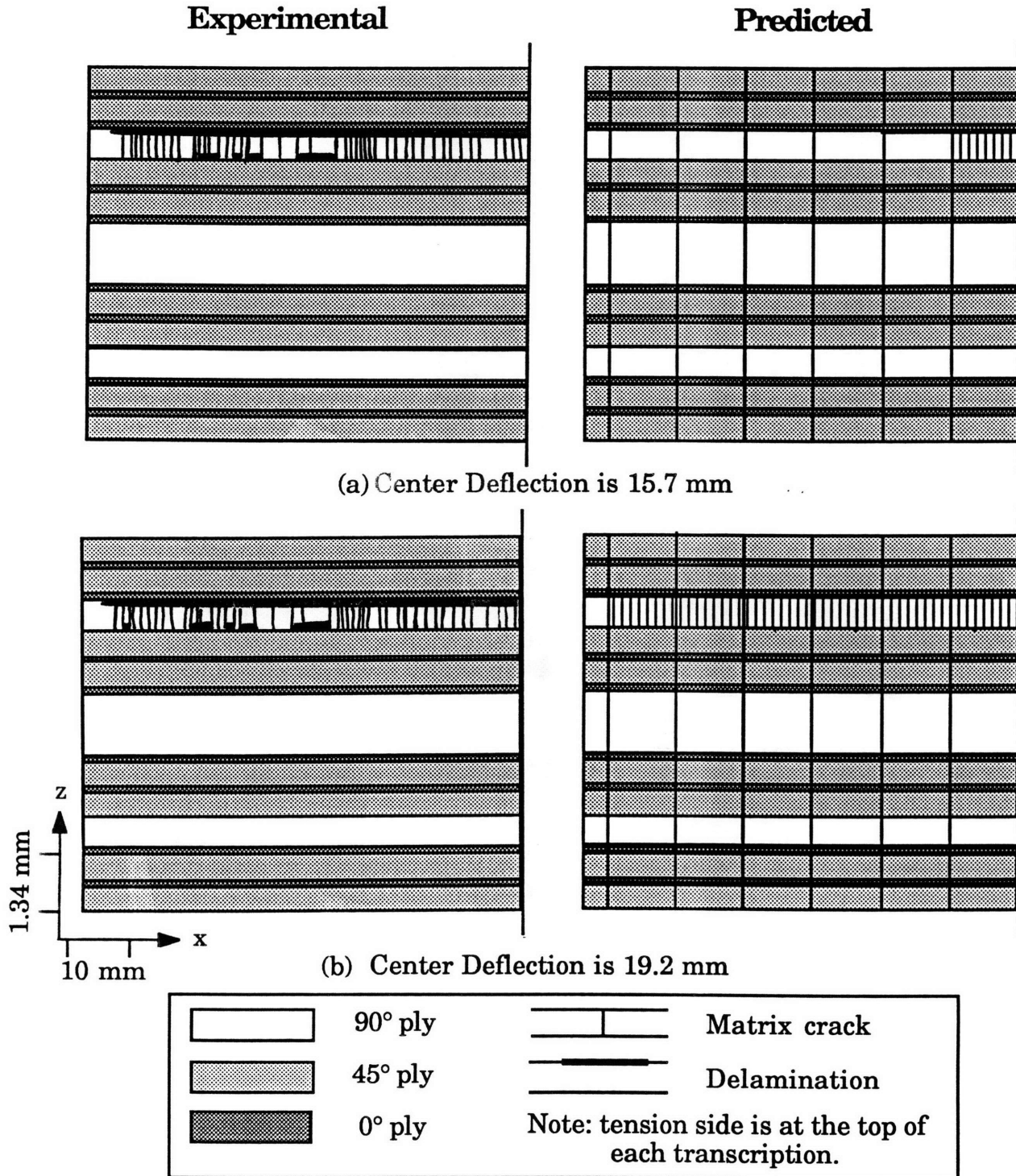


Figure 6.47 Predicted and experimental damage accumulation in the  $[(45^\circ_2/-45^\circ_2/0^\circ)_2/90^\circ_5]_{2s}$  layup (a) at the fourth damage state and (b) beyond.

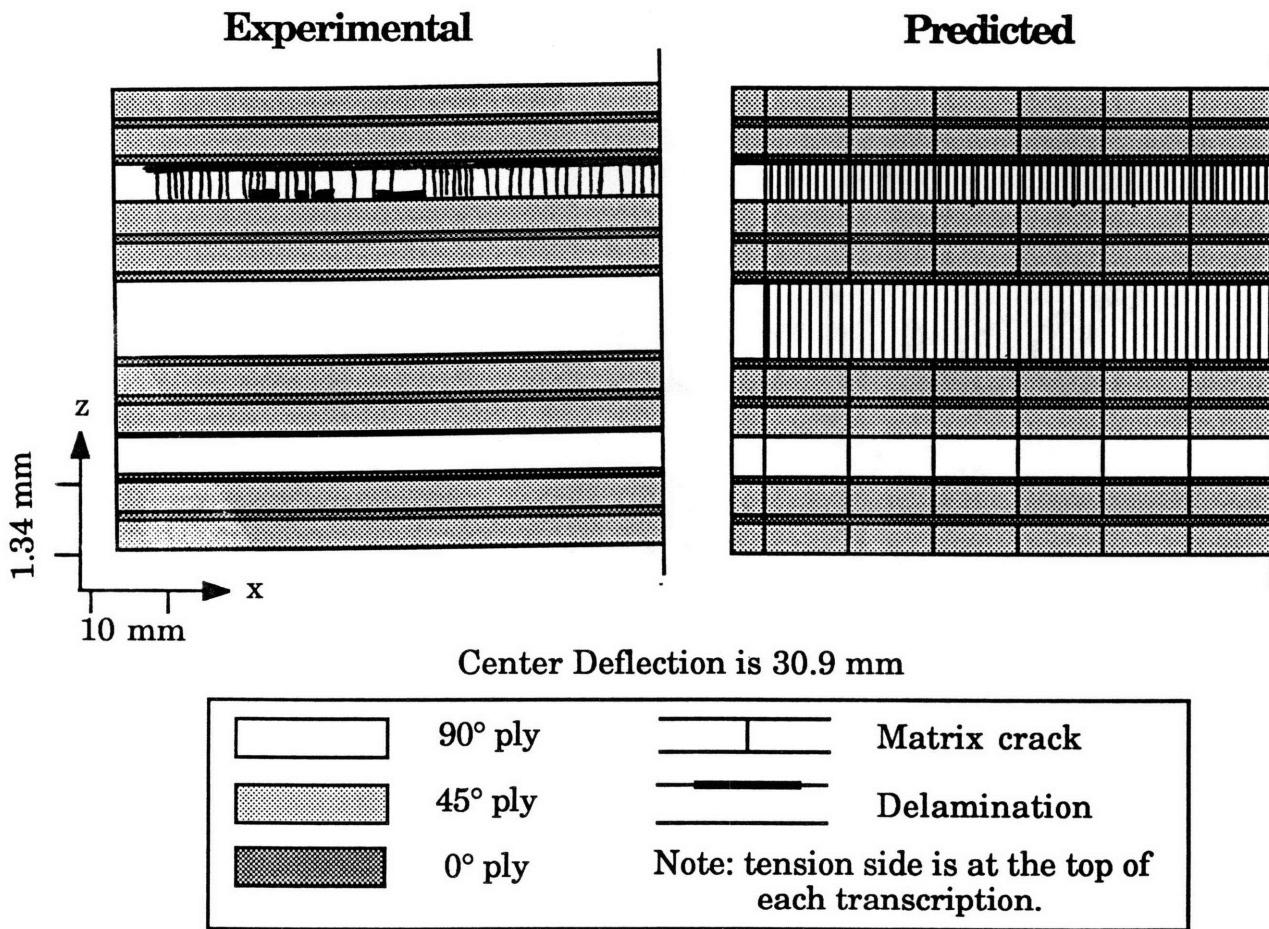


Figure 6.48 Predicted damage accumulation in the  $[(45^\circ_2/-45^\circ_2/0^\circ)_2/90^\circ_5]_{2s}$  layup beyond the fourth damage state.

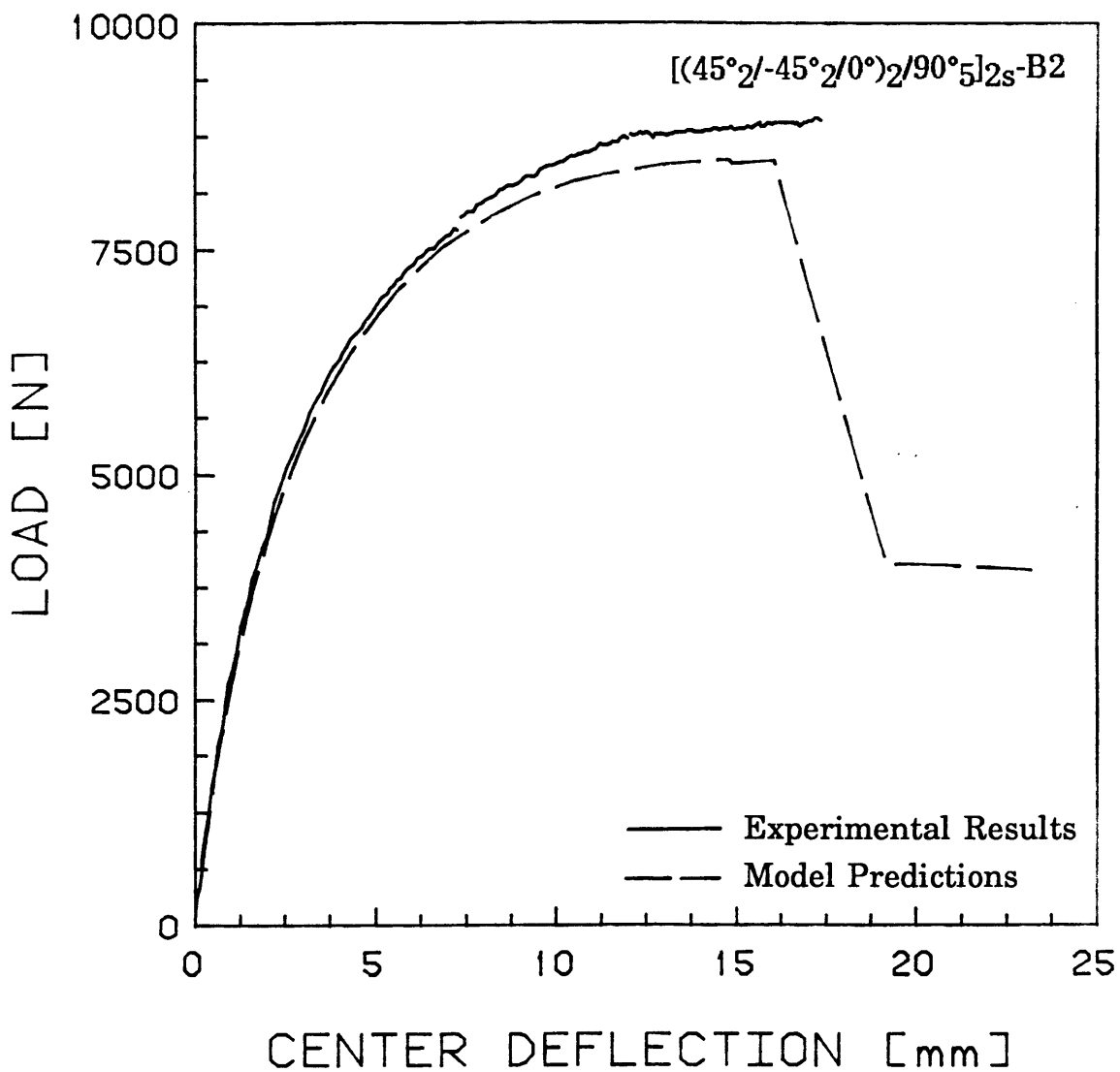


Figure 6.49 Experimental and predicted load versus deflection for  $[(45^\circ_2/-45^\circ_2/0^\circ)_2/90^\circ_5]_{2s}$  layup.

*Chapter 7***DISCUSSION****7.1 Evaluation of the Experiment****7.1.1 The Specimen**

The specimen and test setup met the three criteria set for them. The stress state was straightforward, with strain varying sinusoidally along the length of the specimen and linearly through the thickness. The location of damage initiation was predictable and not directly affected by the load introduction. When damage initiation is affected directly by the boundary conditions, as is often the case in plates constrained at all the edges, complex stress states at the boundaries are often responsible. The progression of damage was observable for all three layups, as the initial damage was always in the form of matrix damage which did not coincide with ultimate failure. This made it possible to put together the three damage accumulation histories.

The load application was made eccentric in order to overcome the effects of friction at the specimens' ends. The eccentricity prevented the column from buckling initially as a clamped column, thus avoiding the high initial buckling load, and the associated stresses, which occurred before the column snapped to the simply-supported mode shape. This eccentricity also made the direction of the center deflection predictable. This was useful in determining the location of the deflection transducer.

The eccentricity was purposely made greater than was strictly necessary so as to make the specimen insensitive to any manufacturing

imperfections in the laminate. This exaggeration made the modelling of the eccentricity straightforward in that this nominal loading eccentricity could be used to accurately model the experiment. Both in terms of modelling and in terms of experimental procedure, the use of eccentric load application was very successful.

The test jig did have one shortcoming. It proved to be very difficult to reliably contain the specimen at ultimate failure. While the lips added to the end pieces reduced the number of instances when the specimen left the jig, there were still some specimens which were not successfully contained. The result of a specimen flying out of the jig is that the damage observed in that specimen after final failure will generally be more severe than that in a similar specimen which was contained.

Other than the shortcoming described above, the test setup worked very well.

### **7.1.2 Damage Detection Procedures**

The Load Drop Technique was used to detect the occurrence of damage, and edge replication and X-ray photography were used to collect data on damage accumulation. This combination proved to be a very effective means of obtaining the damage accumulation history of the layups examined in this work. The Load Drop Technique worked very reliably; examinations after the first two or three load drops usually showed no damage. The first sign of damage generally involved three or four cracks at most. The edge replicas provided very detailed, ply-by-ply information about crack accumulation and delaminations and their propagation at the specimens' edges. It is difficult to obtain such detailed data from the X-ray

photographs because they do not show where in the thickness any damage might be, or whether more than one ply is damaged. Furthermore, information such as crack separation is not as easy to obtain, as the cracks show up rather faintly. This would be expected, given that the cracks are generally contained in four plies in a sixty-ply specimen. However, these photographs clearly show how damage varies along the length of the specimens, and also how damage tends to form at the specimen edges and propagate inward across the width.

The combination of the Load Drop Technique, edge replication and X-ray photography proved to be a very effective means of obtaining the damage accumulation histories for the columns studied in this work.

## **7.2 Characteristics of Damage Accumulation**

In-plane damage initiated at the center of the specimens in the plies where it was expected at the stress levels predicted in all three specimen types. Crack density increased up to saturation, much as described in the literature about damage accumulation in the 90° plies of uniformly loaded laminates. In specimens where in-plane damage initiated in the 90° plies, damage was never observed in the 45° plies prior to final failure. Similarly, in specimens where damage initiated in the 45° plies, damage was never observed in the 90° plies prior to final failure. A significant effect of the stress field being gradient was that the crack density varied along the length according to the local stress levels, and crack density saturation was reached in the central region of the specimen first. In general, when matrix cracks appeared in more than one effective ply, crack density

saturation would be reached in the central region of the first ply before cracks would appear in the second ply.

The results of the destructive examinations show that there is little variation in in-plane damage across the width of the specimens. It was noted that there was some minor variation in matrix crack density across the width in all three specimen types. These variations, however, were considered to be insignificant.

Delamination initiation was observed to be closely tied to matrix cracks. This was expected as the shear stress in the specimens due to transverse deformation was never expected to exceed the maximum allowable interlaminar shear stress. Delamination damage invariably initiated around pre-existing cracks in the form of short, discontinuous delaminations. Delaminations always initiated on the side of the damaged ply nearer the surface, as stresses were higher there than on the other side because of bending in the specimen. These would then join to form a single delamination which spread longitudinally from the specimen center out toward the ends. The destructive examinations showed that there was less delamination damage at the specimen center than at the edges across the width. This indicates that such damage initiated at the edges, probably because of the interaction of the matrix cracks and the effects of the free edge, and propagated inward. The edge effects result in a three-dimensional stress state which exists because of the discontinuity in stresses in the transverse direction. These stresses must be zero at the free edges, but are nonzero in the specimen because of the Poisson's ratio mismatches between plies.

Milestones were recognized in the damage accumulation history of the three laminate types studied, and these were treated as characteristic

damage states. A characteristic damage state was generally considered to have been reached when matrix cracks or delaminations initiated in a specimen, or when such damage initiated in a new location in a previously damaged specimen. A characteristic damage state was also generally considered to have been reached when crack density reached saturation or when discontinuous delaminations became continuous. The point when damage initiated in a second location in a damaged specimen generally coincided with matrix cracks reaching crack density saturation or a discontinuous delamination becoming continuous at the location of the original damage. Four characteristic damage states were identified for each of the specimen types studied. In the cases of all three specimen types, none of the characteristic damage states included damage on the compression side of the specimens.

The damage described above had little effect on the global bending stiffness of the three specimen types studied in this investigation. As is shown in Table 6.4, the experimental Southwell buckling loads of the undamaged specimens exceed those of the specimens at the fourth characteristic damage state by less than 10% for all three specimen types. This is because, prior to final failure, there was no fiber breakage in the 0° plies, which carry most of the load in the specimens, and there was no delamination severe enough to split the specimens apart, thus reducing the bending stiffness. This, however, would not necessarily be true in different parts under more complex loading conditions.

Final failure in the  $[(45^\circ_2/-45^\circ_2/0^\circ)_2/90^\circ_5]_{2s}$  specimens occurred when matrix cracks appeared in the central 90° effective ply, causing a delamination to appear on both sides of the ply and propagate to the ends of the specimens. This effectively reduced the specimens to two laminates,

each with a much lower bending stiffness. In the other two specimen types, final failure was due to fiber breakage in the outermost  $0^\circ$  ply on the tension side. The reduction in bending stiffness due to this ply failure resulted in a higher center deflection and hence higher stresses in the next  $0^\circ$  ply, which subsequently failed. This process was repeated until stress levels were reduced enough for no further damage to occur. As a result of this ultimate failure mode, damage levels in these specimens were more severe after final failure than in the  $[(45^\circ_2/-45^\circ_2/0^\circ)_2/90^\circ_5]_{2S}$  specimens. Though most of this damage was on the tension side, there generally was some damage on the compression side, particularly on the specimens which were not contained by the test jig at final failure.

The results of the stress field being gradient were that the location of damage initiation was predictable. Matrix crack density varied along the length of the specimens, and would generally reach saturation in a given effective ply before cracks appeared in another ply. Delaminations, which always occurred around matrix cracks, initiated first on the side of the damaged ply where the stresses were higher. The extent of damage therefore varied throughout the specimen, and depended on the local stress levels and the extent of the damage in regions of higher stress.

### **7.3 Evaluation of the Model**

#### **7.3.1 The Finite Element Model**

A displacement-based finite element code was used to model the behavior of the specimens. Comparison of experimental results with model predictions show that agreement on load versus deflection and load versus strain behavior is excellent before material nonlinearities from the  $45^\circ$  plies

and from damage become important. After material nonlinearities become important, but before the occurrence of damage, agreement between the model and experimental results is good, though the models tend to exhibit a slightly lower flexural stiffness than was observed experimentally. After the occurrence of damage, model and experiment differ significantly because delamination propagation predictions tend to be inaccurate. The scheme used to find the stresses which were used to predict delamination propagation proved to be inadequate, in that delamination propagation was generally not accurately predicted. This is discussed in more detail below.

The model did have one shortcoming: due to the aspect ratio of the elements used, normal and shear stresses through the thickness could not be obtained directly. Average values for these were obtained for each element from the nodal forces. These aspect ratios varied from 16 to 83, depending on the effective ply thickness. An aspect ratio near unity is considered ideal. This shortcoming could have been overcome by using more elements along the length, thus improving the element aspect ratio. Obtaining an ideal aspect ratio of one would have significantly increased the number of degrees of freedom in the model, and hence the computation time needed.

### **7.3.2 Material Nonlinearity**

The material nonlinearities of the 45° plies were modelled by updating the values of the stiffness and Poisson's ratio for each element modelling a 45° ply proportionally to element strain at each increment in end displacement. This was necessary because of ADINA's inability to model nonlinear orthotropic material properties directly. In Figures 6.25 to

6.30, the experimental results are compared with two versions of the model, one of which takes material nonlinearities into account, while the other does not. The material nonlinearities are less important in the  $[\pm 45^\circ/0^\circ/90^\circ_4]_{2s}$  layup due to the smaller proportion of  $45^\circ$  plies, as can be seen in Figures 6.27 and 6.28. The models of the other two layups exhibit a slightly lower flexural stiffness than the experimental results when these nonlinearities are accounted for. This discrepancy comes about because of the manner in which the material nonlinearities are modelled. The data used was obtained from tests of  $[\pm 45^\circ]_{2s}$  laminates under a uniaxial load. In the specimens studied in this investigation, the  $45^\circ$  plies were subjected to a biaxial state of stress because of the Poisson's ratio mismatch between plies. When the nonlinearities are ignored, the model and experimental results differ significantly at high strain levels.

In comparing the models with and without the material nonlinearities, the differences in results become noticeable at 6000  $\mu$ strain and become significant above 8000  $\mu$ strain, in that the applied loads in the two versions of the models differ by more than 5% in the models of the  $[45^\circ_4/-45^\circ_4/(0^\circ/90^\circ)_4]_{2s}$  and  $[(45^\circ_2/-45^\circ_2/0^\circ)_2/90^\circ_5]_{2s}$  specimen types.

This comparison shows that these nonlinearities cannot be ignored at the strain levels encountered in this work.

### **7.3.3 Damage Accumulation**

Damage initiation predictions matched the experimentally-observed damage initiations well both for in-plane and for delamination damage, in terms of load levels at which damage occurred. To predict the correct ply in which in-plane damage would initiate, the effects of effective ply thickness,

as described in Chapter 4, had to be taken into account. In-plane and delamination damage were predicted to occur simultaneously in all three models. However, in the  $[(45^{\circ}_2/-45^{\circ}_2/0^{\circ})_2/90^{\circ}_5]_{2s}$  and  $[\pm 45^{\circ}/0^{\circ}/90^{\circ}_4]_{2s}$  specimen types, matrix cracks were observed to precede delamination. Delaminations in the models tended to propagate too early and to a greater extent. This distorted the damage accumulation histories completely for the  $[(45^{\circ}_2/-45^{\circ}_2/0^{\circ})_2/90^{\circ}_5]_{2s}$  and  $[\pm 45^{\circ}/0^{\circ}/90^{\circ}_4]_{2s}$  layups, resulting in a predicted final failure mode for the  $[\pm 45^{\circ}/0^{\circ}/90^{\circ}_4]_{2s}$  layup which was incorrect. This would indicate that while the methods of predicting and modelling delaminations are adequate, a better method, or a finer finite element mesh, for predicting delamination propagation is needed. A finer mesh might improve the model because delamination initiation and propagation are both very localized phenomena. While the Quadratic Delamination Criterion has been proven reliable for predicting delamination initiation, its use for the prediction of delamination propagation has not been established.

The destructive examinations show that, while there is little variation in damage across the width, and the variation in crack density is believed to be of little consequence, the variation in delamination damage across the width may be important. Taking edge effects into account might help improve the predictions of damage initiation and would be particularly important in predictions of delamination propagation, as these edge effects probably cause damage to initiate at the edges rather than away from them. While the occurrence of delaminations which appeared at the edges was predicted quite accurately, these delaminations did not necessarily propagate all the way across the width of the specimens as soon as delaminations appeared at the edges. However, when a delamination was

predicted in the model, as the model is two-dimensional, a delamination was effectively introduced across the entire width. When the delamination does not go all the way across the specimen, the bending stiffness is not reduced by as great an extent. The lower bending stiffness in the models leads to higher deflections and higher strains, and thus higher predicted shear stresses.

As they stand, the models do not predict the damage accumulation history accurately all the way to ultimate failure. However, global behavior prior to final failure is predicted accurately. Predictions of load versus deflection behavior are very good, as are the predictions of damage initiation, both in terms of in-plane and delamination damage. Though the final failure mode may not be correctly predicted, the point in all three models where damage starts to become extensive, in that entire plies are removed from the model, can be used as a effective prediction of final failure.

*Chapter 8***CONCLUSIONS AND RECOMMENDATIONS**

A test program to study damage accumulation in simply-supported graphite/epoxy columns was designed and carried out. This was intended as the first step in the development of a design tool to assist in the design of composite structures operating in the postbuckled régime. The mechanisms of damage progression were studied, and the damage accumulation histories of three layups were compiled experimentally and modelled with two-dimensional displacement-based finite element models. In-plane damage was predicted on an element by element basis with the Maximum Stress failure criterion. Delamination was predicted with the Quadratic Delamination Criterion, again on an element by element basis. From this work, the following conclusions have been drawn:

1. A narrow simply-supported column is a good specimen for the study of progressive failure mechanisms, because the stress state in the column is relatively simple, and the lengthwise location of damage initiation is predictable. Eccentricity is necessary in the load application to avoid initial buckling as a clamped column.
2. The Load Drop Technique, in combination with edge replication and X-ray photography, is an excellent tool for obtaining the damage accumulation history of a column specimen.
3. In the specimens studied, delaminations invariably initiated at shear stress concentrations at matrix cracks.

4. In specimens where matrix damage occurred in more than one effective ply, crack density generally reached saturation in the first effective ply to be damaged before cracks appeared in the second ply.
5. Prior to ultimate failure, the damage observed in all three specimen types had little effect on the global bending stiffness of the specimens, as no  $0^\circ$  plies were damaged.
6. Destructive examinations show that the assumption that in-plane damage does not vary across the width is reasonable. However, the effects of the three-dimensional state of stress at the free edges are such that the widthwise variations in delamination damage cannot be ignored.
7. Prior to final failure, damage was seen only on the tension side of the specimens. After final failure, damage extended slightly past the centerline parallel to the x-axis on some specimens.
8. In the  $[45^\circ_4/-45^\circ_4/(0^\circ/90^\circ)_4]_{2s}$  and  $[\pm 45^\circ/0^\circ/90^\circ_4]_{2s}$  specimen types, final failure occurred when the  $0^\circ$  plies on the tension side failed. In  $[(45^\circ_2/-45^\circ_2/0^\circ)_2/90^\circ_5]_{2s}$  specimen type, final failure occurred when delaminations initiated on either side of the central  $90^\circ$  effective ply and propagated to the ends of the specimens.
9. The finite element method is a good way of modelling the stress state in the specimen, as it is flexible enough to model complex damage states.
10. The material nonlinearities of the  $45^\circ$  plies are important in laminates made up of 50% or more  $45^\circ$  plies at strain levels exceeding  $8000 \mu\text{strain}$ , and thus cannot be ignored.

11. With the exceptions of the compressive longitudinal maximum allowable stress and the tensile transverse maximum allowable stress in plies of single-ply effective thickness, the failure criteria used predicted damage initiation well.

12. The scheme used to predict delamination propagation is inadequate.

Based on the results of this work, the following recommendations are made for future work:

1. The modelling of the material nonlinearities of the  $45^\circ$  plies needs to be extended to multiaxial stress states.
2. The importance of the three-dimensional state of stress at matrix cracks at the free edges, and its effect on delamination initiation and propagation both along the length and across the width of the specimens, must be understood and incorporated into the model.
3. The scheme for predicting delamination propagation must be improved. This may be achieved with a finer mesh or through the use of a different criterion.
4. Maximum stress allowables for the compressive longitudinal stress and for the tensile transverse stress in plies of single-ply effective ply thickness must be updated. Associated phenomena must be more clearly understood.
5. Fatigue tests should be conducted on postbuckled column specimens in order to study damage accumulation in a gradient stress field under cyclic loading.

6. Damage accumulation should be studied in a buckled plate in order to examine the progression of damage in the transverse direction as well as along the length of a specimen.

**REFERENCES**

1. Euler, L. "De Curvis Elasticis," Methodus inveniendi lineas curvas maximi minimive proprietate gaudentes, Lausanne & Geneva, 1744.
2. Leissa, A.W., "Buckling of Laminated Composite Plates and Shell Panels," Technical Report AFWAL-TR-85-3069, 1985.
3. Reissner, E. & Stavsky, Y., "Bending and Stretching of Certain Types of Heterogeneous Anisotropic Elastic Plates," Transactions of ASME, *Journal of Applied Mechanics*, Vol.28, No. 3, September 1961.
4. Kicher, T.P. & Mandell, J.F., "A Study of the Buckling of Laminated Composite Plates," *AIAA Journal*, Vol.9, No. 4, April 1971.
5. Ashton, J.E. & Love, T.S., "Experimental Study of the Stability of Composite Plates," *Journal of Composite Materials*, Vol. 3, April 1969.
6. Southwell, R.V., "On the Analysis of Experimental Observations in Problems of Elastic Stability," Proceedings of the Royal Society of London, ser. A, Vol.135, London 1932.
7. Minguet, P.J., Dugundji, J. & Lagace, P.A., "Postbuckling Behavior of Laminated Plates using a Direct Energy Minimization Technique," to be published in the *AIAA Journal*.
8. Jensen, D.W. & Lagace, P.A., "Influence of Mechanical Couplings on the Buckling and Post-Buckling of Anisotropic Plates," *AIAA Journal*, Vol. 26, No. 10, October 1988.

9. Dinardo, M.T. & Lagace, P.A., "Buckling and Postbuckling Behavior of Laminated Composite Plates with Ply dropoffs," *AIAA Journal*, Vol. 27, No. 4, April 1989.
10. Starnes, Jr., J.H. & Rouse, M., "Postbuckling and Failure Characteristics of Selected Flat Rectangular Graphite/Epoxy Plates Loaded in Compression," AIAA/ASME/ASCE/AHS 22nd SDM Conference, Atlanta, Georgia, April 1981.
11. Starnes, Jr., J.H., Knight, Jr., N.F. & Rouse, M., "Postbuckling Behavior of Selected Flat Stiffened Graphite-Epoxy Panels Loaded in Compression," *AIAA Journal*, Vol. 23, August 1983.
12. Nahas, M.N., "Survey of Failure and Post-Failure Theories of Laminated Fiber-Reinforced Composites," *Journal of Composites Technology & Research*, Vol. 8, No. 4, Winter 1986.
13. Hill, R., "The Mathematical Theory of Plasticity," Oxford University Press, 1950.
14. Tsai, S.W. & Wu, E.M., "A Generalized Theory of Strength for Anisotropic Materials," *Journal Of Composite Materials*, Vol. 5, 1971.
15. Dvorak, G.J. & Laws, N., "Analysis of Progressive Matrix Cracking in Composite Laminates II. First Ply Failure," *Journal of Composite Materials*, Vol. 21, April 1987.
16. Brewer, J.C. & Lagace P.A., "Quadratic Stress Criterion for Initiation of Delamination," *Journal of Composite Materials*, Vol. 22, 1988.

17. Kassapoglou, C. & Lagace, P.A., "An Efficient Method for the Calculation of Interlaminar Stresses in Composite Materials," *Journal of Applied Mechanics*, Vol. 108, 1986.
18. Rybicki, E.F., Schmeuser, D.W. & Fox, J., "An Energy Release Rate Approach for Stable Crack Growth in the Free-Edge Delamination Problem," *Journal of Composite Materials*, Vol. 11, October 1977.
19. Wang, A.S.D. & Crossman, F.W., "Initiation and Growth of Transverse Cracks and Edge Delaminations in Composite Laminates. Part 1. An Energy Method," *Journal of Composite Materials*, Vol. 14, Supplement, 1980.
20. O'Brien, T.K., "Characteristics of Delamination and Growth in a Composite Laminate," *Damage in Composite Materials*, ASTM STP 775, K.L. Reifsnider, ed., ASTM 1982.
21. Highsmith A.L. & Reifsnider K.L., "Stiffness-Reduction Mechanisms in Composite Materials," *Damage in Composite Materials*, ASTM STP 775, 1982.
22. Sun, C.T. & Jen, K.C., "On the Effect of Matrix Cracks on Laminate Strength," *Journal of Reinforced Plastics and Composites*, Vol. 6, July 1987.
23. Talug, A., "Analysis of Stress Fields in Composite Laminates with Interior Cracks," Virginia Polytechnic Institute and State University Ph.D. thesis, 1978.

24. Hahn, H.T. & Tsai, S.W., "On the Behavior of Composite Laminates after Initial Failures," *Journal Composite Materials*, Vol.8, July 1974.
25. Swanson, S.R. & Christoforou, A.P., "Progressive Failure in Carbon/Epoxy Laminates under Biaxial Stress," Transactions of the ASME, Vol. 109, January 1987.
26. Ochoa O.O. & Engblom J. J., "Analysis of Progressive Failure in Composites," *Composites Science and Technology* 0266-3538/87, 1987.
27. Chang, Fu-Kuo & Chang Kuo-Yen, "A Progressive Damage Model for Laminated Composites Conyaining Stress Concentrations," *Journal of Composite Materials*, V. 21, September 1987.
28. Dvorak, G.J. & Laws, N., "Analysis of Matrix Cracking in Composite Laminates: Theory and Experiment," ASME Proceodings of the Winter Annual Meeting, New Orleans, LA, December 1984.
29. Flaggs, D.L. & Kural, M.H., "Experimental Determination of the In Situ Transverse Lamina Strength in Graphite/Epoxy Laminates," *Journal Composite Materials*, Vol. 16, March 1982.
30. Lagace, P.A. & Vizzini, A.J., "The Sandwich Column as a Compressive Characterization Specimen for Thin Laminates," *Composite Materials: Testing and Design* (8th Conference), ASTM STP 972, Philadelphia, 1988.
31. Vizzini, A.J. & Lagace, P.A., "The Role of PLY Buckling in the Compressive Failure of Graphite/Epoxy Tubes," *AIAA Journal*, Vol. 23, 1985.

32. Chatterjee, S.N., Pindera, M.J., Pipes, R.B. & Dick, B., "Composite Defect Significance," Report No. NADC-81034-60, Material Science Corp., Spring House, PA, November 1982.
33. *Automated Dynamic Incremental Nonlinear Analysis: User's Manual*, Report ARD 84-1, ADINA R & D, Inc., December 1984.
34. Lagace, P.A., "Nonlinear Stress-Strain Behavior of Graphite/Epoxy Laminates," *AIAA Journal*, Vol. 23, No. 10, October 1985.
35. Unpublished Experimental Data for Hercules AS4/3501-6 graphite/epoxy material system, Technology Laboratory for Advanced Composites, Massachusetts Institute of Technology, Cambridge, MA.
36. Tsai, S.W. & Hahn, H.T., *Introduction to Composite Materials*, Technomic Publishing Company, Westport, Ct, 1980.
37. Lagace, P.A., Brewer, J.C. & Varnerin, C.F., *TELAC Manufacturing Course Notes*, Technology Laboratory for Advanced Composites, TELAC Report 88-4, M.I.T., 1988.
38. Brewer, J.C., "The Effect of Ply Thickness on the Free Edge Delamination of Graphite/Epoxy Laminates," M.I.T. Master's Thesis, 1986.
39. Reifsnider, K.L. & Masters, J.E., "Investigation of Characteristic Damage States in Composite Materials," ASME Winter Annual Meeting, San Francisco, California, December 1978.

## **Appendix A**

This Appendix contains the ADINA inputs for the finite element models types for the initial thirty-five point runs. These inputs are manipulated by a pre-processor which essentially reduces them to tables of numbers, which are themselves the input to the finite element code.

The first part of the input deals with the global degrees of freedom, the type of analysis to be run, including the type of iteration scheme to be used, and the results to be printed out. The next part is made up of the coordinates of the nodes at the ends of the models. This is followed by the material properties, and then the element groups. In the element groups, the "GSURFACE" commands generate meshes of elements within the four specified nodes. As these inputs are for models of undamaged specimens with linear material properties, there are only three element groups, one for each of the three ply orientations. The last part of the inputs determines the boundary conditions.

## Part 1

```
HEADING ' F-TYPICAL; e=2.59, E=nom, S11 '  
*  
MASTER IDOF=100111 NSTEP=35 REACTIONS=NO  
*  
ANALYSIS TYPE=STATIC  
*  
KINEMATICS DISPLACEMENT=LARGE STRAINS=SMALL  
*  
AUTOMATIC-ITERATION NODE=18 DIRECTION=2 DISPLACEMENT=.015 DISPMAX=11  
*  
TOLERANCES PRINT=NO  
*  
PRINTOUT VOLUME=MINIMUM IOUTPT=1 PRINTDEFAULT=NO  
*  
PRINTSTEPS FIRST1=1 LAST1=35 INCR1=1  
*  
PRINTNODES FIRST1=18 LAST1=18 INCR1=1 FIRST2=98 LAST2=98 INCR2=1  
*
```

## Part 2

\* Coordinates at ends; lengths in mm.

COORDINATES

ENTRIES NODE Y Z

1 0 0

STEP 1 TO

9 0 1.0616

STEP 1 TO

25 0 2.1232

STEP 1 TO

33 0 3.1848

STEP 1 TO

65 0 5.308

STEP 1 TO

73 0 6.3696 -

STEP 1 TO

89 0 7.4312

STEP 1 TO

97 0 8.4928

\*

98 112 0

STEP 1 TO

106 112 1.0616

STEP 1 TO

122 112 2.1232

STEP 1 TO

130 112 3.1848

STEP 1 TO

162 112 5.308

STEP 1 TO

170 112 6.3696

STEP 1 TO

186 112 7.4312

STEP 1 TO

194 112 8.4928

\*

## Part 3

- \* Material properties for 45 degree plies; note: all stiffness values
- \* are in GPa.

MATERIAL N=1 TYPE=ORTHOTROPIC EA=20.85 EB=9.81 EC=20.85,  
 NUAB=.0735 NUAC=.737 NUBC=.3 GAB=5.4 GAC=36.71 GBC=5.4 DENSITY=1.52

\*

- \* Material properties for 0 degree plies

MATERIAL N=2 TYPE=ORTHOTROPIC EA=142 EB=9.81 EC=9.81,  
 NUAB=.0207 NUAC=.0207 NUBC=.34 GAB=6.0 GAC=6.0 GBC=4.8 DENSITY=1.52

\*

- \* Material properties for 90 degree plies

MATERIAL N=3 TYPE=ORTHOTROPIC EA=9.81 EB=9.81 EC=142,  
 NUAB=.34 NUAC=.3 NUBC=.3 GAB=4.8 GAC=6.0 GBC=6.0 DENSITY=1.52

\*

- \* Material properties for all non-linear 45's 4500<math>\epsilon\_{11}</math>5500.

MATERIAL N=4 TYPE=ORTHOTROPIC EA=20 EB=9.81 EC=20.85,  
 NUAB=.0735 NUAC=.758 NUBC=.3 GAB=5.4 GAC=36.71 GBC=5.4 DENSITY=1.52

\*

- \* Material properties for tensile non-linear 45's 5500<math>\epsilon\_{11}</math>6500.

MATERIAL N=5 TYPE=ORTHOTROPIC EA=18.58 EB=9.81 EC=20.85,  
 NUAB=.0735 NUAC=.785 NUBC=.3 GAB=5.4 GAC=36.71 GBC=5.4 DENSITY=1.52

\*

- \* Material properties for compressive non-linear 45's 5500<math>\epsilon\_{11}</math>6500.

MATERIAL N=6 TYPE=ORTHOTROPIC EA=18.93 EB=9.81 EC=20.85,  
 NUAB=.0735 NUAC=.759 NUBC=.3 GAB=5.4 GAC=36.71 GBC=5.4 DENSITY=1.52

\*

- \* Material properties for tensile non-linear 45's 6500<math>\epsilon\_{11}</math>7500.

- \* and for compressive non-linear 45's 7500<math>\epsilon\_{11}</math>8500 (nu12=.759)

MATERIAL N=7 TYPE=ORTHOTROPIC EA=17.25 EB=9.81 EC=20.85,  
 NUAB=.0735 NUAC=.821 NUBC=.3 GAB=5.4 GAC=36.71 GBC=5.4 DENSITY=1.52

\*

- \* Material properties for compressive non-linear 45's 6500<math>\epsilon\_{11}</math>7500.

MATERIAL N=8 TYPE=ORTHOTROPIC EA=17.97 EB=9.81 EC=20.85,  
 NUAB=.0735 NUAC=.759 NUBC=.3 GAB=5.4 GAC=36.71 GBC=5.4 DENSITY=1.52

\*

- \* Material properties for tensile non-linear 45's 7500<math>\epsilon\_{11}</math>8500.

MATERIAL N=9 TYPE=ORTHOTROPIC EA=16.25 EB=9.81 EC=20.85,  
 NUAB=.0735 NUAC=.826 NUBC=.3 GAB=5.4 GAC=36.71 GBC=5.4 DENSITY=1.52

\*

- \* Material properties for tensile non-linear 45's 8500<math>\epsilon\_{11}</math>9500.

MATERIAL N=10 TYPE=ORTHOTROPIC EA=15.10 EB=9.81 EC=20.85,  
 NUAB=.0735 NUAC=.865 NUBC=.3 GAB=5.4 GAC=36.71 GBC=5.4 DENSITY=1.52

\*

- \* Material properties for compressive non-linear 45's 8500<math>\epsilon\_{11}</math>9500.

MATERIAL N=11 TYPE=ORTHOTROPIC EA=16 EB=9.81 EC=20.85,  
 NUAB=.0735 NUAC=.759 NUBC=.3 GAB=5.4 GAC=36.71 GBC=5.4 DENSITY=1.52

\*

- \* Material properties for tensile non-linear 45's 9500<math>\epsilon\_{11}</math>10500.

MATERIAL N=12 TYPE=ORTHOTROPIC EA=14.19 EB=9.81 EC=20.85,  
 NUAB=.0735 NUAC=.880 NUBC=.3 GAB=5.4 GAC=36.71 GBC=5.4 DENSITY=1.52

\*

- \* Material properties for compressive non-linear 45's 9500<math>\epsilon\_{11}</math>10500.

MATERIAL N=13 TYPE=ORTHOTROPIC EA=15.05 EB=9.81 EC=20.85,  
 NUAB=.0735 NUAC=.759 NUBC=.3 GAB=5.4 GAC=36.71 GBC=5.4 DENSITY=1.52

\*  
 \* Material properties for tensile non-linear 45's 10500<e11<11500.  
 MATERIAL N=14 TYPE=ORTHOTROPIC EA=13.44 EB=9.81 EC=20.85,  
 NUAB=.0735 NUAC=.939 NUBC=.3 GAB=5.4 GAC=36.71 GBC=5.4 DENSITY=1.52  
 \*

\* Material properties for compressive non-linear 45's 10500<e11<11500.  
 MATERIAL N=15 TYPE=ORTHOTROPIC EA=14.25 EB=9.81 EC=20.85,  
 NUAB=.0735 NUAC=.759 NUBC=.3 GAB=5.4 GAC=36.71 GBC=5.4 DENSITY=1.52  
 \*

\* Material properties for tensile non-linear 45's 11500<e11<12500.  
 MATERIAL N=16 TYPE=ORTHOTROPIC EA=12.45 EB=9.81 EC=20.85,  
 NUAB=.0735 NUAC=1.0 NUBC=.3 GAB=5.4 GAC=36.71 GBC=5.4 DENSITY=1.52  
 \*

\* Material properties for compressive non-linear 45's 11500<e11<12500.  
 MATERIAL N=17 TYPE=ORTHOTROPIC EA=13.28 EB=9.81 EC=20.85,  
 NUAB=.0735 NUAC=.757 NUBC=.3 GAB=5.4 GAC=36.71 GBC=5.4 DENSITY=1.52  
 \*

\* Material properties for tensile non-linear 45's 12500<e11<13500.  
 MATERIAL N=18 TYPE=ORTHOTROPIC EA=11.53 EB=9.81 EC=20.85,  
 NUAB=.0735 NUAC=1.126 NUBC=.3 GAB=5.4 GAC=36.71 GBC=5.4 DENSITY=1.52  
 \*

\* Material properties for compressive non-linear 45's 12500<e11<13500.  
 MATERIAL N=19 TYPE=ORTHOTROPIC EA=12.38 EB=9.81 EC=20.85,  
 NUAB=.0735 NUAC=.752 NUBC=.3 GAB=5.4 GAC=36.71 GBC=5.4 DENSITY=1.52  
 \*

\* Material properties for tensile non-linear 45's 13500<e11<14500.  
 MATERIAL N=20 TYPE=ORTHOTROPIC EA=10.74 EB=9.81 EC=20.85,  
 NUAB=.0735 NUAC=1.223 NUBC=.3 GAB=5.4 GAC=36.71 GBC=5.4 DENSITY=1.52  
 \*

\* Material properties for compressive non-linear 45's 13500<e11<14500.  
 MATERIAL N=21 TYPE=ORTHOTROPIC EA=11.64 EB=9.81 EC=20.85,  
 NUAB=.0735 NUAC=.749 NUBC=.3 GAB=5.4 GAC=36.71 GBC=5.4 DENSITY=1.52  
 \*

\* Material properties for tensile non-linear 45's 14500<e11<15500.  
 MATERIAL N=22 TYPE=ORTHOTROPIC EA=10.07 EB=9.81 EC=20.85,  
 NUAB=.0735 NUAC=1.327 NUBC=.3 GAB=5.4 GAC=36.71 GBC=5.4 DENSITY=1.52  
 \*

\* Material properties for compressive non-linear 45's 14500<e11<15500.  
 MATERIAL N=23 TYPE=ORTHOTROPIC EA=10.97 EB=9.81 EC=20.85,  
 NUAB=.0735 NUAC=.747 NUBC=.3 GAB=5.4 GAC=36.71 GBC=5.4 DENSITY=1.52  
 \*

\* Material properties for tensile non-linear 45's 15500<e11<16500.  
 MATERIAL N=24 TYPE=ORTHOTROPIC EA=9.47 EB=9.81 EC=20.85,  
 NUAB=.0735 NUAC=1.406 NUBC=.3 GAB=5.4 GAC=36.71 GBC=5.4 DENSITY=1.52  
 \*

\* Material properties for compressive non-linear 45's 15500<e11<16500.  
 MATERIAL N=25 TYPE=ORTHOTROPIC EA=10.39 EB=9.81 EC=20.85,  
 NUAB=.0735 NUAC=.726 NUBC=.3 GAB=5.4 GAC=36.71 GBC=5.4 DENSITY=1.52  
 \*

\* Material properties for tensile non-linear 45's 16500<e11<17500.  
 MATERIAL N=26 TYPE=ORTHOTROPIC EA=8.94 EB=9.81 EC=20.85,  
 NUAB=.0735 NUAC=1.4 NUBC=.3 GAB=5.4 GAC=36.71 GBC=5.4 DENSITY=1.52  
 \*

\* Material properties for compressive non-linear 45's  $16500 < \epsilon_{11} < 17500$ .  
MATERIAL N=27 TYPE=ORTHOTROPIC EA=9.88 EB=9.81 EC=20.85,  
NUAB=.0735 NUAC=.708 NUBC=.3 GAB=5.4 GAC=36.71 GBC=5.4 DENSITY=1.52

\*

\* Material properties for damaged 90 degree plies.  
MATERIAL N=30 TYPE=ORTHOTROPIC EA=0.01 EB=9.81 EC=142.,  
NUAB=.0034 NUAC=.003 NUBC=.3 GAB=0.01 GAC=0.01 GBC=6 DENSITY=1.52

\*

\* Material for trusses.  
MATERIAL N=31 TYPE=NONLINEAR-ELASTIC  
1000 100  
0 0  
-1000 -100000

\*

## Part 4

```

EGROUP N=1 TYPE=PLANE SUBTYPE=STRESS2 MATERIAL=1 RESULTS=TABLES
*
GSURFACE N1=194 N2=97 N3=89 N4=186 EL1=10 EL2=4 NODES=8 NCOINCIDE=ALL
GSURFACE N1=170 N2=73 N3=65 N4=162 EL1=10 EL2=4 NODES=8 NCOINCIDE=ALL
*
GSURFACE N1=130 N2=33 N3=25 N4=122 EL1=10 EL2=4 NODES=8 NCOINCIDE=ALL
GSURFACE N1=106 N2=9 N3=1 N4=98 EL1=10 EL2=4 NODES=8 NCOINCIDE=ALL
*
STRESSTABLE 1 P1=9
*
EDATA
ENTRIES EL THICK PRINT
1 38.5 YES TO 160 38.5 YES
*
EGROUP N=2 TYPE=PLANE SUBTYPE=STRESS2 MATERIAL=2 RESULTS=TABLES
*
STRESSTABLE 1 P1=9
*
GSURFACE N1=186 N2=89 N3=87 N4=184 EL1=10 EL2=1 NODES=8 NCOINCIDE=BOUNDARIES
GSURFACE N1=182 N2=85 N3=83 N4=180 EL1=10 EL2=1 NODES=8 NCOINCIDE=BOUNDARIES
GSURFACE N1=178 N2=81 N3=79 N4=176 EL1=10 EL2=1 NODES=8 NCOINCIDE=BOUNDARIES
GSURFACE N1=174 N2=77 N3=75 N4=172 EL1=10 EL2=1 NODES=8 NCOINCIDE=BOUNDARIES
*
GSURFACE N1=162 N2=65 N3=63 N4=160 EL1=10 EL2=1 NODES=8 NCOINCIDE=BOUNDARIES
GSURFACE N1=158 N2=61 N3=59 N4=156 EL1=10 EL2=1 NODES=8 NCOINCIDE=BOUNDARIES
GSURFACE N1=154 N2=57 N3=55 N4=152 EL1=10 EL2=1 NODES=8 NCOINCIDE=BOUNDARIES
GSURFACE N1=150 N2=53 N3=51 N4=148 EL1=10 EL2=1 NODES=8 NCOINCIDE=BOUNDARIES
*
GSURFACE N1=144 N2=47 N3=45 N4=142 EL1=10 EL2=1 NODES=8 NCOINCIDE=BOUNDARIES
GSURFACE N1=140 N2=43 N3=41 N4=138 EL1=10 EL2=1 NODES=8 NCOINCIDE=BOUNDARIES
GSURFACE N1=136 N2=39 N3=37 N4=134 EL1=10 EL2=1 NODES=8 NCOINCIDE=BOUNDARIES
GSURFACE N1=132 N2=35 N3=33 N4=130 EL1=10 EL2=1 NODES=8 NCOINCIDE=BOUNDARIES
*
GSURFACE N1=120 N2=23 N3=21 N4=118 EL1=10 EL2=1 NODES=8 NCOINCIDE=BOUNDARIES
GSURFACE N1=116 N2=19 N3=17 N4=114 EL1=10 EL2=1 NODES=8 NCOINCIDE=BOUNDARIES
GSURFACE N1=112 N2=15 N3=13 N4=110 EL1=10 EL2=1 NODES=8 NCOINCIDE=BOUNDARIES
GSURFACE N1=108 N2=11 N3=9 N4=106 EL1=10 EL2=1 NODES=8 NCOINCIDE=BOUNDARIES
*
EDATA
ENTRIES EL THICK PRINT
1 38.5 NO TO 160 38.5 NO
*
EGROUP N=3 TYPE=PLANE SUBTYPE=STRESS2 MATERIAL=3 RESULTS=TABLES
*
STRESSTABLE 1 P1=9
*
GSURFACE N1=184 N2=87 N3=85 N4=182 EL1=10 EL2=1 NODES=8 NCOINCIDE=BOUNDARIES
GSURFACE N1=180 N2=83 N3=81 N4=178 EL1=10 EL2=1 NODES=8 NCOINCIDE=BOUNDARIES
GSURFACE N1=176 N2=79 N3=77 N4=174 EL1=10 EL2=1 NODES=8 NCOINCIDE=BOUNDARIES
GSURFACE N1=172 N2=75 N3=73 N4=170 EL1=10 EL2=1 NODES=8 NCOINCIDE=BOUNDARIES
*

```

GSURFACE N1=160 N2=63 N3=61 N4=158 EL1=10 EL2=1 NODES=8 NCOINCIDE=BOUNDARIES  
GSURFACE N1=156 N2=59 N3=57 N4=154 EL1=10 EL2=1 NODES=8 NCOINCIDE=BOUNDARIES  
GSURFACE N1=152 N2=55 N3=53 N4=150 EL1=10 EL2=1 NODES=8 NCOINCIDE=BOUNDARIES  
GSURFACE N1=148 N2=51 N3=47 N4=144 EL1=10 EL2=2 NODES=8 NCOINCIDE=BOUNDARIES  
GSURFACE N1=142 N2=45 N3=43 N4=140 EL1=10 EL2=1 NODES=8 NCOINCIDE=BOUNDARIES  
GSURFACE N1=138 N2=41 N3=39 N4=136 EL1=10 EL2=1 NODES=8 NCOINCIDE=BOUNDARIES  
GSURFACE N1=134 N2=37 N3=35 N4=132 EL1=10 EL2=1 NODES=8 NCOINCIDE=BOUNDARIES

\*

GSURFACE N1=122 N2=25 N3=23 N4=120 EL1=10 EL2=1 NODES=8 NCOINCIDE=BOUNDARIES  
GSURFACE N1=118 N2=21 N3=19 N4=116 EL1=10 EL2=1 NODES=8 NCOINCIDE=BOUNDARIES  
GSURFACE N1=114 N2=17 N3=15 N4=112 EL1=10 EL2=1 NODES=8 NCOINCIDE=BOUNDARIES  
GSURFACE N1=110 N2=13 N3=11 N4=108 EL1=10 EL2=1 NODES=8 NCOINCIDE=BOUNDARIES

\*

EDATA

ENTRIES EL THICK PRINT

1 38.5 NO TO 160 38.5 NO

## Part 5

```
*  
* This end is clamped, but allowed to slide up.  
BOUNDARIES IDOF=110111 TYPE=NODES  
98 TO 194  
*  
* This end is on a roller.  
BOUNDARIES IDOF=101011 TYPE=NODES  
18  
*  
* Load is in kN.  
LOADS CONCENTRATED  
18 2 1  
*  
ADINA  
*  
END
```

## Part 1

```
HEADING ' N-TYPICAL, E=LIN, e=2.55, L=112, S11 '  
*  
MASTER IDOF=100111 NSTEP=1 REACTIONS=NO  
*  
ANALYSIS TYPE=STATIC  
*  
KINEMATICS DISPLACEMENT=LARGE STRAINS=SMALL  
*  
AUTOMATIC-ITERATION NODE=13 DIRECTION=2 DISPLACEMENT=2 .07314 DISPMAX=11  
*  
TOLERANCE PRINT=NO  
*  
PRINTOUT VOLUME=MINIMUM IOUTPT=1 PRINTDEFAULT=NO  
*  
* Print load versus center deflection  
PRINTSTEPS FIRST1=1 LAST1=1 INCR1=1  
*  
* Print displacements at constrained node and at center  
PRINTNODES FIRST1=13 LAST1=13 INCR1=1 FIRST2=66 LAST2=66 INCR2=1  
*
```

## Part 2

\* Coordinates at ends; lengths in mm.

COORDINATES

ENTRIES NODE Y Z

1 0 0

STEP 1 TO

7 0 .402

STEP 1 TO

9 0 .938

STEP 1 TO

15 0 1.34

STEP 1 TO

17 0 1.876

STEP 1 TO

23 0 2.278

STEP 1 TO

25 0 2.814

STEP 1 TO

31 0 3.216

STEP 1 TO

35 0 4.288

STEP 1 TO

41 0 4.69

STEP 1 TO

43 0 5.226

STEP 1 TO

49 0 5.628

STEP 1 TO

51 0 6.164

STEP 1 TO

57 0 6.566

STEP 1 TO

59 0 7.102

STEP 1 TO

65 0 7.504

\*

66 112 0

STEP 1 TO

72 112 .402

STEP 1 TO

74 112 .938

STEP 1 TO

80 112 1.34

STEP 1 TO

82 112 1.876

STEP 1 TO

88 112 2.278

STEP 1 TO

90 112 2.814

STEP 1 TO

96 112 3.216

STEP 1 TO

100 112 4.288

STEP 1 TO  
106 112 4.69  
STEP 1 TO  
108 112 5.226  
STEP 1 TO  
114 112 5.628  
STEP 1 TO  
116 112 6.164  
STEP 1 TO  
122 112 6.566  
STEP 1 TO  
124 112 7.102  
STEP 1 TO  
130 112 7.504  
•

## Part 3

\* Material properties for 45 degree plies; note: all stiffness values  
\* are in GPa.

MATERIAL N=1 TYPE=ORTHOTROPIC EA=20.85 EB=9.81 EC=20.85,  
NUAB=.0735 NUAC=.737 NUBC=.3 GAB=5.4 GAC=36.71 GBC=5.4 DENSITY=1.52

\* Material properties for 0 degree plies

MATERIAL N=2 TYPE=ORTHOTROPIC EA=142. EB=9.81 EC=9.81,  
NUAB=.0207 NUAC=.0207 NUBC=.34 GAB=6 GAC=6 GBC=4.8 DENSITY=1.52

\* Material properties for 90 degree plies

MATERIAL N=3 TYPE=ORTHOTROPIC EA=9.81 EB=9.81 EC=142.,  
NUAB=.34 NUAC=.3 NUBC=.3 GAB=4.8 GAC=6 GBC=6 DENSITY=1.52

\* Material properties for all non-linear 45's  $4500 < e_{11} < 5500$ .

MATERIAL N=4 TYPE=ORTHOTROPIC EA=20 EB=9.81 EC=20.85,  
NUAB=.0735 NUAC=.758 NUBC=.3 GAB=5.4 GAC=36.71 GBC=5.4 DENSITY=1.52

\* Material properties for tensile non-linear 45's  $5500 < e_{11} < 6500$ .

MATERIAL N=5 TYPE=ORTHOTROPIC EA=18.58 EB=9.81 EC=20.85,  
NUAB=.0735 NUAC=.785 NUBC=.3 GAB=5.4 GAC=36.71 GBC=5.4 DENSITY=1.52

\* Material properties for compressive non-linear 45's  $5500 < e_{11} < 6500$ .

MATERIAL N=6 TYPE=ORTHOTROPIC EA=18.93 EB=9.81 EC=20.85,  
NUAB=.0735 NUAC=.759 NUBC=.3 GAB=5.4 GAC=36.71 GBC=5.4 DENSITY=1.52

\* Material properties for tensile non-linear 45's  $6500 < e_{11} < 7500$ .

\* and for compressive non-linear 45's  $7500 < e_{11} < 8500$  ( $\nu_{12}=.759$ )

MATERIAL N=7 TYPE=ORTHOTROPIC EA=17.25 EB=9.81 EC=20.85,  
NUAB=.0735 NUAC=.821 NUBC=.3 GAB=5.4 GAC=36.71 GBC=5.4 DENSITY=1.52

\* Material properties for compressive non-linear 45's  $6500 < e_{11} < 7500$ .

MATERIAL N=8 TYPE=ORTHOTROPIC EA=17.97 EB=9.81 EC=20.85,  
NUAB=.0735 NUAC=.759 NUBC=.3 GAB=5.4 GAC=36.71 GBC=5.4 DENSITY=1.52

\* Material properties for tensile non-linear 45's  $7500 < e_{11} < 8500$ .

MATERIAL N=9 TYPE=ORTHOTROPIC EA=16.25 EB=9.81 EC=20.85,  
NUAB=.0735 NUAC=.826 NUBC=.3 GAB=5.4 GAC=36.71 GBC=5.4 DENSITY=1.52

\* Material properties for tensile non-linear 45's  $8500 < e_{11} < 9500$ .

MATERIAL N=10 TYPE=ORTHOTROPIC EA=15.10 EB=9.81 EC=20.85,  
NUAB=.0735 NUAC=.865 NUBC=.3 GAB=5.4 GAC=36.71 GBC=5.4 DENSITY=1.52

\* Material properties for compressive non-linear 45's  $8500 < e_{11} < 9500$ .

MATERIAL N=11 TYPE=ORTHOTROPIC EA=16 EB=9.81 EC=20.85,  
NUAB=.0735 NUAC=.759 NUBC=.3 GAB=5.4 GAC=36.71 GBC=5.4 DENSITY=1.52

\* Material properties for tensile non-linear 45's  $9500 < e_{11} < 10500$

MATERIAL N=12 TYPE=ORTHOTROPIC EA=14.19 EB=9.81 EC=20.85,  
NUAB=.0735 NUAC=.860 NUBC=.3 GAB=5.4 GAC=36.71 GBC=5.4 DENSITY=1.52

```
*  
* Material properties for compressive non-linear 45's 9500<e11<10500  
MATERIAL N=13 TYPE=ORTHOTROPIC EA=15.05 EB=9.81 EC=20.85,  
NUAB=.0735 NUAC=.759 NUBC=.3 GAB=5.4 GAC=36.71 GBC=5.4 DENSITY=1.52  
*  
* Material properties for damaged 90 plies  
MATERIAL N=20 TYPE=ORTHOTROPIC EA=0.01 EB=9.81 EC=142.,  
NUAB=.0034 NUAC=.003 NUBC=.3 GAB=.01 GAC=.01 GBC=6 DENSITY=1.52  
*  
* Material properties for truss elements  
MATERIAL N=21 TYPE=NONLINEAR-ELASTIC  
1000 100  
0 0  
-1000 -100000  
*
```

## Part 4

EGROUP N=1 TYPE=PLANE SUBTYPE=STRESS2 MATERIAL=1 RESULTS=TABLES

\*

STRESSTABLE 1 P1=9

\*

GSURFACE N1=130 N2=65 N3=61 N4=126 EL1=10 EL2=2 NODES=8 NCOINCIDE=BOUNDARIES  
 GSURFACE N1=122 N2=57 N3=53 N4=118 EL1=10 EL2=2 NODES=8 NCOINCIDE=BOUNDARIES  
 GSURFACE N1=114 N2=49 N3=45 N4=110 EL1=10 EL2=2 NODES=8 NCOINCIDE=BOUNDARIES  
 GSURFACE N1=106 N2=41 N3=37 N4=102 EL1=10 EL2=2 NODES=8 NCOINCIDE=BOUNDARIES

\*\*

GSURFACE N1=94 N2=29 N3=25 N4=90 EL1=10 EL2=2 NODES=8 NCOINCIDE=BOUNDARIES  
 GSURFACE N1=86 N2=21 N3=17 N4=82 EL1=10 EL2=2 NODES=8 NCOINCIDE=BOUNDARIES  
 GSURFACE N1=78 N2=13 N3=9 N4=74 EL1=10 EL2=2 NODES=8 NCOINCIDE=BOUNDARIES  
 GSURFACE N1=70 N2=5 N3=1 N4=66 EL1=10 EL2=2 NODES=8 NCOINCIDE=ALL

\*

EDATA

ENTRIES EL THICK PRINT

1 38.5 YES TO 160 38.5 YES

\*

EGROUP N=2 TYPE=PLANE SUBTYPE=STRESS2 MATERIAL=2 RESULTS=FORCES

\*

\*STRESSTABLE 1 P1=9

\*

GSURFACE N1=126 N2=61 N3=59 N4=124 EL1=10 EL2=1 NODES=8 NCOINCIDE=BOUNDARIES  
 GSURFACE N1=118 N2=53 N3=51 N4=116 EL1=10 EL2=1 NODES=8 NCOINCIDE=BOUNDARIES  
 GSURFACE N1=110 N2=45 N3=43 N4=108 EL1=10 EL2=1 NODES=8 NCOINCIDE=BOUNDARIES  
 GSURFACE N1=102 N2=37 N3=35 N4=100 EL1=10 EL2=1 NODES=8 NCOINCIDE=BOUNDARIES

\*

GSURFACE N1=96 N2=31 N3=29 N4=94 EL1=10 EL2=1 NODES=8 NCOINCIDE=BOUNDARIES  
 GSURFACE N1=88 N2=23 N3=21 N4=86 EL1=10 EL2=1 NODES=8 NCOINCIDE=BOUNDARIES  
 GSURFACE N1=80 N2=15 N3=13 N4=78 EL1=10 EL2=1 NODES=8 NCOINCIDE=BOUNDARIES  
 GSURFACE N1=72 N2=7 N3=5 N4=70 EL1=10 EL2=1 NODES=8 NCOINCIDE=BOUNDARIES

\*

EDATA

ENTRIES EL THICK PRINT

1 38.5 YES TO 80 38.5 YES

\*

EGROUP N=3 TYPE=PLANE SUBTYPE=STRESS2 MATERIAL=3 RESULTS=TABLES

\*

STRESSTABLE 1 P1=9

\*

GSURFACE N1=124 N2=59 N3=57 N4=122 EL1=10 EL2=1 NODES=8 NCOINCIDE=BOUNDARIES  
 GSURFACE N1=116 N2=51 N3=49 N4=114 EL1=10 EL2=1 NODES=8 NCOINCIDE=BOUNDARIES  
 GSURFACE N1=108 N2=43 N3=41 N4=106 EL1=10 EL2=1 NODES=8 NCOINCIDE=BOUNDARIES  
 GSURFACE N1=100 N2=35 N3=31 N4=96 EL1=10 EL2=2 NODES=8 NCOINCIDE=BOUNDARIES  
 GSURFACE N1=90 N2=25 N3=23 N4=88 EL1=10 EL2=1 NODES=8 NCOINCIDE=BOUNDARIES  
 GSURFACE N1=82 N2=17 N3=15 N4=80 EL1=10 EL2=1 NODES=8 NCOINCIDE=BOUNDARIES  
 GSURFACE N1=74 N2=9 N3=7 N4=72 EL1=10 EL2=1 NODES=8 NCOINCIDE=BOUNDARIES

\*

EDATA

ENTRIES EL THICK PRINT

1 38.5 YES TO 80 38.5 YES

## Part 5

```
*
* This end is clamped but allows up-down.
BOUNDARIES IDOF=110111 TYPE=NODES
66 TO 130
* This end is pinned-sliding.
BOUNDARIES IDOF=101011 TYPE=NODES
13
*
* Load is in kN.
LOADS CONCENTRATED
13 2 1
*
LIST COORDINATE 841 850
ADINA
*
END
```

## Part 1

```
HEADING ' B-TYPICAL: L=112, E=lin, e=2.66 S11'  
*  
MASTER IDOF=100111 NSTEP=1 REACTIONS=NO  
*  
ANALYSIS TYPE=STATIC  
*  
KINEMATICS DISPLACEMENT=LARGE STRAINS=SMALL  
*  
AUTOMATIC-ITERATION NODE=13 DIRECTION=2 DISPLACEMENT=5.6 DISPMAX=11  
*  
TOLERANCE PRINT=NO ITEMAX=30  
*  
PRINTOUT VOLUME=MINIMUM IOUPT=1 PRINTDEFAULT=NO  
*  
* Print load versus center deflection.  
PRINTSTEPS FIRST1=1 LAST1=1 INCR1=1  
*  
PRINTNODES FIRST1=13 LAST1=13 INCR1=1 FIRST2=56 LAST2=56 INCR2=1  
*
```

## Part 2

COORDINATES  
ENTRIES NODE Y Z  
1 0 0  
STEP 1 TO  
5 0 .532  
STEP 1 TO  
7 0 .665  
STEP 1 TO  
11 0 1.197  
STEP 1 TO  
13 0 1.33  
STEP 1 TO  
15 0 1.995  
STEP 1 TO  
19 0 2.527  
STEP 1 TO  
21 0 2.66  
STEP 1 TO  
25 0 3.192  
STEP 1 TO  
27 0 3.325  
STEP 1 TO  
29 0 4.655  
STEP 1 TO  
31 0 4.788  
STEP 1 TO  
35 0 5.32  
STEP 1 TO  
37 0 5.453  
STEP 1 TO  
41 0 5.985  
STEP 1 TO  
43 0 6.65  
STEP 1 TO  
45 0 6.783  
STEP 1 TO  
49 0 7.315  
STEP 1 TO  
51 0 7.448  
STEP 1 TO  
55 0 7.98  
\*  
56 112 0  
STEP 1 TO  
60 112 .532  
STEP 1 TO  
62 112 .665  
STEP 1 TO  
66 112 1.197  
STEP 1 TO  
68 112 1.33  
STEP 1 TO

70 112 1.995  
STEP 1 TO  
74 112 2.527  
STEP 1 TO  
76 112 2.66  
STEP 1 TO  
80 112 3.192  
STEP 1 TO  
82 112 3.325  
STEP 1 TO  
84 112 4.655  
STEP 1 TO  
86 0 4.788  
STEP 1 TO  
90 0 5.32  
STEP 1 TO  
92 0 5.453  
STEP 1 TO  
96 0 5.985  
STEP 1 TO  
98 0 6.65  
STEP 1 TO  
100 0 6.783  
STEP 1 TO  
104 0 7.315  
STEP 1 TO  
106 0 7.448  
STEP 1 TO  
110 0 7.98  
\*

## Part 3

- \* Material properties for 45 degree plies; all stiffness values  
\* are in GPa.
- MATERIAL N=1 TYPE=ORTHOTROPIC EA=20.85 EB=9.81 EC=20.85,  
NUAB=.0735 NUAC=.737 NUBC=.3 GAB=5.4 GAC=36.71 GBC=5.4 DENSITY=1.52
- \*
- \* Material properties for 0 degree plies
- MATERIAL N=2 TYPE=ORTHOTROPIC EA=142 EB=9.81 EC=9.81,  
NUAB=.0207 NUAC=.0207 NUBC=.34 GAB=6 GAC=6 GBC=4.8 DENSITY=1.52
- \*
- \* Material properties for 90 degree plies
- MATERIAL N=3 TYPE=ORTHOTROPIC EA=9.81 EB=9.81 EC=142,  
NUAB=.34 NUAC=.3 NUBC=.3 GAB=4.8 GAC=6 GBC=6 DENSITY=1.52
- \*
- \* Material properties for all non-linear 45's  $4500 < \epsilon_{11} < 5500$ .
- MATERIAL N=4 TYPE=ORTHOTROPIC EA=20 EB=9.81 EC=20.85,  
NUAB=.0735 NUAC=.758 NUBC=.3 GAB=5.4 GAC=36.71 GBC=5.4 DENSITY=1.52
- \*
- \* Material properties for tensile non-linear 45's  $5500 < \epsilon_{11} < 6500$ .
- MATERIAL N=5 TYPE=ORTHOTROPIC EA=18.58 EB=9.81 EC=20.85,  
NUAB=.0735 NUAC=.785 NUBC=.3 GAB=5.4 GAC=36.71 GBC=5.4 DENSITY=1.52
- \*
- \* Material properties for compressive non-linear 45's  $5500 < \epsilon_{11} < 6500$ .
- MATERIAL N=6 TYPE=ORTHOTROPIC EA=18.93 EB=9.81 EC=20.85,  
NUAB=.0735 NUAC=.759 NUBC=.3 GAB=5.4 GAC=36.71 GBC=5.4 DENSITY=1.52
- \*
- \* Material properties for tensile non-linear 45's  $6500 < \epsilon_{11} < 7500$ .
- \* and for compressive non-linear 45's  $7500 < \epsilon_{11} < 8500$  ( $\nu_{12}=.759$ )
- MATERIAL N=7 TYPE=ORTHOTROPIC EA=17.25 EB=9.81 EC=20.85,  
NUAB=.0735 NUAC=.821 NUBC=.3 GAB=5.4 GAC=36.71 GBC=5.4 DENSITY=1.52
- \*
- \* Material properties for compressive non-linear 45's  $6500 < \epsilon_{11} < 7500$ .
- MATERIAL N=8 TYPE=ORTHOTROPIC EA=17.97 EB=9.81 EC=20.85,  
NUAB=.0735 NUAC=.759 NUBC=.3 GAB=5.4 GAC=36.71 GBC=5.4 DENSITY=1.52
- \*
- \* Material properties for tensile non-linear 45's  $7500 < \epsilon_{11} < 8500$ .
- MATERIAL N=9 TYPE=ORTHOTROPIC EA=16.25 EB=9.81 EC=20.85,  
NUAB=.0735 NUAC=.826 NUBC=.3 GAB=5.4 GAC=36.71 GBC=5.4 DENSITY=1.52
- \*
- \* Material properties for tensile non-linear 45's  $8500 < \epsilon_{11} < 9500$ .
- MATERIAL N=10 TYPE=ORTHOTROPIC EA=15.10 EB=9.81 EC=20.85,  
NUAB=.0735 NUAC=.865 NUBC=.3 GAB=5.4 GAC=36.71 GBC=5.4 DENSITY=1.52
- \*
- \* Material properties for compressive non-linear 45's  $8500 < \epsilon_{11} < 9500$ .
- MATERIAL N=11 TYPE=ORTHOTROPIC EA=16 EB=9.81 EC=20.85,  
NUAB=.0735 NUAC=.759 NUBC=.3 GAB=5.4 GAC=36.71 GBC=5.4 DENSITY=1.52
- \*
- \* Material properties for tensile non-linear 45's  $9500 < \epsilon_{11} < 10500$ .
- MATERIAL N=12 TYPE=ORTHOTROPIC EA=14.19 EB=9.81 EC=20.85,  
NUAB=.0735 NUAC=.880 NUBC=.3 GAB=5.4 GAC=36.71 GBC=5.4 DENSITY=1.52
- \*

\* Material properties for compressive non-linear 45's 9500<math>\epsilon\_{11}</math><math>10500</math>.  
MATERIAL N=13 TYPE=ORTHOTROPIC EA=15.05 EB=9.81 EC=20.85,  
NUAB=.0735 NUAC=.759 NUBC=.3 GAB=5.4 GAC=36.71 GBC=5.4 DENSITY=1.52  
\*

\* Material properties for tensile non-linear 45's 10500<math>\epsilon\_{11}</math><math>11500</math>.  
MATERIAL N=14 TYPE=ORTHOTROPIC EA=13.44 EB=9.81 EC=20.85,  
NUAB=.0735 NUAC=.939 NUBC=.3 GAB=5.4 GAC=36.71 GBC=5.4 DENSITY=1.52  
\*

\* Material properties for compressive non-linear 45's 10500<math>\epsilon\_{11}</math><math>11500</math>.  
MATERIAL N=15 TYPE=ORTHOTROPIC EA=14.25 EB=9.81 EC=20.85,  
NUAB=.0735 NUAC=.759 NUBC=.3 GAB=5.4 GAC=36.71 GBC=5.4 DENSITY=1.52  
\*

\* Material properties for tensile non-linear 45's 11500<math>\epsilon\_{11}</math><math>12500</math>.  
MATERIAL N=16 TYPE=ORTHOTROPIC EA=12.45 EB=9.81 EC=20.85,  
NUAB=.0735 NUAC=1.0 NUBC=.3 GAB=5.4 GAC=36.71 GBC=5.4 DENSITY=1.52  
\*

\* Material properties for compressive non-linear 45's 11500<math>\epsilon\_{11}</math><math>12500</math>.  
MATERIAL N=17 TYPE=ORTHOTROPIC EA=13.28 EB=9.81 EC=20.85,  
NUAB=.0735 NUAC=.757 NUBC=.3 GAB=5.4 GAC=36.71 GBC=5.4 DENSITY=1.52  
\*

\* Material properties for tensile non-linear 45's 12500<math>\epsilon\_{11}</math><math>13500</math>.  
MATERIAL N=18 TYPE=ORTHOTROPIC EA=11.53 EB=9.81 EC=20.85,  
NUAB=.0735 NUAC=1.126 NUBC=.3 GAB=5.4 GAC=36.71 GBC=5.4 DENSITY=1.52  
\*

\* Material properties for compressive non-linear 45's 12500<math>\epsilon\_{11}</math><math>13500</math>.  
MATERIAL N=19 TYPE=ORTHOTROPIC EA=12.38 EB=9.81 EC=20.85,  
NUAB=.0735 NUAC=.752 NUBC=.3 GAB=5.4 GAC=36.71 GBC=5.4 DENSITY=1.52  
\*

\* Material properties for tensile non-linear 45's 13500<math>\epsilon\_{11}</math><math>14500</math>.  
MATERIAL N=20 TYPE=ORTHOTROPIC EA=10.74 EB=9.81 EC=20.85,  
NUAB=.0735 NUAC=1.223 NUBC=.3 GAB=5.4 GAC=36.71 GBC=5.4 DENSITY=1.52  
\*

\* Material properties for compressive non-linear 45's 13500<math>\epsilon\_{11}</math><math>14500</math>.  
MATERIAL N=21 TYPE=ORTHOTROPIC EA=11.64 EB=9.81 EC=20.85,  
NUAB=.0735 NUAC=.749 NUBC=.3 GAB=5.4 GAC=36.71 GBC=5.4 DENSITY=1.52  
\*

\* Material properties for tensile non-linear 45's 14500<math>\epsilon\_{11}</math><math>15500</math>.  
MATERIAL N=22 TYPE=ORTHOTROPIC EA=10.07 EB=9.81 EC=20.85,  
NUAB=.0735 NUAC=1.327 NUBC=.3 GAB=5.4 GAC=36.71 GBC=5.4 DENSITY=1.52  
\*

\* Material properties for compressive non-linear 45's 14500<math>\epsilon\_{11}</math><math>15500</math>.  
MATERIAL N=23 TYPE=ORTHOTROPIC EA=10.97 EB=9.81 EC=20.85,  
NUAB=.0735 NUAC=.747 NUBC=.3 GAB=5.4 GAC=36.71 GBC=5.4 DENSITY=1.52  
\*

\* Material properties for tensile non-linear 45's 15500<math>\epsilon\_{11}</math><math>16500</math>.  
MATERIAL N=24 TYPE=ORTHOTROPIC EA=9.47 EB=9.81 EC=20.85,  
NUAB=.0735 NUAC=1.406 NUBC=.3 GAB=5.4 GAC=36.71 GBC=5.4 DENSITY=1.52  
\*

\* Material properties for compressive non-linear 45's 15500<math>\epsilon\_{11}</math><math>16500</math>.  
MATERIAL N=25 TYPE=ORTHOTROPIC EA=10.39 EB=9.81 EC=20.85,  
NUAB=.0735 NUAC=.726 NUBC=.3 GAB=5.4 GAC=36.71 GBC=5.4 DENSITY=1.52  
\*

\* Material properties for tensile non-linear 45's  $16500 < e_{11} < 17500$ .  
MATERIAL N=26 TYPE=ORTHOTROPIC EA=8.94 EB=9.81 EC=20.85,  
NUAB=.0735 NUAC=1.4 NUBC=.3 GAB=5.4 GAC=36.71 GBC=5.4 DENSITY=1.52  
\*  
\* Material properties for compressive non-linear 45's  $16500 < e_{11} < 17500$ .  
MATERIAL N=27 TYPE=ORTHOTROPIC EA=9.88 EB=9.81 EC=20.85,  
NUAB=.0735 NUAC=.708 NUBC=.3 GAB=5.4 GAC=36.71 GBC=5.4 DENSITY=1.52  
\*  
\* Material properties for damaged 90 degree plies.  
MATERIAL N=30 TYPE=ORTHOTROPIC EA=0.01 EB=9.81 EC=142.,  
NUAB=.0034 NUAC=.003 NUBC=.3 GAB=0.01 GAC=0.01 GBC=6 DENSITY=1.52  
\*  
\* Material for trusses.  
MATERIAL N=31 TYPE=NONLINEAR-ELASTIC  
1000 100  
0 0  
-1000 -100000

## Part 4

```

*
EGROUP N=1 TYPE=PLANE SUBTYPE=STRESS2 MATERIAL=1 RESULTS=FORCES
*
GSURFACE N1=110 N2=55 N3=51 N4=106 EL1=7 EL2=1 NODES=8 NCOINCIDE=BOUNDARIES
GSURFACE N1=104 N2=49 N3=45 N4=100 EL1=5 EL2=1 NODES=8 NCOINCIDE=BOUNDARIES
GSURFACE N1=96 N2=41 N3=37 N4=92 EL1=4 EL2=1 NODES=8 NCOINCIDE=BOUNDARIES
GSURFACE N1=90 N2=35 N3=31 N4=86 EL1=4 EL2=1 NODES=8 NCOINCIDE=BOUNDARIES
*
GSURFACE N1=80 N2=25 N3=21 N4=76 EL1=10 EL2=2 NODES=8 NCOINCIDE=BOUNDARIES
GSURFACE N1=74 N2=19 N3=15 N4=70 EL1=10 EL2=2 NODES=8 NCOINCIDE=ALL
GSURFACE N1=66 N2=11 N3=7 N4=62 EL1=10 EL2=2 NODES=8 NCOINCIDE=BOUNDARIES
GSURFACE N1=60 N2=5 N3=1 N4=56 EL1=10 EL2=2 NODES=8 NCOINCIDE=BOUNDARIES
*
STRESSTABLE 1 P1=9
*
EDATA
ENTRIES EL THICK PRINT
1 38.5 YES TO 160 38.5 YES
*
EGROUP N=2 TYPE=PLANE SUBTYPE=STRESS2 MATERIAL=2 RESULTS=FORCES
*
STRESSTABLE 1 P1=9
*
GSURFACE N1=106 N2=51 N3=49 N4=104 EL1=10 EL2=1 NODES=8 NCOINCIDE=BOUNDARIES
GSURFACE N1=100 N2=45 N3=43 N4=98 EL1=10 EL2=1 NODES=8 NCOINCIDE=BOUNDARIES
GSURFACE N1=92 N2=37 N3=35 N4=90 EL1=10 EL2=1 NODES=8 NCOINCIDE=BOUNDARIES
GSURFACE N1=86 N2=31 N3=29 N4=84 EL1=10 EL2=1 NODES=8 NCOINCIDE=BOUNDARIES
*
GSURFACE N1=82 N2=27 N3=25 N4=80 EL1=10 EL2=1 NODES=8 NCOINCIDE=BOUNDARIES
GSURFACE N1=76 N2=21 N3=19 N4=74 EL1=10 EL2=1 NODES=8 NCOINCIDE=BOUNDARIES
GSURFACE N1=68 N2=13 N3=11 N4=66 EL1=10 EL2=1 NODES=8 NCOINCIDE=BOUNDARIES
GSURFACE N1=62 N2=7 N3=5 N4=60 EL1=10 EL2=1 NODES=8 NCOINCIDE=BOUNDARIES
*
EDATA
ENTRIES EL THICK PRINT
1 38.5 YES TO 80 38.5 YES
*
EGROUP N=3 TYPE=PLANE SUBTYPE=STRESS2 MATERIAL=3 RESULTS=FORCES
*
STRESSTABLE 1 P1=9
*
GSURFACE N1=98 N2=43 N3=41 N4=96 EL1=10 EL2=1 NODES=8 NCOINCIDE=BOUNDARIES
GSURFACE N1=84 N2=29 N3=27 N4=82 EL1=4 EL2=1 NODES=8 NCOINCIDE=BOUNDARIES
GSURFACE N1=70 N2=15 N3=13 N4=68 EL1=10 EL2=1 NODES=8 NCOINCIDE=BOUNDARIES
*
EDATA
ENTRIES EL THICK PRINT
1 38.5 YES TO 30 38.5 YES
*

```

## Part 5

\* This end is clamped but allows up-down.

BOUNDARIES IDOF=110111 TYPE=NODES

56 TO 110

\*

\* This end is pinned-sliding

BOUNDARIES IDOF=101011 TYPE=NODES

13

\*

\* Load is in kN.

LOADS CONCENTRATED

13 2 1

\*

ADINA

\*

END

## **Appendix B**

This Appendix contains the complete set of figures comparing edge replicas of inner and outer edges from the destructive examinations at all four characteristic damage states for the three layups studied in this investigation.

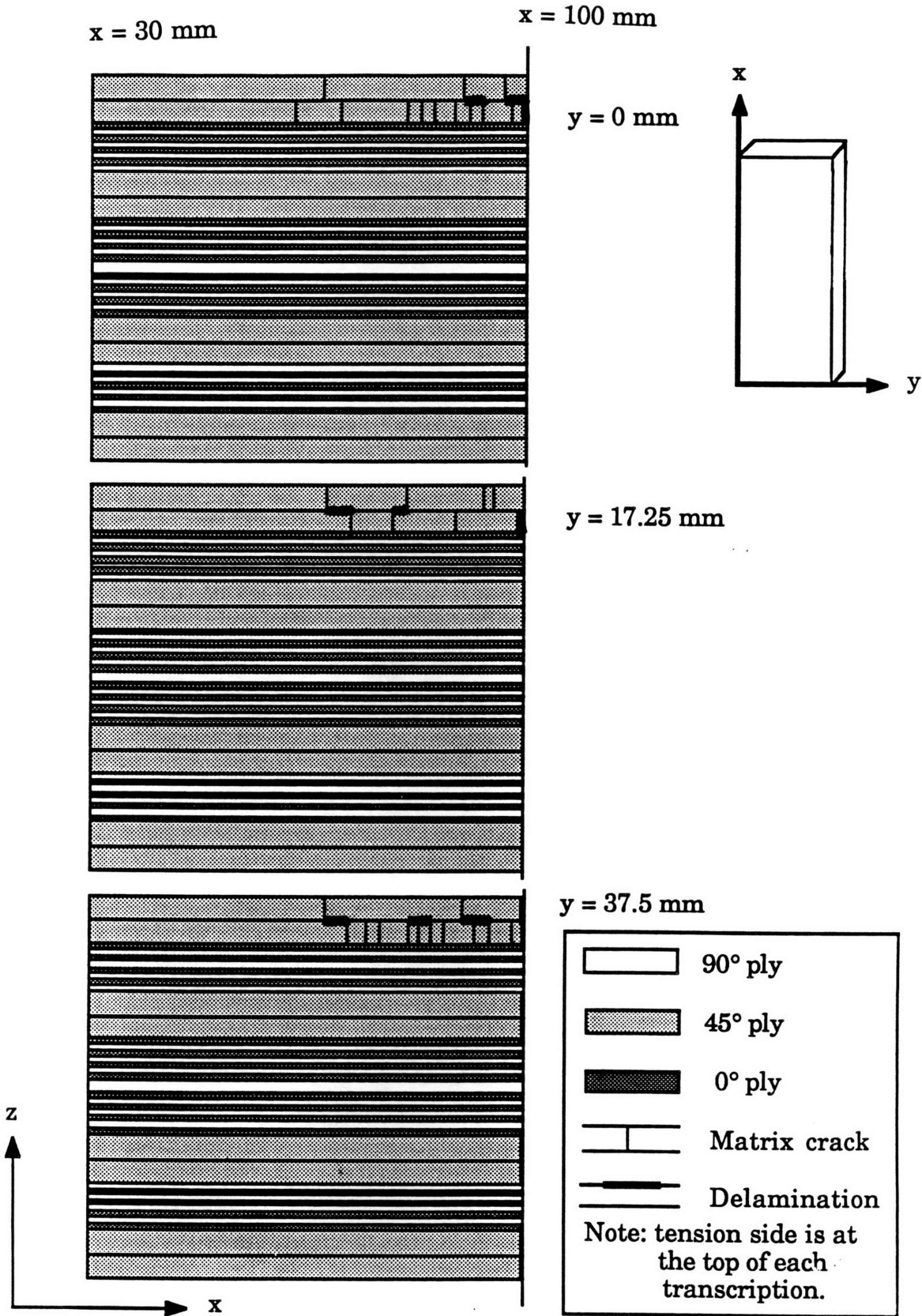


Figure B.1 Comparison of damage across width at the first characteristic damage state of the  $[45^\circ_4/-45^\circ_4/(0^\circ/90^\circ)_4]_{2s}$  layup.

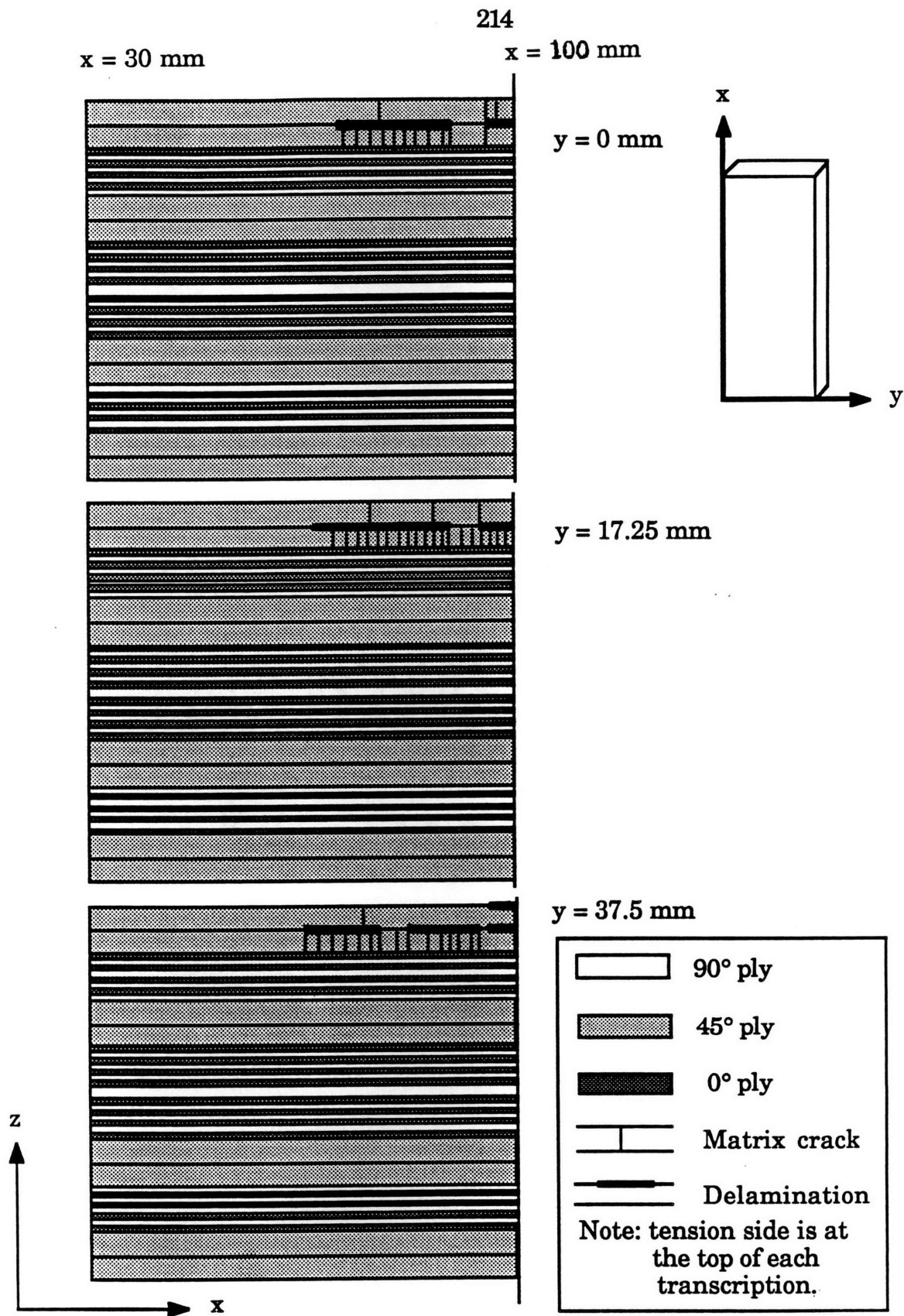


Figure B.2 Comparison of damage across width at the second characteristic damage state of the  $[45^\circ_4/-45^\circ_4/(0^\circ/90^\circ)_4]_{2s}$  layup.



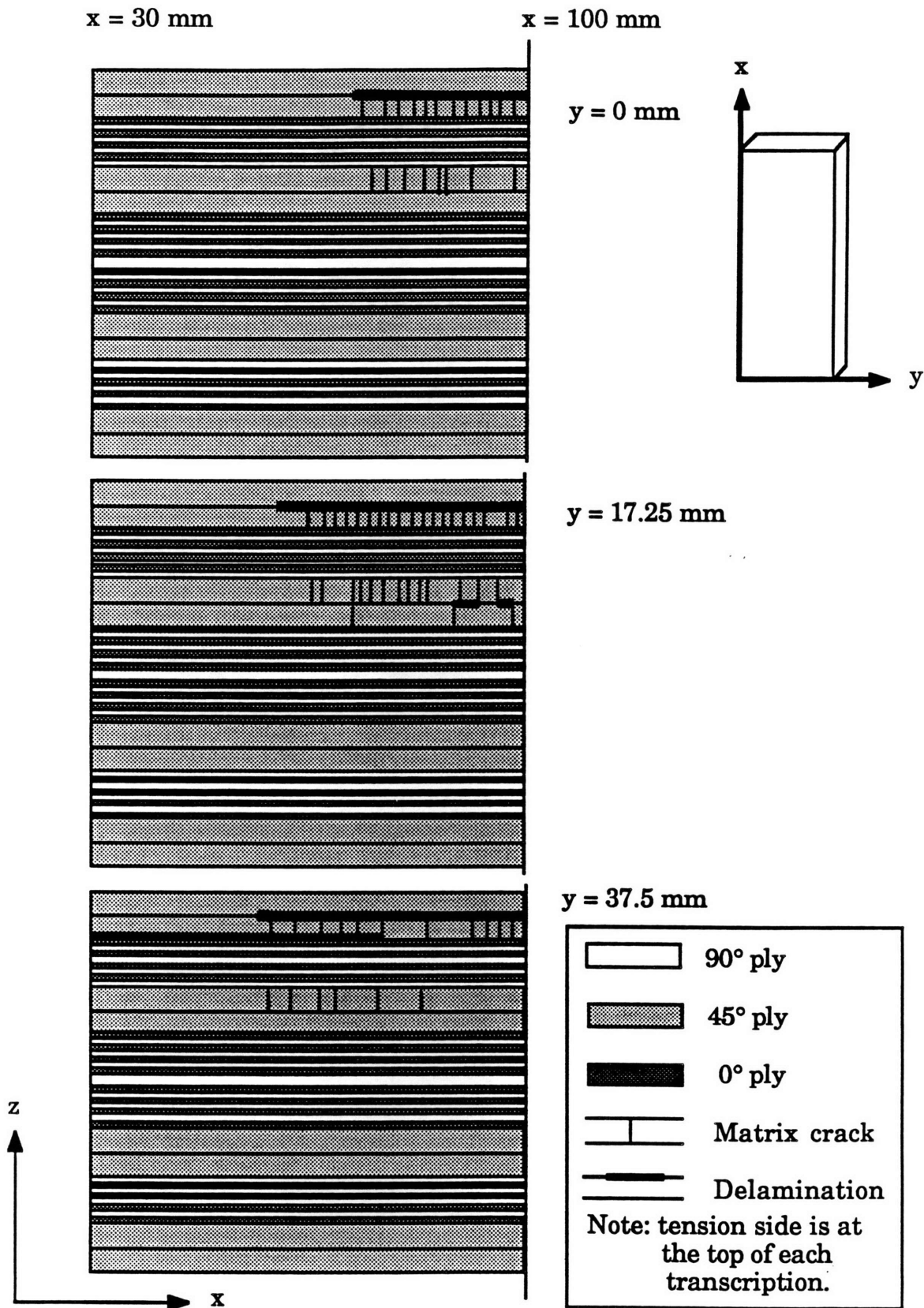


Figure B.4 Comparison of damage across width at the fourth characteristic damage state of the  $[45^\circ_4/-45^\circ_4/(0^\circ/90^\circ)_4]_{2s}$  layup.

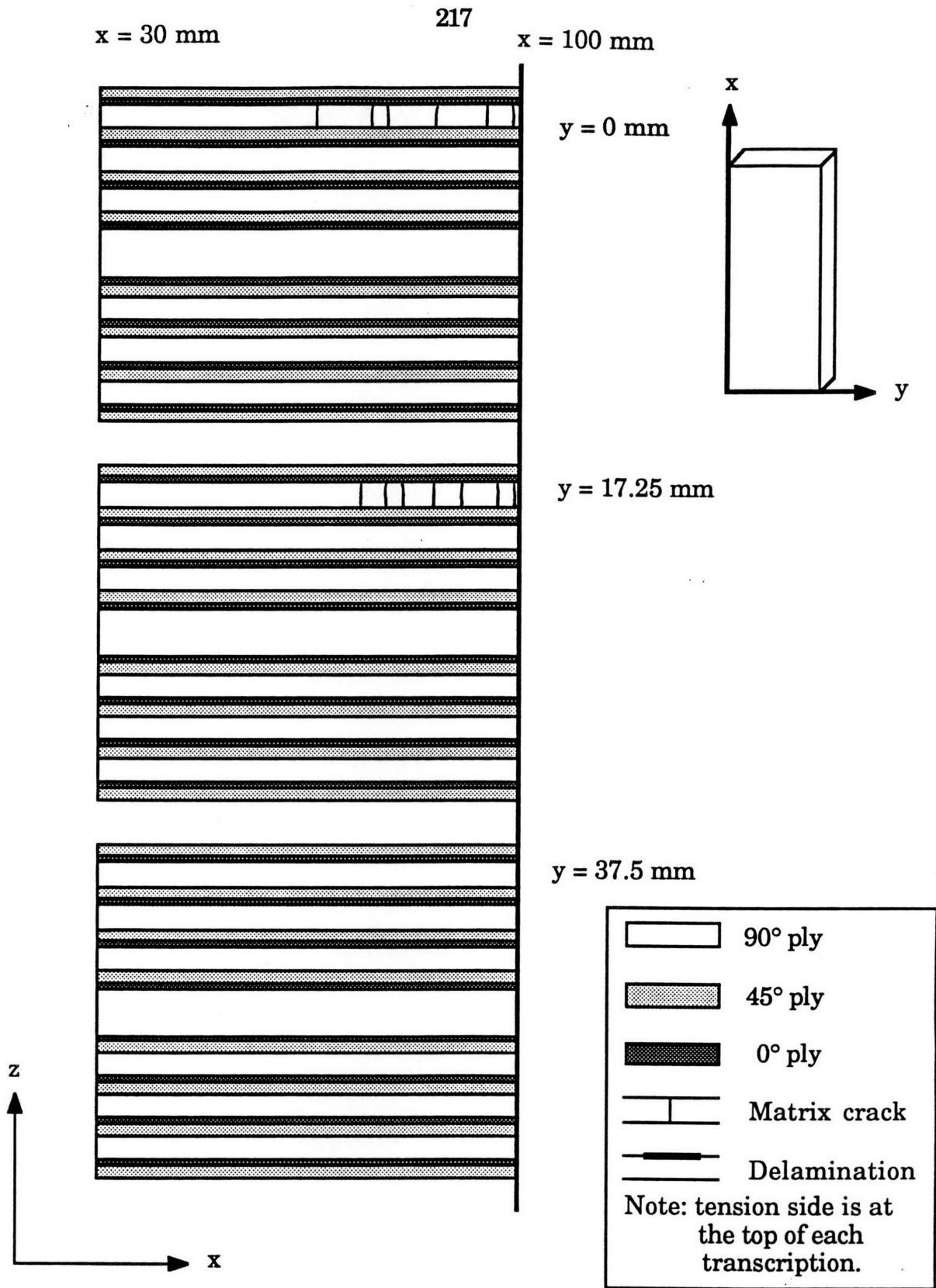


Figure B.5 Comparison of damage across width at the first characteristic damage state of the  $[\pm 45^\circ/0^\circ/90^\circ]_4s$  layup.

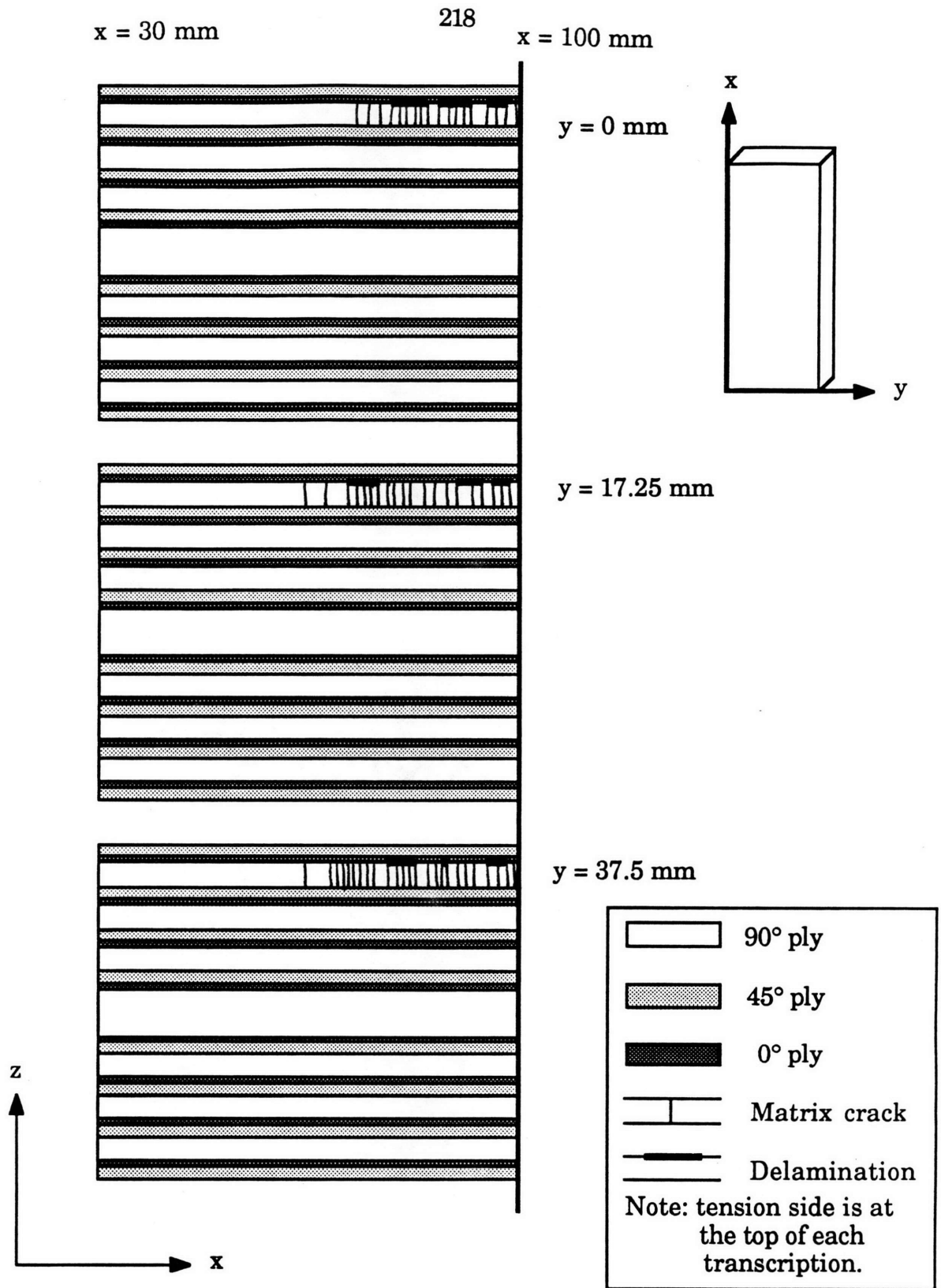


Figure B.6 Comparison of damage across width at the second characteristic damage state of the  $[\pm 45^\circ/0^\circ/90^\circ_4]_{4s}$  layup.

x = 30 mm

x = 100 mm

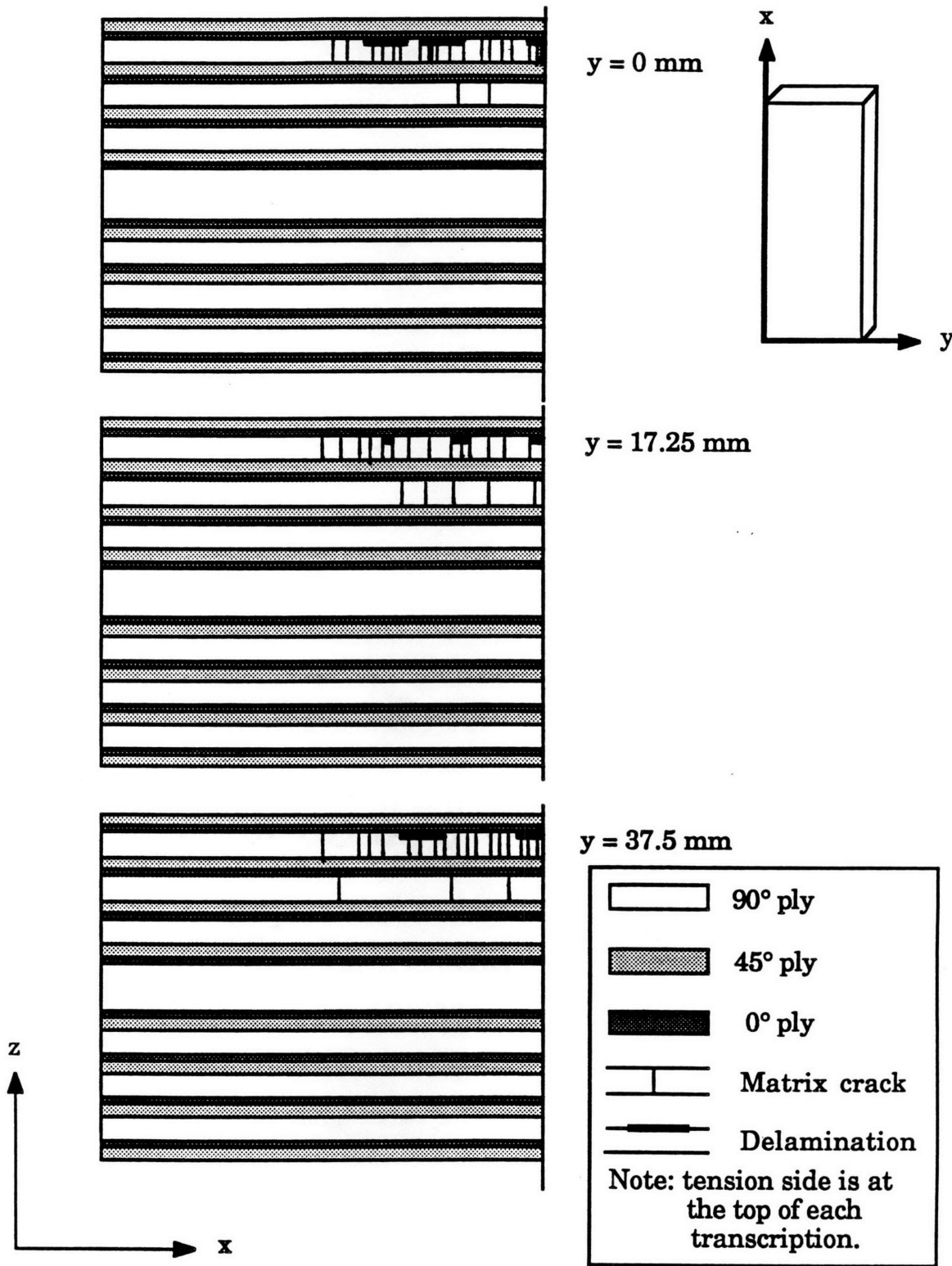


Figure B.7 Comparison of damage across width at the third characteristic damage state of the  $[\pm 45^\circ/0^\circ/90^\circ_4]_{4S}$  layup.

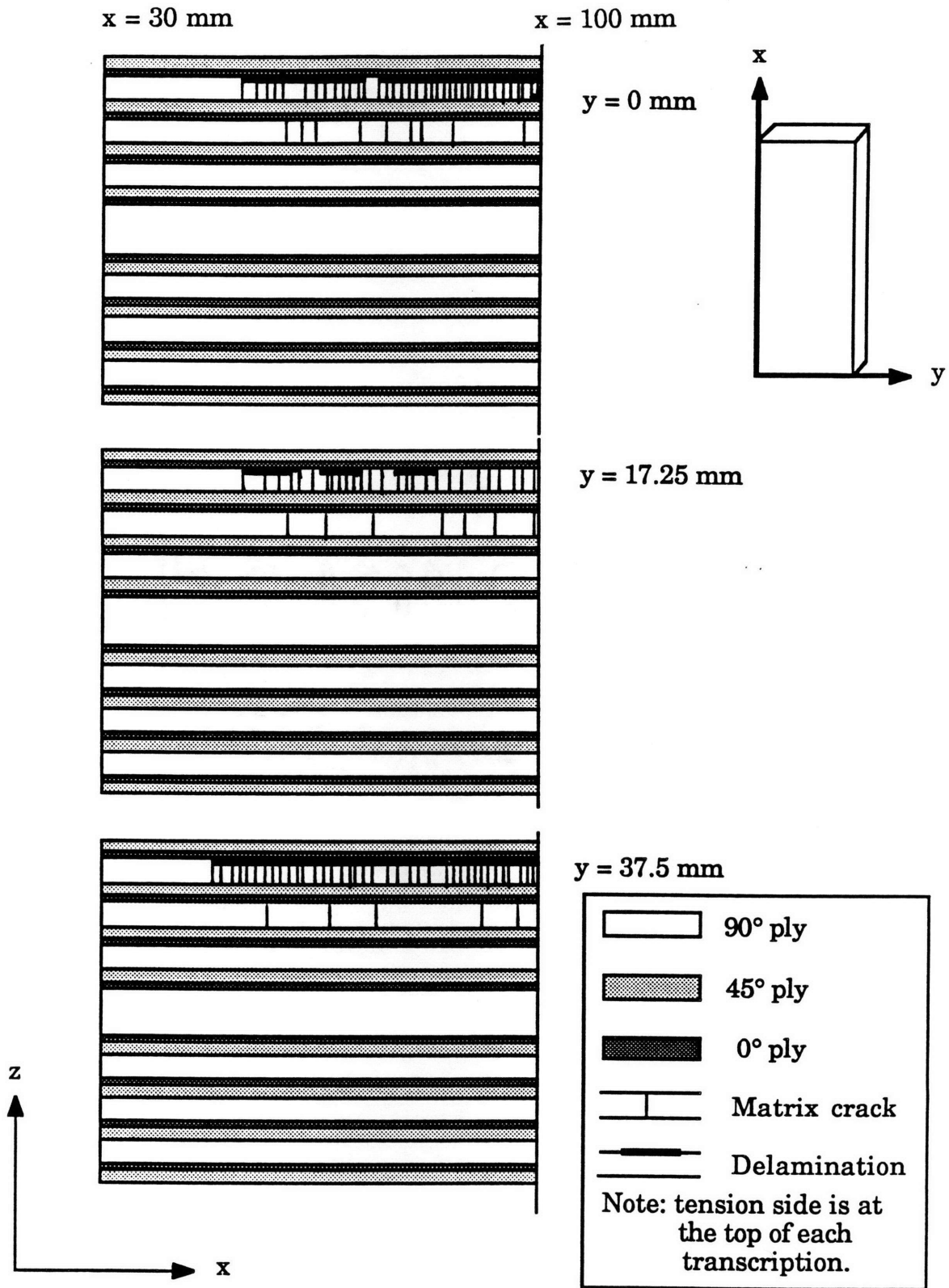


Figure B.8 Comparison of damage across width at the fourth characteristic damage state of the  $[\pm 45^\circ/0^\circ/90^\circ_4]_{4s}$  layup.

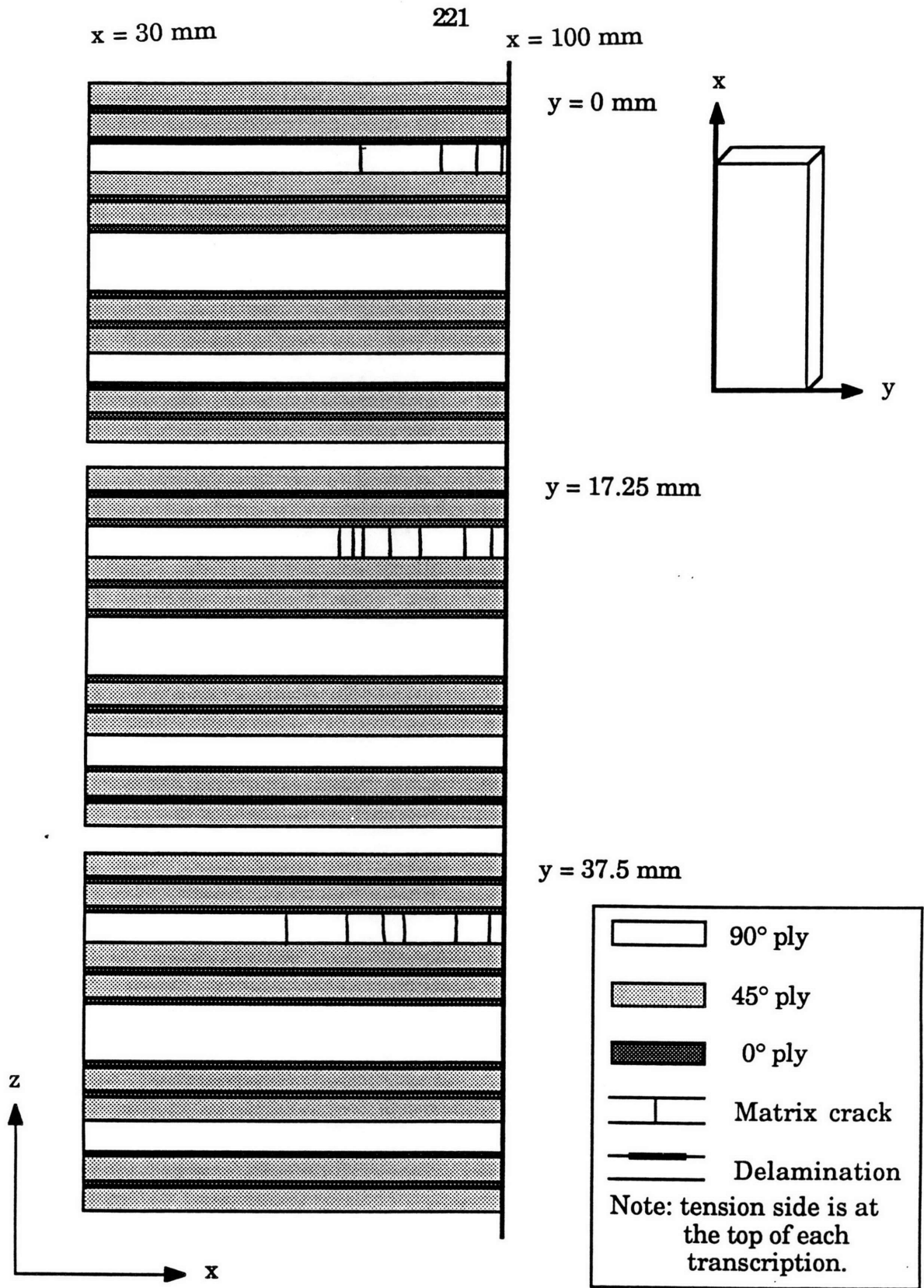


Figure B.9 Comparison of damage across width at the first characteristic damage state of the  $[(45^\circ_2/-45^\circ_2/0^\circ)_2/90^\circ_5]_{2s}$  layup.

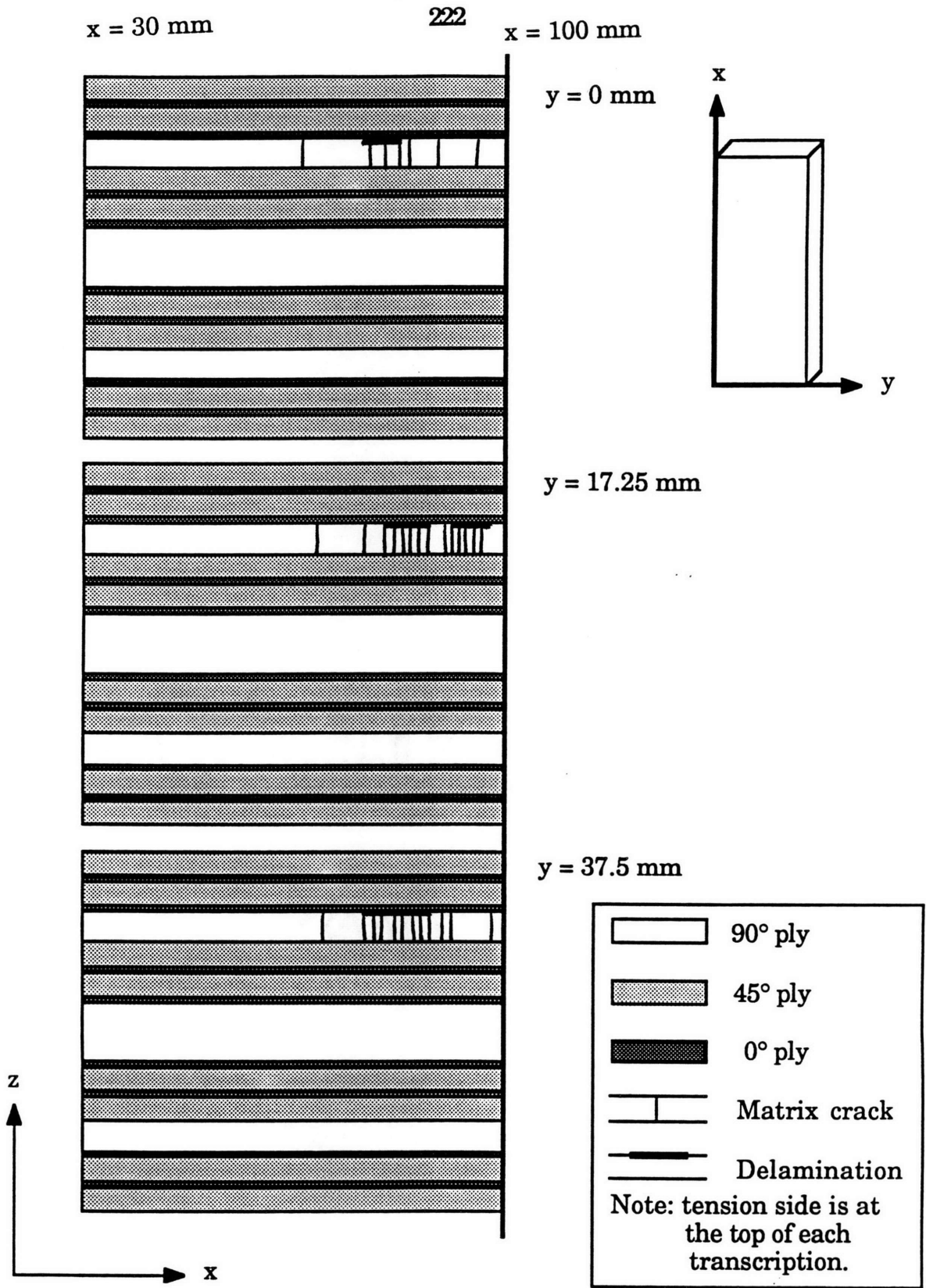


Figure B.10 Comparison of damage across width at the second characteristic damage state of the  $[(45^\circ_2/-45^\circ_2/0^\circ)_2/90^\circ_5]_{2s}$  layup.

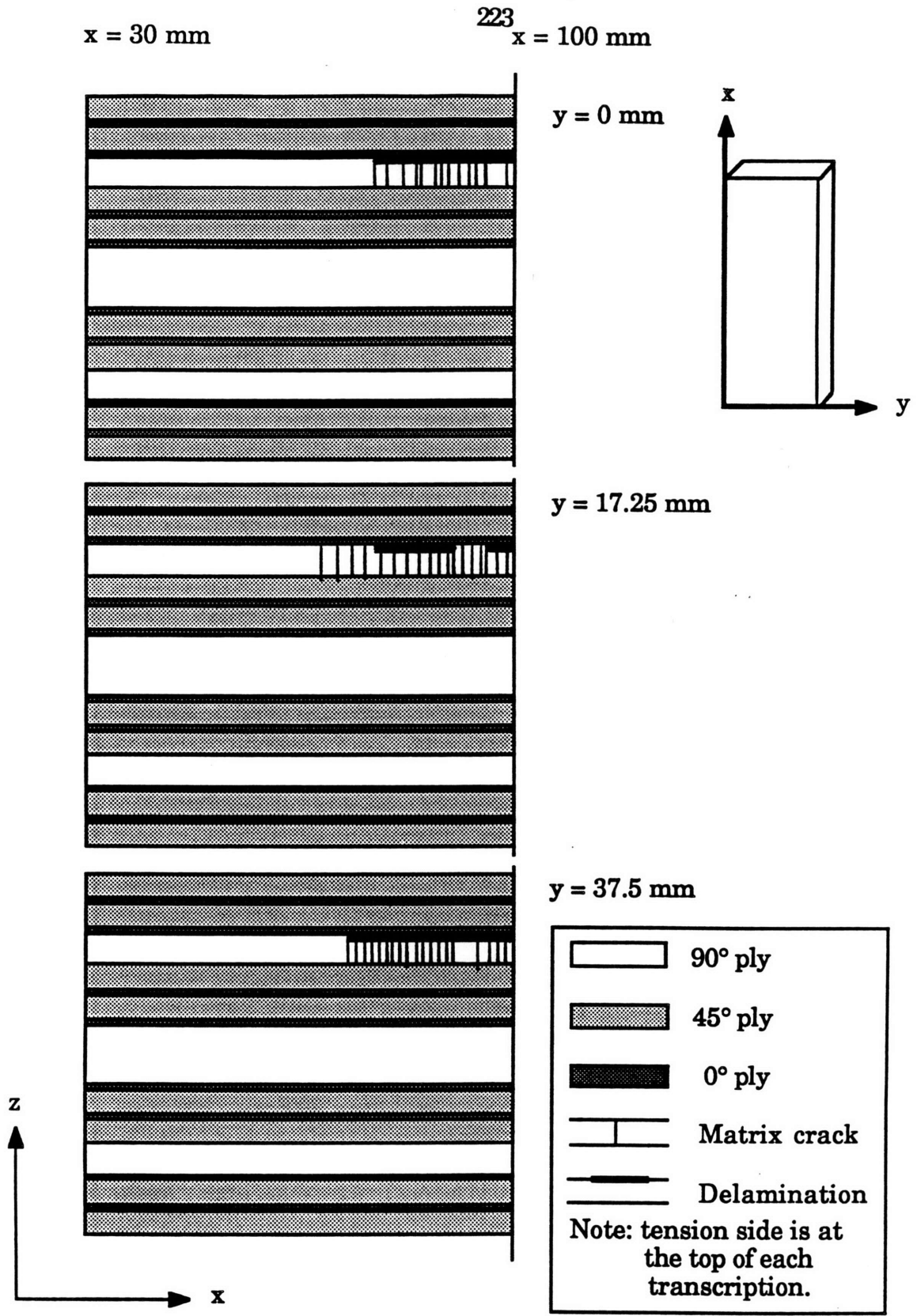


Figure B.11 Comparison of damage across width at the third characteristic damage state of the  $[(45^\circ_2/-45^\circ_2/0^\circ)_2/90^\circ_5]_{2s}$  layup.

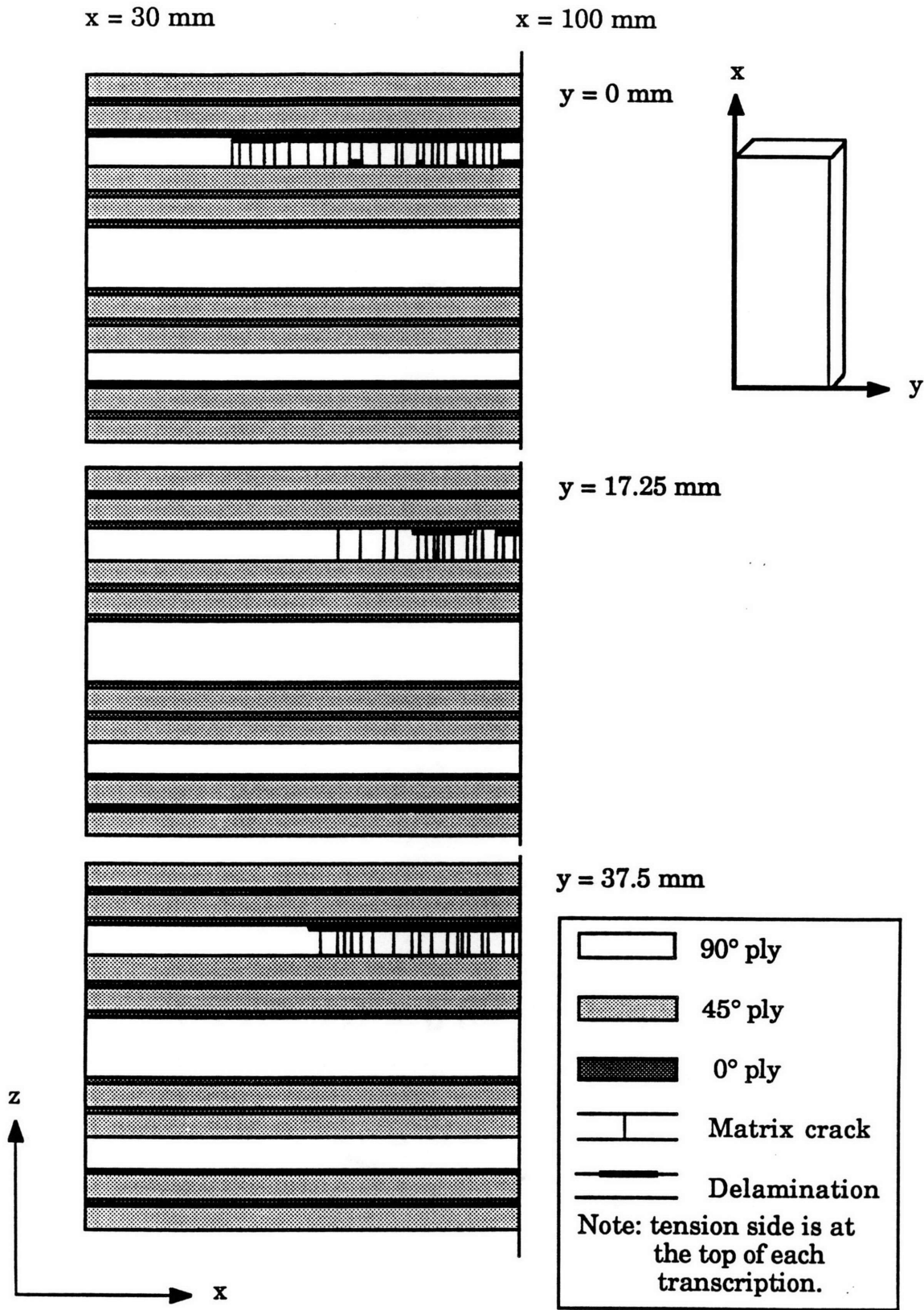


Figure B.12 Comparison of damage across width at the fourth characteristic damage state of the  $[(45^\circ_2/-45^\circ_2/0^\circ)_2/90^\circ_5]_{2s}$  layup.